Asphalt Binder Parameters and their Relationship to the Linear Viscoelastic and Failure Properties of Asphalt Mixtures

by

Ramadan Salim

A Dissertation Presented in Partial Fulfillment
of the Requirements for the Degree
Doctor of Philosophy

Approved April 2019 by the
Graduate Supervisory Committee:

Shane Underwood, Co-Chair
Kamil Kaloush, Co-Chair
Mike Mamlouk

ARIZONA STATE UNIVERSITY

May 2019

ABSTRACT

Asphalt concrete is a non-homogenous viscoelastic material; its behavior depends on the properties of the asphalt binder and the aggregate skeleton. The two major distresses in flexible pavements, fatigue cracking and rutting, have different mechanisms in that the way binders and mixtures behavior are related differ. Further complicating the issues is that distresses in asphalt pavement are dependent on climate, pavement structure, and traffic loads, in addition to factors such as properties of the asphalt mixture itself. Hence, to characterize the multiscale mechanics associated with binder to mixture behaviors, researchers characterized the fatigue and rutting resistance of asphalt binders and mixtures in the laboratory, and established specifications related to how asphalt mixtures would perform in the field.

This dissertation tackles the linkages across length scales with respect to rutting and cracking. Through the literature reviewed, studies regarding the linear and non-linear viscoelastic properties of asphalt mixture and the corresponding bitumen were identified. There was a wealth of data in this area. In addition, the relationship between the laboratory mixture short-term aging and the binder aging conditions were studied, characterized and analyzed.

The literature review showed that there exists a shortage of knowledge that directly examines the relationships between the binder nonlinear viscoelastic damage behaviors and mixture performance. Addressing this knowledge gap is the basic objective of this research. Specifically, the relationships between the non-recoverable creep compliance at 3.2 kPa ($J_{nr3.2}$) and the percent of elastic recovery ($R_{3.2}$) from the multiple stress creep and recovery

(MSCR) test and mixture rutting; and between mixture fatigue and binder linear amplitude sweep (LAS) were studied.

Finally, an aging study was performed to ensure that the binder tests properties reflect the condition of the binder during the mixture test when evaluating binder-to-mixture properties. The propensity to oxidize measured by calculating the aging ratio of various aged conditions (RTFO, PAV, and STOA) were gathered and analyzed.

This dissertation is dedicated to all my teachers and professors who have contributed immensely in shaping my career and helped me achieve my goals. Special dedication to my first teachers, my parents, my sisters, and my brothers for their guidance, support, and love without which none of this would be possible. This work is also dedicated to my dearest wife who has been a constant source of support and encouragement during the challenges of graduate school and life. I am truly thankful for having her in my life. This work is also dedicated to my beloved kids, Raif, Abdallah and Rakan, who have always loved me unconditionally. I can't force myself to stop loving

ACKNOWLEDGMENTS

I begin by expressing my most sincere gratitude, love and respect to my wife. She has been alongside me through this journey and provided companionship and support along the way. Her encouragement during exciting and challenging times helped me to remain focused on the outcome.

I would like to express my sincere gratitude to Dr. Shane Underwood for providing me the opportunity to work with him. I am grateful to him for his mentorship, guidance and valuable inputs throughout my graduate study.

Dr. Kamil Kaloush, my Co-advisor and mentor during my graduate work at Arizona State University, deserves my utmost appreciation and thanks. He was integral in recruiting me to ASU and has since helped me grow academically, professionally, and personally. My interactions with Dr. Kaloush not only enriched me as a researcher but also as a person in general.

I would like to thank Dr. Michael Mamlouk for serving on my committee and teaching me the important aspects of pavement engineering and pushing me in courses and research efforts throughout my graduate studies.

I want to thank Dr. Matthew Witczak and Dr. Claudia Zapata for their support, valuable discussions, ideas and feedback on my research work throughout my graduate studies. Also, I owe much gratitude and thanks to Dr. Jeffrey Stempihar, Dr. Waleed Zeiada, and Dr. Mena Souliman. Their efforts helped my transition to Arizona State University and I want to thank them for their assistance, guidance, friendship and inspiring conversations.

Special thank you to our laboratory managers, Mr. Jeff Long and Mr. Peter Goguen for providing laboratory support assistance and efforts to maintain research. Their time and help has been invaluable.

I express my gratitude to Mr. Robert McGennis from Holly Frontier, Mr. Mohammad Rahman from Delek and Mr. Sam Huddleston from Andeavor for their efforts in identifying and providing materials for the ADOT-SPR 742 project which were used in my dissertation work also.

Special thanks and appreciation is due to Akshay Gundla. His assistance in the laboratory and with data analysis helped immensely with my research projects. Also, collaborating with him on the ADOT-SPR 742 project has been very rewarding.

I'd like to thank all my present, and past colleagues in the Advanced Pavement Laboratory, Akshay Gundla, Jose Medina, Padmini Gudipudi, Ashraf Alrajhi, Hossein Noorvand, Ali Zalghout, Daniel Oldham, Waleed Zeiada, Jeff Stempihar, Craig Rees, Jordan Reed, Daniel Rosenbalm, Abdulaziz Alosta, Matild Dosa, Carmen Parks, Tina Pourshams, David Ramsey, Satish Kannan Nagarajan, Gurpreet Rai, Guru Sai Kumar Karnati, Babu Kanappan, and Ryan Stevens for their support and assistance throughout my studies.

My heartfelt gratitude to all my family members in Libya for their love, support and continuous encouragement.

Finally, I would like to thank the Ministry of Higher Education in Libya and the Arizona Department of Transportation (ADOT) for supporting my Ph.D. study.

TABLE OF CONTENTS

CHAPTER Page

CHAPTER Page

CHAPTER Page

LIST OF FIGURES

Figure Page

Figure Page

Figure Page

Figure Page

Figure Page

LIST OF TABLES

Table Page

Chapter 1. INTRODUCTION

1.1 Background

Asphalt concrete is a non-homogenous viscoelastic material, and its behavior depends on the properties of the asphalt binder and the aggregate skeleton. Cracking is one of the main types of distresses in asphalt pavements. The two major types of pavement distresses, fatigue cracking and rutting, have different failure mechanisms. Fatigue cracking is a load associated type of cracking which occurs when the number of load repetitions exceeds the fatigue life of the pavement; and the average temperature of the pavement layer is at the pavement's critical temperature for fatigue cracking. Rutting is usually caused by shear deformation at high temperatures and high traffic loading. In combination with other potential problems, these distresses impact the serviceability of the road and can lead to some safety issues. Cracking in asphalt pavement is not only dependent on the climate, pavement structure, and traffic loads but also on other factors such as the properties of the asphalt mixture itself. Hence, researchers have tried to characterize the fatigue and rutting resistance of asphalt binders and mixtures in the laboratory and establish specifications related to how asphalt mixtures will perform in the field.

Asphalt binder plays an important role in asphalt mixture performance. Changes in stiffness, relaxation capability and aging condition of the binder can alter the cracking resistance of the mixture. The relationship between binder properties and mixture properties is complicated and is still not completely understood. In the past, many studies have been conducted on the binder and mixture properties that are associated with the cracking performance of asphalt mixtures. However, most of these studies utilized now outdated techniques for the binder and mixture performance testing. The most common

asphalt binder rutting and fatigue specifications are the ratio of dynamic shear modulus to the sine of the phase angle, $|G^*|/\sin\delta$ and $|G^*|\sin\delta$ respectfully, parameters in the Performance Grading (PG) standard. These parameters are measured using an oscillation test in the linear viscoelastic (LVE) range, but in pavements, the deformations and the cracks that occur during damage are substantially higher and involve non-linear viscoelastic (NLVE) behaviors. When the LVE and NLVE behaviors are closely correlated, specifications limited to LVE behaviors can work quite well. However, over the years, experience has shown that the LVE parameter has poor correlation to asphalt mixture rutting and fatigue.

Researchers have developed various cracking index parameters to evaluate the cracking potential of asphalt binders and mixtures, but there is still a question of how mixture properties change with changes in binder characteristics, and how the binder - mixture parameters may otherwise rank the expected performance of materials with respect to cracking. Additionally, there is a question as to how these correlations will relate with polymer modified asphalts.

1.2 Research Objective

The goal of this research is to facilitate better prediction of the asphalt mixture's damage and/or performance under variable temperatures and loading conditions to better reflects asphalt mixtures and pavements behavior. To meet this goal, the objective of this dissertation is to identify and quantify the relationship of existing non-linear viscoelastic asphalt binder tests to damage in asphalt mixtures.

1.3 Research Approach

The scope of this study is confined to the characterization of the linear viscoelastic properties (in the small strain amplitude domain) and the failure properties (in the highly non-linear domain) of bituminous materials when considering a small number of loading cycle, at low and high temperatures.

A research plan including a large experimental program focusing on the thermomechanical behavior of bituminous materials at low and high temperatures is discussed. The aim is to establish the links between the characteristics of the binder and the properties of bituminous mixes. Another parallel objective of the study is to quantify the differences/similarities in asphalt binder between standard laboratory aging protocols of mixtures and binders. Twenty different binders were used with three different types of aggregate sources and grading. In order to achieve this objective, the following steps were followed:

1. Measuring the linear viscoelastic properties of asphalt mixture and the corresponding bitumen to investigate the relationship between the dynamic shear modulus $|G^*|$ of asphalt binders and those of asphalt mixtures $|E^*|$. This objective involves four subtasks.
    a. Performing mix design and measuring the mixture volumetric properties and the aggregate gradation of the study asphalt mixtures.
    b. Performing temperature-frequency sweep experiments on asphalt binders and using time-temperature superposition principle to develop master curves. Using the data from the temperature-frequency sweep experiments, to calculate various LVE parameters.

c. Performing dynamic modulus test on asphalt mixtures at a range of temperatures and loading frequencies. Also, displaying dynamic modulus results for all the mixtures by developing the master curves.

d. Different dynamic modulus $|E^*|$ predictive models will be used for detailing the discussion on the relationship between the dynamic modulus $|E^*|$ and mixture volumetric properties, aggregate gradation, and binder properties

2. Identify the appropriate binder aging method that is demonstrative of short-term oven aging on asphalt mixtures. The specific subtasks are:

   a. Performing the RTFO (rolling-thin film oven) aging for asphalt binders.

   b. Preforming the PAV (pressure aging vessel) aging for asphalt binders.

   c. Implementing the STOA (short-term oven aging) for asphalt mixtures.

   d. Preforming the laboratory procedure of the extraction and recovery of short-term aged loose mix.

   e. Examining the quality of the extraction and recovery asphalt binders by using the Attenuated Total Reflectance Fourier Transform Infrared Spectroscopy (ATR-FTIR).

   f. Performing temperature-frequency sweep experiments on asphalt binders RTFO, PAV, and STOA aged conditions.

   g. Measuring the propensity to oxidize measured by calculating the aging ratio of RTFO, PAV, and STOA aged conditions.

   h. Performing the analyses regarding the development of the best demonstrative of short-term oven aging on asphalt mixtures to the asphalt binders aged conditions.

i. Identify the appropriate binder aging method that is demonstrative of short-term oven aging on asphalt mixtures.

3. Estimating the HMA laboratory rutting and equivalent parameters for rutting for asphalt binder in the lab. Also, studying the relative merits of these two parameters. This objective involves three subtasks.
    a. Performing AASHTO M320 for the asphalt binder and estimating the linear viscoelastic binder rutting parameter (ratio of dynamic modulus to the sine of the phase angle, $|G^*|/\sin\delta$). Also, performing AASHTO M332, and estimating the nonlinear viscoelastic binder rutting parameter (the non-recovered creep compliance, J_{nr}, is used for this purpose).
    b. Performing for each mixture two rutting performance tests: Hamburg wheel test and repeated load permanent deformation (flow number) test and estimating the mixture rutting.
    c. Correlating the two binder rutting parameters to one another for non-polymer and polymer modified asphalts. Also, correlating the two binder rutting parameters to both mixture rutting tests (Hamburg wheel and flow number).
4. Justifying the exact position of the relationship between the non-recoverable creep compliance at 3.2 kPa ($J_{nr3.2}$) and the percent of elastic recovery ($R_{3.2}$) from the multiple stress creep and recovery (MSCR) test (included in AASHTO M332 specification) based on binder performance. This objective involves five subtasks.
    a. Preparing polymer-modified binders with similar $J_{nr3.2}$ and varying MSCR $R_{3.2}$ and splitting into four groups based on their $J_{nr3.2}$ value.

b. Performing AASHTO M332 and estimating the nonlinear viscoelastic binder rutting parameter ($J_{nr3.2}$ and MSCR $R_{3.2}$).

c. Performing the dynamic modulus test, Hamburg Wheel Tracking test, and axial fatigue test for the lab blended asphalt mixtures.

d. Comparing the results from the dynamic modulus test, Hamburg Wheel Tracking test, and axial fatigue test to $R_{3.2}$.

e. Improving and presenting an alternative $J_{nr3.2}$ vs $R_{3.2}$ relationship based on this study's results.

5. Estimating the binder fatigue parameters and axial fatigue test for asphalt mixtures. Also, studying the results and the connections between the relative merits of these two parameters. This objective involves three subtasks.

   a. Performing AASHTO M320 for the asphalt binder and estimating the linear viscoelastic binder fatigue parameter ($|G^*|\sin\delta$). Also, performing AASHTO TP 101-12 (Linear Amplitude Sweep (LAS)), and estimating the nonlinear viscoelastic binder fatigue parameter.

      Performing axial fatigue test to assess the resistance of the current Arizona asphalt mixtures to fatigue damage. Also, displaying in the fatigue test data results for all the mixtures using simplified viscoelastic continuum damage theory (S-VECD) formulation.

   b. Correlating the two binder fatigue parameters to axial fatigue test for non-polymer and polymer modified asphalts by using different fatigue failure criteria predictive methods.

The experimental plan adopted to achieve the above-mentioned study objectives is presented in Figure 1-1.

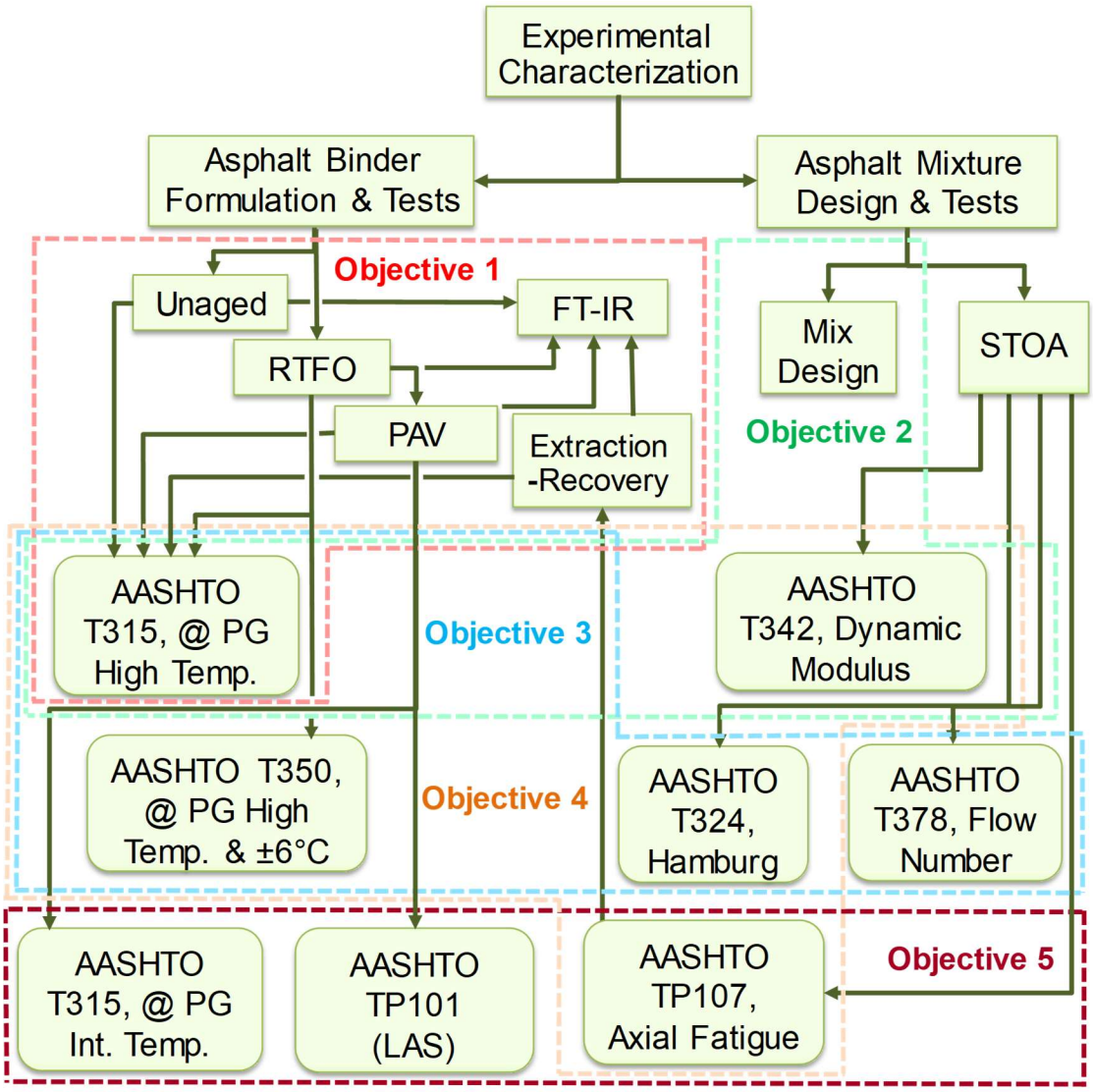

FIGURE 1-1EXPERIMENTAL LAYOUT OF THE RESEARCH STUDY.

1.1 DISSERTATION OUTLINE

This document is divided into nine chapters.

Chapter 1: This chapter provides an overall introduction and background of this study, the need for this research as well as the research objectives.

Chapter 2: This chapter reviews the literature regarding relating dynamic shear modulus |G^*| of asphalt binders to HMA dynamic modulus |E^*|, HMA laboratory rutting and equivalent parameters to estimate rutting for asphalt binder in the lab, and HMA laboratory fatigue and equivalent methods to estimate asphalt binder fatigue in the lab.

Chapter 3: In this chapter, the study materials and the experimental techniques that will be used in the study are described in detail. Information pertaining to the types of asphalt, modification, suppliers, and the crude sources will be provided. The sample preparation techniques are also discussed.

Chapter 4: This chapter uses a study wherein the linear viscoelastic properties of asphalt mixture and the corresponding bitumen are measured to investigate the relationship between the dynamic shear modulus |G^*| of asphalt binders to those of asphalt mixtures |E^*|.

Chapter 5: In this chapter, the relationship between the mixture short-term aging in the laboratory and the binder aging are explained.

Chapter 6: In this chapter, HMA laboratory rutting and equivalent parameters to estimate rutting for asphalt binder in the lab are studied.

Chapter 7: In this chapter, the effect of percent recovery from the multiple stress creep and recovery (MSCR) test on performance of asphalt mixtures is investigated

Chapter 8: This chapter provides details regarding HMA laboratory fatigue and equivalent methods to estimate asphalt binder fatigue in the lab.

Chapter 9: Summary, Conclusions and Future Work - This chapter provides a summary of conclusions drawn from the research conducted and the scope of future work. Also, this chapter provides the achieved lessons from the study.

Chapter 2. LITERATURE REVIEW

This chapter reviews the literature regarding to the linear viscoelastic properties and non-linear viscoelastic behaviors of asphalt mixture and the corresponding bitumen. The chapter is segmented into four main parts. In the first part, the relationship between the laboratory mixture short-term aging and the binder aging conditions are discussed. In the second part, the relationship between the dynamic shear modulus $|G^*|$ of asphalt binders to HMA dynamic modulus $|E^*|$ are presented. In the third part, HMA laboratory rutting and equivalent parameters to estimate rutting for asphalt binder in the lab are searched out. Finally, a detailed discussion on the relationship between the HMA laboratory fatigue and equivalent methods to estimate asphalt binder fatigue in the lab are identified.

2.1 The Relationship between the Mixture Short-Term Aging in the Laboratory and the Binder Aging

Heating of asphalt during production and construction causes the volatilization and oxidation of binders used in mixes. Volatilization and oxidation cause degradation of asphalt pavements by increasing the stiffness of the binders. Degradation of asphalt binders by volatilization and oxidation due to high production temperature occur during early stages of pavement life and are known as Short Term Aging (STA). Superpave binder specifications recognize the importance of STA and require the asphalt binder to be tested in three critical stages: the first stage is represented by an original asphalt binder which has to be transported, stored, and handled prior to mixing with the aggregate, the second stage is represented by the aged asphalt binder after hot mix asphalt (HMA) production and construction (short-term aging), and the third stage is represented by an asphalt binder which undergoes further aging during a long period of service [1]. For asphalt binders, the

rolling-thin film oven (RTFO) aging test simulates the second stage. For asphalt mixtures, the recommended laboratory procedure for short-term aging is to heat the loose mix in a forced draft oven for 4 h at a temperature of 135ºC [2]. The short-term oven aging (STOA) simulates the aging of the asphalt mixture during the construction process.

Many studies have been conducted to evaluate the aging characteristics of asphalt binders since these properties can be easily measured using a rotational viscometer, a dynamic shear rheometer, a bending beam rheometer, and a direct tension tester, among others [3,4,5,6,7,8]. Quite a few studies dating back to the 1960s and further evaluated the short-term aging of asphalt mixtures in the field, and a consistent conclusion was obtained that most short-term aging of asphalt mixtures occurred during production and construction due to the high temperatures involved [79-81]. More recent studies have identified several factors of asphalt mixtures and production parameters that could significantly affect the short-term aging characteristics of asphalt mixtures; these factors include binder source, binder type, aggregate absorption, plant type, production temperature, and silo storage time [80-89].

Both the rolling thin film oven test (RTFOT) and the short-term oven aging (STOA) methods are used in the laboratory to represent the aging of an asphalt binder during plant mixing, transportation and paving. The standard practice for laboratory asphalt mix design is to simulate the binder absorption and aging that occurs during production and construction by short-term oven aging (STOA) or conditioning the loose mix prior to compaction for a specified time and temperature. For HMA, the recommended procedure in AASHTO R 30 for preparing specimens for volumetric mixture design is 2 hours at the compaction temperature (Tc), while it is 4 hours at 275°F (135°C) for preparing specimens

for performance testing [78]. The rolling thin film oven test (RTFOT) measures the effect of heat and air on a moving film of semi-solid asphaltic binder and the test is conducted at 163°C for 85 min as recommended by AASHTO T 240 and ASTM D 2872 [90]. However, previous studies on asphalt mixture aging were found short-term oven aging method of asphalt mixtures to have a more aging effect than RTFO aging method.

A study by Aschenbrener and Far was conducted to evaluate the short-term aging of HMA [91]. Nine projects were selected throughout Colorado and four different laboratory STOA protocols including 0, 2, 4, and 8 hours at field compaction temperatures were used to fabricate laboratory specimens. The specimens were tested to determine their theoretical maximum specific gravity (G_{mm}) values and Hamburg wheeltracking test (HWTT) results in accordance with AASHTO T 209 and AASHTO T 324, and the results were compared against results obtained on counterpart mixtures produced in the field. The performance of the laboratory specimens in the HWTT was highly dependent upon the STOA time. In addition, laboratory specimens that were short-term aged for 1 to 3 hours at the field compaction temperature exhibited equivalent HWTT performances compared to field specimens. Thus, according to the G_{mm} and HWTT results, researchers recommended conditioning the laboratory-produced samples for 2 hours at the field compaction temperature in order to simulate asphalt aging during plant production.

NCHRP Project 9-49 performed a laboratory conditioning experiment focused on evaluation of the moisture susceptibility of WMA technologies and recommended a laboratory STOA protocol of 2 hours at 275°F (135°C) for HMA and 2 hours at 240°F (116°C) for WMA in order to simulate the short-term aging of the asphalt mixture occurring during production and construction [92]. In the study, five different laboratory

STOA protocols were selected based on the available literature and used for fabricating HMA and WMA LMLC (laboratory mix and laboratory compact) specimens. These specimens were tested to determine the effect of each laboratory STOA protocol on mixture resilient modulus (MR) stiffness. Laboratory STOA protocols were able to produce asphalt mixtures with significantly increased stiffness. Additionally, the effect from the short-term aging temperature was more pronounced than the short-term aging time. The final recommendation of NCHRP Project 9-49 for HMA LMLC specimens was 2 hours at 275°F (135°C).

Previous study on asphalt mixture aging, based on the increase in the large molecular size (LMS) ratios, was found RTFO aging method to have a less aging effect than short-term oven aging methods of asphalt mixtures [9]. In this study, to compare the aging effect of the rolling thin film oven test (RTFOT) and the short-term oven aging (STOA) methods, nine asphalt binders (three control, three SBS modified, and three rubber-modified binders) were prepared, and five aging times in the RTFOT and four aging treatments in the STOA were used in this study. A series of gel permeation chromatography (GPC), rotational viscosity (RV), and dynamic shear rheometer (DSR) tests were conducted. From these results, the study concluded that based on the increase in the LMS ratios from GPC test, the RTFOT method (85 min at 163 C) was found to have less aging effect on the binders than the STOA methods for asphalt mixtures in the laboratory. The study presented the average increase of LMS ratios (LMS ratio = LMS value after aging/LMS value before aging) of nine asphalt binders after the RTFOT and the four STOA treatments. Since the original LMS contents are different from one another, it is appropriate to use LMS ratios in the analysis. The RTFOT resulted in an average increase of 21% in LMS ratios of

samples, while the increase from the STOA treatment is 34% (at 135 C for 4 h). These results indicate that the RTFOT has less effect on the aging of asphalt binders than the STOA treatments for the materials used in this study.

The NCHRP Project 9-36 compares aging indices from the mixture testing with those from the RTFOT, for an unaged binder modulus of 10 kPa, the lowest stiffness included in the mixture testing conditions. The study shows a reasonable correlation between the AASHTO R30 mixture aging and the RTFOT. The slope of the relationship indicates that the aging index from the short-term binder aging test (RTFOT) is less than that obtained from short-term aging of mixtures in accordance with AASHTO R30. The research concluded that the binder aging that occurs when a mixture is short-term conditioned in a forced draft oven for 4 hours at 135°C per AASHTO R30 generally exceeds the aging that occurs in the short-term binder aging procedures. They found that the aging was greater by 25-50% [10].

The objectives of NCHRP project 9-52 Phase I were to develop a laboratory STOA protocol for asphalt loose mix prior to compaction to simulate the aging and asphalt absorption by the aggregate as it is produced in a plant and then loaded into a truck for transport, and to identify factors with significant effects on the performance-related properties of short-term aged asphalt mixtures [93]. Nine field sites in Texas, New Mexico, Connecticut, Wyoming, South Dakota, Iowa, Indiana, and Florida were included in the Phase I experiment. Cores at construction and plant mixed, plant-compacted (PMPC) specimens were obtained for each mixture at each field site, in conjunction with raw materials including asphalt binder, aggregates, and RAP and RAS used for LMLC specimen fabrication. Based on previous research for NCHRP Project 9-49 the laboratory

STOA protocols of 2 hours at 275°F (135°C) for HMA was used for conditioning loose mix prior to compaction. All these asphalt mixtures subjected to short-term aging during production and compaction in the field or laboratory were tested with the MR, $|E^*|$, and HWTT tests. Binders were extracted from short term aged asphalt mixtures from three field sites (i.e., Indiana, Florida, and Texas II), recovered, and then tested with the DSR and Fourier transform infrared spectroscopy (FT-IR) to characterize their rheological and chemical properties, including continuous performance grade (PG) and complex shear modulus $|G^*|$ at 77°F (25°C), and chemical characteristics in terms of the FT-IR carbonyl area (CA). The determination of the continuous PG was helpful in characterizing the change in asphalt binder properties with short-term aging, and the parameter $|G^*|$ at 77°F (25°C) was included in order to provide additional information on binder stiffness measured at the same temperature as the mixture MR stiffness. The mixture and binder results for LMLC specimens fabricated using the selected STOA protocols were compared against those for cores at construction and PMPC specimens to validate the laboratory STOA protocol of 2 hours at 275°F (135°C) for HMA. Additionally, a second set of comparisons was performed to evaluate the effects of mixture and production factors on the short-term aging of asphalt mixtures for each type of sample, i.e., cores at construction, PMPC specimens, and LMLC specimens. Recommended changes to the current AASHTO R 30 short-term aging protocol are given in the report. The basic changes resulting from this project include

1. fixing the compaction temperatures for WMA at 240°F (116°C) and HMA at 275°F (135°C).

2. conditioning the sample for 2 hours at the compaction temperature regardless of whether the sample is being prepared for volumetric mix design or performance testing.

It should be noted that RTFO and PAV instruments are not intended to directly replicate in-service conditions (although some approximate guidelines and correlations are proposed in the literature). Instead, they are meant to provide some qualified estimate of the aging sensitivity of asphalt. Furthermore, the motivation for this work need is a preliminary study at Arizona State University advanced pavements laboratory that showed similar results. In that study, asphalt binder was extracted and recovered from an asphalt mixture after short-term oven aging and the binder tested for modulus and evaluated for an increase in double bonded oxygen. These changes were then compared to what was observed in original, RTFO, and PAV aged asphalt. It was found that the short-term oven aging most closely resembled the PAV binder at some cases. The significance of this finding is that during the grading process, the sensitivity of the asphalts to oxidation may be incorrectly assessed for Arizona conditions with the existing RTFO and PAV aging conditions and will help this specific research to use the equivalent asphalt properties when the relationship between the mixture and the binder will be recognized.

2.1.1 Findings from the Literature Review for Short-Term Aging.

In general, the main findings of the previous studies on short-term aging of asphalt mixtures can be summarized as follows:

- Substantial aging in the field occurs during production through placement and compaction.

- Binder type, binder source, aggregate absorption, recycled materials (i.e., RAP and/or RAS), production temperature, and silo storage are factors that have a significant effect on mixture short-term aging characteristics.
- An increase in laboratory STOA temperature, time, or both increases asphalt mixture stiffness. Short-term aging is more sensitive to STOA temperature than STOA time.
- Researchers recommended conditioning the laboratory-produced samples for 2 hours at the field compaction temperature in order to simulate asphalt aging during plant production.
- Several research concluded that the binder aging that occurs when a mixture is short-term conditioned in a forced draft oven for 4 hours at 135°C per AASHTO R30 generally exceeds the aging that occurs in the short-term binder aging procedures.

2.1.2 Knowledge of Gaps for Short-Term Aging.

Despite the previous research efforts, there are still some aspects of the short-term aging of asphalt mixtures that have not been fully resolved, which include the following:

- A study to ensure that the properties of the binder represent the one that exist inside the mixture when testing the asphalt binder in the laboratory.
- A standard laboratory short-term aging protocols that guarantee the binder tests properties reflect the condition of the binder during the mixture test when evaluating binder-to-mixture properties.

2.2 Relating Dynamic Shear Modulus |*G**| of Asphalt Binders to HMA Dynamic Modulus of Elasticity |*E**|

HMA mixtures are subjected to a wide range of load and environmental conditions. The response to these conditions is complex and involves the elastic, viscoelastic and plastic characteristics of the material used in the pavement. The stiffness of a HMA mix is a specific material response parameter that determines the strains and displacements pavement structure as it is loaded or unloaded. In the early 1950's, Van der Poel of the Shell Oil Company introduced the term "stiffness" (or stiffness modulus) [73]. The stiffness of a HMA mix is a modulus that is dependent upon the loading time and temperature of the mix. Due to the immense importance of stiffness in the analysis, design and performance evaluation of HMA mixture and flexible pavement structures; researchers have been trying to develop accurate stiffness (modulus) laboratory test protocols as well as to develop accurate predictive models and equations. Over the last sixty years, numerous models and regression equations have been developed to predict the stiffness of a HMA mix. Historically, the stiffness predictive models and equations were developed based on the conventional multivariate linear regression or non-linear regression analysis of laboratory test data and the established or anticipated basic engineering behavior and/or properties of the HMA mixture and/or its components.

The dynamic modulus, |*E**|, is an important property that defines the stiffness characteristics of hot mix asphalt (HMA) mixtures as a function of loading rate and temperature. There are at least three most significances of this material property. First, it is one of the principal material property inputs in the Mechanistic-Empirical Pavement Design Guide (MEPDG) and software developed by NCHRP Project 1-37A (ARA, 2004) [11]. The MEPDG uses a master curve and time-temperature shift factors in its internal computations. In the MEPDG, the master curve is constructed using a hierarchical structure of inputs ranging from laboratory tests on HMA

mixtures and binders to estimates based on properties of the HMA mixtures. Second, the |*E**| is one of the primary HMA properties measured in the Superpave simple performance test protocol that complements the volumetric mix design. Third, the |*E**| is one of the fundamental linear viscoelastic (LVE) material properties that can be used in advanced HMA and pavement models that are based on viscoelasticity.

In this part, previous experimental comparisons of mixture modulus and binder rheology studies are reviewed. Also, the existing models used to estimate |*E**| values models are evaluated. In addition to that, the fundamental binder properties used in these models are described as well.

2.2.1 Predictive Models for the Dynamic Modulus, |E*|

Several alternative predictive relationships have been developed to estimate the |*E**| from simpler material properties and volumetric properties. These predictive relationships can be used to estimated |*E**| values. The predictive relationships identified by the research team are Original Witczak Equation (NCHRP 1-37A), Modified Witczak |*G**| Equation (NCHRP 1-40D), Hirsch Model, Al-Khateeb model, Simplified Global Model, Improved Hirsch Model, Van der Poel (Shell Oil's Early Version) Model, Law of Mixtures Parallel Model, ANN Model, and *MR*-|*E**| Model. The first five relationships will be used in chapter 4 analysis. The predictive relationships described briefly in the following subsections.

2.2.1.1 Van der Poel (Shell Oil's Early Version) Model.

One of the earliest, but most well-known asphalt binder viscosity (stiffness) predictive models, was developed by Van der Poel of the Shell Oil Company based upon over 20 years of laboratory work at "Koninklijke/Shell-Laboratorium, Amsterdam (KSLA)" [73]. This predictive method is a part of the well-known "KSLA Method". It uses a nomographic

solution to obtain the asphalt binder stiffness (S_b), which is assumed to be a function of the temperature, time of loading and the characteristics of the bitumen in a mix expressed in terms of the penetration index (PI). The Shell Oil nomograph is shown in Figure 2-1.

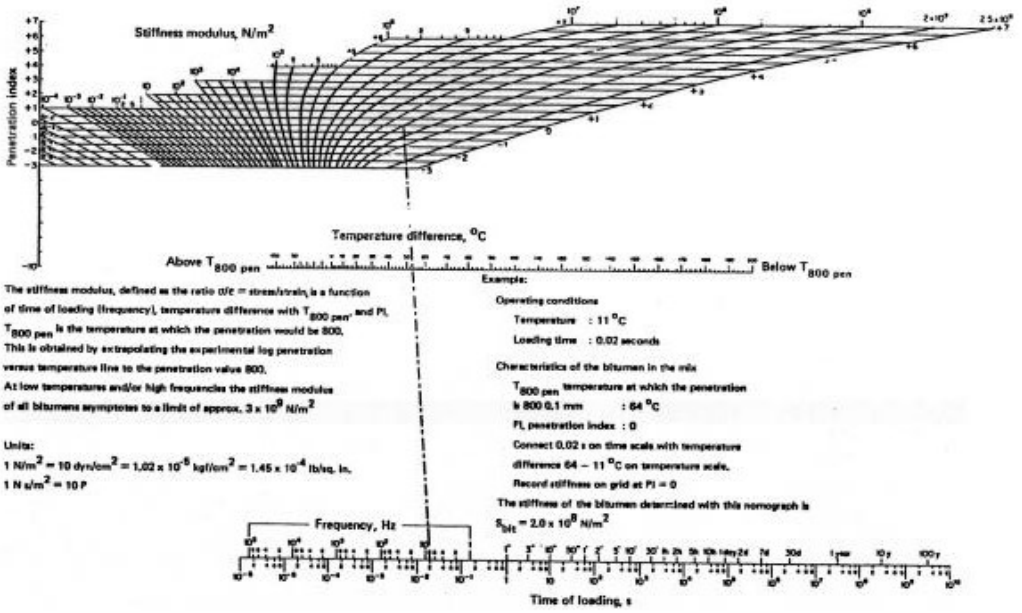

Figure 2-1 Nomograph for Stiffness of Asphalt Binders [73]

The binder properties needed in the nomograph are the viscosity at T_{800pen} and PI. T_{800pen} is the temperature at which the penetration would be 800. It was found that all asphalts have an equiviscous magnitude or penetration of 800 at their Ring and Ball Softening Point ($T_{R\&B}$). Thus,

$$T_{dif} = T_{RB} - T, \tag{2-1}$$

defines a normalized temperature under which differences in viscous behavior types disappear. For the intermediate (viscoelastic) behavior, use of the penetration index (*PI*) is made as follows:

$$\frac{20-PI}{10+PI}=50\left(\frac{\partial \log Pen}{\partial T}\right) \tag{2-2}$$

In other words:

$$\frac{20-PI}{10+PI}=50\left(\frac{\log 800-\log Pen}{T_{RB}-T}\right) \tag{2-3}$$

The binder PI is calculated as follows:

$$A=\frac{\log\left(Penetration\ at\ T\right)-\log 800}{T-T_{R\&B}} \tag{2-4}$$

where,

Pen = penetration at the temperature of interest as obtained from the standard Penetration Test, 0.1 mm

A = temperature susceptibility (see equation 2-4)

T = temperature of interest, ºC

In lab, the binder stiffness can be determined by either a creep test with a loading time t or dynamic shear test under an angular loading frequency of ω (or a sinusoidal loading frequency of f_s). Van der Poel defined t as follows:

$$t=\frac{1}{\omega}=\frac{1}{2\pi f_s} \tag{2-5}$$

2.2.1.2 Original Witczak Equation (NCHRP 1-37A)

Andrei et al. (1999) revised the original Witczak $|E^*|$ predictive equation based on data from 205 mixtures with 2750 data points. The revised equation is [11,12].:

$$\log_{10}\left|E^*\right| = -1.249937 + 0.02923\,p_{200} - 0.001767\left(p_{200}\right)^2 - 0.002841\,p_4 - 0.05809\,V_a$$
$$-0.082208\left(\frac{V_{beff}}{V_{beff}+V_a}\right) + \frac{3.871977 - 0.0021\,p_4 + 0.003958\,p_{3/8} - 0.000017\left(p_{3/8}\right)^2 + 0.00547\,p_{3/4}}{1+\exp\left(-0.603313 - 0.313351\log f - 0.393532\log\eta\right)} \quad (2\text{-}6)$$

where,

$|E^*|$ = dynamic modulus of HMA (105 psi);

p_{200} = percentage of aggregate passing #200 sieve;

p_4 = percentage of aggregate retained in #4 sieve;

$p_{3/8}$ = percentage of aggregate retained in 3/8 inch sieve;

$p_{3/4}$ = percentage of aggregate retained in 3/4 inch sieve;

V_a = percentage of air voids (by volume of mix);

V_{beff} = percentage of effective asphalt content (by volume of mix);

f = loading frequency (Hz); and

η = binder viscosity at temperature of interest (106 poise).

Witczak's equation is based on a nonlinear regression analysis using the Generalized Reduced Gradient optimization approach in Microsoft Excel's Solver. This model incorporates mixture volumetric properties and aggregate gradation.

The limitations of original Witczak's equation, acknowledged by Bari et al. (2005), include reliance on other models to translate the currently used $|G^*|$ measurement into binder viscosity [13]. It is also noted that because the model is based on regression analysis, extrapolation beyond the calibration database should be restricted. Bari et al. (2005) also mentioned limited volumetric influence (precision) when the model is compared to the Shell Oil Model. Other researchers have also noted the need for improved sensitivity to volumetric properties, such as voids in mineral aggregate (VMA), voids filled with asphalt (VFA), asphalt content percentage (%AC) and air void percentage (%AV) [14].

Several studies have indicated that the Witczak $|E^*|$ models show significant scatter especially at the low and/or high $|E^*|$ modulus extremes [94-99]. There are also suggestions by Schwartz in 2005 that the Witczak $|E^*|$ predictive models are dominated by the influence of temperature and understate the influence of other mixture parameters [95]. This indicates that these $|E^*|$ predictive models may not be able to predict successfully the performance differences among different HMA mixtures under a given set of project-specific environmental conditions and design traffic.

2.2.1.3 Modified Witczak Equation Based on $|G^*|$ (NCHRP 1-40D)

Due to the desire to include binder $|G^*|_b$ in the predictive model, Witczak reformulated the model in Equation (2-7) to include the binder variable directly. The updated model is:

$$\log_{10}\left|E^*\right| = -0.349 + 0.754\left(\left|G^*\right|_b^{-0.0052}\right)\left(\begin{array}{l} 6.65 - 0.032p_{200} - 0.0072(p_{200})^2 + 0.011p_4 - 0.0001(p_4)^2 \\ +0.006p_{3/8} - 0.00014(p_{3/8})^2 - 0.08V_a - 1.06\left(\dfrac{V_{beff}}{V_{beff}+V_a}\right) \end{array}\right) + \frac{2.558 + 0.032V_a + 0.713\left(\dfrac{V_{beff}}{V_{beff}+V_a}\right) + 0.0124p_{3/8} - 0.0001(p_{3/8})^2 - 0.0098p_{3/4}}{1+\exp\left(-0.7814 - 0.5785\log\left|G^*\right|_b + 0.8834\log\delta_b\right)} \quad (2\text{-}7)$$

where,

$|G^*|_b$ = dynamic shear modulus of asphalt binder (psi); and

δ_b = binder phase angle associated with $|G^*|_b$, (degrees).

As with the NCHRP 1-37A model, Equation (2-7) is based on a nonlinear regression analysis using 346 mixtures with 7400 total data points. The measured results of the unmodified binders have a better correlation with the model ($R^2 = 0.87$) compared to those of the modified binders ($R^2 = 0.79$) in arithmetic scale. In the logarithmic scale, both binder types have $R^2 = 0.99$. The binder phase angle is predicted using an empirical equation ($R^2 = 0.83$).

Because some of the mixtures in this database do not contain $|G^*|_b$ data, the Cox-Mertz rule using correction factors for the non-Newtonian behaviors, i.e., Equation (2-8), is used to calculate $|G^*|_b$ from A-VTS values:

$$\left|G^*\right|_b = 0.0051 f_s \eta_{f_s,T} (\sin \delta_b)^{7.1542 - 0.4929 f_s + 0.0211 f_s^2} \tag{2-8}$$

$$\begin{aligned} \delta_b &= 90 + (-7.3146 - 2.6162 * VTS') * \log(f_s * \eta_{f_s,T}) \\ &+ (0.1124 + 0.2029 * VTS') * \log(f_s * \eta_{f_s,T})^2 \end{aligned} \tag{2-9}$$

$$\log\log \eta_{f_s,T} = 0.9699 f_s^{-0.0527} * A + 0.9668 f_s^{-0.0575} * VTS' \log T_R \tag{2-10}$$

where,

f_s = dynamic shear frequency;

δ_b = binder phase angle predicted from Equation (2-9) (degrees);

$\eta_{fs,T}$ = viscosity of asphalt binder at a particular loading frequency (fs) and temperature (T) determined from Equation (2-10) (cP); and

T_R = temperature in Rankine scale.

2.2.1.4 General "2S2P1D" Model and Relation between the Linear Viscoelastic Behaviors of Bituminous Binders and Mixes

A research including a large experimental campaign on the characterization of the viscoelastic behavior of different bituminous materials was developed in this study [74]. The aim is to establish the links between the viscoelastic properties (which are observed in the small strain domain) of binders and those of bituminous mixes. The viscoelastic behavior of bituminous binders and mixes has been studied by performing complex modulus tests at different temperatures and frequencies. A unique rheological model has been developed for the modeling of linear viscoelastic properties of both bituminous binders and mixes. This model consists of a generalization of the Huet-Sayegh analogical

model. Nine very different bitumens were selected to be investigated in order to study the influence of the binder: five hard pure bitumens (0/10, 10/20, 20/30, 35/50 and 50/70 penetration grade), two bitumens modified with a low content of elastomer, with or without crosslinking and two bitumens modified with a high content of elastomer or plastomer. Also, four different bituminous mixes, made respectively from two polymer modified and two pure bitumens with one type of aggregate and grading, have been tested. The mixture samples had 3±1% void content and a binder content of 6% by weight of the aggregate. The viscoelastic behavior of bituminous binders and mixes was evaluated using complex modulus tests. Analyses on test data for nine different binders and four mixes, with one mix design, show that the introduced model fits quite well the measurements. The following conclusions was drawn.

1. The construction of the polymer modified binders and mixes master curves relies on the introduced "Partial Time-Temperature Superposition Principle" (PTTSP). The PTTSP is considered as an effective approximate approach for analyzing viscoelastic data.
2. A general model "2S2P1D" (generalization of the Huet-Sayegh model) valid for both the bituminous binders and mixtures and based on a simple combination of physical elements (spring, dashpot and parabolic element) has been proposed.
3. The model translates the linear viscoelastic behavior of nine very different binders and four mixes (with one mix design) for any range of frequencies and temperatures.
4. The use of the introduced general model "2S2P1D" confirmed that the rheology of bituminous mixes can be correlated to that of binders.

2.2.1.5 Hirsch Model

Christensen et al. (2003) examined four different models based on the law of mixtures and chose the model that incorporates the binder modulus, VMA, and VFA because it provides accurate results in the simplest form [15]. The other, more complicated forms attempt to incorporate the modulus of the mastic or the film thickness, which are difficult parameters to measure. The suggested model for the $|E^*|$ estimation is as follows:

$$\left|E^*\right|_m = p_c\left[4{,}200{,}000\left(1-\frac{VMA}{100}\right)+3\left|G^*\right|_b\left(\frac{VFA*VMA}{10{,}000}\right)\right]+\frac{(1-p_c)}{\frac{\left(1-VMA/100\right)}{4{,}200{,}000}+\frac{VMA}{3\left|G^*\right|_b(VFA)}} \quad (2\text{-}11)$$

$$\varphi = -21(\log p_c)^2 - 55\log p_c \quad (2\text{-}12)$$

$$p_c = \frac{\left(20+3\left|G^*\right|_b(VFA)/(VMA)\right)^{0.58}}{650+\left(3\left|G^*\right|_b(VFA)/(VMA)\right)^{0.58}} \quad (2\text{-}13)$$

where,

$|E^*|_m$ = dynamic modulus of HMA in psi;

P_c = the aggregate contact volume;

VMA = percentage of voids in mineral aggregate in the compacted mixture;

VFA = percentage of voids filled with asphalt in the compacted mixture; and

φ = phase angle of HMA.

A strength of this model is the empirical phase angle equation, which is important for the interconversion of the $|E^*|$ to the relaxation modulus or creep compliance. Weaknesses of the model include the lack of a strong dependence on volumetric parameters, particularly at low air void and VFA conditions. Also, questions arise regarding the ability of the $|G^*|_b$ parameter to account for the possible beneficial effects of modifiers (Al-Khateeb et al., 2006) [16]. In addition, it must be noted that only 206 data points were used in determining the coefficients

in the Hirsch model, compared to 2750 data points for the original Witczak model and 7400 data points for the modified Witczak model.

2.2.1.6 Improved Hirsch Model

Christensen and Bonaquist (2015) presented an improved version of the Hirsch model for estimating the modulus of hot-mix asphalt (HMA) from asphalt binder modulus and mixture composition [17]. The original Hirsch model was developed in 2002 and has been shown by several independent researchers to be reasonably accurate. However, the authors believed that the model could be improved by addressing several issues: (1) simplifying the Hirsch equation mathematically; (2) including aggregate specific gravity as a predictor, which indirectly accounts for variations in aggregate modulus; (3) including strain level as a factor; (4) recalibrating the model using a data set gathered using the asphalt mixture performance tester following current standard protocols; and (5) addressing steric hardening during testing. Although it appears that under normal testing conditions strain sensitivity and steric hardening are not significant factors affecting HMA dynamic modulus, the goals were achieved. Verification of the model using a limited amount of independently collected data suggests that the improved model eliminates or reduces a tendency of the original model to underestimate HMA dynamic modulus values.

As discussed in the previous section, the Hirsch model is a mechanical analog for estimating the modulus of HMA. It consists of a parallel element of asphalt, aggregate and air, and a series element with the same composition. In applying the Hirsch model to HMA, it is assumed that the contact factor varies with temperature so that in effect, the relative proportions of material in the HMA that behaves as if they are in a series versus parallel arrangement also change with temperature. However, in analyzing the data generated during their research, it was discovered that the effect of the parallel element on modulus values estimated with the Hirsch model is

always negligible. This does not mean that the Hirsch model does not apply; again, it means only that the effects on the modulus of the HMA material behaving as a parallel element are negligible when compared to the effects of the material behaving as a series element. This leads directly to the following modified version of the Hirsch model:

$$\left|E^*\right|_{mix} = p_c\left[H_6 G_{agg}^{H_7}\left(1-\frac{VMA}{100}\right)+3\left|G^*\right|_{binder}\left(\frac{VFA*VMA}{10,000}\right)\right] \tag{2-14}$$

Where:

$$p_c = H_1+\left(1-H_1\right)\frac{\exp[H_2+H_3\ln\left(VFA/100\times\left|G^*\right|\right)+H_4 VMA+H_5\ln(\varepsilon)]}{1+\exp[H_2+H_3\ln\left(VFA/100\times\left|G^*\right|\right)+H_4 VMA+H_5\ln(\varepsilon)]} \tag{2-15}$$

Where:

$|E^*|_{mix}$ = dynamic complex modulus of an HMA mixture, in extension, MPa;

$|G^*|_{binder}$ = dynamic complex modulus of the asphalt binder in the mixture, in shear, Pa;

VMA = voids in the mineral aggregate for the HMA mixture, volume %;

VFA = voids filled with asphalt for the HMA mixture, volume %.

ε = strain level

$H_1, H_2, H_3 \ldots H_7$ are coefficients fitted to the model

H_1 (Logistic minimum) = 0.0060

H_2 (Logistic constant) = 0.6628

H_3 Ln (binder $|G^*|$) = 0.5861

H_4 (VMA) = −0.1287

H_5 Ln (Strain) = −0.1706

H_6 (Aggregate Gs) = 7960

H_7 (Aggregate exponent) = 1.5874

The standard error of the logarithms of $|E^*|$ for the modified model was, after rounding, exactly the same as the original model (0.0905). Furthermore, the standard error of the difference between the predicted $|E^*|$ values for the two models was extremely small – less than 0.2% – indicating that these forms of the Hirsch model are for practical purposes interchangeable. Again, it should be emphasized that this modified version of the Hirsch model does not mean that the original formulation is not valid, only that the second component of the model the part representing the series element in the mechanical analog – is negligible compared to the series component.

2.2.1.7 Law of Mixtures Parallel Model (Al-Khateeb Model) [98]

Based on their findings from the Hirsch model, Al-Khateeb et al. (2006) suggest the following model:

$$\left|E^*\right|_m = 3\left(\frac{100-VMA}{100}\right)\left(\frac{\left(90+10{,}000\left(\left|G^*\right|_b / VMA\right)\right)^{0.66}}{1{,}100+\left(900\left(\left|G^*\right|_b / VMA\right)\right)^{0.66}}\right)\left(\left|G^*\right|_g\right) \quad (2\text{-}16)$$

where,

$|G^*|_g$ = dynamic shear modulus of binder at the glassy state (assumed to be 145,000 psi).

Like the Hirsch model, this formulation is based on the law of mixtures for composite materials. In this model, the different material phases (aggregate, asphalt binder, and air) are considered to exist in parallel. This model, therefore, is a simpler interpretation of the Hirsch model. The researchers note that their model addresses one of the primary shortcomings of the Hirsch model, i.e., the Hirsch model's inability to accurately predict the $|E^*|$ of the mixture at low frequencies and high temperatures.

Strengths of this model include the improved prediction of high temperature and low frequency $|E^*|$ data for mixtures used in the Federal Highway Association Accelerated Loading Facility

(FHWA ALF) test strips. Weaknesses include a lack of model verification and the fact that the researchers who developed this model did so based on |*E**| values obtained from tests at higher than recommended strain amplitudes (200 με versus the recommended maximum of 75-150 με).

2.2.1.8 The ANN |*E**| Models [106]

In 2007, researchers at Iowa State University developed an approach for predicting HMA |*E**| using an artificial neural network (ANN) methodology using the same input parameters as the Witczak 1999 and 2006 |*E**| models [103]. Bari's comprehensive |*E**| database containing 7,400 data records used in the development of the Witczak 2006 model was also used in developing the ANN-based models [13,97]. The ANN methodology encompasses a wide array of computational tools loosely patterned after biological processes [104]. All ANNs are interconnected assemblages of mathematically simple computational elements. These computational elements contain a very limited amount of local memory and perform rudimentary mathematical operations on data passing through them. The computational power of ANN comes from parallelism—input data are concurrently operated upon processed by multiple computational elements. Details regarding the ANN methodology are available in the book by Tsoukalas and Uhrig [105]. A typical four-layered (i.e., one input-two hidden-one output layer) feed forward error-back propagation ANN architecture, as shown in Figure 2-2, was used in the development of the ANN |*E**| predictive models. The eight input variables of the Witczak 1999 and Witczak 2006 equations were used in the ANN 1999 and ANN 2006 models, respectively. The predicted dynamic modulus |*E**| was the sole output variable in all of the ANN models. For the ANN models, the 7,400 data were divided randomly into two different subsets: a training (calibration) subset containing

6,900 data points and a testing (validation) subset containing the remaining 500 data points. The training data subset was used to train the back-propagation ANN |*E**| prediction model, and the testing data subset was used to examine the statistical accuracy of the developed ANN model. Note that this is in contrast to standard regression techniques, where all of the data are used to calibrate the model and no data are held back for subsequent validation.

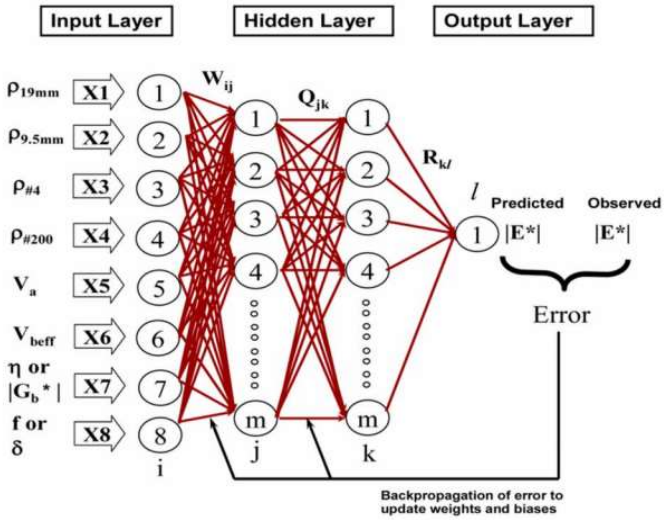

Figure 2-2 ANN 1999 and ANN 2006 [103]

The trained ANN models were also finally evaluated using all the 7,400 data points to obtain the overall predictive accuracy and compare it with the existing |*E**| predictive models. Several network architectures with two hidden layers were examined via parametric study to determine the optimum number of hidden layer nodes. Overall, the training and testing mean squared errors (MSEs) decreased with an increasing number of neurons in the hidden layers. The 8-30-30-1 architecture (eight inputs, 30 and 30 hidden neurons, and one output neuron, respectively), was chosen as the best architecture for both the ANN 1999 and ANN 2006 models based on its lowest training and testing MSEs. Details of the development of ANN-based |*E**| models outlined above are described in Ceylan et al. 2007(103).

2.2.1.9 ANN MODELS

In 2015 and during the FHWA-HRT-10-035 project, The North Carolina State University research team employed the ANN technique to develop new |*E**| predictive models (107). The primary advantage of this approach over statistical regression is that the functional form of the relationship is not needed a priori. Considering that so many variables affect |*E**| values and their interactions, the ANN technique captures complicated nonlinear relationships between |*E**| and other mixture variables better than regression analysis. The ANN technique was used in the research to develop several different models. Between the developed models, three ANN models were highlighted to be the most predictive ones. Statistical analysis and engineering judgment were utilized to rank the predictive models, with the MR ANN model being the best, the VV ANN model being the second best, and the GV ANN model being the third best. Each model differs according to the required input parameters. The most accurate ANN model was found to be the one that utilizes the resilient modulus as its primary input parameter. The other two models use mixture volumetric properties as well as a binder property as input variables. One model, the VV ANN, uses the binder viscosity and input frequency whereas the other model, the GV ANN, uses the binder shear modulus property. This ANN models are described in the final report of LTPP computed parameter: dynamic modulus (107).

Most of the database used to develop the models contains a comprehensive set of test data which itself is based on 14,341 test data points from 801 HMA mixtures. This database consists of the processed Witczak, Federal Highway Administration (FHWA) Mobile Trailer, WRI and Citgo databases, and NCSU database. In addition, the LTPP database was populated with |*E**| values at five temperatures and six frequencies by using the prioritized ANN models. This database contains information for a total of 1,806 layers. These layers have binder data available at a combination of different aging conditions, including unaged or original-

, RTFO-, PAV-, or field-aged. In the field-aged data, 2,223 records are available because, for some layers, properties may have been measured at different dates. The total resulting number of records is 7,641.

All of the ANN models developed in the study contain a mapping ANN architecture and are based on supervised learning. In the developed network, the learning method used is a feed forward back propagation, and the sigmoidal function is the transfer function. The three-layer network with two hidden layers was selected as the best configuration. The number of nodes in each layer differs according to the selected model. These node numbers were determined after a systematic study of each model. In each case, the network follows the same basic structure that is schematically illustrated in FIGURE 2-3. A more formal mathematical representation for each of these models is given in the final report of LTPP computed parameter: dynamic modulus [107].

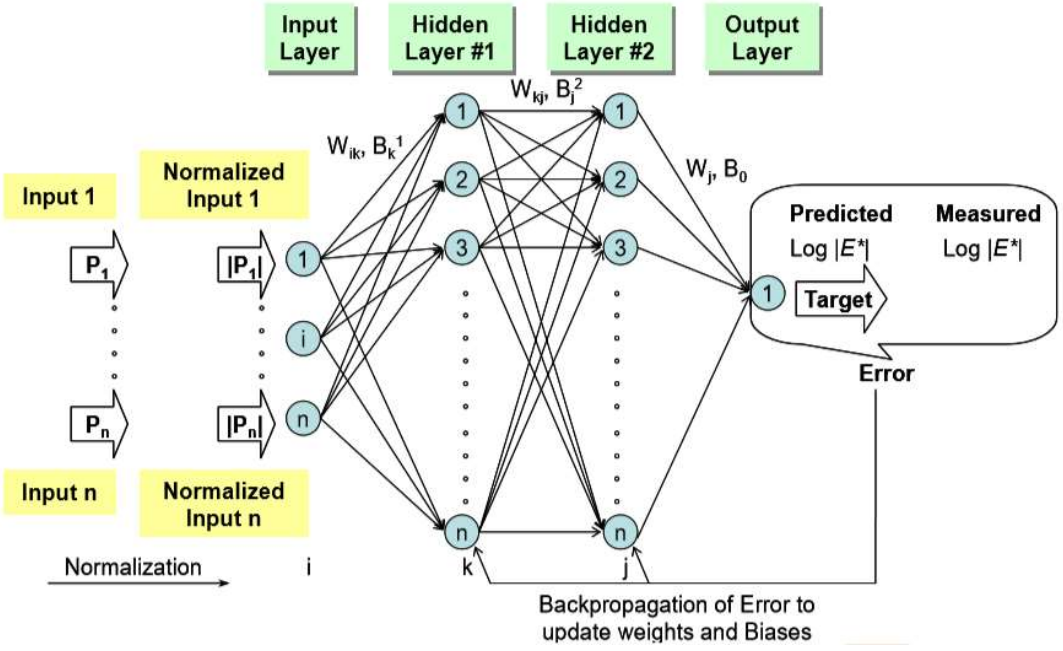

Figure 2-3 Illustration. Network structure used for training the ANN models [107].

2.2.1.10 Simplified Global Model:

In 2011, a subset of the NCSU database was used to develop a series of regression models for estimating the dynamic modulus of HMA mixtures. The series of models include two regression models (closed-form models #1 and #2), and a set of individual temperature-based models that were calibrated for typical testing conditions, including: -10, 4.4, 21.1, 37.8 and 54.4 °C. The first proposed closed-form model (global model) is a rational model for predicting the dynamic modulus of HMA mixtures. The development of this model is based on an established procedure using the time-temperature superposition concept. The model was fully optimized using various mixture and binder properties and calibrated using the calibration dataset which consists of 6,336 data points from 233 mixtures. The model formulation is based on the sigmoidal function adopted as its mathematical structure. The second proposed closed-form model (simplified global model) is also a rational model for predicting the dynamic modulus of HMA mixtures. The development of this model is based on the observations and findings from the first modeling approach that was thoroughly evaluated and verified using the calibration database. The development of this second model is based on using mixture and binder properties. This model consists of 6,336 data points from 233 mixtures. The mathematical structure of this model is the sigmoidal function. Both of the closed-form models developed for estimating the dynamic modulus values of HMA mixtures have a similar mathematical structure as the models implemented in the NCHRP 1-37A MEPDG. The called simplified global model is expressed as follows:

$$\log\left|E^*\right| = 6.39411 - 0.00015p_{34}^2 - 0.00546p_{38} - 0.1175p_{200} - 0.05544V_a - 0.15791V_{beff} + 0.00464V_{beff}^2 + \frac{0.6014 + 0.0004p_{34} + 0.00696p_{38} + 0.16224p_{200} - 0.0053p_{200}^2 + 0.019V_a + 0.15541V_{beff} - 0.00568V_{beff}^2}{1 + e^{1.8645 - 0.95991\log\left|G^*\right|}} \quad (2\text{-}17)$$

where

$|E^*|$ = the dynamic modulus (psi),

p_{34} = cumulative percentage retained on the 3/4" sieve (19 mm),

p_{38} = cumulative percentage retained on the 3/8" sieve (9.5 mm),

p_{200} = percentage passing the #200 sieve (0.075 mm),

V_a = air void content (%),

V_{beff} = effective bitumen content (% by volume),

$|G^*|$ = dynamic shear modulus of binder (psi), and

2.2.2 Experimental Comparisons of Mixture Modulus and Binder Rheology

Many researchers have focused on the prediction of a mixture-complex modulus from binder properties. For practitioners, this would be a very useful tool to spare testing time. This is also an interesting topic for researchers in order to better understand the complex behavior of mixes. A considerable amount of work has already been done and presented in the literature to relate binder and mix moduli for a given mix design [74, 100-103]; among others. However, the relationships between binder and mixture moduli are often valid over a narrow range of frequencies and temperatures, or even only for one type of given mixture. For very different conditions of temperature and frequency, or different mixes, these relationships are no longer valid. In the last two decades, many researchers discusses the accuracy and robustness of the various predictive models for estimating the HMA $|E^*|$.

Several studies have indicated that the Witczak $|E^*|$ models show significant scatter especially at the low and/or high $|E^*|$ modulus extremes [94-99]. Schwartz in 2005 also suggested that the Witczak $|E^*|$ predictive models are dominated by the influence of temperature and understate the influence of other mixture parameters [95]. This indicates

that these |E^*| predictive models may not be able to predict successfully the performance differences among different HMA mixtures under a given set of project-specific environmental conditions and design traffic. In 2007, Ceylan et al. developed a series of ANN-based models and compared the predictions with the ones estimated from few existing dynamic modulus predictive models [106]. The results showed that ANN-based |E^*| model showed a better performance than Witczak model both in terms of fitness and bias [106]. Also, the model demonstrated an improved sensitivity to mixture variables at different temperatures and frequencies of testing.

Singh et al. developed a model that utilizes aggregate shape parameters (i.e., angularity, texture and form) in estimating the dynamic modulus of asphalt mixes. The performance of this model was compared with the widely accepted Witczak model that does not use shape parameters of the aggregates. The results indicated that the mean average relative error for the Witczak model was estimated significantly higher than the developed model [108].

Dai developed a micromechanical finite-element (FE) model for predicting the dynamic modulus and phase angle of asphalt mixtures. The simulation results of the asphalt mixture samples showed good correlations with the numerical calibration of asphalt mastic specimen. The results of this study also indicated that the developed micromechanical FE model can provide a computational tool for predicting the global viscoelastic properties of asphalt mixtures with captured microstructure and ingredient properties [109].

You et al. utilized a clustered distinct element method for modeling asphalt concrete microstructure to predict compressive dynamic modulus of asphalt mixtures. This modeling approach showed promising results in terms of estimating the dynamic modulus

and was implemented to portray bulk material behavior in conjunction with fracture models to study crack behavior in hot mix asphalt as well [110].

In 2015 M.S. Sakhaeifar et al, two regression models (global and simplified global) were developed in this study for estimating the dynamic modulus of HMA mixtures. These models are shown to estimate more accurate and less biased dynamic modulus values than those predicted by the $|E^*|$ predictive model used in the current MEPDG and Hirsch model over a wider range of testing conditions which include critical zones of very low and high temperatures [111].

In 2010 Bonaquist, R. studied Wisconsin mixture characterization using the Asphalt Mixture Performance Tester (AMPT) on historical aggregate structures (WHRP 09-03). This research evaluated the stiffness and permanent deformation properties of typical Wisconsin Department of Transportation (WisDOT) asphalt mixtures using the AMPT and associated test and analysis procedures [75]. Dynamic modulus master curve was collected for 12 different good performing asphalt mixtures representing typical mixture design practice in Wisconsin. The mixtures represented 4 different sources, two design traffic levels, and two binder grades. The data were analyzed to determine the sensitivity of the AMPT tests to the following key mixture design factors: design traffic level, aggregate angularity, design voids in the mineral aggregate (VMA), and binder grade.

The measured dynamic modulus values were compared to dynamic modulus values predicted using the Hirsch model and two forms of the Witczak dynamic modulus equation. All three models provide the capability to estimate mixture dynamic modulus from mixture composition and binder properties. These comparisons showed the following:

1. The Hirsch model provides a reasonable prediction of the dynamic modulus for the 12 mixtures that were tested. On average the Hirsch model overestimates the measured dynamic modulus by only 2 % and has errors that are reasonably distributed about zero with maximum errors of approximately ± 50 percent of the measured value. The Hirsch model requires a binder modulus master curve for the binder in the mixture and mixture volumetric properties that are available from mixture design data.
2. The latest version of the Witczak dynamic modulus equation, using measured binder modulus and phase angle data, provided the poorest fit to the measured data. On average, this model overestimated the measured dynamic modulus by 64 percent with errors ranging from –25 to + 150 percent of the measured value. The bias in this model appears to have been introduced by the relationships used in the calibration of this model to predict binder moduli and phase angles from historical viscosity temperature susceptibility data.
3. The viscosity based Witczak dynamic modulus equation with typical viscosity temperature susceptibility parameters for PG 58-28 and PG 70-28 binders provided a better fit to the measured data than the latest Witczak dynamic modulus equation. On average this model overestimated the dynamic modulus by 19 percent with errors ranging from –50 to +150 percent of the measured value.

2.3 HMA Laboratory Rutting and Equivalent Parameters to Estimate Rutting for Asphalt Binder in the Lab.

Rutting is considered one of the main distresses in asphalt pavements. It is usually caused by shear deformation at high temperatures and high traffic loading. In the company of different potential problems, rutting affects the serviceability of the road and leads to some

safety issues such as hydroplaning. Hence, researchers have tried to characterize the rutting resistance of asphalt binders and mixtures in the laboratory, and establish rutting specifications, to indicate whether asphalt mixtures will perform well in the field. The most common asphalt binder rutting specification is the $|G^*|/\sin\delta$ parameter in the Performance Grading (PG) specification that was developed based on the Strategic Highway Research Program (SHRP). This parameter is measured using the oscillation test, at a frequency of 10 rad/s and a strain magnitude of approximately 12%. This parameter is evaluated in the linear viscoelastic range, while the deformation that occurs at high temperatures and/or slow traffic loading, is in the non-linear viscoelastic range. Over the years, experience has shown that this parameter has a poor correlation to asphalt mixture rutting as reported by other researchers [21]. It is argued that the reason for the poor correlation is the strain level and that it is necessary to evaluate binders under conditions similar to what occurs in the field. The Multiple Stress Creep and Recovery test (MSCR, AASHTO T350) and its associated specification, AASHTO M332, has been proposed to eliminate the inaccuracies in rutting prediction. This test subjects the binder sample to a repeated cycle of shear creep (1 s) and recovery (9 s). The test is conducted at two stress levels, 0.1 kPa to simulate the linear viscoelastic region, and 3.2 kPa to simulate the non-linear viscoelastic region.

2.3.1 The Superpave Parameter, $|G^*|/Sin\delta$, and Rutting.

Quite a few researchers have attempted to compare SHRP rutting parameter ($|G^*|/\sin\delta$) and mixture rut depth and J_{nr} and rut depth. One typical limitation in these studies is the number of mixes and binder evaluated, typically only one or two non-polymer modified asphalts are included, which may be insufficient to carry out any reliable correlation comparisons. By comparison, when the $|G^*|/\sin\delta$ value was proposed, Leahy et

al. evaluated a factorial combination of sixteen binders (all unmodified), two aggregate sources (high and low absorption limestone and greywacke), and two air void levels (4 and 7%). The wheel tracking test was employed to measure the rut depth after 5000 passes. Both the binder and wheel tracking tests were conducted at 40°C. With this high number of mixtures, the variation became clearer, but the correlation between rut depth and $|G^*|/\sin\delta$ was poor with a coefficient of determination of 0.3. $|G^*|/\sin\delta$ was also correlated to the normalized rut rate which was the rate of increase in rut depth between 2000 and 4000 passes divided by the contact stress of the wheel. The correlation coefficient achieved in this case was even lower, 0.18. The authors attributed this low correlation to three factors: (i) the size of the wheel tracking equipment used and the surface area of the mix specimen were relatively small, considering that the aggregates size was typical of that used in a conventional pavement, (ii) the variability obtained in the wheel tracking tests was high, and (iii) the binder and wheel tracking tests were conducted at 40°C, which may not have been sufficiently high to allow the viscous characteristics of binders to affect mixture performance [25]. Apart from the wheel tracking tests, repeated simple shear tests at constant height were also conducted by Leahy et al. [25]. The correlation parameters, in this case, were for $|G^*|/\sin\delta$ and both the number of load cycles at 2% permanent strain and the cumulative shear strain after 5000 cycles. The correlation coefficient was higher than that obtained for the wheel tracking tests, 0.52 and 0.58 respectively. Bouldin et al. reports data from four modified and two unmodified binders to support the relationship between $|G^*|/\sin\delta$ and rutting. The data compared the rutting rate and $|G^*|/\sin\delta$ and the rate of strain accumulation and $|G^*|/\sin\delta$. Both relationships had a very good correlation

coefficient of 0.96 and 0.98 respectively [26]. The test temperature for both binder tests and the wheel tracking tests was 60°C and the test frequency for binders was 1 rad/s.

2.3.1 The Non-Recoverable Creep Compliance, J_{nr}, and Rutting

Several researchers have attempted to compare both SHRP and J_{nr} rutting parameters. D'Angelo et al. compared the rutting in the Federal Highway Administration Accelerated Load Facility (ALF) sections to $|G^*|/\sin\delta$ as well as the J_{nr} values measured from the MSCR test. A substantial improvement was seen in the correlation between the mixture rutting and the binder rutting parameter when J_{nr} was chosen as the binder rutting parameter as compared to $|G^*|/\sin\delta$ [22]. The study also included a field investigation of the pavement sections on Interstate I-55 in the state of Mississippi. The study compared six years of rutting data to J_{nr} and obtained a R^2 value of about 0.75. Also, the rutting was estimated using the Hamburg wheel tracking test (HWTT) and the rut depth was correlated to the J_{nr} at 12.8 kPa. The correlation measure, R^2, achieved was greater than 0.9. Similar observations were made by a Minnesota study, which evaluated asphalt binder [21]. Another study measured the rutting of Texas asphalt mixtures using HWTT and compared it to the J_{nr} at 0.1 and 3.2 kPa. It must be noted that the evaluations were performed on plant mixtures, so the binder tests were performed after extracting the binder from these mixtures. The authors reported a good correlation between J_{nr} and rutting with R^2 more than 0.75 and 0.85 in most of the cases [23]. In a more recent study by Laukkanen et al., both $J_{nr3.2}$ and $|G^*|/\sin\delta$ were related to the mixture rutting. There were two rutting parameters that the authors used for developing the relationship. The first parameter was the rate of rutting, which was measured as the linear slope of the rut depth and number of cycles relationship between 10,000 and 50,000 cycles. The second rutting parameter is

based on the functional fit of the relationship between rut depth and number of cycles. The authors fit the data to a power law function with the functional form. Where "y" is the rut depth, "x" is the number of cycles, a and b are constants (b value represents the slope of the function). The authors found that the rate of rutting and (b) value both related poorly to $|G^*|/\sin\delta$ with R^2 values of 0.401 and 0.502 respectively when the data was fit to a linear function, and 0.758 and 0.741 respectively when the data was fit to a power law function. However, this was still lower than the R^2 values observed in the relationship with $J_{nr3.2}$, which was assessed in the linear domain [24]. Another study used the flow time test to assess the relationship between mixture rutting and the J_{nr} parameter. The study was done on both conventional asphalt mixtures, and unconventional asphalt mixtures as Reclaimed Asphalt Pavement (RAP) and Warm Mix Asphalt (WMA). The results revealed that both Superpave parameter $|G^*|/\sin\delta$ and MSCR percentage recovery parameter didn't correlate well with mixture rutting, however, the J_{nr} parameter had a good correlation [27].

In summary, previous studies correlated SHRP parameter $|G^*|/\sin\delta$ and J_{nr} parameter with Hamburg Wheel, or Repeated Load Permanent Deformation test (RLPD) with a limited number of mixtures that did not cover a wide range of modified and unmodified binders. Hence, studying the correlation between the two rutting parameters with different types of binders, and identifying the correlation between those parameters and the rutting mixture still contains some knowledge gaps. This paper evaluates both rutting parameters $|G^*|/\sin\delta$ and J_{nr} by correlating it to both HWTT and RLPD test results.

2.4 HMA Laboratory Fatigue and Equivalent Methods to Estimate Asphalt Binder fatigue in the Lab.

There are three main defects in asphalt pavements namely, moisture susceptibility, rutting, and fatigue cracking [28–31]. Fatigue cracking is one of the major distresses of flexible pavements which usually appear in the form of alligator cracking on the surface of pavement caused by repetitive stresses and strains due to traffic loading and environmental factors [30, 32–34]. Fatigue behavior of asphalt mixtures is affected by many factors such as loading, environmental conditions, mixtures characteristics, binder and aggregate characteristics, etc. It is reported that from the mixture components, binder plays the most important role in fatigue behavior of asphalt mixtures [35–38]. Hence, it is important to find a promising test method for evaluation of asphalt binder fatigue performance.

The search for finding a time and cost-effective method for evaluating asphalt binder fatigue performance is an on-going effort. The $|G^*|\sin\delta$ fatigue index, which was introduced as an asphalt binder fatigue criterion during the SHRP program, has received considerable criticism as it does not account for the traffic and pavement structure [37,39]. During the NCHRP 9–10 Project, the time sweep test, at which specimen is subjected to a repeated cyclic loading using Dynamic Shear Rheometer (DSR) until a specific criterion such as stiffness level is met, was introduced. Although time sweep test was proved as a reliable test method for asphalt binder fatigue evaluation, it was questionable due to its long-lasting testing time [37,40,41]. In response to this issue, additional investigations started to find a more time effective asphalt binder fatigue test method which led to the Linear Amplitude Sweep (LAS) test [42]. The LAS test was introduced by Bahia and his associates as a promising time-saving test to estimate the binder fatigue performance [43].

Moreover, the results of the LAS test have correlated fairly well with Long-Term Pavement Performance (LTPP) field fatigue cracking data [44].

The LAS test results are analyzed using Viscoelastic Continuum Damage (VECD) model principles. The VECD model has been successfully used for characterizing fatigue performance of asphalt mixtures by many researchers [45–52]. This method predicts the damage growth in asphalt mixtures based on Schapery's elastic-viscoelastic correspondence principle and the work potential theory [44]. However, the use of this model for predicting asphalt binders fatigue performance has encountered a number of problems such as duration of test methods as well as difficulties in analyzing the results when the modified binder is used. These problems were solved in the LAS testing method [44].

Although many researchers have investigated the asphalt binder fatigue test methods, a few numbers of literature have compared the effectiveness of $|G^*|\sin\delta$ fatigue index and LAS test in estimating the mixture fatigue performance. In addition, asphalt binders with a wide range of stiffness were not always used in these studies.

2.4.1 The Superpave Parameter, $|G^*|^*Sin\delta$, and Fatigue.

It is well known that the binder rheology has an impact on asphalt cracking resistance. For the first time, Strategic Highway Research Program (SHRP) developed a new measure of binder rheology ($|G^*|\sin\delta$) as criteria for fatigue cracking performance of asphalt mixtures at intermediate temperature. The maximum value of 5000 kPa is considered for asphalt binders subjected to long-term laboratory aging. Although introducing this measure by combining stiffness and relaxation of binder was progress, it is accepted that $|G^*|\sin\delta$ is not able to adequately represent the fatigue cracking behavior [75].

Subsequent research has shown that $|G^*|\sin\delta$ lacks the ability to indicate resistance to fatigue damage [77]. The primary concern is that $|G^*|\sin\delta$ is merely an initial measure of undamaged linear viscoelastic properties, and it may be unsuitable to extrapolate this property to predict damage after the multiple loading cycles typically associated with fatigue damage.

In 2013, Zhou et al. [42] investigated the $|G^*|\sin\delta$ parameter, elastic recovery, Multiple Stress Creep Recovery (MSCR), LAS, and the Double Edge Notch Tension (DENT) asphalt binder fatigue tests on six different binders and compared the results with the push-pull asphalt mixture fatigue test of corresponding mixtures. They confirmed the poor performance of $|G^*|\sin\delta$ parameter and also claimed that neither the MSCR nor the LAS test methods show good correlation with asphalt mix fatigue performance. However, the DENT and elastic recovery test methods could provide the same ranking as the asphalt mix fatigue test [42].

In 2018 research, Sabouri et al. [54], studied the effectiveness of $|G^*|\sin\delta$ parameter in predicting fatigue behavior of asphalt mixtures containing binders with a wide range of stiffness, neat binders as well as SBS and Gilsonite modified binders were employed and the correlation between $|G^*|\sin\delta$ as binder fatigue parameter was investigated. In addition, FBB test was conducted on selected asphalt mixtures and the correlations between binder fatigue parameters with FBB test results were studied to better understand their effectiveness in predicting the fatigue behavior of asphalt mixtures. The results showed that SHRP binder fatigue index ($|G^*|\sin\delta$), as a traditional binder fatigue index, was evaluated which did not show a strong correlation with either LAS or FBB tests.

2.4.2 The LAS Parameter and Fatigue

The LAS test was introduced by Bahia and his associates as a promising time-saving test to estimate the binder fatigue performance [43]. The LAS test has become an efficient tool to characterize fatigue resistance of asphalt binders.

In 2010, Johnson [77], compare the Linear Amplitude Sweep with Accelerated Pavement Testing (TPF-5(019) experiment). The test section has four different mixtures: unmodified control binder (PG70-22), CR-TB Modified, SBS-LG Modified, and ethylene terpolymer. The test sections were subjected to repeated wheel loading, with their fatigue performance being recorded as cumulative crack length (m) due to fatigue failure after 100,000 passes, and number of passes to 50-m in cumulative crack length. The test sections were produced using a single dense gradation of 12.5-mm Superpave mix design, and were constructed in two lifts of 50-mm over a crushed aggregate base. The accelerated wheel testing was performed at a controlled temperature of 19°C with a simulated wheel load of 74 kN. For LAS binder testing, RTFO-aged material was used in order to simulate the short term age (oxidative state) of the binders in the test sections. All tests were performed at 19°C. Results of the LAS testing and the measured fatigue cracking after 100,000 passes for the accelerated pavement testing lanes were listed and compared. The best performing pavement is the SBS-LG, but is ranked second-to-last based on the LAS ranking. However, when compared against each other, the remaining three binders rank consistently between LAS and accelerated pavement results. With only three data points, it is difficult to attribute the correlation to the fatigue performance of the binders. However, the removal of the outlier gives a near-perfect correlation that would indicate that higher values of A35 lead to reduced cracking under simulated traffic loading.

In 2012, Clopotel et al. [53] employed the LAS and the Single-Edge Notched Beam (SENB) tests to investigate the correlation between the binder and mixture fatigue behavior at intermediate and low temperatures and found a fairly good correlation between them.

In 2018, Sabouri et al. [54], Studied the effectiveness of LAS test in predicting fatigue behavior of asphalt mixtures containing binders with a wide range of stiffness, neat binders as well as SBS and gilsonite modified binders were employed and the correlation between LAS and $|G^*|\sin\delta$ as binder fatigue parameters was investigated. In the research, LAS test was conducted on several asphalt binders modified by different percentages of gilsonite and Styrene-Butadiene-Styrene (SBS) polymer. Asphalt mixtures were also made from some of the study binders and tested for fatigue resistance using Four-point Bending Beam (FBB) fatigue test. The results showed that a strong correlation exists between LAS and FBB rankings at all the tested strain levels. It was concluded that the LAS test seems to be an effective binder fatigue test in predicting asphalt mixtures' fatigue performance.

2.4.2.1 Existing failure definition

Defining material failure under fatigue loading is always challenging. Ideally, fatigue failure should be determined based on physical characteristics of intensity and distribution of damage within the material body. However, it is unrealistic, if not impossible at all, to capture and monitor material's internal physical state during loading. The alternative definition from phenomenological perspective has been commonly adopted by researchers and practitioners. In general, developing a phenomenological failure definition calls for a comprehensive and balanced consideration of factors such as experimental observations, theoretical soundness, and analytical convenience. There are five existing failure definition:

i. The traditional definition of fatigue failure simply employs a certain percentage of reduction in observed stiffness or modulus. For example, the four-point bending beam test conventionally adopted in fatigue characterization of asphalt mixtures has been using 50% drop in flexural stiffness as the threshold for material failure [60].

ii. In the current AASHTO standard for the beam fatigue test, failure is defined as the point at which the product of flexural stiffness and cycle number reaches the maximum [61]. This alternative definition yields a more convenient identification of fatigue life and appears to be indicative of localization of cracking [62]. Given the similar nature of loading in bending beam test and TS test (both under sinusoidal oscillation with constant amplitude), similar failure definitions have been applied in TS [63,64], i.e., 50% drop in modulus, and peak of C* N where N denotes cycle number and C is the normalized modulus.

iii. When the LAS test was first proposed, Johnson [65] determined 35% reduction in material integrity (as represented by $|G^*|\sin\delta$) as the threshold of fatigue failure. This level of reduction was selected because good agreement was observed between LAS and TS test results, and also because a satisfactory correlation was found between an LAS-based parameter and fatigue performance of field pavements [65]. Despite the fact that a limited number and types of binders were investigated, this failure definition as well as the problematic formulation have been standardized in an AASHTO specification and are still retained in the current version [66].

iv. Alternatively, fatigue failure in LAS has been determined by identifying the maximum shear stress amplitude τ, and by the peak of C* N as already employed for the TS test. With the linear ramping LAS version that is currently adopted and favored by researchers, these two definitions have been shown to be equivalent [63]. Hence, the peak of C * N can be considered as the first unified definition of fatigue failure for LAS and TS tests.

v. More recently, Wang et al. [63] proposed another unified failure definition, the peak of τ * N. It was demonstrated that for the TS test this definition reduces to the peak of C * N given the constant strain amplitude. Meanwhile, for LAS this definition is equivalent to peak of $W^R(N)$, which suggests that failure occurs when material starts to lose its capability in storing more pseudo-strain energy.

2.4.2.2 Existing failure criterion

As is well known, the results of beam fatigue test on asphalt mixtures have been traditionally represented by a power-law relation between the control parameter (e.g., strain or stress level) and the observed number of cycles to failure. This relation can be deemed as an early version of failure criterion and has been used to discriminate mixtures based on fatigue resistance and to make predictions on fatigue performance of asphalt pavements. However, a major drawback of this methodology lies in that the obtained relationship is dependent on the mode of control (e.g., strain control versus load control) and test temperature.

i. G^R failure criterion

Recently, Sabouri and Kim [67] developed the so-called G^R failure criterion which unified all possible test control modes (load, displacement, and on-specimen strain

controls) in uniaxial fatigue test on asphalt mixture. It has been demonstrated in a number of studies that this unified failure criterion also appeared to be independent of test temperature and load level [67-69]. The G^R failure criterion states that for a given asphalt mixture, there exists a unique power-law relationship between G^R and the number of cycles to failure:

$$G^R = \lambda(N_f)^{\zeta} \tag{2-18}$$

where λ and ζ are regression constants, N_f denotes the number of cycles to failure, and G^R is defined as

$$G^R = \frac{W^R_{r,sum}}{N_f^2} \text{ with } W^R_{r,sum} = \sum_1^{N_f} W^R_r \tag{2-19}$$

In which,

$$W^R_r = \frac{1}{2} DMR \cdot (1 - C_i)(\gamma^R_i)^2 \tag{2-20}$$

where W^R_r denotes released pseudo-strain energy in a cycle, and $W^R_{r,\mathrm{sum}}$ is the total released pseudo-strain energy accumulated up to failure.

The G^R failure criterion then found its application in fatigue characterization of asphalt binders using LAS and TS tests. Moreover, it has been demonstrated that this failure criterion is able to unify LAS and TS tests in that for a given binder the G^R-N_f relations from the two tests fall on the same curve [63,70]. Despite the success of the G^R failure criterion as documented in literature so far, the validity and its unifying nature has been in some sense disguised by the way how G^R is defined as in Eq.(2-19).

ii. W^R failure criterion

Given the unreliability of the existing G^R failure criterion as illustrated in [71], a new failure criterion is proposed for fatigue modeling of asphalt binder below. The new failure criterion was developed based on the new failure definition peak of C2 * N *(1-C). the new failure criterion is proposed as a power law relating the total pseudo-strain energy $W_{r,\text{sum}}^R$ with a variable named Straining Effort (SE) as a function of the loading condition:

$$W_{sum}^R = K.\ SE^{\mu} \tag{2-21}$$

Where k and μ are regression constants, and SE is defined by

$$SE = \left(\sum_{i=1}^{N_f} \gamma_i\right).(|G^*|_{LVE})^2 \tag{2-22}$$

where γ_i denotes the strain amplitude in the i-th cycle, and $|G^*|_{\text{LVE}}$ is the undamaged shear modulus. SE is used to represent the amount of mechanical effort required to deform and damage the material until failure. Note that SE is not the physical work input to the material during the course of fatigue loading. Incorporation of $|G^*|_{\text{LVE}}$ in SE is for the purpose of accommodating the effects of temperature and loading frequency given the viscoelastic nature of asphalt binders, as more effort is required to deform and damage the material when tested under lower temperatures and/or higher frequencies. Further, the rationale behind the use of exponent on $|G^*|_{\text{LVE}}$ lies in the consistent consideration of the role of $|G^*|_{\text{LVE}}$ in both $W_{r,\text{sum}}^R$ and SE; the purpose is to eliminate the temperature and frequency dependence in the resulting $W_{r,\text{sum}}^R$ -SE relation.

iii. D^R failure criterion

The D^R failure criterion is based on experimental observations by Wang and Kim [72] that the average loss of integrity per cycle throughout an asphalt mixture's fatigue life, that is, D^R in the following equation, is constant regardless of temperature, mode of loading, and load amplitude:

$$D^R = \frac{\int_0^{N_f}(1-C)dN}{N_f} = \frac{\text{sum}(1-C)}{N_f} \tag{2-23}$$

According to the definition of D^R given in Equation 6, D^R is the slope of the linear relationship between the sum of (1 – C) to failure and Nf. Wang and Kim demonstrated that the slope of D^R is a ductility parameter because it indicates the brittleness or ductility of a mixture [72].

2.4.3 Knowledge of Gaps for Fatigue Study.

Despite the previous research efforts, the knowledge of gaps is as following:

- A few numbers of literature have compared the effectiveness of $|G^*|\sin\delta$ fatigue index and LAS test in estimating the mixture fatigue performance.
- Asphalt binders with a wide range of stiffness were not always used in the previous studies.
- It is difficult to use the S-VECD fatigue model when correlating binder test data to fatigue performance of asphalt mixtures having a wide range of stiffnesses and being tested at multiple strain levels and failure criteria than the one used for Mixture fatigue.

Chapter 3. EXPERIMENTAL METHODS AND USED MATERIALS

In this chapter, the experimental techniques and the study materials used in the study will be discussed. In total, twenty asphalt binder samples and three aggregate supplies have been acquired for the experimental phase of this study. These materials are obtained from Arizona suppliers to ensure results from the study are directly applicable to materials used in the state. Specific details of these materials are provided in the following sections.

3.1 Study Materials

3.1.1 Asphalt Binder

Overall, twenty different asphalt binders have been sourced from the three asphalt suppliers in Arizona (Alon Asphalt Company, Holly Frontier, and Western Refining). Seven of the twenty binders are non-polymer modified (referred to as the Group 1 Asphalts) and five are polymer modified from suppliers (referred to as the Group 2 Asphalts) and eight are polymer modified lab blended binders (referred to as the Group 3 Asphalts).

Group 1 materials have been obtained to reflect the current and likely future asphalt usage in the state as well and to give as equal as possible representation from each of the individual suppliers in the state. Two suppliers, X and Y., have provided the crude sources of the asphalts. All asphalt binders from supplier X are based out of crude from Canadian Bow River. The non-polymer modified binders of supplier Y are based on Western Canadian Select (WCS) crude, whereas its polymer modified binders are a blend of WCS and West Texas Intermediate (WTI).

With respect to the Group 2 asphalts, the materials have been selected based on those that would likely be supplied in the state under a future AASHTO M332-like specification. The current ADOT specifications only list one type of polymer modified asphalt (PG 76-22

TR+). Other modified asphalts may be used presently in the state of Arizona. A third group of asphalts (Group 3 materials) are also used in this study to identify the effects of percent recovery on the asphalt mixture performance. These asphalts are lab blended in order to more accurately control the recovery and compliance values.

3.1.1.1 Group 1 - Base Graded Asphalt Binders.

The Group 1 asphalts selected for use in this study are listed in Table 3-1. The basis of these selections is current usage and likely usage under an AASHTO M332 system for the state of Arizona. Figure 3-1 was used to first identify the most prevalent grades specified in ADOT projects. The three most prevalent grades in Arizona (PG 64-22, PG 70-10, and PG 76-16) constitute approximately 89% of the asphalt (by lane mileage). Of these, PG 76-16 is the singularly most used asphalt grade. Based on this usage, PG 76-16 and PG 64-22 are sampled from two of the three suppliers and PG 70-10 has been sampled from just one of the three suppliers. Other relevant grades in the state included PG 70-22 and PG 70-16, which have also been sampled based on the supplier's current usage.

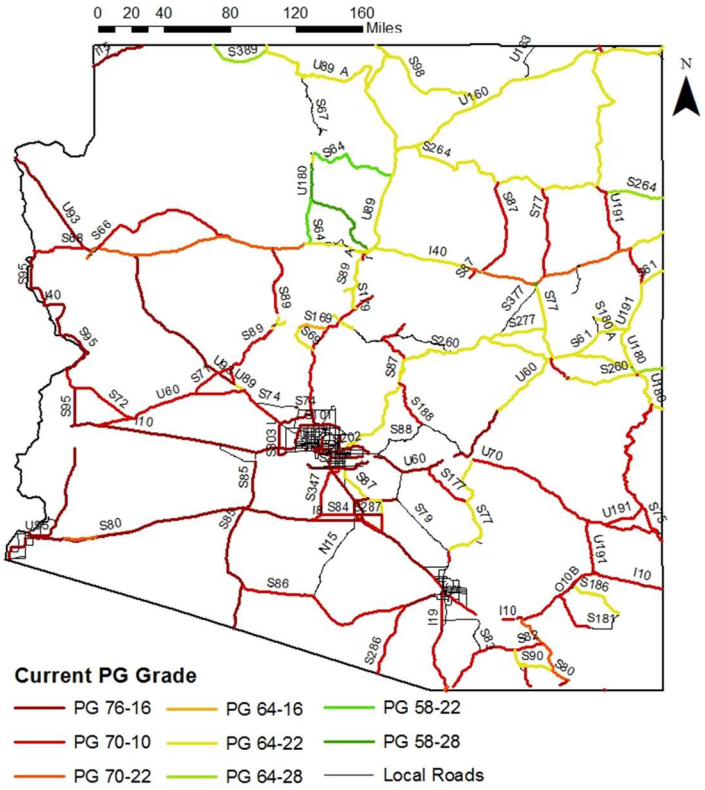

Figure 3-1. Distribution of Current Asphalt Binder Grades across Arizona.

Table 3-1. Asphalt Binder Grades Used in the Current Study and their Notations.

Group 1			Group 2			Group 3	
Supplier	Notation	Grade	Supplier	Notation	Grade	Notation	Grade
X	X1	PG 70-10	X	X3	PG 64H-22*	A3	PG 64H-22
Y	Y1	PG 64-22		X4	PG 64V-22	A2-B	PG 64H-22
	Y3	PG 70-16		X5	PG 76-22TR+	A4	PG 70S-28
	Y4	PG 76-16	Y	Y5	PG 70H-16*	A3-B	PG 70S-28
Z	Z1	PG 64-22		Y6	PG 70V-16	B2	PG 70H-28
	Z2	PG 70-22	*Used as both Group 2 and Group 3 Asphalt			D0.5	PG 70H-28
	Z4	PG 76-16				B5	PG 76V-28

3.1.1.1 Group 2 - Polymer Modified Asphalt Binders. (From Suppliers)

Currently, the use of polymer modified asphalt binders is not prevalent in the state of Arizona, with PG 76-22TR+ being the only such material specified. As shown in Table 3-1, five different polymer modified asphalts have been selected. These include, first, the PG 76-22TR+ binder that is currently specified in the state and then four other polymer modified asphalts that meet the AASHTO M332 specification and that could likely be

supplied in Arizona under a similar specification. The suppliers X and Y expressed the capability of supplying PG 64(H,V)-22 and PG 70(H,V)-16 respectively.

While the polymer used in PG 64(H,V)-22 and PG 70(H,V)-16 is SBS, the type of SBS and its dosage is proprietary to the supplier. However, since PG 76-22 TR+ is a specification binder, details regarding its composition are available. The binder has 8-10% of digested crumb rubber, along with 3% of SBS.

3.1.1.1 Group 3 - Polymer Modified Asphalt Binders. (Lab Blended)

These asphalt binders have been prepared at the Arizona State University laboratory using a high shear mixer with varying levels of polymer modification. The goal for testing these mixtures is to evaluate the sensitivity of rutting performance to changes in the elastic recovery measured in the MSCR experiment, $R_{3.2}$. Asphalts in this group have varying recovery levels, but are grouped according to similar $J_{nr3.2}$. A total of nine asphalts are split into one of Four groups based on their $J_{nr3.2}$. Each group has two asphalts with similar $J_{nr3.2}$ and varying recovery levels. The ranges of $J_{nr3.2}$ identified for the three groups are (i) $J_{nr3.2} < 0.1$; (ii) $0.1 < J_{nr3.2} < 0.5$; (iii) $0.5 < J_{nr3.2} < 1$; and (iv) $1 < J_{nr3.2} < 2$. Two of these asphalts (PG 70V-16, and PG 64H-22) are also Group 2 asphalts. The remaining seven polymer modified asphalts have been prepared in the Arizona State University laboratory using a high shear mixer. The base asphalt for all these asphalts is PG 58-28, the polymer used is an SBS linear polymer, Kraton D1192. Crosslinking agents such as sulfur and polyphosphoric acid (PPA) are used where required. The dosages of SBS, sulfur, and PPA for the seven asphalts along with the detailed laboratory procedure of the polymer modified asphalt binder preparation are provided in Appendix A.

3.1.2 Aggregates

The aggregates used in this current study have been sourced from three suppliers in Arizona: Hanson Aggregates in Globe, Brimhall-Sand, and Rock in Snowflake, and Granite Construction in Tucson. A brief description of the aggregates and their corresponding characteristics are provided in the sections below.

3.1.2.1 Globe

The aggregate sourced from Globe, AZ consist of four stockpiles; washed sand, crusher fines (CF), 3/8" aggregate, 3/4" aggregate, and a portland cement admixture. The characteristics of these stockpiles and the individual stockpile gradations are provided in Table 3-2 and

Table 3-3 respectively.

Table 3-2. Characteristics of Aggregates Sourced from Globe.

Aggregate Properties	Coarse Aggregate	Fine Aggregate	Spec. Limits	Admixture (Type II portland cement)
Bulk Specific Gravity	2.570	2.556	2.350-2.850	3.14
SSD Specific Gravity	2.605	2.592		
Apparent Specific Gravity	2.664	2.651		
Sand Equivalent	1.37	1.40	0-2.5%	-
1 Fractured Face (%)	85		Min. 55	
2 Fractured Face (%)	94		Min. 92%	
Uncompacted Voids (%)	90		Min. 85%	
Flat and Elongated Agg. (%)	46.5		Min 45%	
Carbonates (%)	1%		Max. 10%	
L.A. Abrasion, 100 rev. (% loss)	-		Max. 20%	
L.A. Abrasion, 500 rev. (% loss)	6		Max. 9%	
Sand Equivalent	24		Max. 40%	

Table 3-3. Gradation of Aggregate Stockpiles Sourced from Globe.

Standard	Metric (mm)	Washed Sand	CF	3/8″ Aggregate	3/4″ Aggregate	Cement
2″	50	100	100	100	100	100
1.25″	31.5	100	100	100	100	100
1″	25	100	100	100	100	100
3/4″	19	100	100	100	98	100
1/2″	12.5	100	100	100	42	100
3/8″	9.5	100	100	100	11	100
1/4″	6.3	100	100	87	1	100
No. 4	4.75	100	99	57	1	100
No. 8	2.36	88	80	2	1	100
No. 10	2	82	73	2	1	100
No. 16	1.18	62	53	1	1	100
No. 30	0.6	40	36	1	1	100
No. 40	0.425	29	30	1	1	100
No. 50	0.3	20	25	1	1	100
No. 100	0.15	7	16	1	1	100
No. 200	0.075	1.5	10.5	1.0	0.7	100.0

3.1.2.2 Snowflake

The aggregate sourced from Snowflake, AZ consists of four stockpiles; washed crusher fines (CF), crusher fines (CF), 3/8" SHRP chips, 7/8" rock, and a portland cement admixture. The characteristics of these stockpiles and the individual stockpile gradations are provided in Table 3-4 and Table 3-5 respectively.

Table 3-4. Characteristics of Aggregates Sourced from Snowflake, AZ.

Aggregate Properties	Coarse Aggregate	Fine Aggregate	Spec. Limits	Admixture (Type II portland cement)
Bulk Specific Gravity	2.562	2.589	2.350-2.850	3.14
SSD Specific Gravity	2.59	2.619		
Apparent Specific Gravity	2.635	2.67		
Water Absorption (%)	1.08	1.17	0-2.5%	-
Sand Equivalent	79		Min. 55	
1 Fractured Face (%)	95		Min. 92%	
2 Fractured Face (%)	92		Min. 85%	
Uncompacted Voids (%)	46.2		Min 45%	
Flat and Elongated Agg. (%)	0		Max. 10%	
Carbonates (%)	2		Max. 20%	

Aggregate Properties	Coarse Aggregate	Fine Aggregate	Spec. Limits	Admixture (Type II portland cement)
L.A. Abrasion, 100 rev. (% loss)	5		Max. 9%	
L.A. Abrasion, 500 rev. (% loss)	24		Max. 40%	

Table 3-5. Gradation of Aggregate Stockpiles Sourced from Snowflake, AZ.

Standard	Metric (mm)	Washed CF	CF	3/8″ SHRP Chips	7/8″ Rock	Cement
2″	50.0	100	100	100	100	100
1.25″	31.5	100	100	100	100	100
1″	25.0	100	100	100	100	100
3/4″	19.0	100	100	100	92	100
1/2″	12.5	100	100	100	31	100
3/8″	9.5	100	100	100	12	100
1/4″	6.3	100	100	79	2	100
No. 4	4.75	100	100	37	1	100
No. 8	2.36	79	67	5	1	100
No. 10	2.00	74	60	4	1	100
No. 16	1.18	61	45	4	1	100
No. 30	0.600	44	34	3	1	100
No. 40	0.425	35	30	3	1	100
No. 50	0.300	22	24	2	1	100
No. 100	0.150	5	16	2	1	100
No. 200	0.075	1.1	11.0	1.0	0.2	100.0

3.1.2.3 Tucson

The aggregate sourced from Tucson, AZ consists of five stockpiles; crusher fines (CF), washed crusher fines, 3/8" mineral aggregate (MA), 1/2" mineral aggregate (MA), 3/4" mineral aggregate (MA), and a portland cement admixture. The characteristics of these stockpiles and the individual stockpile gradations are provided in Table 3-6 and Table 3-7 respectively.

Table 3-6. Characteristics of Aggregates Sourced from Tucson, AZ.

Aggregate Properties	Coarse Aggregate	Fine Aggregate	Spec. Limits	Admixture (Type II portland cement)
Bulk Specific Gravity	2.587	2.581	2.350-2.850	3.14
SSD Specific Gravity	2.614	2.610		
Apparent Specific Gravity	2.657	2.657		
Water Absorption (%)	1.02	1.11	0-2.5%	-
Sand Equivalent	84		Min. 55	
1 Fractured Face (%)	99		Min. 92%	
2 Fractured Face (%)	92		Min. 85%	
Uncompacted Voids (%)	47.9		Min 45%	
Flat and Elongated Agg. (%)	-		Max. 10%	
Carbonates (%)	0.2		Max. 20%	
L.A. Abrasion, 100 rev. (% loss)	3		Max. 9%	
L.A. Abrasion, 500 rev. (% loss)	18		Max. 40%	

Table 3-7. Gradation of Aggregate Stockpiles Sourced from Tucson, AZ.

Standard	Metric (mm)	CF	Washed CF	3/8" MA	1/2" MA	3/4" MA	Cement
2″	50	100	100	100	100	100	100
1.25″	31.5	100	100	100	100	100	100
1″	25	100	100	100	100	100	100
3/4″	19	100	100	100	100	83	100
1/2″	12.5	100	100	100	60	12	100
3/8″	9.5	100	100	100	29	8	100
1/4″	6.3	100	100	68	10	6	100
No. 4	4.75	100	100	33	8	4	100
No. 8	2.36	78	75	6	6	2	100
No. 10	2	71	67	6	6	2	100
No. 16	1.18	54	48	4	5	2	100
No. 30	0.6	39	30	4	4	1	100
No. 40	0.425	32	22	3	4	1	100
No. 50	0.3	26	16	3	3	1	100
No. 100	0.15	17	6	3	3	1	100
No. 200	0.075	11.5	1.3	2.1	2.2	0.8	100.0

3.2 Mix Design

All the asphalt mixtures developed in the study are in line with the current ADOT Superpave mix design criteria. The mix design parameters of interest for all asphalt mixtures are detailed in Table 3-8. The limits for the parameters shown in table below are for ADOT's 417 Superpave mixture. The prefix "T", "S", and "G" to the binder notation in the table below indicates the source of the aggregate, which is Tucson, Snowflake, and Globe respectively.

Table 3-8. Mix Design Properties of Arizona Asphalt Mixtures Used in the Study.

Group	Mixture	Mix Design Property						
		Asphalt Binder Content (%)	Absorbed Asphalt (%)	% VMA	% VFA	%G_{mm} @ $N_{initial}$	% G_{mm} @ N_{max}	Dust Proportion (%)
1	GY3	5.3	1.09	14.4	65.3	80.9	90.4	0.85
	GY4	5.3	0.99	14.6	65.8	80.7	90.4	0.83
	GZ2	5.3	1.05	14.4	65.3	80.9	90.6	0.86
	SY1	5.5	0.59	17.3	63	84.2	93.5	0.96
	SZ1	5.3	0.09	17.8	64.1	84.9	94.7	0.91
	TX1	5.8	0.71	17.5	63.5	85.5	93.6	0.73
	TZ4	5.8	0.74	17.5	63.5	85.5	93.6	0.74
2	GX4	5.2	0.88	14.6	65.9	81.5	91.4	0.84
	GX5	5.4	0.96	14.8	66.2	80.7	90.3	0.82
	GY6	5.3	0.96	14.6	65.7	80.8	90.5	0.84
	SX3	5.6	0.43	17.8	64.1	82.1	92.2	0.91
	TY5	5.5	0.49	17.6	63.6	84.9	93.6	0.75

3.3 Asphalt Binder Experiments

The asphalt binder experiments conducted in this study utilize the dynamic shear rheometer (DSR) for determining the intermediate and high temperature linear and non-linear viscoelastic properties of the asphalts and the bending beam rheometer (BBR) for determining the low temperature properties. These testing has been conducted on asphalt binder after different age conditioning.

3.3.1 Conditioning Protocols

The experiments in this study are conducted on asphalt binder samples that have been conditioned to three different oxidative states; unaged, short-term aged, and long-term aged. Other than initial heating to separate the asphalt from the as-delivered 5gallon pails into test quantities, unaged asphalts are not subjected to any specialized process. They represent the asphalt as it exists at the time of mixing. For short-term aging AASHTO T240 (Rolling Thin Film Oven, RTFO) has been followed and for long-term aging AASHTO R28 (Pressure Aging Vessel, PAV) has been carried out. The conditioning temperature for PAV has been chosen based on the current ADOT guidelines, which means that for PG 64-XX PAV aging is conducted at 100°C and for PG 70-XX and PG 76-XX it is 110°C. As per the R28 standards, all PAV aged asphalt is subjected to the RTFO procedure prior to being aged in the PAV. In the interest of brevity these samples are referred to simply as PAV aged instead of RTFO+PAV aged.

3.3.2 Shear Modulus and Phase Angle

The AASHTO T315 standard protocol for oscillatory, parallel plate testing has been conducted to determine the asphalt shear modulus, $|G^*|$, and phase angle, □, of the asphalt binders. Tests are performed using either a 25-mm parallel plate geometry (for temperatures greater than 58°C) or an 8-mm parallel plate geometry (for temperatures between 22°C and 37°C). As described in the protocol, all tests are carried out at a 10 radians/s frequency. The strain levels and test temperatures used in the experiments are summarized for both test geometries in Table 3-9.

Table 3-9. Summary of AASHTO T315 Testing Conditions.

Geometry	Aging Level	Test Temperatures	Strain Level (%)
25 mm	Unaged	AASHTO M320 high temperature grade and ±6°C	12[a]
	RTFO	AASHTO M320 high temperature grade and ±6°C	10[a]
	PAV	AASHTO M320 high temperature grade	0.5[b]
8 mm	Unaged	AASHTO M320 intermediate temperature grade	1.0
	RTFO	AASHTO M320 intermediate temperature grade	1.0
	PAV	AASHTO M320 intermediate temperature grade and ±3°C	1.0[a]

[a] Strain levels chosen from guidelines in AASHTO T315

[b] Strain level chosen from strain sweep experiment

3.3.3 Flexural Creep Stiffness

The bending beam rheometer (BBR) test, AASHTO T313, is used to measure the flexural creep stiffness (*S*) and the logarithmic change in the creep stiffness at 60 s (*m-value*). In this study, the BBR test is conducted at the standard temperature for the given grade (10°C higher than the low temperature grade of the asphalt binder) and ±6°C of this value. For example, with a PG 64-22 asphalt, the test temperatures are -6°C, 12°C, and -18°C.

3.3.4 Percent Recovery and Non Recoverable Creep Compliance

The multiple stress creep recovery (MSCR) test has been conducted according to the procedure standardized in AASHTO T350. The four parameters extracted from this test are the non-recoverable compliance at both 3.2 kPa and 0.1 kPa stress levels, $J_{nr3.2}$ and $J_{nr0.1}$ respectively, the percentage of difference between these two quantities (J_{nrdiff}), and the percent of strain recovery during the 3.2 kPa loading, $R_{3.2}$. Details of the calculations are presented in Appendix A. The tests are conducted at the AASHTO M320 high temperature grade of the asphalt and at ±6°C, except for the PG 76-XX asphalts, which are tested at 76, 70, and 64°C.

3.3.5 The Linear Amplitude Sweep (LAS)

The Linear Amplitude Sweep (LAS) test has been conducted according to the procedure standardized in AASHTO TP101. The LAS test evaluates the ability of asphalt binder to resist fatigue damage. This test is basically an oscillatory strain sweep test that generates damage to the binder by applying linearly increasing load amplitudes. The LAS test consists of two steps: first, a frequency sweep is performed in order to get information about undamaged material properties and evaluate the rheological characteristics of the binder. Second, the damage characteristics of the binder is measured employing a linear amplitude strain sweep test.

In this study, frequency sweeps were conducted at a strain amplitude of 0.1% with a range of frequencies from 0.2 to 30 Hz according to AASHTO TP101. Amplitude sweep test was done at a constant frequency of 10 Hz. The testing protocol consisted of applying a linearly increasing load from zero to 30% over 3100 cycles of loading. All tests were conducted using DSR device with an 8-mm diameter parallel plate and a 2-mm gap. The test was carried out on PAV aged binders at 18 °C. Two replicates were run for each binder. The number of cycles to failure was calculated. Details of the calculations are presented in Appendix A. The failure definition in the LAS test is defined as 35% reduction in the initial modulus.

3.3.6 Fourier Transform Infrared Spectroscopy (FT-IR Spectroscopy)

In the present study, the changes to the chemical properties due to oxidation are measured using the Attenuated Total Reflectance Fourier Transform Infrared Spectroscopy (ATR-FT-IR) method. The test measures the infrared spectrum of energy absorption of the aged and unaged binder at multiple wavelengths. The spectra resulting from the ATR-FT-IR

method contains peaks at wavenumbers that correspond to different types of bonds within the asphalt cement. Oxidation results in an increase in the number of double bonds between hydrocarbons and oxygen, which can be detected with the ATF-FT-IR test. The two specific functional groups examined in this study are the carbonyl and sulfoxide groups. Studies have linked the increase in absorbances at these groups to oxidation of asphalt. The metrics adopted are the area under the carbonyl and sulfoxide peaks from Jemison et al. 1992 and Petersen and Glaser 2011), referred to as CA and CA+S respectively [112, 113]. The effect of oxidation quantified by examining the changes in these quantities with RTFO and PAV aging.

3.4 Asphalt Mixture Experiments

The asphalt mixture tests conducted in this study include AASHTO T342 (dynamic modulus test), AASHTO TP107 (axial fatigue test), and AASHTO T324 (Hamburg wheel tracking test). These tests are used to respectively identify the ability of the mixtures to resist deformation, their ability to resist fatigue, and their ability to resist rutting. The sections below highlight the specific details of each test as it is most relevant to the current study, but the detailed experimental setup and analysis methods applied for each experiment is presented in Appendix A.

3.4.1 Dynamic Modulus

The axial dynamic modulus, $|E^*|$, test is performed using a servo-hydraulic testing machine and involves repeated sinusoidal loading of a cylindrical specimen along its symmetrical axis. The test itself is standardized in AASHTO T342 and involves subjecting test specimens to cyclic compression loading at frequencies of 25, 10, 5, 1, 0.5, and 0.1 Hz and at temperatures of -10, 4.4, 21.1, 37.8, and 54°C. Tests are conducted in an increasing order

of temperature and in a decreasing order of loading frequency. The load is varied with temperature and frequency so that the on-specimen strains remain in the range of 40-80 micro-strains. As per the standard, $|E^*|$ is calculated by sinusoidal regression of the stress and strain responses of the last five cycles of each temperature and frequency combination.

3.4.2 Axial Fatigue

The uniaxial fatigue test is conducted according to the procedure documented in AASHTO TP107, and involves the repeated sinusoidal displacement of a cylindrical sample until it fails. The cylindrical specimen is 150 mm tall and 75 mm in diameter. The test temperature is selected based on the 98% reliability performance grade of the asphalt binder used in the mixture. The general guideline as per AASHTO TP107 is that the testing temperature should be determined as the average of high and low temperature PG grades minus 3°C. For example, the test temperature for PG 64-22 asphalt is 18°C. If the calculated test temperature exceeds 21°C, 21°C is used as the testing temperature. The uniaxial fatigue test is run until a sudden decrease in phase angle is observed, which indicates that a crack has localized, and that failure has occurred.

3.4.3 Flow Number Test

The flow number test (also known as the repeated load permanent deformation, or RLPD test) is conducted according to the procedure documented in AASHTO T378. The flow number test applies repeated load pulses for several thousand cycles and records the cumulative permanent deformation as a function of the applied cycles. A haversine pulse load of 0.1 second duration and 0.9 seconds of rest time is applied. The deformations are measured using LVDTs mounted to the surface of the sample. The test is performed under atmospheric conditions, and prior to testing, a thin and lubricated membrane is placed

between the sample ends and the loading platens to create frictionless surface conditions. For this study, the RLPD test is performed at only 50°C and always at a stress level of 400 kPa.

3.4.4 Hamburg Wheel Tracker

The Hamburg wheel-track (HWT) test, AASHTO T324, is a test method to evaluate the rutting and moisture susceptibility of asphalt mixtures. The equipment consists of a reciprocating wheel, which simulates a moving concentrated load. Test specimens are compacted using the Superpave gyratory compactor and have a diameter of 150 mm. Following ADOT and AASHTO protocols all tests are performed at a loading frequency of 52 ± 2 passes per minute and for a maximum of 20,000 passes. Tests are conducted at temperatures based on the S-grade of the asphalt binder in question, see Table 3-10. It is worth noting that ADOT has been conducting its HWT tests at 50°C, irrespective of the binder grade. So, in line with ADOT practice, mixtures with PG 76S-XX asphalt will also be tested at 50°C, apart from 56 and 62°C.

Table 3-10. HWT Test Temperatures by Asphalt Binder Grade.

Asphalt Binder Grade	Test Temperatures (°C)
PG 76S-XX	62 and 56
PG 70S-XX	56 and 50
PG 64S-XX	50 and 44

3.4.5 Specimen Fabrication

All test specimens are compacted using a Servopac Superpave Gyratory compactor. The ram pressure, gyration angle, and gyration speed are 600 kPa, 1.16°, and 30 gyrations per minute respectively. All specimens are compacted with a diameter of 150 mm. Specimens for dynamic modulus and axial fatigue samples are first compacted to a height of 180 mm

while those for Hamburg are compacted to a height of 100 mm. Hamburg tests are conducted on the as compacted samples, but dynamic modulus and fatigue specimens are cored from the compacted samples (100 mm core for dynamic modulus and 75 mm core for axial fatigue) and cut to a final test height of 150 mm. This process is followed to ensure as uniform of an air void distribution as possible throughout the test specimen.

After obtaining specimens of the appropriate dimensions, air void measurements are taken via the AASHTO T166 method, and specimens are stored until testing. The air voids for the dynamic modulus and axial fatigue specimens in this study are between 6.0 and 7.0 percent, while those for Hamburg tests are between 6 and 8 percent. During storage, specimens are sealed in bags and placed in an unlit cabinet to reduce aging effects. Furthermore, no test specimens are stored for longer than 2 weeks before testing.

Chapter 4. RELATIONSHIP BETWEEN DYNAMIC SHEAR MODULUS |*G**| OF ASPHALT BINDERS AND HMA DYNAMIC MODULUS OF ELASTICITY |*E**|

The dynamic modulus, |*E**|, is a fundamental property that defines the strain response characteristics of asphalt concrete mixtures as a function of loading frequency, temperature, and load magnitude. The main goal of this chapter is to show how well-known dynamic modulus |*E**| predictive models predict changes in |*E**| as a function of changes in mixture volumetric properties, aggregate gradation, binder properties (viscosity (η) and binder shear modulus |*G**|), and test conditions (temperature and loading frequency) for Group 1 and Group 2 lab mixtures. The mixtures are described in Chapter 3. Also, the other objective is to identify the best |*E**| predictive model that will be used in Chapter 5 to examine the aging behaviors of the study mixtures. The chapter is segmented into four main parts. In the first part, the mixture volumetric properties and the aggregate gradation of the study asphalts measured in the lab are discussed. In the second part, the binder properties of the study asphalts deduced from the temperature-frequency test are presented. In the third part, the dynamic modulus |*E**| of the study asphalt mixtures was performed at a range of temperatures and loading frequencies. Also displayed in this part the dynamic modulus results for all the mixtures using master curves. Finally, different dynamic modulus |*E**| predictive models was used and a detailed discussion on the relationship between the dynamic modulus |*E**| and mixture volumetric properties, aggregate gradation, and binder properties are presented.

4.1 Mixture Volumetric Properties and the Aggregate Gradation

4.1.1 Aggregate Gradation

The aggregates used in this current study have been sourced from three suppliers in Arizona: Hanson Aggregates in Globe, Brimhall-Sand and Rock in Snowflake, and Granite Construction in Tucson. A brief description of the aggregates and their corresponding characteristics are provided in Chapter 3. The aggregate gradation that required as an input for dynamic modulus $|E^*|$ predictive models was presented in Appendix C.

4.1.2 Mixture Volumetric Properties

All the asphalt mixtures developed in the study are in line with the current ADOT Superpave mix design criteria. The mix design parameters of interest for all asphalt mixtures are detailed in Chapter 3 and Appendix C.

4.2 Binder Properties

4.2.1 Results from Temperature-Frequency Test

The asphalt binder characterization is performed using temperature-frequency sweep experiments. The specific details of the test were provided in Chapter 3. The outputs from the temperature – frequency tests are the dynamic shear modulus $|G^*|$ and the phase angle (δ). Temperature and frequency sweeps were conducted at 10, 20, 30, 40 and 54°C and at a frequency range of 30 - 0.1 Hz (30, 14, 6.5, 3, 1.4, 0.65, 0.3, 0.14, 0.1 Hz). The tests were performed on a Anton-Paar MCR 302 dynamic shear rheometer. Prior to all testing a strain sweep experiment was conducted and the tests were performed at strain levels below the linear viscoelastic limit but above the resolution limits of the equipment (100 – 400 με).

Tests were conducted from low temperature to high temperature and from high frequency to low frequency. The modulus and phase angle values used in subsequent calculations were taken directly from the test equipment's internal calculation; however, the quality of the torque and encoder signals were monitored continuously throughout the testing to ensure that the calculated results were representative of the test.

After experimental characterization of the dynamic modulus, the Christensen-Anderson-Marasteanu (CAM) model shown in Equation (4-4) is used to develop the $|G^*|$ mastercurves and the William-Landel-Ferry (WLF) equation shown in Equation (4-5) is used to model the time-temperature shift. Non-linear optimization used to develop the $|G^*|$ mastercurves for asphalt. For this purpose, researcher have found the "solver" function of Microsoft Excel quite convenient and accurate. To use the solver function, the observed values are first compared with the predicted values. For each set of data, the difference between the logarithmic predicted and logarithmic observed value gives the error amount for that data point. The sum of all error squares is first minimized by changing the values of the fitting parameters included in the model under consideration by the use of the built-in "solver" function of Microsoft Excel. This process gives the optimized model with minimal scatter.

$$\left|G^*\right| = \frac{10^g}{\left(1+\left(\frac{\omega_c}{\omega_R}\right)^k\right)^{\frac{m_e}{k}}} \tag{4-1}$$

$$\log a_T = \frac{C_1(T-T_R)}{C_2+T-T_R} \tag{4-2}$$

where; $|G^*|$ is the dynamic shear modulus (Pa), 10^g is the binder glassy modulus (Pa) (determined through optimization), ω_c is the crossover frequency (rad/s) (a fitting coefficient), m_e and k are fitting coefficients, T is the test temperature (°C), T_R is the reference temperature (°C), and C_1 and C_2 are the time-temperature shift factor function fitting coefficients.

The master curves are developed at a reference temperature of 15°C and for all 12 study binders at three aging levels, i.e. original, RTFO, and PAV. For the sake of brevity, master curves of only two asphalts one non-polymer modified (PG 64-22(Z)) and one polymer modified asphalt (PG 64V-22(X)) are shown in Figure 4-1 and Figure 4-2 respectively. The master curves of the remaining asphalts are shown in Appendix B [153]. In both binders, it can be seen that the modulus increases with aging level. However, what is worth noticing is the vertical spacing between aged and original conditions between the two asphalts. It can be clearly observed that vertical spacing between original and aged conditions is greater in non-polymer modified asphalt, PG 64-22(Z) than polymer modified asphalt, PG 64V-22(X). These visual observations can be quantified using the aging ratio parameter, which is the ratio of aged dynamic shear modulus to complex shear modulus at the original or unaged condition for a given temperature and frequency (shown in Chapter 5).

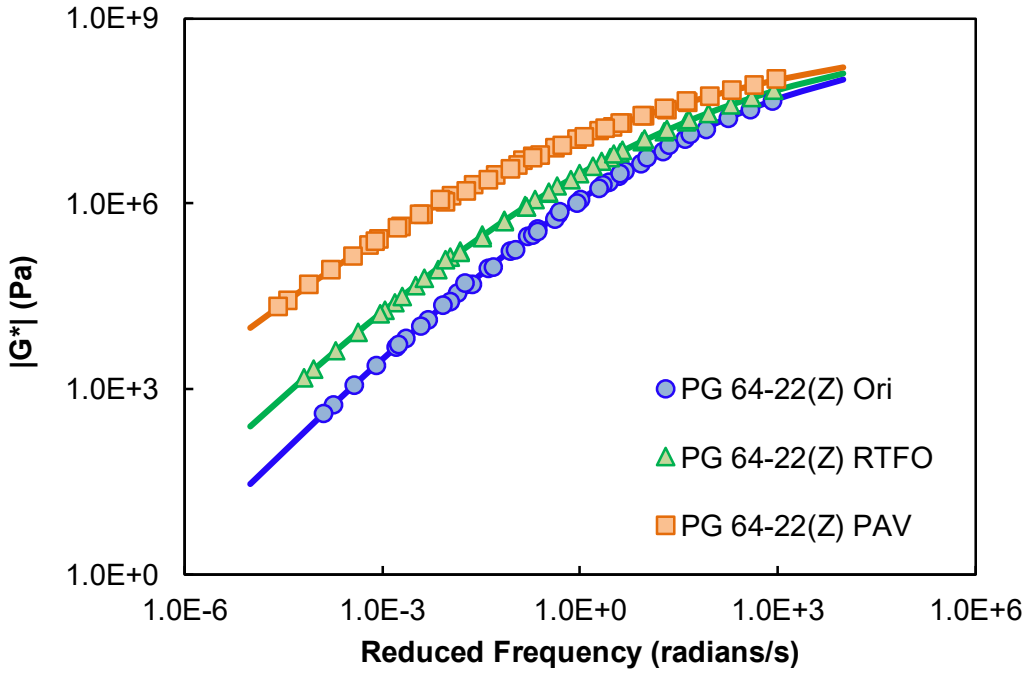

Figure 4-1 Dynamic Modulus Mastercurves for PG 64-22(Z) at Original, RTFO, and PAV Aged Conditions.

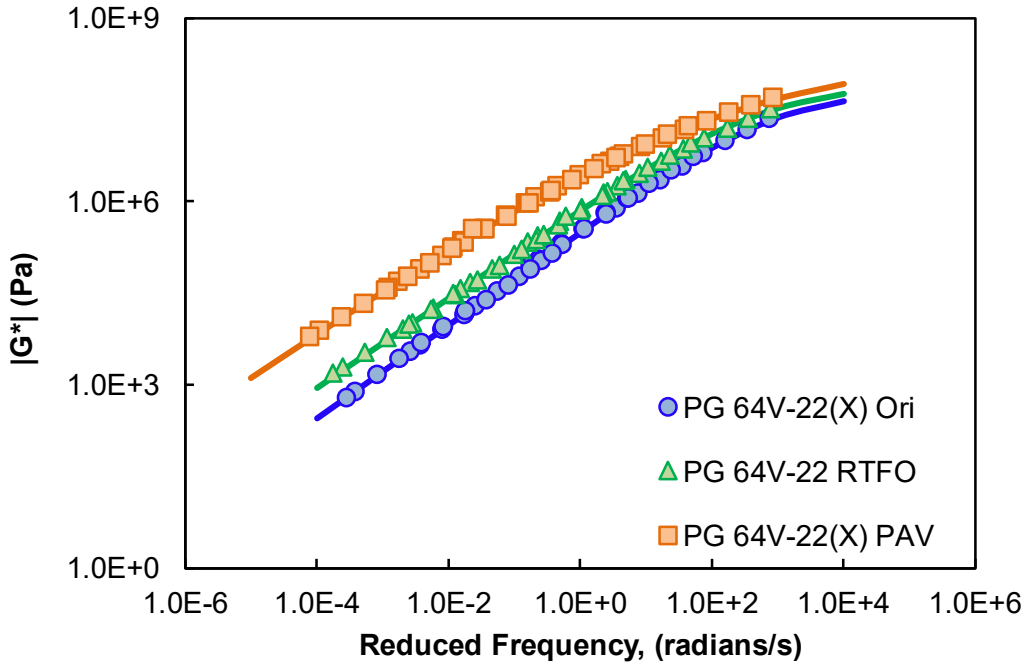

Figure 4-2: Dynamic Modulus Mastercurves for PG 64V-22(X) at Original, RTFO, and PAV Aged Conditions.

4.3 Dynamic Modulus Test

The dynamic modulus test is performed to measure the asphalt mixture stiffness at a range of temperatures and loading frequencies. Additional details regarding the test and the test conditions were provided in Chapter 3 and Appendix A.

4.3.1 Dynamic Modulus Results for Group 1 and Group 2 Mixtures:

The dynamic modulus results for all twelve mixtures (Group 1 and Group 2 binders) are included in Appendix C; the results are best displayed using master curves as Figure 4-3. Detailed master curves with the individual data points at multiple temperatures and frequencies are also presented in Appendix C. It can be seen from Figure 4-3 that GY4 has the highest modulus followed by TX1 and GX5. For ease of observation, the results in Figure 4-3 have been separated by aggregate type and are shown in Figure 4-4 through Figure 4-6 respectively. The first group (Figure 4-4) consists of three mixtures prepared with aggregates procured from Snowflake, binder X3 (a polymer modified binder) and binders Y1 and Z1 (non-polymer modified binders). It can be seen from Figure 4-4 that the polymer-modified mixture has a lower modulus compared to both SY1 and SZ1, which have similar modulli.

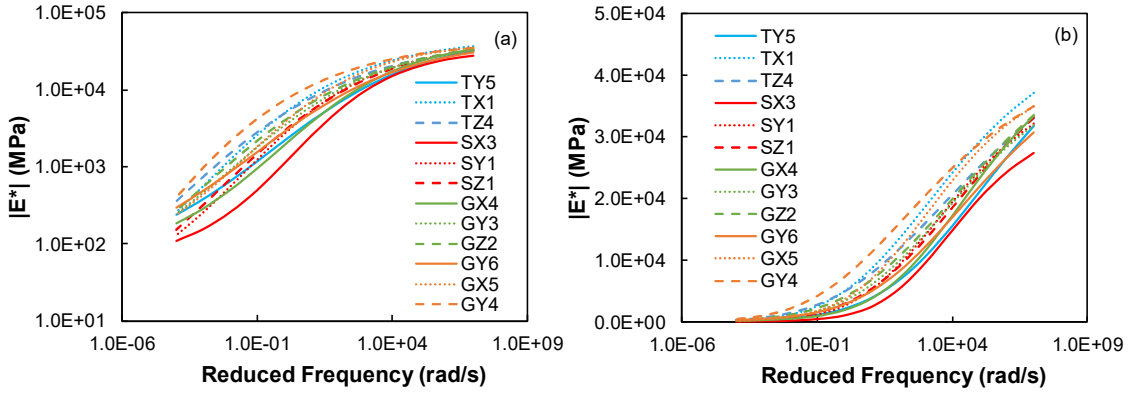

Figure 4-3. Dynamic Modulus Results for All Asphalt Mixtures in (a) log-log Scale and (b) semi-log Scale.

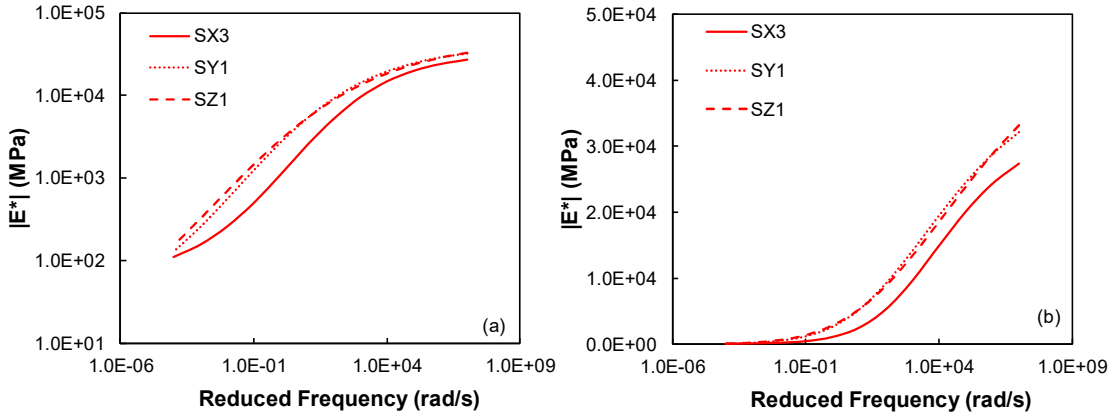

Figure 4-4. Dynamic Modulus Results for Asphalt Mixtures Prepared with Aggregate Procured from Snowflake in (a) log-log Scale and (b) semi-log Scale.

The second group (Figure 4-5) consists of mixtures prepared with aggregate procured from Tucson, binder Y5 (a polymer modified binder) and binders X1 and Z4 (non-polymer modified binders). Again, for this group, the polymer-modified mixture TY5 has a lower modulus than the other two mixtures. TX1 has highest moduli at lower temperatures, but at high temperatures, TZ4 (using PG 76-16) has higher moduli.

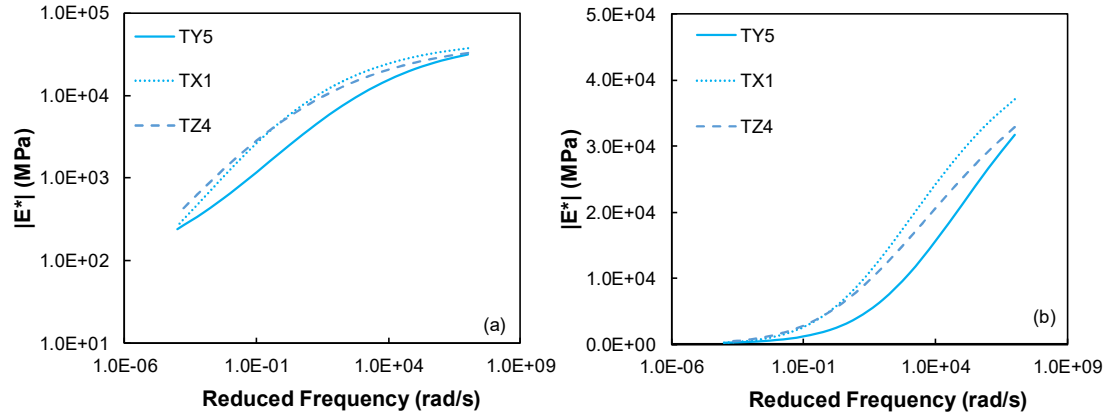

Figure 4-5. Dynamic Modulus Results for Asphalt Mixtures Prepared with Aggregate Procured from Tucson in (a) log-log Scale and (b) semi-log Scale.

The final group consists of mixtures prepared with aggregate from Globe (Figure 4-6). This group includes six mixtures; three polymer-modified (X4, X5, and Y6) and three non-polymer modified (Y3, Y4, and Z2). The mixture GY4 (using PG 76-16) has the highest modulus.

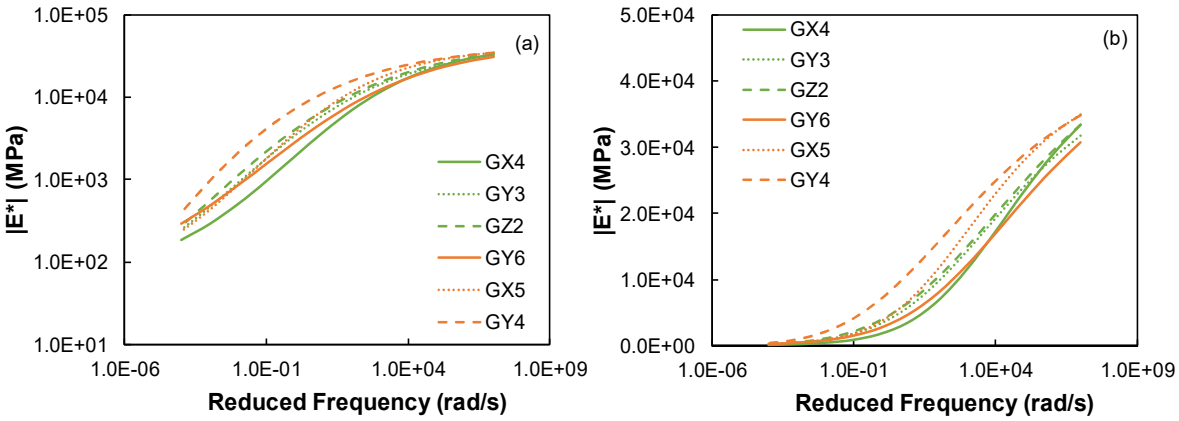

Figure 4-6. Dynamic Modulus Results for Asphalt Mixtures Prepared with Aggregate Procured from Globe in (a) log-log Scale and (b) semi-log Scale.

The mixture GX5 (using PG 76-22TR+) ranks second at low and intermediate temperatures; however, at high temperatures, the modulus is lower than other non-polymer modified mixtures GZ2 and GY3. The remaining two polymer modified mixtures rank lowest in modulus, with GX4 mixture having the least modulus.

Overall, the mixture modulus results rank and go hand-in-hand with the binder modulus results. That is, polymer modified mixtures predominantly having lower moduli than non-polymer modified mixtures.

4.3.2 Dynamic Modulus Results for Group 3 Mixtures:

The dynamic modulus results for all Group 3 asphalts are included in Appendix C; the results are best displayed using master curves as shown in Figure 4-7. Detailed master curves with the individual data points at multiple temperatures and frequencies are also

presented in Appendix C. It can be seen from this figure that TD0.5 is has the highest modulus and TX3 has the lowest modulus. The prefix "T" to the binder notation in the mixture performance results below indicates the source of the aggregate, which is Tucson in this case. The binders have been color-coded to reflect the group they belong to.

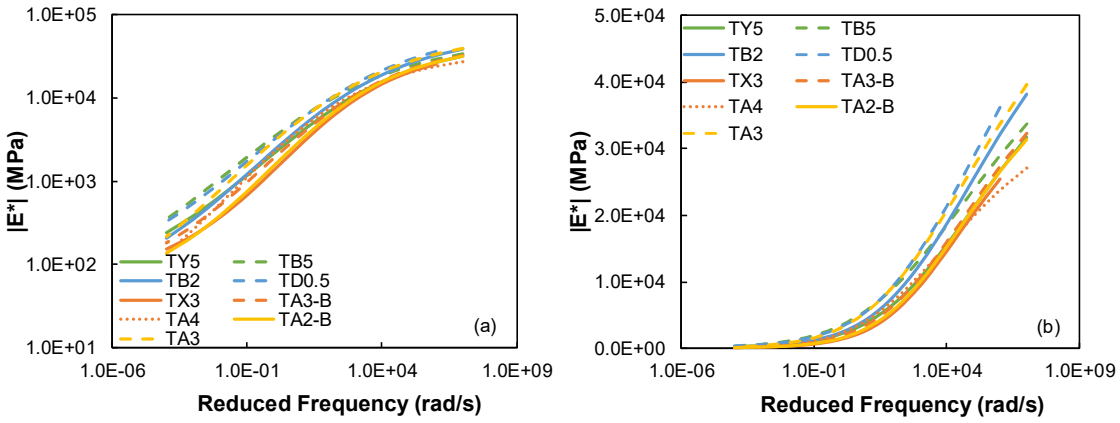

Figure 4-7. Dynamic Modulus Results for Group 3 Asphalt Binders in (a) log-log Scale and (b) semi-log Scale.

4.3.2.1 Binders in Group J.

This group consisted of two asphalts, Y5 and B5. Based on the binder $|G^*|$values at 64°C, B5 has the highest $|G^*|$. Similar trends are observed in the mixture dynamic modulus also. The results from the dynamic modulus tests are presented in Figure 4-8. TB5 has a higher modulus than TY5 at all temperatures and frequencies. The differences between the two mixtures were checked for statistical significance by performing a two-tail t-test at 95% significance level at all five test temperatures at the test frequency of 10 Hz. It was found that the modulus of the two mixtures is only statistically different at intermediate and high temperatures but not at low temperatures, 4.4°C, and -10°C.

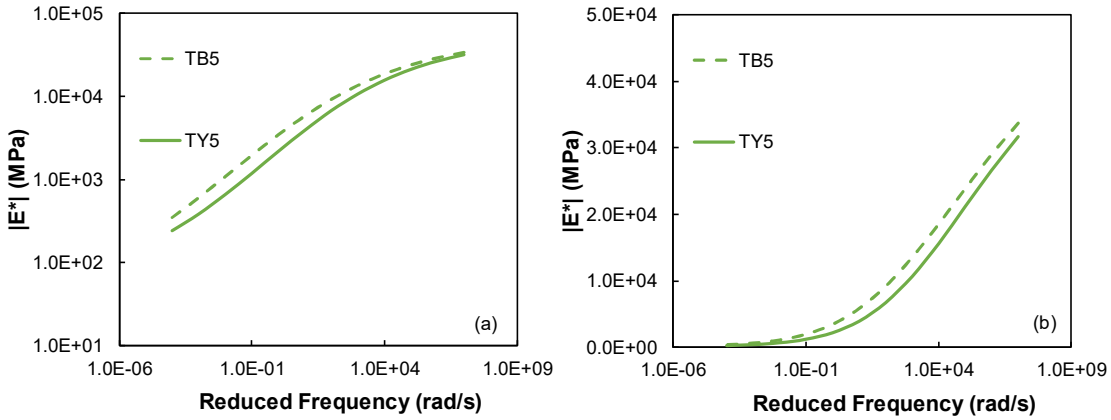

Figure 4-8. Dynamic Modulus Results for Group J Asphalt Binders in (a) log-log Scale and (b) semi-log Scale.

4.3.2.2 Binders in Group K.

This group consists of two binders, B2 and D0.5. With regards to the binder modulus at 64°C, D0.5 has a higher $|G^*|$ than B2 and similar trend is seen with the mixture dynamic modulus results also. The dynamic modulus results for the two binders are presented in Figure 4-9. Similar to the previous comparison, the modulus of the mixtures, TD0.5 and TB2 are significant only at intermediate and high temperatures.

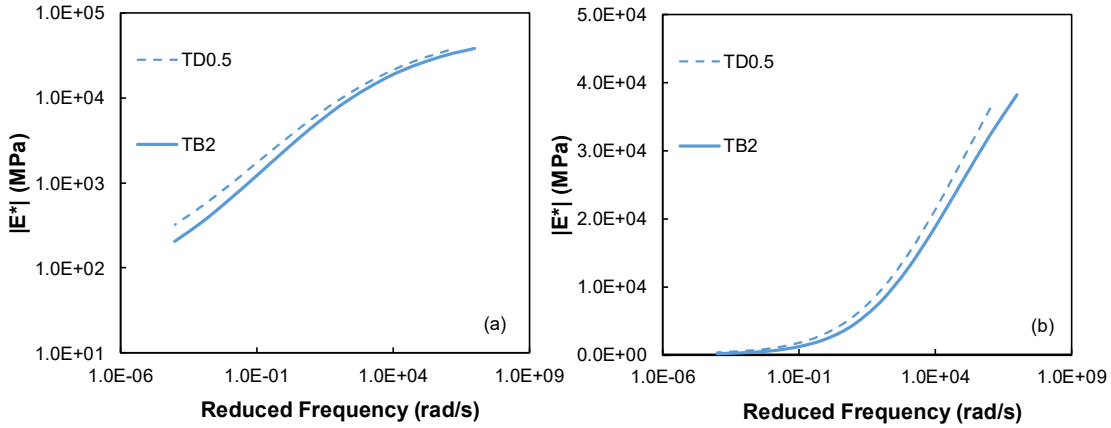

Figure 4-9. Dynamic Modulus Results for Group K Asphalt Binders in (a) log-log Scale and (b) semi-log Scale.

4.3.2.3 Binders in Group L.

This group consists of three binders, X3, A3-B, and A4. Based on the $|G^*|$ values of the three asphalts at 64°C, A4 has the highest modulus followed by A3-B and X3. Similar

trend is seen in the mixture modulus results also, as seen in Figure 4-10. However, the statistically significant difference is seen only between TA4 and TX3 at intermediate and high temperatures. All other combinations of comparisons, i.e. TA4 vs TA3-B, and TA3-B vs TX3 are found to be statistically insignificant at 95% significance level.

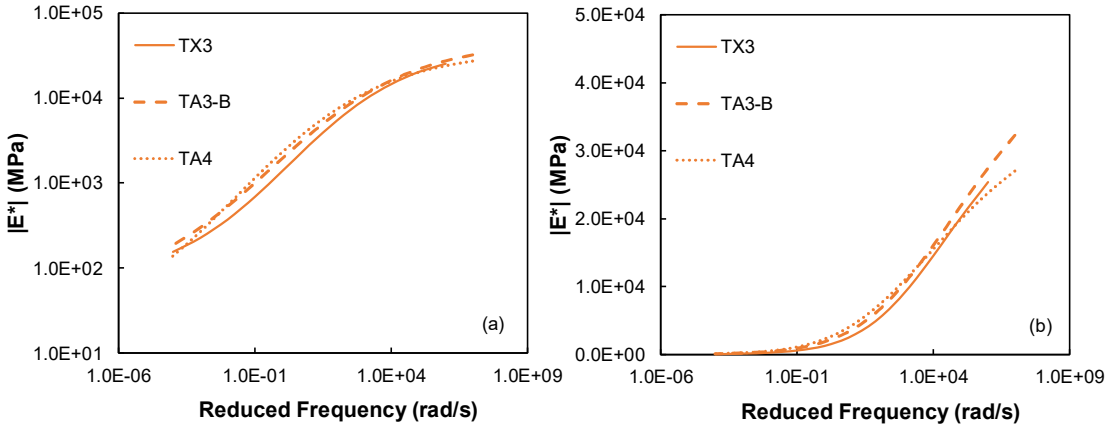

Figure 4-10. Dynamic Modulus Results for Group L Asphalt Binders in (a) log-log Scale; and (b) semi-log Scale.

4.3.2.4 Binders in Group M.

This group consisted of two binders, A2-B and A3. Based on the binder $|G^*|$ of the two asphalts, A3 has a higher binder $|G^*|$ than A2-B. Similar trend is observed in the mixture dynamic modulus results as seen in Figure 4-11. Also, statistically significant differences were seen between the two mixtures at all temperatures except -10°C.

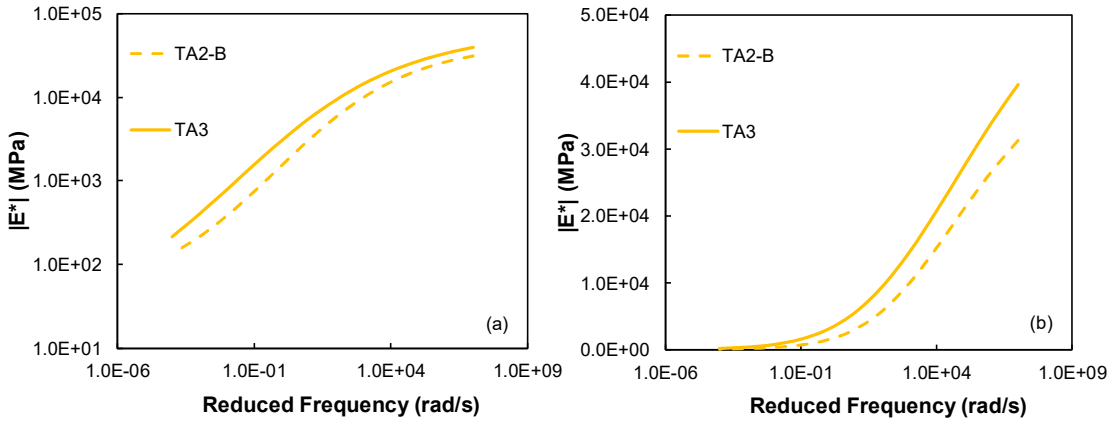

Figure 4-11. Dynamic Modulus Results for Group M Asphalt Binders in (a) log-log Scale; and (b) semi-log Scale.

Overall the conclusions from the dynamic modulus test are:

(i) The mixture dynamic modulus results rank and go hand-in-hand with the binder modulus results $|G^*|$.

(ii) The polymer modified mixtures predominantly having lower moduli than non-polymer modified mixtures.

4.4 Relationship between the Dynamic Modulus $|E^*|$ and Mixture Volumetric Properties, Aggregate Gradation, and Binder Properties:

Several alternative predictive relationships have been developed to estimate the $|E^*|$ from simpler material properties and volumetric properties. These predictive relationships can be used to estimate $|E^*|$ values. The predictive relationships that are used in the analysis here are; Original Witczak Equation (NCHRP 1-37A), Modified Witczak $|G^*|$ Equation (NCHRP 1-40D), Hirsch Model, Al-Khateeb model, Simplified Global Model, Improved Hirsch Model, Van der Poel (Shell Oil's Early Version) Model, Law of Mixtures Parallel Model, ANN Model, and *MR*-$|E^*|$ Model. The predictive relationships are summarized in Chapter 2. The first five relationships were used in the analysis for this study..

4.4.1 Evaluation of Predictive Models

In this section, five selected existing models (including the modified Witczak, Hirsch, and Al-Khateeb, simplified global models) are evaluated along with measured $|E^*|$ using the Group 1 and Group 2 asphalt binder at only three temperatures (21.1, 37.8, and 54.4°C) as shown in Figure 4-13 through Figure 4-15. It should be noted here that the binder data at these three temperatures are estimated by using the CAM model. However, at low temperatures of 4.4 and -10°C the dynamic modulus comparison in this evaluation are excluded from the analysis. The main reason for excluding the data is that the binder data measurements lower than 10°C are not measured and this research did not conduct tests that validate the CAM extrapolation. If the CAM model was used to extrapolate these binders at low temperatures, the difference between the extrapolated data and the true values could be very large and lead to incorrect results when using this data to estimate the asphalt mixture data. The detailed statistics obtained from the model would provide a more meaningful comparison as shown in Table 4-1.

The first observation from this analysis is shown in Figure 4-12 for the Al-Khateeb model. As the data demonstrates, a significant bias (i.e., a power trend between the predicted $|E^*|$ and the measured $|E^*|$ values) is observed for many of the predictions. Due to the extreme bias relative to the other existing models, it was decided that this model would be dropped from consideration in any future ageing analysis.

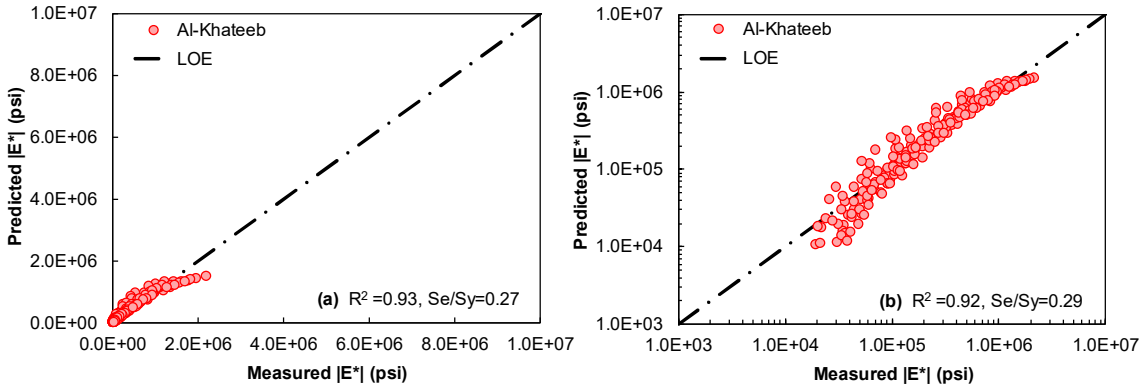

Figure 4-12 Predicted Modulus Values Using Al-khateeb Model for Group 1and Group 2 Binders in; (a) Arithmetic and (b) Logarithmic Scales.

Table 4-1 Statistics of Predictive Models for Group 1 and Group 2 of Asphalt Binders.

Parameter	Predictive Models for η-|Gb*| of Asphalt Binders				
	Original Witczak Model	Modified Witczak Model	Hirsch Model	Al-Khateeb Model	Simplified Global Model
Total binders	12	12	12	12	12
Data Points, N	216	216	216	216	216
	Goodness of Fit in Logarithmic Scale				
Se/Sy	0.30	0.39	0.20	0.29	0.27
R^2	0.91	0.86	0.96	0.92	0.93
	Goodness of Fit in Arithmetic Scale				
Se/Sy	0.49	0.81	0.20	0.27	0.33
R^2	0.77	0.40	0.96	0.93	0.90

As seen in Table 4-1, the Original Witczak and the Modified Witczak models had very good to excellent goodness of fit statistics in the logarithmic scale for the measured data used for validating the models. The Original Witczak model had $R^2 \approx 0.91$ and Se/Sy ≈ 0.30, while the Modified Witczak model had $R^2 \approx 0.86$ and Se/Sy ≈ 0.39.

It should be noted here that similar to the other models, the Original Witczak and the Modified Witczak models were optimized based on minimizing the sum of error squares obtained from the prediction of log (stiffness) [13]. As a result, these two models had only fair good goodness of fit statistics in arithmetic domain. The Original Witczak model had

$R^2 \approx 0.77$ and Se/Sy ≈ 0.49, while the Modified Witczak model had $R^2 \approx 0.81$ and Se/Sy ≈ 0.40. Figure 4-13 shows the plots of observed versus predicted $|E^*|$ for the Original Witczak model. For the Original Witczak model, the binder viscosity, η, of the binder was used to predict $|E^*|$, construct the plot, and calculate the goodness of fit statistics. The very small data scatter seen in Figure 4-13 was contributed mainly by the variability in the type and amount of modification present in the modified binders used in this study. The viscosity is an input for the Original Witczak model. In this work, the viscosity was estimated for each binder by using the shear modulus and the phase angle at different frequencies and temperatures. The variability of phase angle by using CAM model is high especially for the modified binders. The phase angle variability was noted to be even higher at high temperature.

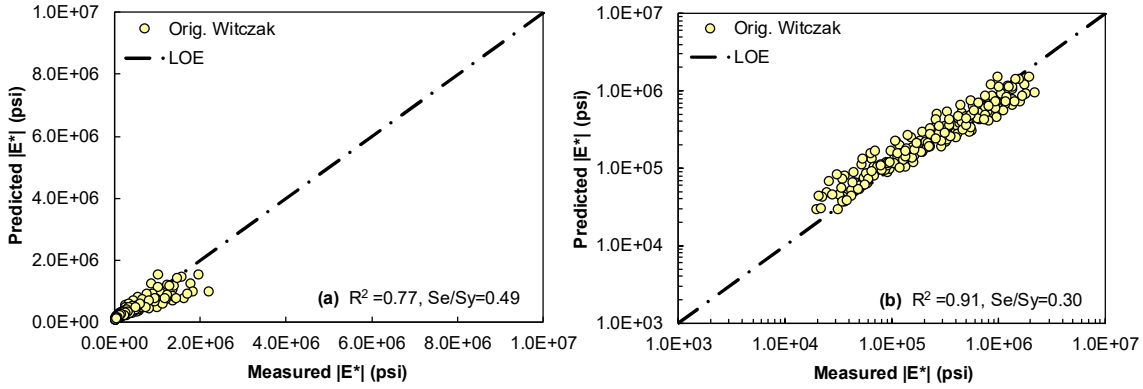

Figure 4-13 Predicted Modulus Values Using Original Witczak Model for Group 1and Group 2 Binders in; (a) Arithmetic and (b) Logarithmic Scales.

This scatter is even worse when using the Modified Witczak model as shown in Figure 4-14. Based on the finding it was concluded that both Witczak models were non-ideal for the purposes of back calculating the complex shear modulus of the binder (see Chapter 5).

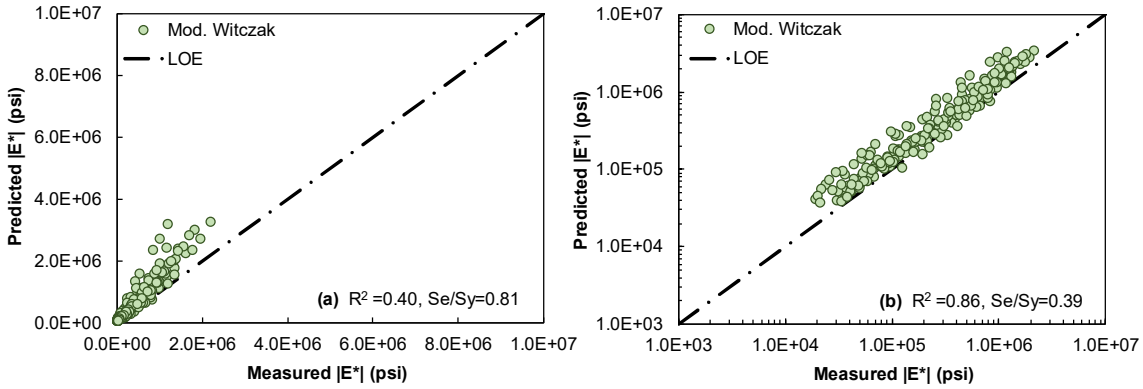

Figure 4-14 Predicted Modulus Values Using Modified Witczak Model for Group 1 and Group 2 Binders; in (a) Arithmetic and (b) Logarithmic Scales.

The comparisons of the predicted versus measured dynamic modulus values for the simplified global model is presented in both arithmetic and logarithmic scales in Figure 4-15. The model is expressed as follows: The statistical measurements for the simplified global model indicate an excellent fit with high correlation coefficients and error terms of $R^2 = 0.93$ and Se/Sy = 0.27, and $R^2 = 0.90$ and Se/Sy = 0.33 in arithmetic and logarithmic scales, respectively.

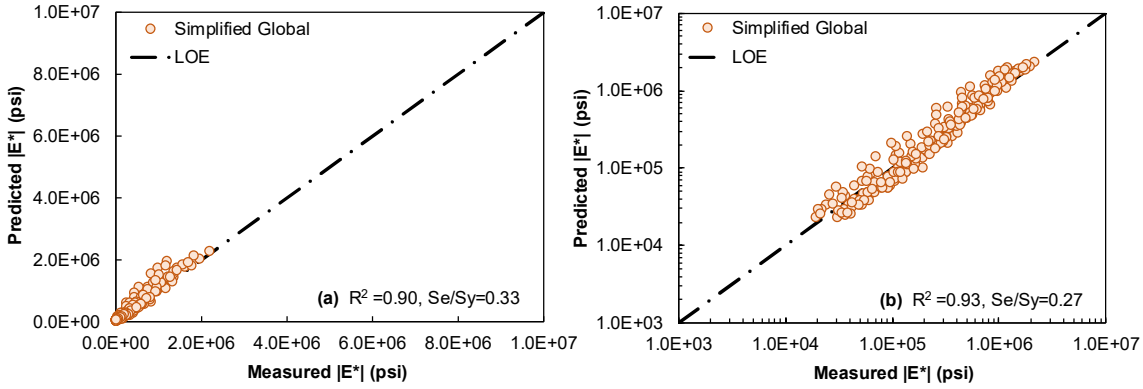

Figure 4-15 Predicted Modulus Values Using Simplified Global Model for Group 1and Group 2 Binders in (a) Arithmetic and (b) Logarithmic Scales.

When the prediction is good, the expectation is that a group of data points following the LOE with an oval shape in the LOE graph would be seen. In this respect, the Hirsch model demonstrates a high correlation. The comparisons of the predicted versus measured

dynamic modulus values almost on the line of equality (LOE) as shown in Figure 4-16. The statistical measurements for the simplified global model indicate a tremendous fit with high correlation coefficients and error terms of $R^2 = 0.96$ and $S_e/S_y = 0.20$, and $R^2 = 0.96$ and $S_e/S_y = 0.20$ in arithmetic and logarithmic scales, respectively. Both Hirsch model and simplified global model will be used to estimate the complex shear module of asphalt binder for STOA condition study in Chapter 5.

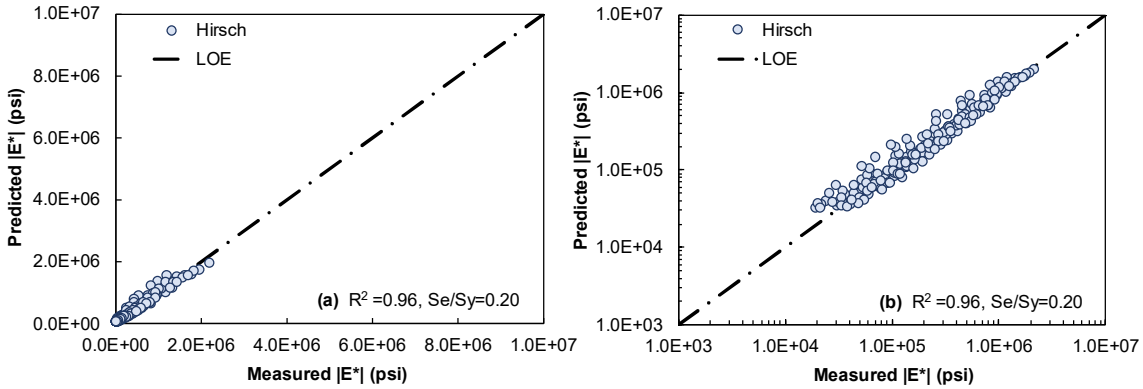

Figure 4-16 Predicted Modulus Values Using Hirsch Model for Group 1 and Group 2 Binders in (a) Arithmetic and (b) Logarithmic Scales.

4.4.2 Statistical Analysis

4.4.2.1 Model Comparison

While comparing models predictions to known data, there are three important considerations to note: precision, accuracy and bias. In the case of the predictive model, precision refers to how close the predicted and observed data are to each other. The scatter in a plot of observed versus predicted data reflects the precision. Accuracy is the conformity of prediction to the true observed value. Bias is a tendency of predicted data to deviate in one direction from the observed data. In other words, bias is a systematic error between predicted and observed data. Accuracy, precision and bias are influenced by the

errors in optimization, factors omitted from the model and wrong function or structure used in the model [13].

4.4.2.2 Goodness of Fit

Goodness of fit indicates how well the model input parameters fit into the model. To determine the goodness of fit, the predicted values are calculated using the model and are then compared with the measured values at the same input conditions. The comparison is obtained by finding the error in the prediction for each data point. The following are the equations that are used to compare the prediction and measure the goodness of fit of the model.

$$Error, \varepsilon_i = \left(predicted\ data\right)_i - \left(measured\ data\right)_i \tag{4-3}$$

$$Sum\ of\ Error = \Sigma\varepsilon_i \tag{4-4}$$

$$Sum\ of\ Squared\ Error,\ SSE = \sum\left(\varepsilon_i\right)^2 \tag{4-5}$$

The goodness of fit was evaluated in two ways; in logarithmic scale and in arithmetic scale. For analyzing the goodness of fit in arithmetic scale, the dependent variable is defined by $|E^*|$ (in psi), error is defined by "predicted $|E^*|$ - measured $|E^*|$" and S_y is defined by the standard deviation of the measured $|E^*|$ values. For analyzing the goodness of fit in logarithmic scale, the dependent variable is defined by log $|E^*|$ ($|E^*|$ in psi), error is defined by "predicted log $|E^*|$ - measured log $|E^*|$" and S_y is defined by the standard deviation of the observed log $|E^*|$values.

Sum of Squared Error, $SSE_{normal} = \sum\left[\left|E^*\right|_{predicted} - \left|E^*\right|_{measured}\right]^2$ (4-6)

Sum of Squared Error of logarithm, $SSE_{\log} = \sum\left[\log\left(\left|E^*\right|_{predicted}\right) - \log\left(\left|E^*\right|_{measured}\right)\right]^2$ (4-7)

$$\text{Standard Error}, S_e = \sqrt{\left(\frac{SSE}{n-1}\right)} \tag{4-8}$$

$$\textit{Standard Deviation}, \ \mathrm{S_y} = \sqrt{\frac{1}{n-1}\sum_{i=1}^{n}\left(x_i - \bar{x}\right)^2} \tag{4-9}$$

$$\textit{Arithmetic Mean}, \bar{x} = \frac{1}{n}\sum_{i=1}^{n} x_i \tag{4-10}$$

where,

i = data point number

x_i = value of i-th data point

n = number of data points

For a model with p number of fitting coefficients, the values of the coefficient of determination (R^2) can be computed using the following equation. This process provides the adjusted R^2 for the model taking into account the degrees of freedom.

$$\mathrm{R^2} = 1 - \frac{n-p}{n-1}.\left(\frac{\mathrm{S_e}}{\mathrm{S_y}}\right)^2 \tag{4-11}$$

where,

n = number of data points

p = number of regression constants

$n - p$ = degrees of freedom

S_e = standard error

S_y = standard deviation of observed data

4.4.2.3 Model Optimization

Once the general mathematical structure of a model is defined, the fitting coefficients need to be optimized. Through optimization, the regression coefficients or fitting parameters

within the model are assigned specific values in such a way that the model equation provides the minimum error when the predicted and observed data are compared. There are two considerations considered during this process; reduction in scatter and elimination of bias. The sum of the squared error ($\sum \varepsilon_i^2$) should be minimized to reduce the scatter in the data, while the bias is eliminated by setting the sum of errors ($\sum \varepsilon_i$) to zero.

Non-linear optimization is almost a mandatory approach for asphalt binder and mixture stiffness prediction models due the complex structure of the models. For this purpose, researchers have found the "solver" function of Microsoft Excel quite convenient and accurate. To use the solver function, the observed values are first compared with the predicted values. For each set of data, the difference between the predicted and observed values gives the error amount for that data point. The sum of all error square is first minimized by changing the values of the fitting or regression parameters included in the model under consideration by the use of the built-in "solver" function of Microsoft Excel. This process gives the optimized model with minimal scatter. The arithmetic sum of all errors is then minimized by further changing the values of the fitting parameters by using the solver function again. When proper seed values of the fitting parameters are used, this process gives an unbiased optimized model equation with a minimum S_e/S_y and a maximum coefficient of determination (R^2). This combination (S_e/S_y and R^2) can further be used to compare the statistical goodness of fit of different candidate models.

4.5 Conclusions

Overall the conclusions from the dynamic modulus test are:

(i) For all study binders at three aging levels, i.e. original, RTFO, and PAV, the modulus increases with aging level.

(ii) The vertical spacing between aged and original conditions is greater in non-polymer modified asphalt than polymer modified asphalt. These visual observations can be quantified using the aging ratio parameter.

Overall the conclusions from the dynamic modulus test are:

(i) The mixture dynamic modulus results rank and go hand-in-hand with the binder modulus results $|G^*|$.

(ii) The polymer modified mixtures predominantly having lower moduli than non-polymer modified mixtures.

The findings from the evaluation of the predictive models are summarized as follows:

(i) The Al-Khateeb model displays a significant bias relative to the other existing models and, therefore, the model dropped from future ageing analysis.

(ii) Both of Witczak models had less goodness of fit statistics comparing by the other models, and both of them have two variables (phase angle and binder shear module) and can't be used to back calculate the binder shear module. For both of these reasons were excluded from the models list.

(iii)The statistical measurements for the simplified global and Hirsch models indicate an excellent fit with high correlation. Both of the models performs very well and show the least scatter with the least bias overall. So, they will be used to estimate the complex shear module of binder for STOA condition study in Chapter5.

Chapter 5. MIXTURE SHORT-TERM AGING IN THE LABORATORY AND BINDER AGING

To effectively characterize the multiscale mechanics associated with the binder to mixture behaviors, it is important that the asphalt binder tested in the laboratory represent what exists inside the mixture. The main goal of this chapter is to ensure that the binder test properties reflect the condition of the binder during the mixture test. There are two ways to show that this is important, one is to age mixture with different binders at different levels and show how the effect of aging is inconsistent (or consistent) and the other way is to do the same in binder and show the aging is inconsistent. To demonstrate the importance of this aging level coordination to make accurate inferences about binder to mixture relationships, an analysis showing how relative and absolute changes in asphalt binder properties from different suppliers and grades can vary under laboratory aging conditions is conducted. The specific task is to compare the RTFO (rolling-thin film oven) and the PAV (pressure aging vessel) aging for asphalt binders and the STOA (short-term oven aging) for asphalt mixtures. The chapter has been segmented into three parts. First, the propensity of the asphalt binder to oxidize is measured by calculating the aging ratio of RTFO and PAV aged conditions. Second, the effects of the laboratory procedure for short-term aging are evaluated using extraction and recovery of binder from compacted mixtures. Finally the changes to the asphalt binders in the compacted mixtures as a result of oxidation were gauged by three different methods: 1) performing binder rheology testing of binder, 2) using the Attenuated Total Reflectance Fourier Transform Infrared Spectroscopy (ATR-FTIR), and 3) back calculating the binder |G*| by using calibrated |E^*| predictive models. Subsequently, the analyses performed with regard to the development of the best

demonstrative of short-term oven aging on asphalt mixtures to the asphalt binders aged conditions are discussed.

5.1 Background

Heating of asphalt during production and construction causes the volatilization and oxidation of binders used in mixes. Volatilization and oxidation cause degradation of asphalt pavements. Degradation of asphalt binders by volatilization and oxidation from the high production temperature that occurs during the production and early stages of pavement life and are known as Short Term Aging (STA). Superpave binder specifications recognize the importance of STA and require the asphalt binder to be tested in three critical stages: the first stage is represented by an original asphalt binder, which has to be transported, stored, and handled prior to mixing with the aggregate. The second stage is represented by the aged asphalt binder after hot mix asphalt (HMA) production and construction (short-term aging). The third stage is represented by an asphalt binder which undergoes further aging during a long period of service. For asphalt binders, the rolling-thin film oven (RTFO) aging test simulates the second stage. For asphalt mixtures, the recommended laboratory procedure for short-term aging is to heat the loose mix in a forced draft oven for 4 h at a temperature of 135ºC [75].

However, previous studies on asphalt mixture aging, based on the increase in the large molecular size (LMS) ratios, has found that the RTFO aging method results in less aging effect than short-term oven aging methods of asphalt mixtures [9]. In NCHRP Project 9-36, researchers showed that the binder aging that occurs when a mixture is short-term conditioned in a forced draft oven for 4 hours at 135°C per AASHTO R 30 generally exceeds the aging that occurs in the short-term binder aging procedures [10]. The

motivation for this specific research need is a preliminary study at Arizona State University advanced pavements laboratory that showed similar results.

To study the correlations between the binder and the mixture properties, it is important that when asphalt binder will be tested in the laboratory there is a reasonable expectation that the tested binder represents the binder that exists inside the mixture. The hypothesis is that, it is a necessary condition when evaluating binder-to-mixture properties that the binder tests reflect the condition of the binder during the mixture test. There are two ways to show that this is important, one is to age mixture with different binders at different levels and show how the effect of aging is inconsistent (or consistent) and the other way is to do the same in binder and show the aging is inconsistent. The analysis in this chapter fallowed the second approach for only Group 1 and Group 2 binders. To demonstrate the importance of this aging level coordination to make accurate inferences about binder to mixture relationships, an analysis showing how relative and absolute changes in asphalt binder properties from different suppliers and grades can vary under laboratory aging conditions is conducted.

5.2 Varying Effect of Oxidation on Binder Rheology

An important characteristic of an asphalt binder is its resistance to oxidation. In the current study, the propensity to oxidize is measured by calculating the aging ratio, which is the ratio of aged shear modulus to the unaged shear modulus at a fixed temperature and frequency as shown in Equation (5-1).

$$AR = \left(\frac{|G^*|\left(\omega_i, T_j\right)_{after\ aging}}{|G^*|\left(\omega_i, T_j\right)_{Original}} \right) \tag{5-1}$$

This parameter is examined in order to determine whether RTFO aging method have comparable aging effect with short-term oven aging methods of asphalt mixtures. Also how consistent the RTFO and PAV aging ratio crossover all the mixtures. This potential and the resultant consequences on aging if any are will be explained in a detailed manner in the later sections.

5.2.1 Aging Ratio for Non-modified Asphalt (Group 1)

The aging ratios at intermediate and high temperatures as calculated for Y1 (PG 64-22) and Y6 (PG 70V-16) are shown in Figure 5-1 and Figure 5-2 respectively. The aging ratio increases with aging level and varies with temperature. Different asphalts have different aging behaviors based on their respective grades and inherent formulations. The aging ratio provides one such methodology to gauge these propensities. The aging ratios for only Group 1 and Group 2 asphalts binders at three different temperatures are presented in Table 5-1.

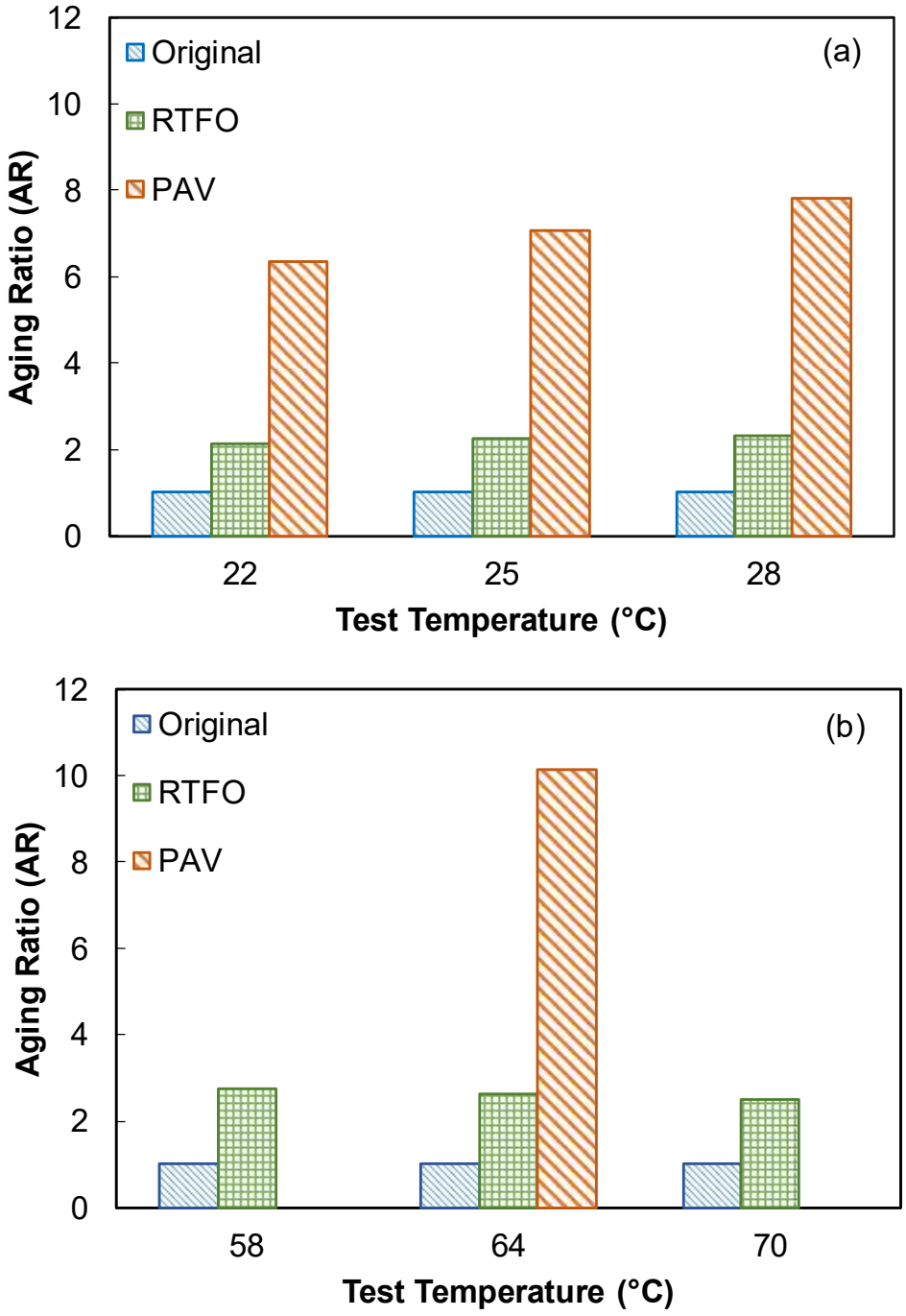

Figure 5-1. Variation of Aging Ratio at; (a) Intermediate Temperature and (b) High Temperature for Binder Y1.

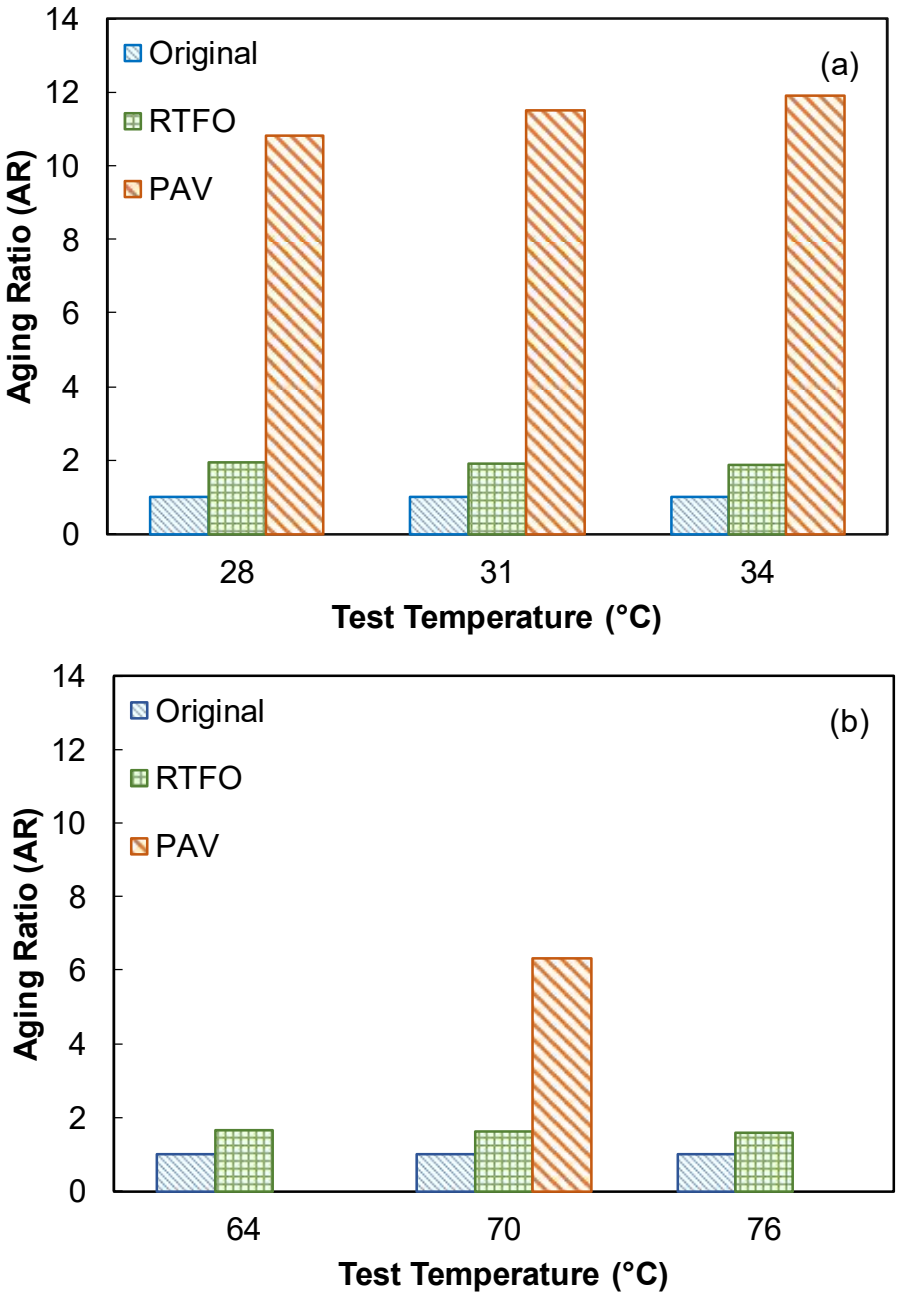

Figure 5-2. Variation of Aging Ratio at; (a) Intermediate Temperature and (b) High Temperature for Binder Y6.

Table 5-1. Aging Ratios of the Study Binders at Intermediate and High Temperatures.

Temperature (°C)	Aging Condition	PG Grade											
		Group 1 Binder							Group 2 Binder				
		PG 64-22	PG 64-22	PG 70-22	PG 70-10	PG 76-16	PG 76-16	PG 70-16	PG 64H-22	PG 64V-22	PG 76-22 TR	PG 70H-16	PG 70V-16
		Y1	Z1	Z2	X1	Y4	Z4	Y3	X3	X4	X5	Y5	Y6
22	Original	1.00	1.00	-	-	-	1.00	1.00	1.00	1.00	1.00	1.00	1.00
	RTFO	2.14	2.64	-	-	-	-	-	2.04	2.07	-	-	-
	PAV	6.36	6.83	-	-	-	-	-	6.21	6.01	-	-	-
25	Original	1.00	1.00	1.00	-	-	1.00	1.00	1.00	1.00	1.00	1.00	1.00
	RTFO	2.25	2.77	2.30	-	-	-	-	2.04	2.03	-	-	-
	PAV	7.06	7.80	8.44	-	-	-	-	6.60	6.14	-	-	-
28	Original	1.00	1.00	1.00	-	-	1.00	1.00	1.00	1.00	1.00	1.00	1.00
	RTFO	2.32	2.90	2.37	-	-	-	1.82	2.07	2.02	1.66	1.95	1.92
	PAV	7.81	8.72	9.63	-	-	-	8.48	6.94	6.28	5.74	9.51	10.82
31	Original	-	-	1.00	1.00	1.00	1.00	1.00	1.00	1.00	1.00	1.00	1.00
	RTFO	-	-	2.46	2.24	1.82	2.26	1.88	-	-	1.65	1.94	1.91
	PAV	-	-	10.91	8.30	5.76	8.00	9.64	-	-	6.08	10.45	11.50
34	Original	-	-	-	1.00	1.00	1.00	1.00	1.00	1.00	1.00	1.00	1.00
	RTFO	-	-	-	2.31	1.89	2.33	2.16	-	-	1.62	1.92	1.88
	PAV	-	-	-	9.32	6.61	9.00	10.79	-	-	6.25	11.15	11.90
37	Original	-	-	-	-	1.00	1.00	1.00	1.00	1.00	1.00	1.00	1.00
	RTFO	-	-	-	-	1.95	2.41	-	-	-	-	-	-
	PAV	-	-	-	-	7.51	10.07	-	-	-	-	-	-
58	Original	1.00	1.00	-	-	1.00	1.00	1.00	1.00	1.00	1.00	1.00	1.00
	RTFO	2.76	3.10	-	-	-	-	-	1.86	1.87	-	-	-
	PAV	-	-	-	-	-	-	-	-	-	-	-	-
64	Original	1.00	1.00	1.00	1.00	1.00	1.00	1.00	1.00	1.00	1.00	1.00	1.00
	RTFO	2.64	2.99	3.12	2.15	2.18	3.11	2.33	1.87	1.85	1.28	1.85	1.63
	PAV	10.13	12.08	-	-	-	-	-	5.00	4.82	-	-	-
70	Original	1.00	1.00	1.00	1.00	1.00	1.00	1.00	1.00	1.00	1.00	1.00	1.00
	RTFO	2.50	2.78	3.09	2.06	2.20	3.07	2.36	1.88	1.81	1.43	1.83	1.61
	PAV	-	-	25.77	10.75	-	-	21.43	-	-	-	10.65	6.31
76	Original	-	-	1.00	1.00	1.00	1.00	1.00	1.00	1.00	1.00	1.00	1.00
	RTFO	-	-	3.01	1.96	2.16	3.11	2.37	-	-	1.33	1.83	1.58
	PAV	-	-	-	-	15.83	21.87	-	-	-	3.56	-	-
82	Original	-	-	-	-	1.00	1.00	1.00	1.00	1.00	1.00	1.00	1.00
	RTFO	-	-	-	-	2.10	3.04	-	-	-	1.22	-	-
	PAV	-	-	-	-	-	-	-	-	-	-	-	-

Figure 5-1 and Figure 5-2 show that the *AR* varies with temperature and in general the *AR* at intermediate temperatures are lower than the aging ratios at high temperature. However, much more interesting observations can be made by comparing the *AR's* of binders of the same grade. The aging ratios of Group 1 and Group 2 binders at intermediate and high temperature are tabulated in Table 5-1. Comparisons can be made between binders Y1 and Z1 for PG 64-22; Z2 for PG 70-22, X1 for PG 70-10, and Y3 for PG 70-16; and Y4 and Z4 for PG 76-16. For PG 64-22, as seen in Table 5-1, binder Y1 has lower *AR* at all test temperatures. For PG 70-XX, binder X1 has lower *AR* at all test temperatures. Among the PG 76-16 binders, Y4 has lower aging ratios at both intermediate and high temperatures than that of Z4 binder. The main conclusion from the comparison of aging ratios of binders of the same grade is that the oxidative properties of the binders are source and formulation dependent. Similar PG grade does not necessarily equate to similar oxidative properties as was evidenced by the different *AR* values.

5.2.2 Aging Ratio for polymer-modified Asphalt (Group 2)

The secondary observation of performing the *AR*-based analysis was to evaluate the effect of polymer modification on asphalt binder oxidation. This evaluation was achieved by comparing binders Y1 and Z1, which are PG 64-22 unmodified binders, to X3 (PG 64H-22) and X4 (PG 64V-22) which are polymer modified binders. The data is presented in Table 5-1. At intermediate temperatures, even though the polymer modified binders have lower aging ratios, the ratios are similar to the neat binders. At 25°C for PAV aged condition, the maximum difference in *AR* among the two sets of binders is between X4 and Z1, which was 1.66. At 64°C, there is a greater difference in *AR*'s between the same two

binders, 7.26, with the polymer modified binders showing lower aging ratios. The percentage difference between the *AR's* at the PAV aged condition is approximately 140%, which shows that the polymer modified have a clearly lower oxidation potential. One other comparison that was possible was between binder Y3 which is unmodified PG 70-16 binder and binders Y5 (PG 70H-16) and Y6 (PG 70V-16), which are polymer modified asphalts. Even in this case, the aging ratios of the unmodified and polymer modified binders are very similar at intermediate temperatures with the latter having a lower aging ratio. However, at higher temperatures, the polymer modified asphalts have a noticeably lower aging ratio than the neat binder (4.91 on average versus 11.1 at 64°C). The difference between the *AR's* at the PAV aged condition of Y3 and Y5 was 101% and Y3 and Y6 was 239%. The AR based analysis clearly shows that the polymer modified asphalts have a lower propensity to aging.

5.3 Extraction and Recovery for Short-Term Oven Aging (STOA)

The results so far confirm what is known from the literature, which is that binders oxidize differently. Therefore, one has to be careful what binder aging condition they choose for comparisons since different correlations may emerge. This section will establish the background and describe the experiment carried out to determine what binder aging condition most closely approximates the condition that exists in short term oven aging.

5.3.1 Short-Term Oven Aging (STOA)

For all asphalt mixtures, the standard laboratory procedure for short-term aging involves heating he loose mix in a forced draft oven for 4 h at a temperature of 135ºC. After the asphalt samples mixtures are aged, they are compacted and then tested for a number of

properties including modulus, damage, and rutting propensity. In this research, a number of mixtures were selected to perform extraction and recovery to check the aging level. Not all the mixtures that were subject to STOA were tested by the extraction and recovery processes. The processes for selecting these mixtures are presented in the next section by ranking the mixtures aging ratio at the same |*G**| original for each binder.

5.3.2 Mixture Selecting for Extraction and Recovery by RTFO Aging Ratio Ranking

The main purpose of doing the analysis herein is to choose binders at different aging ratios (high, medium, and low) to perform extraction and recovery processes and determine the aging level of STOA condition. To make a valid of different binder's aging ratios, the evaluated binders have to be at the same |*G**| original for each binder. After the aging ratio was estimated at different values of intermediate and high temperatures as presented in Table 5-1, the asphalt binders were classified into high, average, and the low aging ratio at the same |*G**| of original binder. Four values of |*G**| original were selected as shown in Figure 5-3. These values were selected to fit between the measured |*G**| values at intermediate and high temperatures as presented in Table 5-1. For aging ratio at intermediate temperatures |*G**| values of 400 kPa, and 500 kPa were chosen for neat binder (un-aged). Also, |*G**| values of 1 kPa, and 2 kPa were selected for aging ratio at high temperatures. Then, the aging ratios were calculated at these |*G**| values by interpolating the data presented in Table 5-1. The RTFO aging ratios for all the study asphalts at four |*G**| values are sorted from low to high and presented in Table 5-2. The red color represented the polymer modified binder and the black is for non-modified asphalt binder.

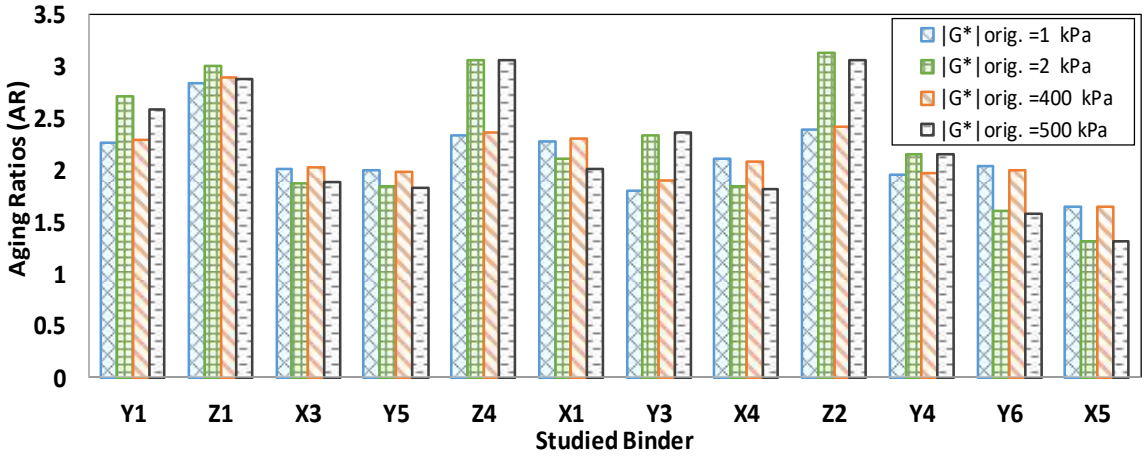

Figure 5-3 Aging Ratios of the Study Binders at |*G**| orig. 1, 2, 400, and 500 kPa

Table 5-2 . Ranking Aging Ratios of the Study Binders at |*G**| orig. 1, 2, 400, and 500 kPa

Rank	**|*G**|orig. =1 kPa**		**|*G**|orig. =2 kPa**		**|*G**|orig. =400 kPa**		**|*G**|orig. =500 kPa**	
	AR	**Binder**	**AR**	**Binder**	**AR**	**Binder**	**AR**	**Binder**
1	1.31	X5	1.31	X5	1.64	X5	1.65	X5
2	1.57	Y6	1.60	Y6	1.90	Y3	1.80	Y3
3	1.81	X4	1.84	X4	1.96	**Y4**	1.95	**Y4**
4	1.83	Y5	1.85	Y5	1.98	Y5	1.99	Y5
5	1.88	X3	1.87	X3	2.00	Y6	2.01	X3
6	2.02	X1	2.10	X1	2.02	X3	2.03	Y6
7	2.14	**Y4**	2.15	**Y4**	2.08	X4	2.11	X4
8	2.36	Y3	2.34	Y3	2.29	**Y1**	2.26	**Y1**
9	2.58	**Y1**	2.71	**Y1**	2.31	X1	2.28	X1
10	2.88	**Z1**	3.00	**Z1**	2.36	**Z4**	2.33	**Z4**
11	3.05	**Z4**	3.06	**Z4**	2.42	**Z2**	2.39	**Z2**
12	3.06	**Z2**	3.12	**Z2**	2.88	**Z1**	2.84	**Z1**

After the aging ratio was estimated at different values of intermediate and high temperatures, the asphalt binders were classified into high, average, and the low aging ratio at the same |*G**| of original binder. Table 5-3 presented the selected binder to perform short-term oven aging (STOA) simulation study. Five non-modified binders were selected; Y4 binder to represent low aging ratio, Y1 to designate average aging ratio, and Z1, Z4, and Z2

for high aging ratio. Three binders at high aging ratio were selected to perform extraction because they have different PG grading.

Table 5-3 Binder Selected to Perform Extraction for the Aging Study.

AR	Binder	PG Grade
Low	Y4	PG 76-16(Y)
Average	Y1	PG 64-22 (Y)
high	Z1	PG 64-22 (Z)
	Z4	PG 76-16(Z)
	Z2	PG 70-22(Z)

5.3.3 Extraction and Recovery Procedure of the Asphalt Binder

All selected mixtures were subjected to short-term aging by heating the loose mix in a forced draft oven for 4 h at a temperature of 135^{o}C. After the samples were compacted and tested for axial fatigue test, the asphalt was extracted and recovered. Before the extraction, the sample was placed in the oven at 110^{o}C for 50 minutes. Then, the oven temperature was reduced to 50^{o}C and the cores were broken down to remove any potential moisture (Figure 5-4-a). After 15 minutes, the asphalt mixture was split into the extraction sample size. After that, the sample was placed in the centrifuge bowl (Figure 5-4-b) to undergo extraction. The sample was extracted by following ASTM D2172-17- Method A *"Quantitative of Bitumen from Bituminous Paving Mixtures"* by using the centrifuge. Then, the sample was soaked in Trichloroethylene (TCE) solvent to take away the asphalt from the aggregates (Figure 5-4-c). The asphalt mixture was immersed in the TCE for 1 hour to allow time for the TCE to interact with the binder. After 5 minutes, the extraction started by running the centrifuge machine to collect all the solution of binder and TCE from the bowl. Figure 5-4-d shows the aggregates after removing the asphalt.

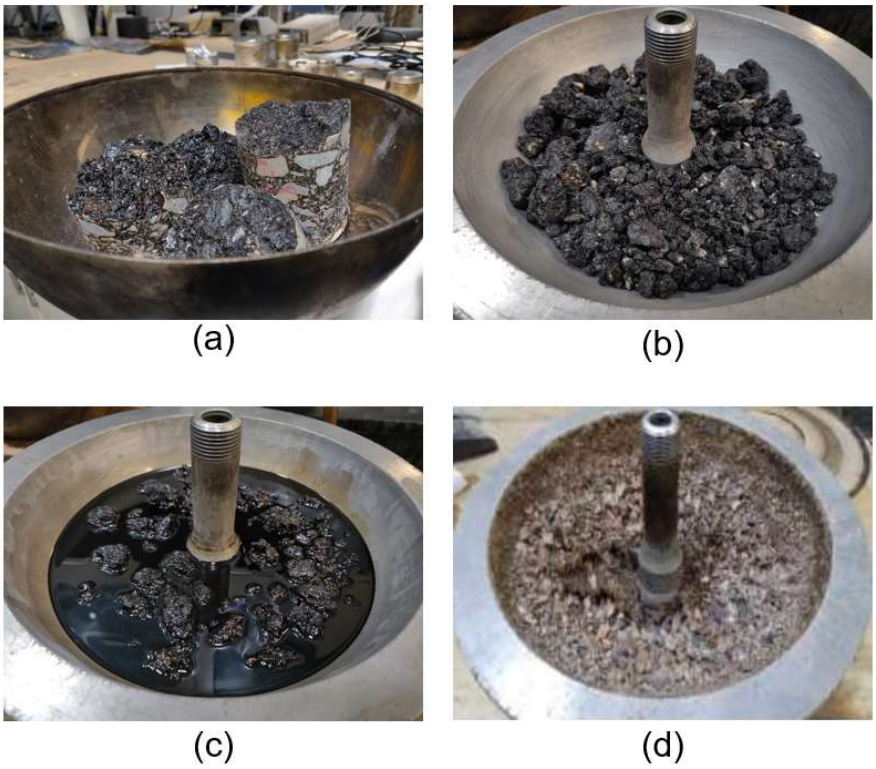

Figure 5-4 Asphalt Binder Extraction Process During: (a) Specimen Preparation; (b) Specimen Placement in the Bowl; (c) Adding TCE Solvent; and (d) After Extraction,

After 15 minutes, the recovery process was performed according to ASTM D5404-12 *"Standard Practice for Recovery of Asphalt from Solution Using the Rotary Evaporator"*. For this purpose, the RotoVap equipment (Figure 5-5-a) was used. In this method, the asphalt recovery procedures were performed for the extracted solution of TCE and asphalt by placing the sample in a bath at 90^{o}C. The solvent was distilled from the extractant by partially immersing the rotating distillation flask of the rotary evaporator in a heated oil bath while the solution was subjected to a partial vacuum and a flow of nitrogen gas to prevent binder oxidation. Figure 5-5-b shows the binder in the flask that is immersed in a hot oil bath during the recovery process. Then, the oil bath temperature was gradually increased

while decreasing the vacuum and the rotation of the flask until no drops of TCE were collected. After that, the recovered sample was removed from the flask and placed in the oven at 163ºC for 10 minutes. Finally, the recovered binder was removed from the oven and weighed. After 10 minutes, the recovered binder was poured in small tins. Before preforming any binder testing, the existence of any TCE or silica in the extracted binder was checked be by using the Attenuated Total Reflectance Fourier Transform Infrared Spectroscopy (ATR- FT-IR).

Figure 5-5 Binder Recovery: (a) RotoVap Setup; and (b) Binder Flask Immersed in the Hot Oil Bath

5.4 Effect of Oxidation by Fourier Transform Infrared Spectroscopy and Complex Shear Modulus

In the current study, the changes to the asphalt binders as a result of oxidation were also gauged based on the chemical formation of oxidation products assessed using the Attenuated Total Reflectance Fourier Transform Infrared Spectroscopy (ATR- FT-IR). The test measures the infrared spectrum of energy absorption of the aged and unaged binder at multiple wavelengths. The spectra resulting from the ATR-FT-IR method contains peaks at wavenumbers that correspond to different types of bonds within the asphalt cement. The

details regarding the test have been explained in detail in Appendix A. Figure 5-6 shows the FT-IR spectra for the study binder PG 64-22(Y).

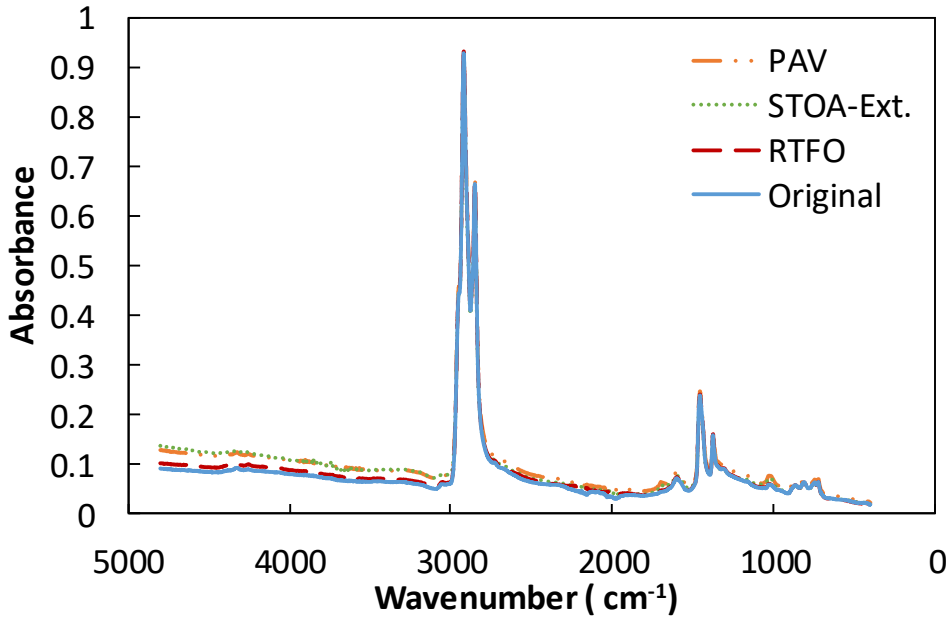

Figure 5-6. FT-IR Spectra for Original, RTFO, PAV, and STOA Aged Conditions for PG 64-22(Y).

Oxidation results in an increase in the number of double bonds between hydrocarbons and oxygen, which can be detected with the ATF-FT-IR test. The two specific functional groups examined in this study are the carbonyl and sulfoxide groups. Studies have linked the increase in absorbances at these groups to oxidation of asphalt. The metrics adopted are the area under the carbonyl and sulfoxide peaks (Jemison et al. 1992, Petersen and Glaser 2011), referred to as CA and CA+S respectively [112, 113]. The effect of oxidation quantified by examining the changes in these quantities with RTFO, PAV, and STOA aging. This can be seen in Figure 5-7 wherein the carbonyl and the sulfoxide regions for different aging levels of PG 64-22(Y) are shown.

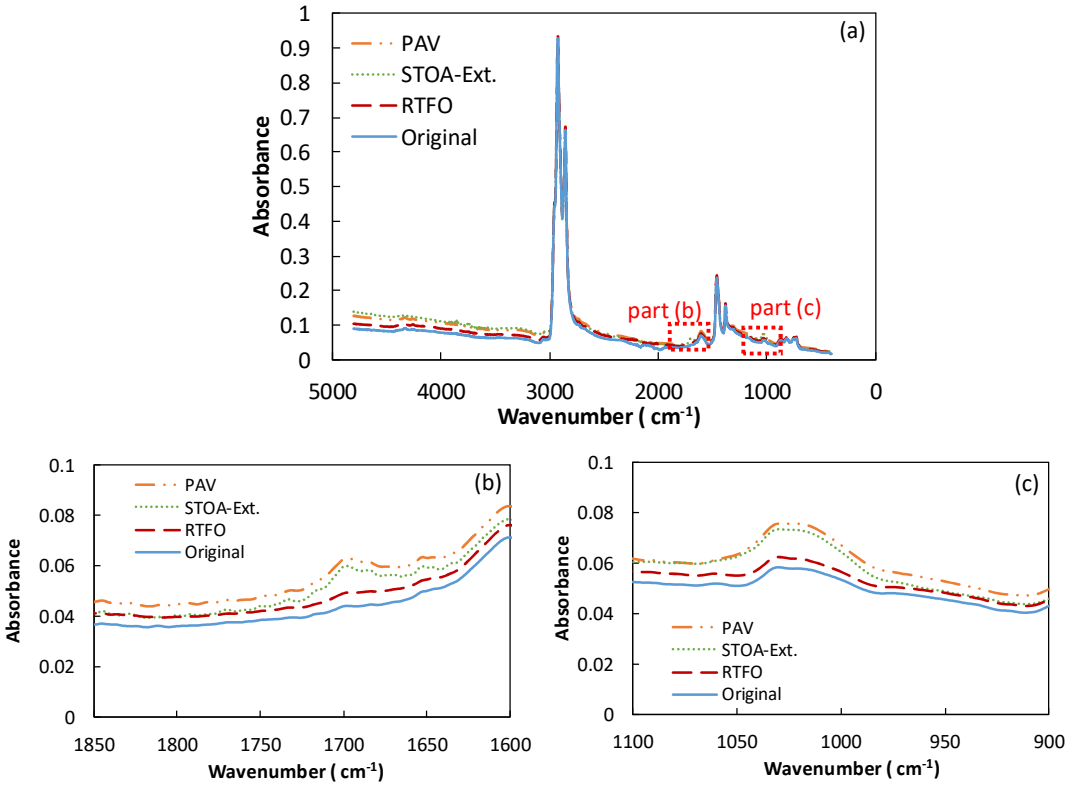

Figure 5-7. FT-IR Spectra for 64-22(Y) at Original, RTFO, PAV, and STOA Aging Conditions; (a) Overall Spectra, (b) Carbonyl Region and (c) Sulfoxide Region.

The main objective of the FT-IR testing was to obtain the chemical signature of the asphalts and to confirm the changes in $|G^*|$ because of oxidation. Also, the other goal was to check if there is any TCE (wavenumber ≅ 750 cm^{-1}) or silica (wavenumber ≅ 750-800 cm^{-1}) mixed with the binder for the extracted STOA binder. From the graph what was seen with respect to these two peaks, there is no evidence of TCE and there and silca. The carbonyl and the sulfoxide areas were calculated using the program as described in Appendix A. The sum of carbonyl and sulfoxide areas (CA+SA) for all the study asphalts are shown Figure 5-8. It can be seen from the figure that the CA+SA increases with an increase in aging level.

Thus, higher overall CA+SA. Although, CA+SA provides information regarding the chemical signatures of these asphalts.

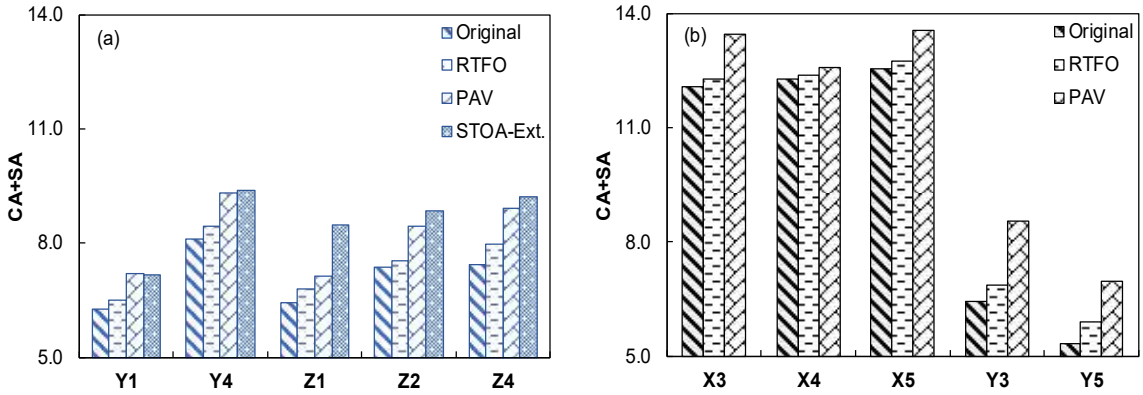

Figure 5-8. The Sum of Carbonyl and Sulfoxide Areas at; (a) Original, RTFO, PAV and Ext. STOA Aged Condition, (b) Original, RTFO, and PAV Aged Condition.

What is more important is the relative increase in CA+SA with aging. The ratio of CA+SA after aging to the original condition, as shown in Equation (5-2) was used as the parameter to calculate this increase.

$$AR_{FT-IR} = \frac{(Carbonyl\ Area + Sulfoxide\ Area)_{Aged}}{(Carbonyl\ Area + Sulfoxide\ Area)_{Original}} \quad (5\text{-}2)$$

This parameter was termed as $AR_{FT\text{-}IR}$. The values of $AR_{FT\text{-}IR}$ for all study asphalts are summarized in Figure 5-9. It can be seen from the Figure that the values of AR increase with aging level. This supports the observations from the rheological testing wherein polymer modified asphalts were seen to have a lower aging ratio. Figure 5-9-a showed the RTFO aging method to have less aging effect than short-term oven aging methods of all asphalt mixtures. Also, in the study, from the $AR_{FT\text{-}IR}$ presented in Figure 5-9-a, and Table 5-4,

showed PAV aging method to have similar aging effect with short-term oven aging method of asphalt mixtures.

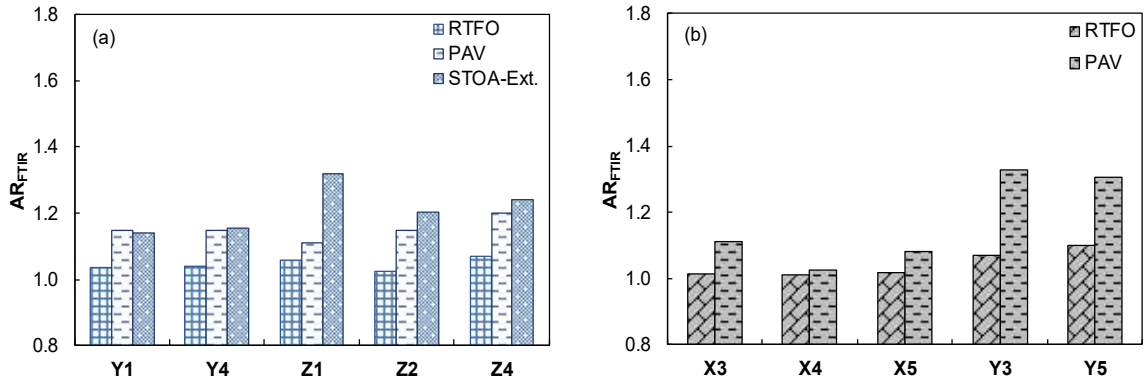

Figure 5-9. FT-IR based Aging Ratios for, (a) the Unmodified Asphalt Binders at RTFO, PAV and Ext. STOA Aged Condition, (b) RTFO, and PAV Aged Condition.

The effect of oxidation is quantified by estimating the dynamic shear modulus $|G^*|$ at the PG grading temperature and examining the changes area under the carbonyl and sulfoxide peaks in FT-IR spectrum with an original binder and RTFO, PAV and extracted STOA binder aging condition for all extracted binders. The values of sum of the area under CA and CA+S peaks *and* $AR_{FT\text{-}IR}$ are the extracted binders summarized in Table 5-4.

Table 5-4. The Sum of Carbonyl and Sulfoxide Areas at Original, RTFO, PAV, and STOA Aging Conditions and FT-IR based Aging Ratios for the Tested Asphalt Binder

Binder	Aging Condition	Sum of the area under CA and CA+S peaks				AR		
		Original	RTFO	PAV	STOA-Ext.	RTFO	PAV	STOA-Ext.
Y1	CA Area	4.53	4.74	5.11	4.99	1.04	1.13	1.10
	S Area	1.73	1.76	2.10	2.17	1.01	1.21	1.25
	C+ S Area	6.27	6.49	7.21	7.16	1.04	1.15	1.14
Z1	CA Area	4.81	4.97	4.98	6.06	1.03	1.04	1.26
	S Area	1.61	1.83	2.14	2.40	1.14	1.33	1.49
	C+ S Area	6.42	6.80	7.13	8.46	1.06	1.11	1.32
Z2	CA Area	5.21	5.32	5.93	6.39	1.02	1.14	1.23

Binder	Aging Condition	Sum of the area under CA and CA+S peaks				AR		
		Original	RTFO	PAV	STOA-Ext.	RTFO	PAV	STOA-Ext.
	S Area	2.14	2.21	2.53	2.45	1.03	1.18	1.14
	C+ S Area	7.36	7.53	8.46	8.84	1.02	1.15	1.20
Y4	CA Area	5.69	6.02	6.66	6.81	1.06	1.17	1.20
	S Area	2.41	2.41	2.64	2.56	1.00	1.10	1.06
	C+ S Area	8.10	8.43	9.31	9.37	1.04	1.15	1.16
Z4	CA Area	5.14	5.66	6.40	6.51	1.10	1.24	1.27
	S Area	2.28	2.29	2.50	2.71	1.00	1.10	1.19
	C+ S Area	7.43	7.96	8.90	9.22	1.07	1.20	1.24

In addition, the complex shear modulus and aging ratios of the extracted binders at original, RTFO, PAV, and STOA aging conditions are summarized in Figure 5-10, and Table 5-5.The preliminary study showed the RTFO aging method to have less aging effect than short-term oven aging methods of asphalt mixtures. Also, in the study, from the dynamic shear rheometer presented in Figure 5-10, and Table 5-5, showed PAV aging method to have higher aging effect with short-term oven aging methods of asphalt mixtures.

Table 5-5 Complex Shear Modulus and Aging Ratios of Tested Binder at Original, RTFO, PAV, and STOA Aging Conditions.

Binder	Temperature (°C)	Complex Shear Modulus $\|G^*\|$ (kPa)				Aging Ratios-AR		
		Orig.	RTFO	STOA-Ext.	PAV	RTFO	STOA-Ext.	PAV
Y1	64	1.15	3.03	10.94	11.62	2.6	9.5	10.1
Z1	64	1.35	4.03	5.57	16.28	3.0	4.1	12.1
Z2	70	1.03	3.17	11.19	26.48	3.1	10.9	25.8
Y4	76	1.13	2.44	8.03	17.87	2.2	7.1	15.8
Z4	76	1.13	3.51	10.24	24.67	3.1	9.1	21.9

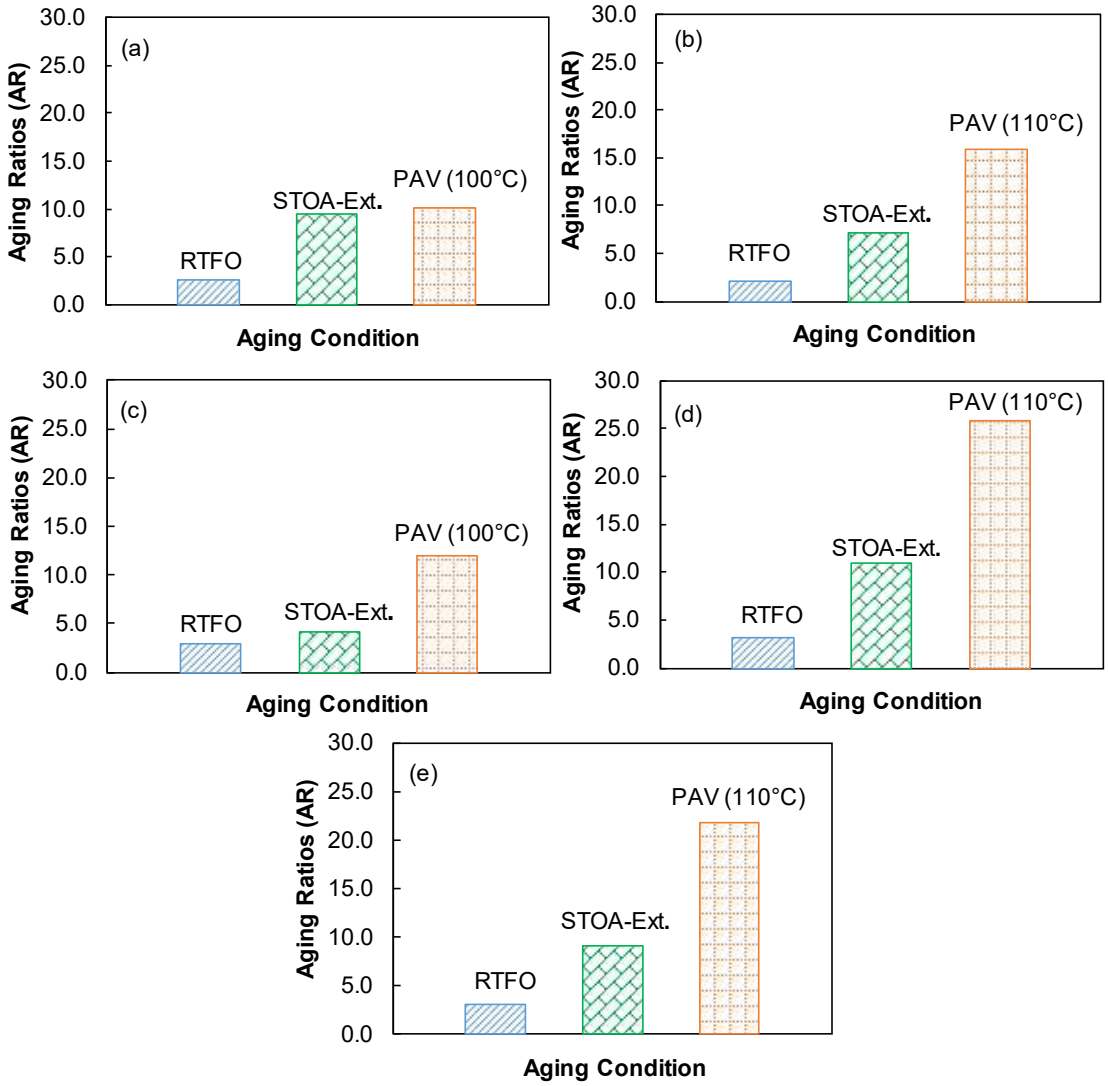

Figure 5-10 Rheological Testing based Aging Ratios at the PG Gradeing Temperature and RTFO, PAV, and STOA Aging Conditions for, (a) Y1 Binder, (b) Y4 Binder, (c) Z1 Binder, (d) Z2 Binder, and (e) Z4 Binder.

5.5 Complex Shear Modulus Back Calculation

The main purpose of this chapter is to ensure that the binder tests properties reflect the condition of the binder during the mixture test when evaluating binder-to-mixture properties. In the previous subsections, the RTFO and the PAV aging for asphalt binders were compared to and the STOA for asphalt mixtures for only five unmodified asphalt

mixtures. These five mixtures will used herein to calibrate the |*E**| predictive models that Chapter 4 analysis suggested to use (Hirsch Model and Simplified Global Model). In this task, the aging ratio of the rest of seven mixtures for STOA condition will be estimated by back calculating the complex shear modulus using the calibrated |*E**| predictive models. Finally, the capabilities of the calibrated |*E**| predictive models will be checked by using the five measured STOA-Ext asphalt mixtures data to make sure that both of the calibrated |*E**| predictive models are working well to estimate complex shear binder modulus for all binders.

5.5.1 Hirsch Model

One of the |*E**| predictive models that Chapter 4 analysis suggested to use is Hirsch Model. Hirsch Model explained in detail in Chapter 2. The simplest form of the model that incorporates the complex shear binder modulus, VMA, and VFA was used to calibrate the |*E**| predictive model for STOA Condition by using the five measured STOA-Ext asphalt mixtures data. The calibration factor (F_C) of the STOA condition new model assumed to be a common factor for all parts of Hirsh Model as shown in equation (6-2). For this purpose, researchers have found the "solver" function of Microsoft Excel quite convenient and accurate. To use the solver function, the observed values are first compared with the predicted values. For each set of data, the difference between the logarithmic predicted and logarithmic observed value gives the error amount for that data point. The sum of all error squares is first minimized by changing the value of the calibration factor (F_C) included in the model under consideration by the use of the built-in "solver" function of Microsoft Excel. This process gives the optimized model with minimal scatter. The calibrated suggested model for the |*E**| estimation is as follows:

$$\left|E^*\right|_m = F_c * \left(p_c \left[4,200,000\left(1-\frac{VMA}{100}\right) + 3\left|G^*\right|_b \left(\frac{VFA*VMA}{10,000}\right)\right] + \frac{(1-p_c)}{\frac{\left(1-VMA/100\right)}{4,200,000} + \frac{VMA}{3\left|G^*\right|_b (VFA)}} \right) \quad (5\text{-}3)$$

$$p_c = \frac{\left(20+3\left|G^*\right|_b (VFA)/(VMA)\right)^{0.58}}{650+\left(3\left|G^*\right|_b (VFA)/(VMA)\right)^{0.58}} \quad (5\text{-}4)$$

where,

Fc = Calibration factor for STOA Condition = **0.780027**

$|E^*|_m$ = dynamic modulus of HMA in psi;

P_c = the aggregate contact volume;

VMA = percentage of voids in mineral aggregate in the compacted mixture;

VFA = percentage of voids filled with asphalt in the compacted mixture; and

φ = phase angle of HMA.

5.5.2 Simplified Global Model:

The other $|E^*|$ predictive models that Chapter 4 analysis suggested to use is Simplified Global Model. This model is explained in detail in Chapter 2. The same process that was used to calibrate Hirsch model are adopted herein to calibrate Simplified Global Model and estimate the calibration factor (F_C). This calibration factor for STOA condition new model assumed to be multiply by all simplified global model parameters as shown in equation (6-4). The called calibrated suggested simplified global model is expressed as follows:

$$\log\left|E^*\right| = \mathrm{F}_c * \left(\frac{6.39411 - 0.00015p_{34}^2 - 0.00546p_{38} - 0.1175p_{200} - 0.05544V_a - 0.15791V_{beff} + 0.00464V_{beff}^2}{+\frac{0.6014 + 0.0004p_{34} + 0.00696p_{38} + 0.16224p_{200} - 0.0053p_{200}^2 + 0.019V_a + 0.15541V_{beff} - 0.00568V_{beff}^2}{1+\mathrm{e}^{1.8645-0.95991\log\left|G^*\right|}}} \right) \quad (5\text{-}5)$$

where

F_c = Calibration factor for STOA Condition = **0.751397**

$|E^*|$ = the dynamic modulus (psi),

p_{34} = cumulative percentage retained on the 3/4" sieve (19 mm),

p_{38} = cumulative percentage retained on the 3/8" sieve (9.5 mm),

p_{200} = percentage passing the #200 sieve (0.075 mm),

V_a = air void content (%),

V_{beff} = effective bitumen content (% by volume),

$|G^*|$ = dynamic shear modulus of binder (psi), and

5.5.3 Excellence of Calibrated Hirsch and Calibrated Simplified Global Models:

In this section, the quality for the calibrated $|E^*|$ predictive models were checked by using the five measured STOA-Ext asphalt mixtures data to make sure that both of the calibrated $|E^*|$ predictive models are working well to estimate complex shear binder modulus for all the other seven binders. The two selected models are evaluated along with measured $|G^*|$ using the extracted $|G^*|$ asphalt binder at two temperatures (21.1, and 54.4°C) shown in Figure 5-11. The first observation from this analysis as shown in Figure 5-11 for Hirsch model. As the data demonstrates, a significant bias (i.e., a power trend between the predicted $|G^*|$ and the measured $|G^*|$ values) is observed for both temperatures. Due to the great bias relative to the other model, it was decided that this model would be dropped from consideration in any future rutting and fatigue analysis.

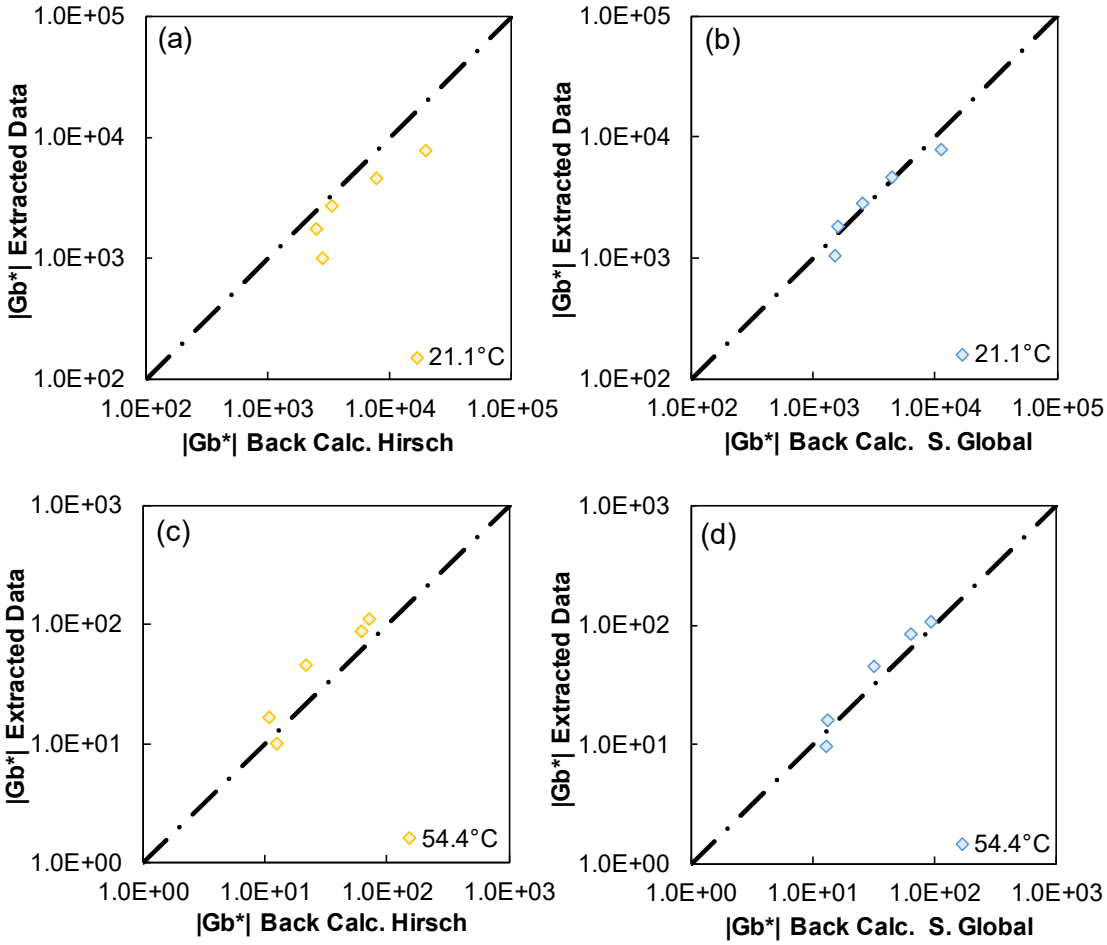

Figure 5-11 Back Calculated Predicted Binder Shear Modulus Values Using Calibrated Hirsch Model; (a) at 21.1°C and (c) at 54.4°C; and Using Calibrated Simplified Global Model; (b) at 21.1°C and (d) at 54.4°C.

5.5.4 Prediction of |G| Values by Using Calibrated Simplified Global Model:*

The calibrated simplified global model is used in the section to back calculate the |*G**| values of STOA condition for Group 1 and Group 2 binders. The aging ratio of STOA condition was estimated by dividing the |*G**| values of STOA condition by the |*G**| values of original condition for all Group 1 and Group 2 binders. A frequency of 10 Hz was used for the calculation of STOA aging ratio at three different temperatures (21.1°C, 37.8°C, and

54.4°C). The ratio between back calculated STOA aging ratio and RTFO aging ratio (AR_{STOA}/AR_{RTFO}) at the same frequency and temperature was calculated for Group 1 and Group 2 binders as shown in Figure 5-12. This ratio it has to be equal to one if both aging condition are equivalent.

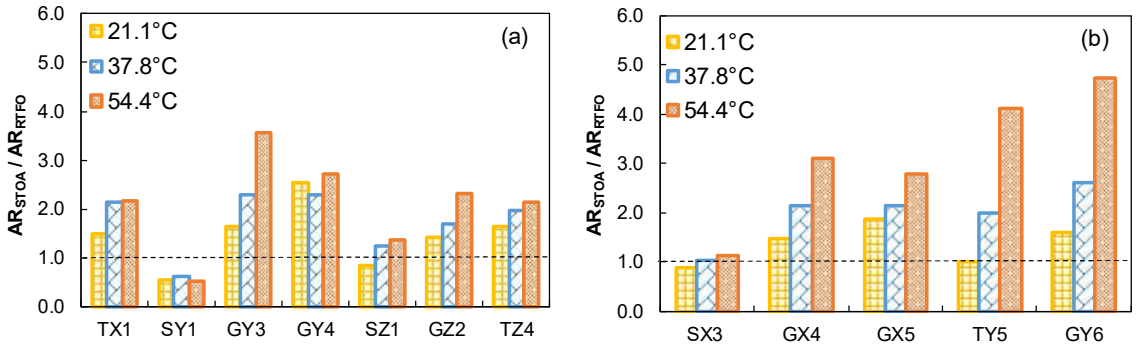

Figure 5-12 The Ratio between Back Calculated STOA Aging Ratio of Mixture and RTFO Aging Ratio of Binder; (a) Group 1 Binders , and (b) Group 2 Binders.

From Figure 5-12 the AR_{STOA}/ AR_{RTFO} ratio values are found to vary by temperature and PG grade of the binder. In general, this ratio is increasing by the increase of temperature. The AR_{STOA}/ AR_{RTFO} ratio is found to be around one for the lower high temperature PG grade binders (X3, Y1, and Z1). This ratio is higher than one (2 to 4) for higher high temperature PG grade binders. RTFO aging condition by using AASHTO R 30 procedure was found to be unstable with the short-term oven aging condition and does not really simulate what happens in the mixture. In addition, the short-term oven aging method of asphalt mixtures was found to have more aging effect than RTFO aging method for higher high temperature PG grade binders. This difference was higher at high temperatures. Therefore, the analysis concluded that the binder aging that occurs when a mixture is short-term conditioned in a forced draft oven for 4 hours at 135°C per AASHTO R 30 generally

exceeds the aging that occurs in the short-term binder aging procedures. This finding is very important for this study, as it should be considered when evaluating the impact of any rutting correlation that will be created between binder and asphalt mixture, which will be established in the next chapter.

On the other hand, one of the tasks in this study is to correlate binder and mixture fatigue parameters. Since the binder fatigue was measuring at PAV aging condition and mixture fatigue at STOA condition, it is very important to see how the PAV aging condition will correlate with the STOA condition at mid temperature. Therefore, similar comparison as shown in Figure 5-12 will be establish herein between PAV aging condition with STOA condition (AR_{PAV}/ AR_{STOA}). A frequency of 10 Hz also was used for STOA aging ratio calculation at three different temperatures (21.1°C, 37.8°C, and 54.4°C). The AR_{PAV}/ AR_{STOA} ratio at the same frequency and temperature was calculated for Group 1 and Group 2 binders as shown in Figure 5-13. This ratio needs to be consistence to have a minimum effect on any correlation between binder and mixture fatigue that will be studied latter.

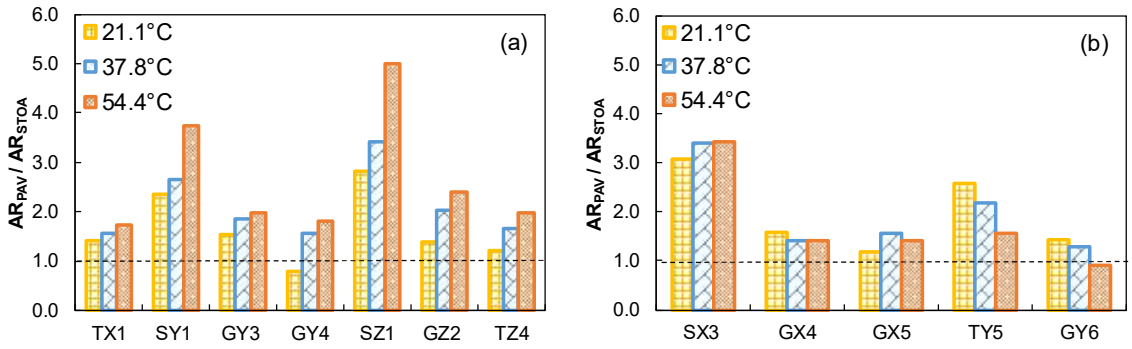

Figure 5-13 The Ratio between PAV Aging Ratio of Binder and Back Calculated STOA Aging Ratio of Mixture; (a) Group 1 Binders , and (b) Group 2 Binders.

From Figure 5-13 the AR_{PAV}/ AR_{STOA} ratio values are vary by different temperature and different PG grading. This ratio is increasing by increasing the temperature for most of the binders. The AR_{PAV}/ AR_{STOA} ratio found to be stable for the higher high temperature PG grade binders between 1.0 to 1.5 times for (X1, Y3, Z2, Z4, X4, X5, and Y6). This ratio noted to be higher and inconsistence for lower high temperature PG grade binders (X3, Y1, and Z1). This difference (for the lower high temperature PG grade binders) is important especially at mid temperatures. This finding is possibly will have an impact at any fatigue correlation that will be formed between binder and asphalt mixture especially for lower high temperature PG grade binders, which will be established in latter.

5.6 Conclusions from Aging Study

In this Study, the propensity to oxidize measured by calculating the aging ratio of RTFO, PAV, and STOA aged conditions is gathered for analysis. The focus of the analysis is to ensure that the binder tests properties reflect the condition of the binder during the mixture test when evaluating binder-to-mixture properties. Based on the binder and mixture datasets analyzed and presented in this chapter, following conclusions can be made:

1. The main conclusion from the comparison of aging ratios of binders of the same grade is that the oxidative properties of the binders are source and formulation dependent. Similar PG grade does not necessarily equate to similar oxidative properties as was evidenced by the different *AR* values.
2. The *AR* based analysis clearly shows that the polymer modified asphalts have a lower propensity to aging. However, at intermediate temperatures the aging ratios of the unmodified and polymer modified binders are very similar with the latter

having a lower aging ratio. Furthermore, at higher temperatures, the polymer modified asphalts have a noticeably lower aging ratio than the neat binder.

3. The binder aging that occurs when a mixture is short-term conditioned in a forced draft oven for 4 hours at 135°C per AASHTO R30 generally exceeds the aging that occurs in the short-term binder aging procedures. The difference is noted to be higher at high temperatures and lower high temperature PG grade binders. This finding is very important for this study, because it may possibly have negative impacts on any rutting correlation that will be created between binder and asphalt mixture.
4. The AR_{PAV}/ AR_{STOA} ratio values vary by temperature and PG grade. This ratio is increasing with increases in the temperature for most of the binders. The AR_{PAV}/ AR_{STOA} ratio found to be stable for the higher high temperature PG grade binders between 1.0 to 1.5 times and inconsistence for lower high temperature PG grade binders. This difference is important especially at mid temperatures when fatigue correlation will be formulated between binder and asphalt mixture.

Chapter 6. RELATIONSHIP BETWEEN ASPHALT BINDER PARAMETERS AND ASPHALT MIXTURE RUTTING

6.1 Abstract

The selection and specification of asphalt binder is one of the factors that ultimately affect the long-term performance of asphalt pavements. Many agencies currently follow AASHTO M320 for their binder specifications, where the ratio of dynamic modulus to the sine of the phase angle, $|G^*|/\sin\delta$, is the binder rutting parameter. However, an alternative now exists, AASHTO M332, which uses the non-recovered creep compliance, J_{nr} for this purpose. In this paper, the relative merits of these two parameters are compared using experimental results from 21 different asphalt mixtures from Arizona. The rutting parameters according to AASHTO M332 and M320 were determined for each of the binders in these mixtures. Also, for each mixture two rutting performance tests: Hamburg wheel test and flow number test were performed. The two binder rutting parameters demonstrated very high correlation to one another for non-polymer modified asphalts, but inconsistent correlation for polymer modified asphalts. Both Hamburg wheel and flow number tests showed positive correlation to both $|G^*|/\sin\delta$ and J_{nr}. It was concluded that while both parameters showed good correlation that the J_{nr} of the binder relates better to mixture rutting than $|G^*|/\sin\delta$. Considering the results in this study, it is believed that J_{nr} is slightly better rutting parameter for the binder specifications.

The parts of this chapter are accepted for publication as: Salim, R., Gundla, A., Zalghout A, Underwood, B.S., and K. E. Kaloush, (2019). Relationship between Asphalt Binder Parameters and Asphalt Mixture Rutting. *Transportation Research Record: Journal of the Transportation Research Board*, TRB, National Research Council. Washington, D.C.[*134*]

6.2 Introduction

Rutting is considered one of the main distresses in asphalt pavements. It is usually caused by shear deformation at high temperatures and high traffic loading [*114*]. In the company of different potential problems, rutting affects the serviceability of the road, and leads to safety issues such as hydroplaning. Hence, researchers have tried to characterize the rutting resistance of asphalt binders and mixtures in the laboratory and establish specifications related to how asphalt mixtures will perform in the field. The most common asphalt binder rutting specification is the ratio of dynamic shear modulus to the sine of the phase angle, $|G^*|/\sin\delta$, parameter in the Performance Grading (PG) standard. This parameter is measured using an oscillation test in the linear viscoelastic (LVE) range, but in pavements, the deformations that occur during rutting are substantially higher and involve non-linear viscoelastic (NLVE) behaviors. When the LVE and NLVE behaviors are closely correlated, specifications limited to the LVE behaviors can work quite well. However, over the years, experience has shown, that the LVE parameter has poor correlation to asphalt mixture rutting as reported by other researchers [*115-119*]. The Multiple Stress Creep and Recovery test (MSCR, AASHTO T350) and its associated specification, AASHTO M332, has been proposed to characterize and grade asphalts based on their NLVE behaviors.

Quite a few researchers have attempted to compare the $|G^*|/\sin\delta$ parameter and MSCR test parameter, non-recoverable creep compliance (J_{nr}), to mixture rut depth. Generally, these studies find positive correlations between both parameters and mixture rutting (often assessed with laboratory tests like loaded wheel, repeated simple shear, and repeated axial loading), but the strength of the correlation varies considerably [*115-122*].

Studies that have compared both parameters to mixture rutting have typically found improved correlation to J_{nr} than $|G^*|/\sin\delta$ parameter. While these previous studies have correlated the two parameters to mixture rutting, most use only a limited number of mixes and binder, and typically have only one or two non-polymer modified asphalts. Hence, studying the correlation between the two rutting parameters with different types of binders, and identifying the correlation between those parameters and the rutting mixture still contains some knowledge gaps. This paper attempts to address these gaps by evaluating both $|G^*|/\sin\delta$ and J_{nr} and their correlation to both Hamburg Wheel Tracking Test (HWTT) and Repeated Load Permanent Deformation (RLPD) test results

6.3 Objective

The main objective of this paper is to determine if the MSCR test parameter is a better indicator of the rutting performance than the currently used M320 parameter by comparing the binder rutting parameters $|G^*|/\sin\delta$ and J_{nr} to mixture rutting.

6.4 Materials

6.4.1 Asphalt Binders

For this study, a total of 20 different asphalt binders (12 from binder suppliers and 8 from laboratory blends) and three different aggregate sources and gradations have been combined to create 21 different asphalt concrete mixtures. Of the supplier provided binders, seven are non-polymer modified (Group 1) and five are polymer modified (Group 2). Group 1 materials have been obtained to reflect the current usage in Arizona as well and to give as equal as possible representation from each of the individual suppliers in the state. With

respect to the Group 2 asphalts, the materials have been selected based on those that could likely be supplied under a future AASHTO M332-like specification. Asphalt binder grades used in the current study and their notations are listed in Table 6-1. For the supplier provided asphalts the letter designation conveys the supplier and the number has no significance to the current study.

Table 6-1 Asphalt Binder Grades Used in the Current Study and their Notations

Group 1		Group 2		Group 3					
Name	Grade	Name	Grade	Name	Grade	Asphalt*	SBS*	Sulfur*	PPA*
X1	PG 70-10	X3	PG 64H-22	A3	PG 64H-22	97.000	3.0	0.000	0.0
Y1	PG 64-22	X4	PG 64V-22	A2-B	PG 64H-22	97.933	2.0	0.067	0.0
Y3	PG 70-16	X5	PG 76H-22	A4	PG 70S-28	96.000	4.0	0.000	0.0
Y4	PG 76-16	Y5	PG 70H-16	A3-B	PG 70S-28	95.925	3.0	0.075	1.0
Z1	PG 64-22	Y6	PG 70V-16	B2	PG 70H-28	97.433	2.0	0.067	0.5
Z2	PG 70-22			D0.5	PG 70H-28	97.983	0.5	0.017	1.5
Z4	PG 76-16			B5	PG 76V-28	94.417	5.0	0.083	0.5
				C3	PG 76V-28	96.925	3.0	0.075	0.0

* Percent by weight

The eight remaining Group 3 asphalts have been prepared in the Arizona State University laboratory using a high shear mixer. The lab blended asphalts were prepared by blending a base asphalt binder, PG 58-28, with various dosages of linear SBS polymer, sulfur, and polyphosphoric acid (PPA). The SBS was blended with the base binder at a temperature range of 195-200°C for 1.5 hours using a high shear mixer at 6000 rpm. After 1.5 hours, the temperature was lowered to 178°C and the mixing speed reduced to 3300 rpm. At this point sulfur was added and the blending was continued for 1.0 hour. Next, PPA was added, and the blending was continued for yet another 30 minutes. If PPA or sulfur were not blended, then the process stopped after the 1.5 hour blending at 6200 rpm. At the

end of the blending, the samples were poured into smaller tins for storage to be used for asphalt mixture preparation. The speed for the mixing process, was chosen such that no vortex formed while shearing, as this occurrence could result in oxidation of the asphalt. To confirm that the mixing process itself did not introduce any aging effects, the entire process was used with just PG 58-28 binder (e.g., without adding SBS, sulfur or PPA). Samples were taken at various time intervals throughout the mixing process, and in each case no increase in stiffness was observed. The naming convention adopted for the lab blended asphalts conveys the SBS dosage rate (the number), whether PPA was included (A = 0%, B = 0.5%, C= 1%, and D = 1.5%). The dosages of SBS, sulfur, and PPA for the eight asphalts are provided in Table 6-1. Also, there exist two binders which have a suffix "B" attached to their binder designation. These binders were sampled after adding Sulfur and shearing for 0.5 hr. There is no PPA in these binders.

6.4.2 Aggregates

The aggregates used in this study have been sourced from three suppliers in Arizona and differ in origin and composition. A brief description of the aggregates and their corresponding characteristics are provided Table 6-2 and the aggregate gradation used to prepare asphalt concrete samples in shown in Figure 6-1. In addition, Arizona Department of Transportation (ADOT) standard practice permits the use of portland cement as an anti-stripping admixture and this was duly added to aggregate before preparation of the mixtures.

Table 6-2 Characteristics of Aggregates Sourced from the Three Suppliers

Aggregate Properties	Globe		Snowflake		Tucson		Spec. Limits
	Coarse Agg.	Fine Agg.	Coarse Agg.	Fine Agg.	Coarse Agg.	Fine Agg.	
Bulk Specific Gravity	2.570	2.556	2.562	2.589	2.587	2.581	2.350-2.850
SSD Specific Gravity	2.605	2.592	2.59	2.619	2.614	2.61	
Apparent Specific Gravity	2.664	2.651	2.635	2.67	2.657	2.657	
Water Absorption (%)	1.37	1.399	1.08	1.17	1.02	1.11	0-2.5%
Sand Equivalent	85		79		84		Min. 55
1 Fracture Face (%)	94%		95%		99%		Min. 92%
2 Fracture Face (%)	90%		92%		92%		Min. 85%
Uncompacted Voids	46.50%		46.20%		47.90%		Min 45%
Flat and Elongated Agg.	1%		0%		-		Max. 10%
Carbonates	-		2		0.20%		Max. 20%
L.A. Abrasion, 100 rev., % loss	6		5		3		Max. 9
L.A. Abrasion, 500 rev., % loss	24		24		18		Max. 40

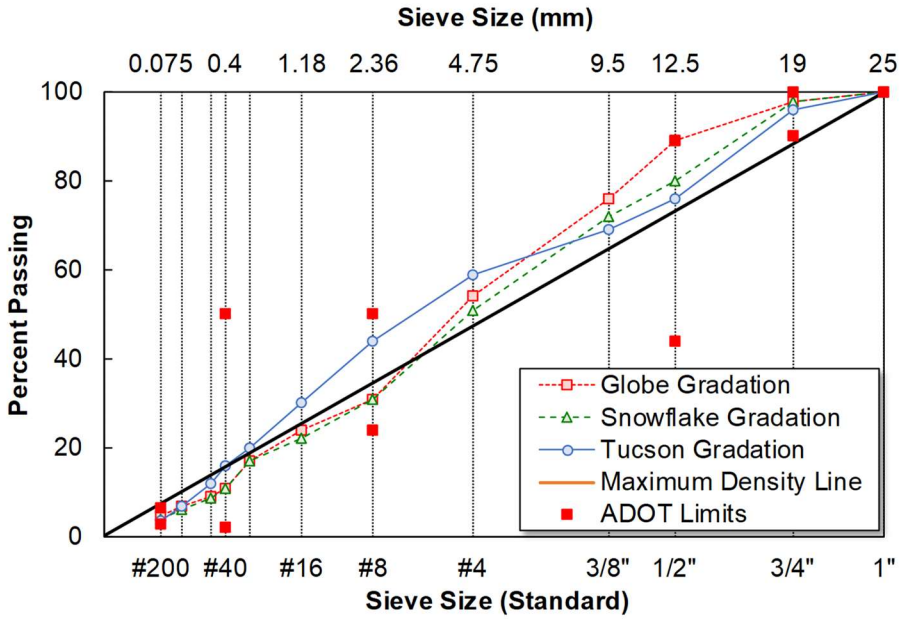

Figure 6-1 Gradations of Study Mixtures.

6.5 Methodology

The experimental program for the current study is summarized in Figure 6-2 and consists of tests on asphalt binders as well as asphalt mixtures. The asphalt binder tests are used to measure the properties of the asphalts in both the AASHTO M320 and AASHTO M332 specification systems. Asphalt mixture tests are conducted to establish how changes in asphalt binder properties will affect the rutting in asphalt mixture. Summaries of the most relevant aspects of the test methods as they apply to this study are given below in Figure 6-2.

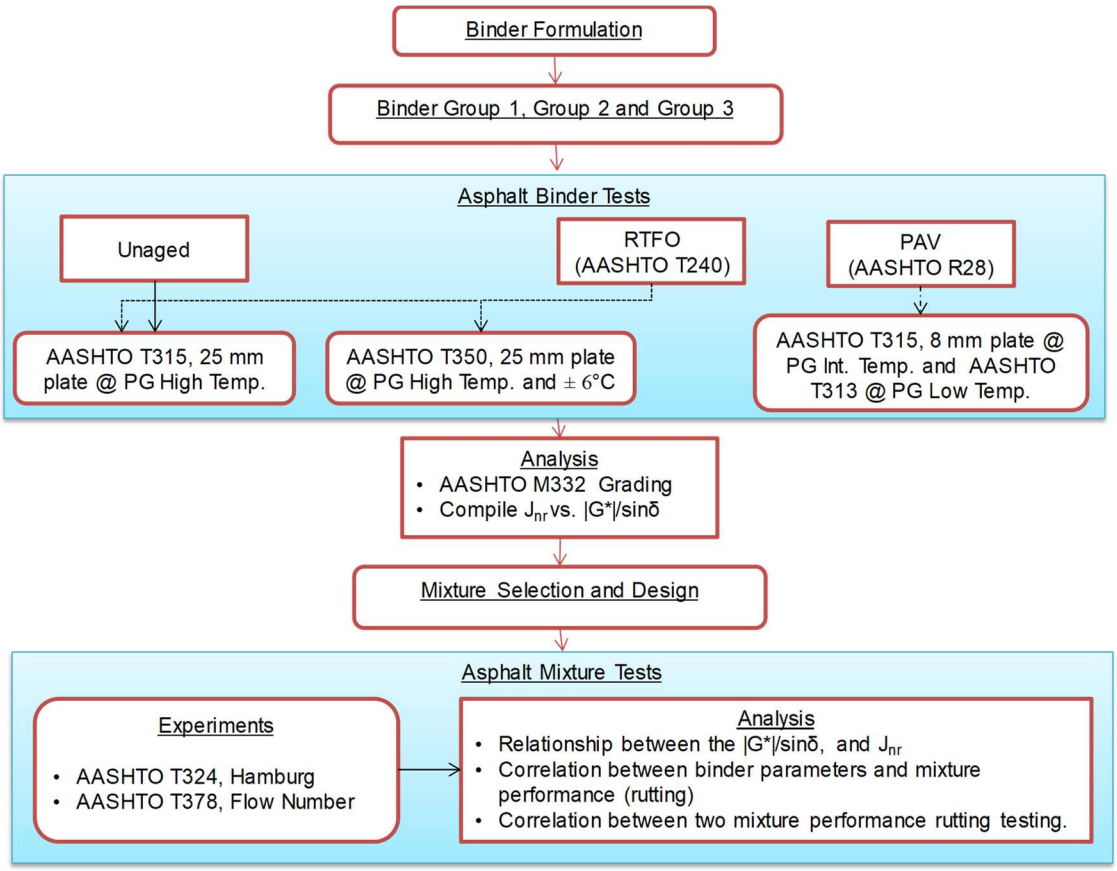

Figure 6-2 Flowchart of the Experimental Program for the Study.

6.6 Asphalt Binder Testing

As Figure 6-2 demonstrates, the asphalt binder experiments conducted in this study utilize the dynamic shear rheometer (DSR) for determining the intermediate and high temperature linear and non-linear viscoelastic properties of the asphalts and the bending beam rheometer (BBR) for determining the low temperature properties. Figure 6-2 also shows that testing has been conducted on asphalt binder after different age conditioning.

6.6.1 Shear Modulus and Phase Angle

The AASHTO T315 protocol for oscillatory, parallel plate testing has been conducted to determine $|G^*|$ and δ of the asphalt binders. Tests are performed using either a 25-mm parallel plate geometry (for temperatures greater than 58°C) or an 8-mm parallel plate geometry (for temperatures between 22°C and 37°C). As described in the protocol, all tests are carried out at a 10 radians/s frequency. The strain levels and test temperatures used in the experiments are as described in the protocol [123] and two samples were tested for each test condition.

6.6.2 Percent Recovery and Non-Recoverable Creep Compliance

The multiple stress creep recovery (MSCR) test has been conducted according to AASHTO T350 [124]. A sample of asphalt 25 mm in diameter and 1 mm thick is situated between two parallel plates mounted to a DSR; the sample is conditioned to a fixed and specified temperature; the sample is loaded repeatedly with a series of square shaped stress-rest pulses (1 second loading and 9 seconds rest) at 0.1 kPa and 3.2 kPa; and quantities relating the stress input to the strain response are calculated. For each loading cycle the initial strain (ε_0), maximum strain at the end of the loading (ε_c), and strain at the end of the recovery portion (ε_r) are recorded. These values are used to calculate four parameters, the non-recoverable creep compliance at 0.1 kPa and 3.2 kPa ($J_{nr0.1}$ and $J_{nr3.2}$), the percentage of difference between these two quantities (J_{nrdiff}), and the percent of strain recovery during the 3.2 kPa loading, $R_{3.2}$. The equations used to calculate these parameters and the averaging process are detailed in the standard. The tests are conducted at the AASHTO M320 high

temperature grade of the asphalt and at ±6°C, except for the asphalts with high temperature grades of 76, which are tested at 76, 70, and 64°C.

6.7 Asphalt Mixture Experiments

6.7.1 Specimen Fabrication

All test specimens are first short-term aged by heating the loose mix in a forced draft oven for 4 h at a temperature of 135ºC and then compacted using a Servopac Superpave Gyratory compactor to a diameter of 150 mm. The ram pressure, gyration angle, and gyration speed are 600 kPa, 1.16°, and 30 gyrations per minute respectively. Hamburg tests are conducted on the as compacted samples (60 mm tall) while RLPD tests are cut and cored from 180 mm tall samples to a testing geometry of 100 mm diameter x 150 mm tall After obtaining specimens of the appropriate dimensions, air void measurements are taken via the AASHTO T166 method, and specimens are stored until testing [*125*]. The air voids for Hamburg tests are between 6 and 8 percent following ADOT guidelines while the RLPD test specimen air voids are between 6.0 and 7.0 percent. During storage, specimens are sealed in bags and placed in an unlit cabinet to reduce aging effects. It is to be noted that for the HWTT, two specimens were fabricated and tested. For the dynamic modulus, and flow number test three specimens were tested and for the axial fatigue test, four specimens were tested.

6.7.2 Hamburg Wheel Tracker

The HWTT uses equipment that consists of a reciprocating wheel to apply loads to the test specimens Following ADOT and AASHTO protocols all tests are performed at a loading frequency of 52 ± 2 passes per minute and for a maximum of 20,000 passes. In this study

the reported rut depth from the HWTT is based on the maximum sensor reading from the testing device. This method follows current ADOT practice and one methodology proposed in AASHTO T324. Each asphalt mixture is tested at a minimum of two temperatures based on its PG "S" grade. These temperatures are related to the effective temperature, T_{eff}, as defined by the NCHRP 9-22 study [*126*]. The effective temperatures for various cities in Arizona were calculated using Equation (7-1) [*126*].

$$T_{eff} = 14.62 - 3.361\ln(\text{freq}) - 10.94(z) + 1.121(\text{MAAT}) + 1.718(\sigma_{MAAT}) - 0.431(\text{wind}) + 0.333(\text{sunshine}) + 0.08(\text{rain}) \quad (6\text{-}1)$$

The inputs for MAAT (Mean Annual Air Temperature), standard deviation of MAAT (σ_{MAAT}), wind, sunshine, and rain were obtained from the AASHTOWare climatic database. Z value was used to estimate T_{eff} is 20 mm (0.787 in). A frequency of 10 Hz was used for the calculation of T_{eff}, which reportedly corresponds to a vehicle traveling at a speed of 50 mph (80 km/hr) and having a 14-inch (35.6 cm) tire radius [*127*].

The T_{eff} values calculated for 14 cities in Arizona are shown in Table 6-3 and a strong relationship between the required asphalt binder grade and T_{eff} is observed. Four HWTT temperatures were selected for testing based on these results (44, 50, 56, and 62°C). The analysis shows that T_{eff} for binders with PG high temperatures of 58, 64, 70, and 76°C correspond most closely to HWTT temperatures of 44, 50, 56, and 62°C respectively. HWTT testing was also conducted at the next greatest or next lowest temperature increment except for the binders with a PG high temperature of 76C. In this case testing was performed at 50, 56, and 62°C because ADOT conducts its HWTT tests at 50°C, irrespective of the

binder grade. When correlating the two rutting parameters with HWTT results, just the HWTT results at 50°C were related to both $|G^*|/\sin\delta$ and $J_{nr3.2}$ at 64°C.

Table 6-3 HWTT Temperatures by Asphalt Binder Grade and Effective Temperature.

Location	PG Grade	T_{eff} (°C)	HWTT Temperature (°C)
Flagstaff	PG 58/64	41.4	44
Grand Canyon	PG 58	43.0	44
Window Rock	PG 58	44.7	50
Prescott	PG 64/70	47.5	50
St. Johns	PG 64	48.3	50
Winslow	PG 70	49.5	50
Page	PG 64	51.8	56
Nogales	PG 70	52.5	56
Bisbee	PG 70	52.9	56
Kingman	PG 70	53.3	56
Tucson	PG 70/76	55.8	56
Safford	PG 70	56.7	62
Phoenix	PG 76	59.3	62
Scottsdale	PG 76	60.0	62

6.7.3 Repeated Load Permanent Deformation Test

The RLPD or flow number test applies repeated load pulses for several thousand cycles and records the cumulative permanent deformation as a function of the applied cycles. A haversine pulse load of 0.1 second duration and 0.9 seconds of rest time is applied [*126*]. The deformations are measured using LVDTs mounted to the surface of the sample. The test is performed under atmospheric conditions, and prior to testing a thin and lubricated membrane is placed between the sample ends and the loading platens to create frictionless surface conditions. This test is performed using an IPC UTM-25 general purpose servohydraulic machine. For this study, the RLPD test is performed at only 50°C and always at a stress level of 400 kPa.

6.8 Results, Discussion and Analysis

6.8.1 Binder

AASHTO T315, T313, and T350 were performed on all asphalts in the study and used to first determine the PG grade for each asphalt (see Table 6-1). The $J_{nr3.2}$ and $|G^*|/\sin\delta$ at four different temperature values for the binders are shown in Table 6-4. Note that the binder test temperatures and mixture test temperatures were different but coordinated. Asphalt mixture and asphalt binder researchers establish test temperatures in different ways. For binder, the pavement temperature that is the basis for the testing conditions is based on regressive equations based on pavement temperatures and/or effective damage growth [*128,129*]. Mixture test temperatures are determined based on effective rutting temperatures as determined by performance models. Mixture test temperatures are also established based on the test ability of asphalt concrete specimens (asphalt concrete mixtures may experience damage under their own weight at extremely high temperatures). While the two temperatures differ, they are correlated as the effective temperature analysis shown above demonstrate. Considering this condition, this research matched binder tests at a given temperature to the approximate T_{eff} for that temperature. This meant that binder tests at 58, 64, 70, and 76°C were coordinated to rutting results at 44, 50, 56, and 62°C respectively.

Table 6-4 $J_{nr3.2}$ and $|G^*|/\sin\delta$ for Study Binders

Group	Notation	$J_{nr3.2}$ (kPa^{-1})				$\|G^*\|/\sin\delta$ (kPa)			
		58°C	64°C	70°C	76°C	58°C	64°C	70°C	76°C
Group 1	X1	—	1.59	4.03	8.60	—	5.68	2.48	1.15
	Y1	1.29	3.24	—	—	6.94	3.05	—	—
	Y3	—	1.36	3.53	7.97	—	5.61	2.74	—
	Y4	—	0.64	1.73	2.46	—	13.00	5.34	4.17
	Z1	0.90	2.40	—	—	9.33	4.06	—	—
	Z2	—	1.13	2.89	6.82	—	6.83	3.26	—
	Z4	—	0.38	1.03	2.54	—	18.60	7.33	3.61
Group 2	X3	0.47	1.02	—	—	6.38	3.61	—	—
	X4	0.40	0.98	2.31	—	—	3.71	—	—
	X5	—	0.11	0.28	1.10	—	7.62	4.02	2.49
	Y5	—	0.06	0.12	0.39	—	5.02	3.13	1.97
	Y6	—	0.02	0.04	0.07	—	6.56	4.36	2.96
Group 3	B5	—	0.08	—	0.66	—	18.11	10.71	6.33
	D0.5	—	0.41	1.26	—	—	9.39	5.06	2.74
	B2	—	0.48	1.49	—	—	6.93	3.75	2.03
	A3-B	0.30	0.88	2.51	—	—	5.50	2.93	1.59
	A4	—	0.95	2.29	—	—	7.07	3.57	1.84
	A2-B	0.60	1.87	—	—	7.42	3.69	1.88	—
	A3	—	1.83	—	—	—	4.55	2.22	1.12
	C3	—	0.08	—	0.88	—	14.41	8.63	5.10

6.8.2 Mixture

6.8.2.1 Hamburg Wheel Tracking Test

As described earlier, for the HWTT each asphalt mixture was tested at a minimum of two temperatures based on the binder's PG "S" grade. The results from the HWTT for all the mixtures and their corresponding temperatures are presented in Figure 6-3 through Figure 6-5. Arizona DOT's current acceptance criteria for rutting resistance is based on the test results at 50°C. The rutting should be less than 20 mm at this temperature, and as can be seen from the figures, all the mixtures are below this threshold. It should also be noted that

while most of the tests showed no stripping, some did exhibit stripping. These tests are highlighted with a dark black border in Figure 6-3 through Figure 6-5 and are not included in correlation assessments.

The values in Figure 6-3 through Figure 6-5 are the average of the measured rut depths from the left and right wheel. Currently there does not exist a precision and bias statement in the AASHTO T324 specification, so the variability measure taken for this study is simply the difference between the specimens in the right and left wheel paths. This difference is presented in the form of error bars in Figure 6-3 through Figure 6-5 for each group of binder. In total, 45 HWTT tests were conducted across mixtures and temperatures. For 24 of these tests, the difference between the left and right wheels was less than 10% of the mean rut depth. For 12 of these tests, this difference was between 10 and 20%. For three tests it was between 20 and 25%; and for six tests this difference was greater than 25%. The tests where the difference was greater than 25% were: TX3 at 50°C, TA4 and TX1 at 56°C and GX5, GY6, and TY5 at 62°C. For all six tests in which the variability exceeded 25%, stripping was observed under one of the wheels but not the other. The stripped sample produced larger deformation than the sample that did not experience stripping, and therefore may be the cause for higher variability.

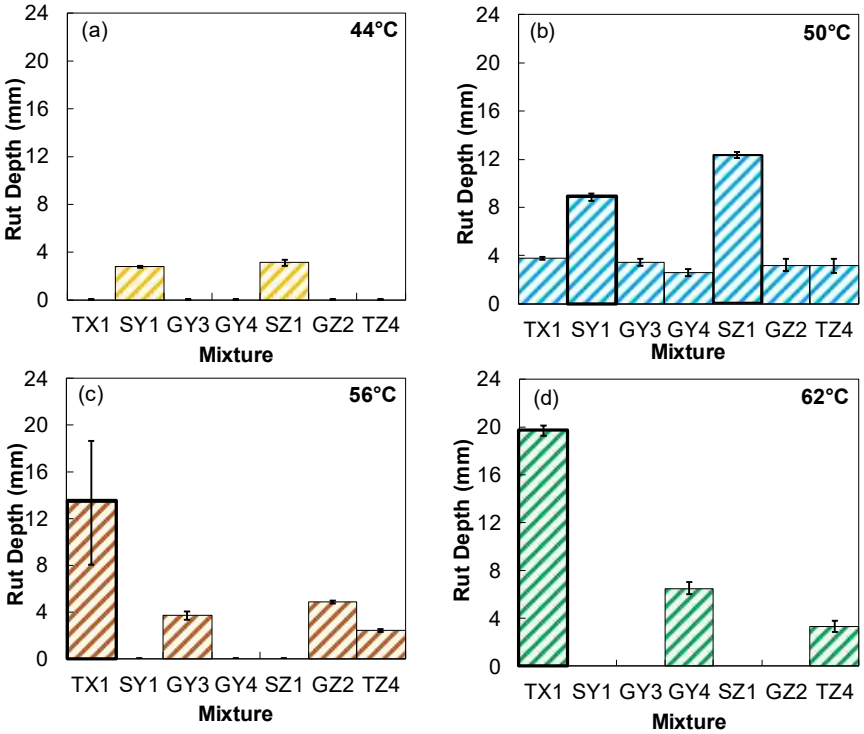

Figure 6-3. Rut Depths for Group 1 Mixtures at; (a) 44°C, (b) 50°C, (c) 56°C, and (d) 62°C.

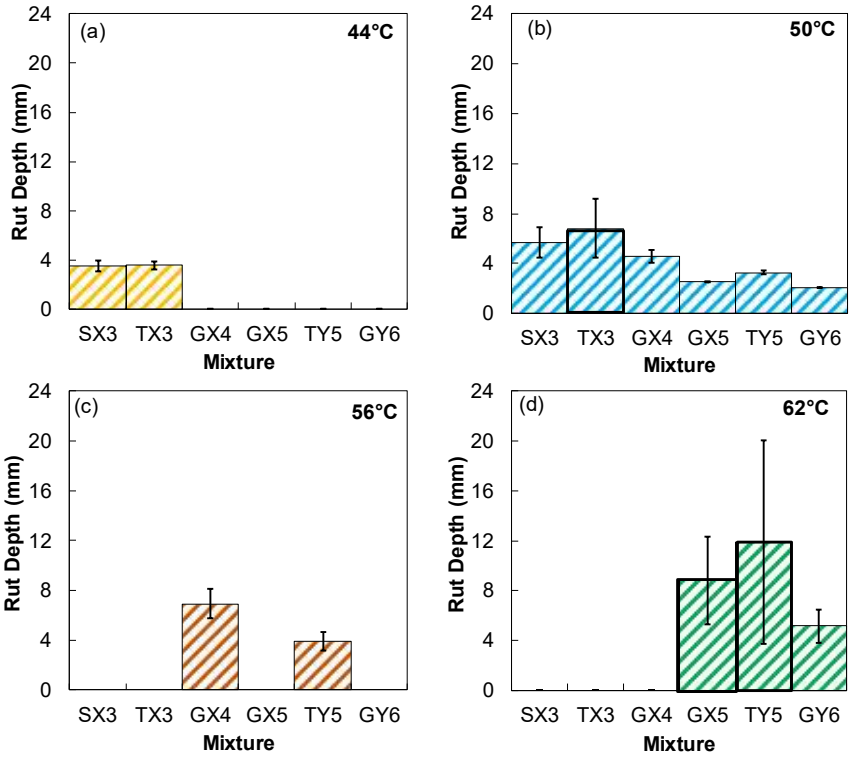

Figure 6-4. Rut Depths for Group 2 Mixtures at; (a) 44°C, (b) 50°C, (c) 56°C, and (d) 62°C.

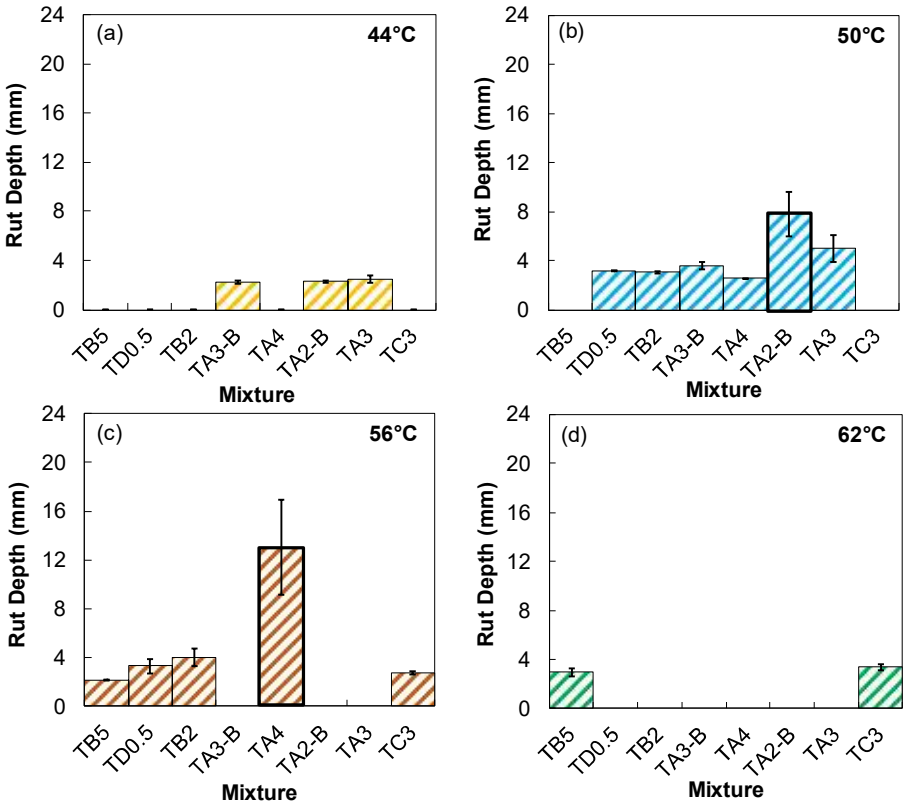

Figure 6-5. Rut Depths for Group 3 Mixtures at; (a) 44°C, (b) 50°C, (c) 56°C, and (d) 62°C.

6.8.2.2 Flow Number Test

Figure 6-6 shows the typical relationship between the total cumulative plastic strain and the number of load cycles during a flow number test. This relationship is generally defined by three regions: primary, secondary, and tertiary. In the primary region, permanent deformations accumulate rapidly. The incremental permanent deformations decrease reaching a constant value in the secondary region. Finally, the incremental permanent deformations again increase, and permanent deformations accumulate rapidly in the tertiary region. The starting point, or cycle number, at which tertiary flow occurs, is referred to as the Flow Number (FN).

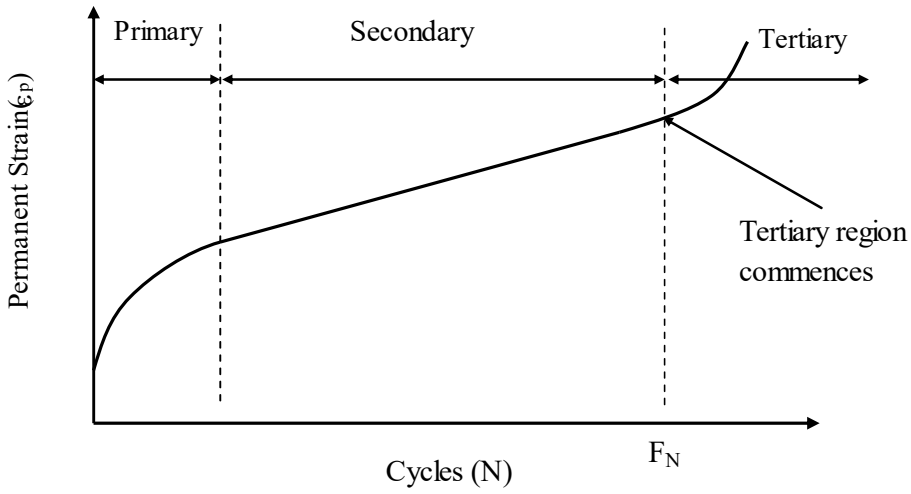

Figure 6-6 Typical Relationship between Total Cumulative Plastic Strain and Number of Load Cycles.

Two basic analyses are performed with the data in these tests; (1) identifying the FN and (2) establishing strain accumulation coefficients for structural performance assessment. To identify the FN value, a statistical analysis technique, the Franken model, is often utilized. This model structure, shown in Equation (7-2), has been selected because it combines both a power function, which characterizes the primary and secondary regions, and an exponential function that fits the tertiary region.

$$\varepsilon_p(N) = AN^B + C\left(e^{DN} - 1\right) \tag{6-2}$$

where:

$\varepsilon_p(N)$ = permanent deformation or permanent strain;

N = number of loading cycles; and

A, B, C and D = regression constants.

In this study, the average slope for the secondary region was estimated and used to investigate correlations between the binder parameters and mixture permanent deformation

resistance. It is recognized that multiple indices could be used, but the slope of the secondary region was adopted due to research that relates this slope to the rate of rutting accumulation in asphalt pavements [*128*]. The average slope for the secondary region was defined by first identifying the FN cycle using after optimizing the Franken model to the measured permanent strain data. This cycle was taken to be the end of the secondary region. Then, the beginning of the secondary region was estimated as the cycle that was 50% of the FN cycle, Finally, the average slope of the Franken model fitting between these two cycles was calculated. Table 6-5 shows the accumulated strain during the RLPD tests for the mixtures from each group of binder and summarizes the relevant parameters from the test. The measured data shown in this table was fitted using the Franken model (which was described earlier) and used to define flow number, cycles to equivalent tertiary slope, and the average slope for the secondary region. The results of this analysis are shown in Table 6-5.

Table 6-5 Summary of Results from RLPD Tests for All the Mixtures

Group	Mixture	Flow Number (Cycles)	Axial Permanent Strain at Failure ε_p (%)	Average Slope for Secondary Region	COV (FN)
Group 1	TX1	559	1.04	1.3×10^{-3}	18.28
	SY1	351	1.02	1.9×10^{-3}	0.68
	GY3	795	1.18	9.5×10^{-4}	2.95
	GY4	1535	1.22	5.2×10^{-4}	6.15
	SZ1	355	1.13	2.2×10^{-3}	9.49
	GZ2	879	1.45	1.0×10^{-3}	7.12
	TZ4	3183	0.86	1.5×10^{-4}	5.56
Group 2	SX3	211	1.17	3.6×10^{-3}	6.11
	TX3	221	1.00	2.9×10^{-3}	7.98
	GX4	349	1.34	2.5×10^{-3}	12.55
	GX5	1251	1.48	7.3×10^{-4}	10.58
	TY5	3343	0.95	1.3×10^{-4}	46.36
	GY6	8095	1.23	7.0×10^{-5}	17.88

Group	Mixture	Flow Number (Cycles)	Axial Permanent Strain at Failure ε_p (%)	Average Slope for Secondary Region	COV (FN)
Group 3	TB5	22271	0.93	2.2×10^{-5}	3.56
	TD0.5	1535	1.04	4.0×10^{-4}	8.84
	TA3-B	991	1.13	6.3×10^{-4}	6.60
	TA4	601	1.03	1.0×10^{-3}	10.49
	TA2-B	347	1.19	2.0×10^{-3}	14.22
	TA3	443	0.86	1.3×10^{-3}	31.66
	TC3	10175	1.35	6.3×10^{-3}	14.58

6.9 Correlation Analysis

6.9.1 Relationship between $|G^*|/\sin\delta$ and $J_{nr3.2}$

To more closely examine the two different rutting parameters, the values from the study binders as well as those from an historical database of ADOT binders [*132*], were compared. Figure 6-7 shows the results of this comparison with the data segregated according to the historical database at the AASHTO M320 high temperature grade, part (a), Group 1 binders in this study at multiple temperatures, part (b), Group 2 binders in this study at multiple temperatures, part (c), and Group 3 binders in this study at multiple temperatures, part (d). In this figure the very high values of $J_{nr3.2}$ and $|G^*|/\sin\delta$ are unrealistic for grading purposes. They appear here when asphalts are tested at temperatures that are either higher or lower than that which would be used to grade the asphalts. They are included to demonstrate that the observed relationship between the two parameters spans a large range of rheological behavior even outside what the grading specifications would allow. It can be observed from this figure that for non-polymer modified asphalts there exists a very strong correlation regardless of binder (grade or supply) between the $|G^*|/\sin\delta$ and J_{nr} parameters, Figure 6-7

(a) and (b). Also, from Figure 6-7 (d) there is a strong correlation for the Group 3 asphalts, where the base binder, modifier, and cross-linking agents (PPA and sulfur) are all identical. This correlation is different from that of the non-polymer modified asphalts. In Group 2 asphalts, Figure 6-7 (c), where the base binder, modifier, and any potential other admixtures differ, the correlation varies greatly. Though not shown here in the interest of brevity, data from many other polymer-modified asphalts from the states of Nevada and Montana were evaluated and also showed a non-consistent correlation. This difference can be simply explained by the fact that at high strain levels, the polymer network is engaged and yields more complex and different behaviors relative to the linear region than non-polymer modified asphalts. The significance of the findings lies in the fact that for the unmodified binders, the $J_{nr3.2}$ value may not provide any fundamentally new information about the rheology that is not already embedded into the $|G^*|/\sin\delta$ parameter. It also means that the expected correlation between the two parameters and mixture rutting is likely to have varying forms (e.g., one may have a linear relationship to rutting while the other may vary as a power law with rutting).

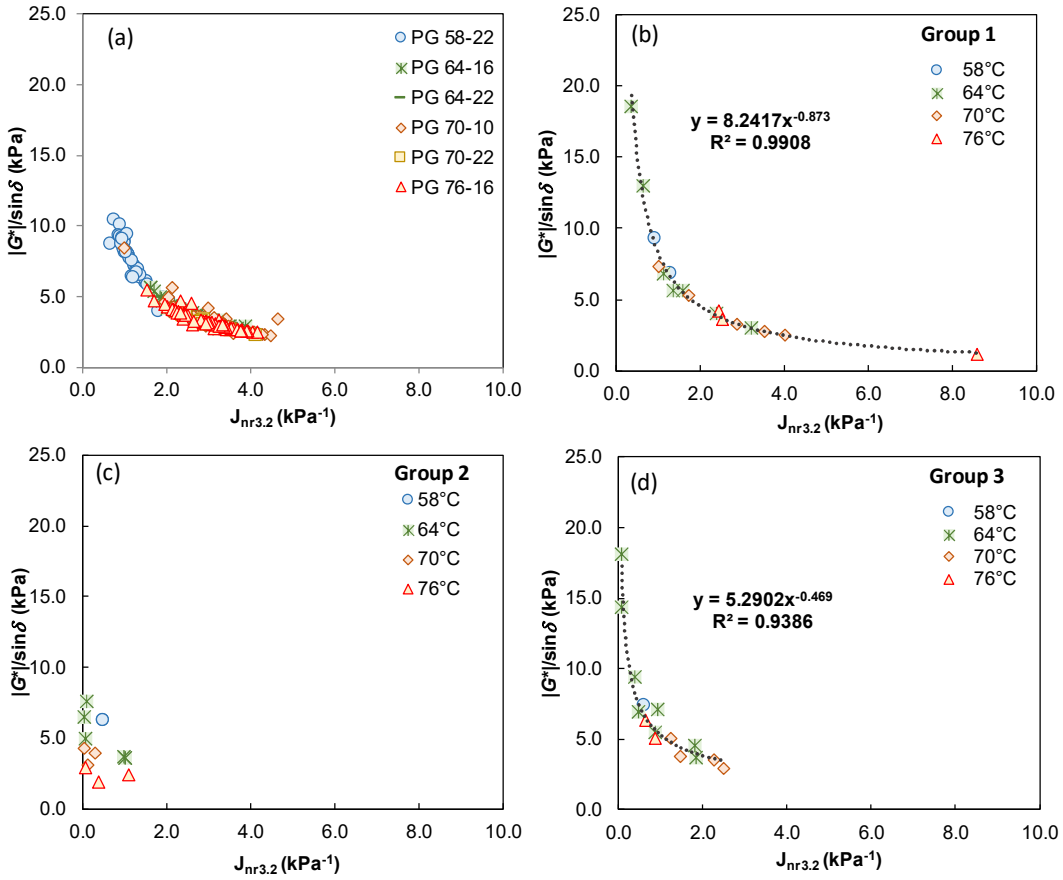

Figure 6-7 Relationship Between $|G^*|/\sin\delta$ and $J_{nr3.2}$; (a) Historical Database, (b) Group 1, (c) Group 2, and (d) Group 3.

6.9.2 Comparing the HWTT and RLPD Tests

The rutting parameters identified from HWTT and RLPD tests are compared in Figure 6-8. The rut depth at 50°C from the HWTT test correlates very closely to the slope of the secondary region of the RLPD test at 50°C. A good correlation with a R^2 value of 0.69 was obtained between the two test parameters. These results are in line with what others have found [118]. Also, a better correlation with R^2 value of 0.79 was obtained between the rut depth from the HWTT test and the flow number from RLPD test. It is important to see a good agreement between the tests and no apparent bias in the polymer modified versus non-

polymer modified asphalts. Note that these comparisons can only be made at 50°C since this was the only test temperature used for RLPD testing.

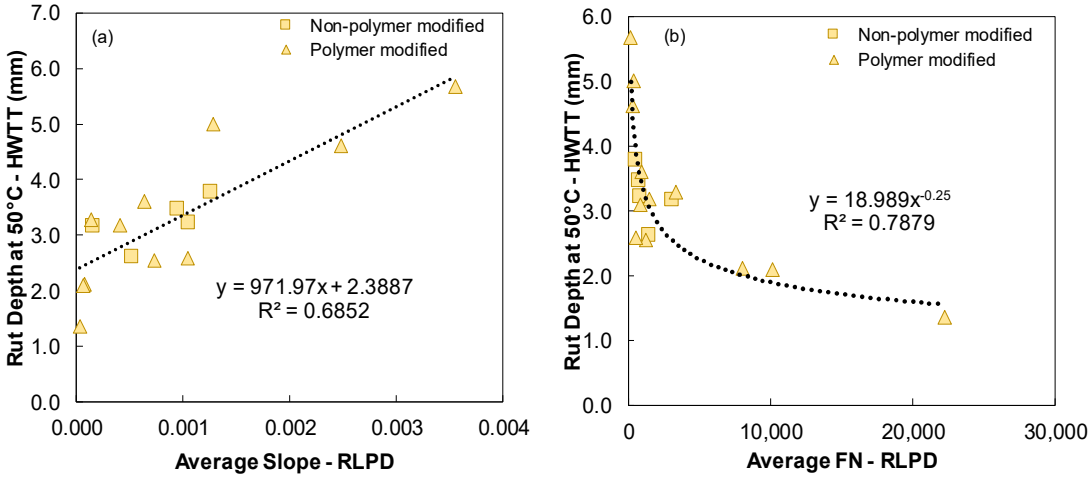

Figure 6-8 Correlation between Rut Depth from HWTT Test and (a) Slope of the Secondary Region (b) Flow Number of the RLPD Test.

6.9.3 Correlation of Binder Rutting Parameters with Hamburg Wheel Test Results

The HWTT results at 50°C were related to both $|G^*|/\sin\delta$ and $J_{nr3.2}$ at 64°C and the results are presented in Figure 6-9. In part (a), the rut depth from the HWTT test is plotted against $|G^*|/\sin\delta$. Historically, the relationship between this binder parameter and mixture rutting parameters is fit to a linear function and the correlation is reported to be poor. However, in this research the function is found to be better described using a power law function. In the case of the relationship with $J_{nr3.2}$, a linear function is found to best describe the relationship between the two parameters. With the earlier findings relating $J_{nr3.2}$ and $|G^*|/\sin\delta$ the fact that two different functional forms exist is mathematically consistent. Overall, these relationships have low correlation coefficients. It is also important to note that in Figure 6-9 there are four data points that were not included as those mixtures were subjected to

stripping. While the correlation would have improved with the inclusion of those points, it would have been incorrect to do so. The main point to observe in this figure is a lack of visually observable bias in the results between polymer-modified and non-polymer modified asphalts.

The correlation at other temperatures were similar, but generally suggested a better overall relationship between HWTT rut depth and $|G^*|/\sin\delta$ than with $J_{nr3.2}$. A limitation to this analysis is the fact that aggregate source changes somewhat between each mixture and therefore pairwise comparisons where $|G^*|/\sin\delta$ are similar but $J_{nr3.2}$ differ were evaluated. The approach to this assessment was to identify mixtures with binders of similar $J_{nr3.2}$ and $|G^*|/\sin\delta$ and then compare the individual changes in rut depth for these mixtures. A statistical segregation technique called k^{th} moment clustering was used to cluster and identify the binders by group [*131*]. The basic principle of the technique is to segregate the data into different clusters or groups based on the proximity from a mean value. The process is completed in multiple steps (two are used for this study) wherein arbitrary cluster mean values are first assumed to represent the mean and 25th and 75th quartiles of the data. The data are then clustered to the closest value based on their proximity (calculated based on the minimum squared distance from the given observation to each assumed mean value). Once the initial clustering is completed, the mean values for each cluster are calculated, the proximity of each observation to the new means are determined, and the results re-clustered. If the initial step eliminates a group altogether then in the second iteration the mean of that cluster is assumed equal to the average of the other two. This process is repeated until convergence, which for this study was two iterations. The output from the clustering

operation were binders with similar $J_{nr3.2}$ and similar $|G^*|/\sin\delta$ at 64°C and 70°C as shown in Figure 6-10. Based on the obtained clusters, mixtures prepared with these binders were then organized into pairs along with their corresponding rut depths. If the similarities in $J_{nr3.2}$ or $|G^*|/\sin\delta$ existed at 64°C, the rut depth considered was at 50°C. For binder similarities or differences at 70°C the rut depth at 56°C was considered. A t-test was conducted at 95% confidence interval on the rut depths of mixtures produced using the clustered binders to check if similarities existed in rut depths as well.

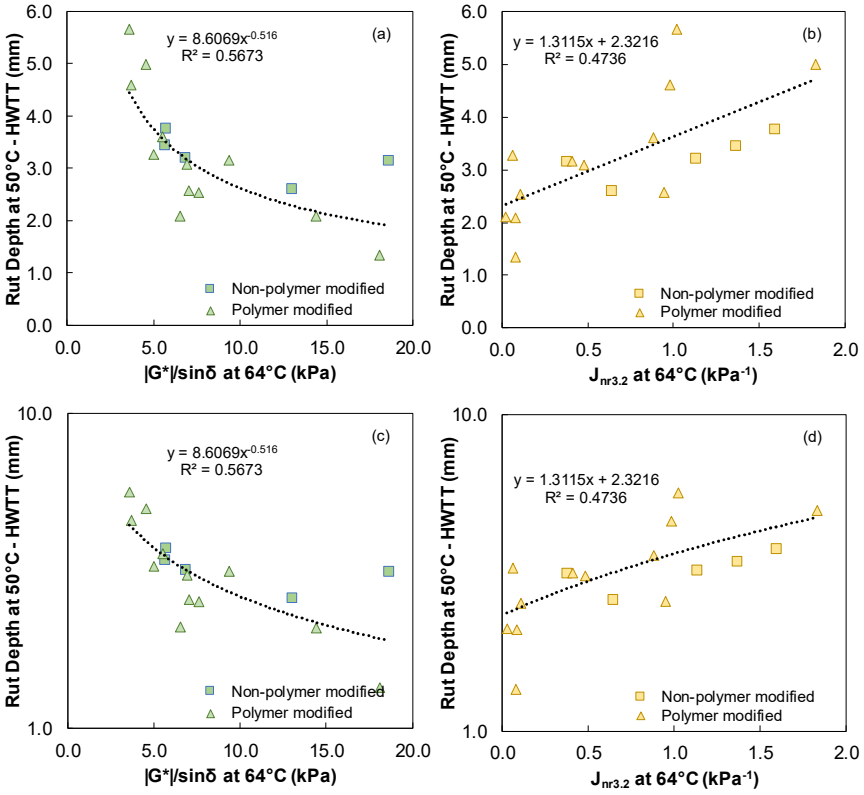

Figure 6-9 Correlation of Rut Depth from HWTT Results to; (a) $|G^*|/\sin\delta$ and (b) $J_{nr3.2}$.

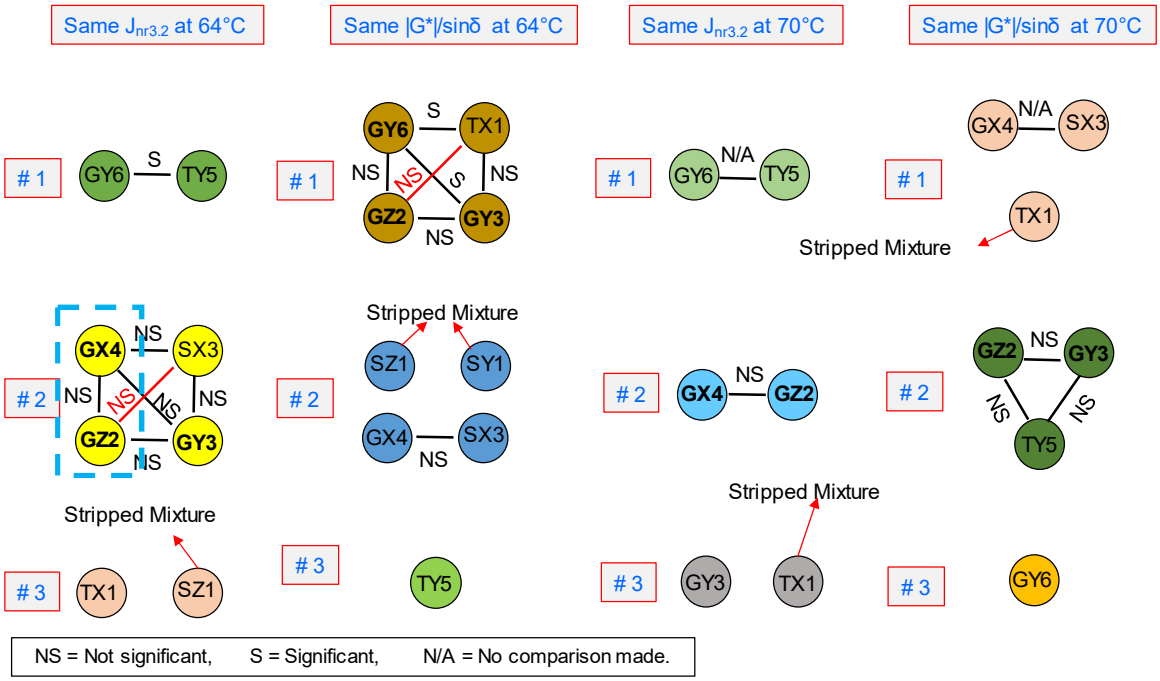

Figure 6-10 The Significance Testing Output for HWTT Rut Depth from kth Moment Clustering Operation for $J_{nr3.2}$ and $|G^*|/\sin\delta$ at 64 and 70°C.

The results from t-test are shown in Figure 6-10. It is to be noted that the samples which experienced stripping during the Hamburg test are excluded from the analysis. Also, the mixture pairs sharing the same aggregate type have been highlighted in bold in Figure 6-10. The inferences based on such mixtures pairs can be considered to have higher degree of accuracy, given that they share the same aggregate. To understand the outcomes of this analysis and its significance, consider the comparison between GX4 and GZ2 (shown outlined in a blue dashed box for easy identification), which has same $J_{nr3.2}$ at 64°C. As per the results from the t-test, at 95% confidence level, there is no statistically significant difference in rutting among the two mixtures, is indicated in the figure using the abbreviation "NS". This means that for the pair under consideration, $J_{nr3.2}$ is a good indicator

of rutting and vice-versa if there is a statistically significant difference "S". This exercise was repeated for all pairs shown in Figure 6-10.

Based on the above assessment, and as shown graphically in Figure 6-10, seven out of eight (87%) mixture pairs which possessed binders with similar $J_{nr3.2}$ were found to have similar rut depths. This is in comparison to eight out of ten (80%) of mixture pairs which possessed binders with similar $|G^*|/\sin\delta$ were found to have similar rut depths. It is believed that the above assessment, taken in combination with the linear functional fit with respect to rut depth and $J_{nr3.2}$, supports the conclusion that $J_{nr3.2}$ is a better indicator of rutting than $|G^*|/\sin\delta$ for Arizona mixtures.

6.9.4 Correlation of Binder Rutting Parameters with Repeated Load Permanent Deformation Test Results

Figure 6-11 shows the correlation between the binder rutting parameters and average slope from RLPD tests. It can be seen from the figure that the binder parameters relate better to RLPD results than Hamburg wheel rutting results. When average slope is used as a mixture rutting indicator, the correlation with respect to $J_{nr3.2}$ is much greater than the correlation with $|G^*|/\sin\delta$, reduces marginally. It is to be noted that there are three points that are excluded from the correlations shown in Figure 6-11 (b). These mixtures correspond to binders X3, and X4. Elimination of these mixtures is partially responsible for the improved R^2 value (when they are included the R^2 value reduces to a value similar to what is seen with $|G^*|/\sin\delta$. They are eliminated solely based on the fact that they have values so different from the other mixtures. No clear reason for this difference could be identified and is

admittedly a shortcoming in the current work, unfortunately materials were limited and retesting for either binder or mixture behaviors was not possible.

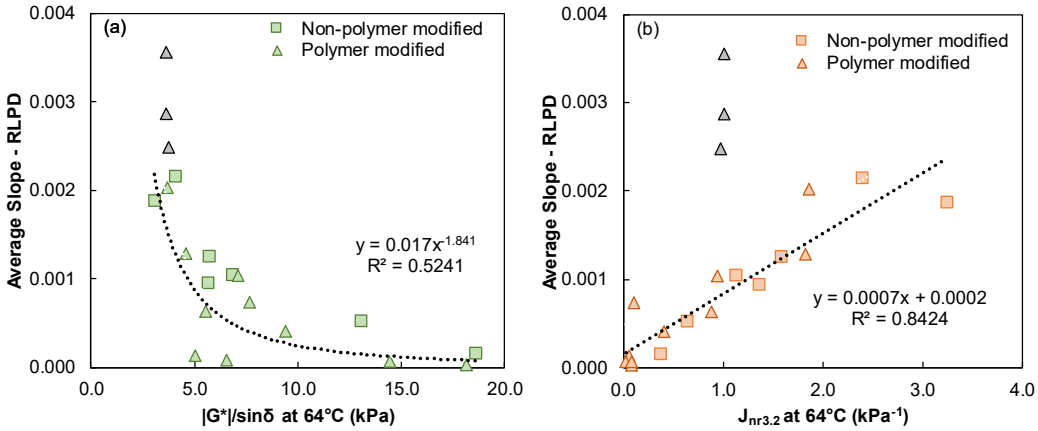

Figure 6-11 Correlations of RLPD Test Results to; (a) $|G^*|/\sin\delta$; (b) $J_{nr3.2}$.

Pairwise comparisons similar to those carried out with the HWTT are shown for the RLPD results in Figure 6-12. The k^{th} moment clustering was used to cluster and identify the binders by group. The output from the clustering operation were binders with similar $J_{nr3.2}$ and similar $|G^*|/\sin\delta$ at 64°C as shown in Figure 6-12. Based on the obtained clusters, mixtures prepared with these binders were then organized into pairs along with their corresponding average slope. For this analysis, the similarities in $J_{nr3.2}$ or $|G^*|/\sin\delta$ existed at 64°C, the average slope considered was at 50°C. A t-test was conducted at 95% confidence interval on the rut depths of mixtures produced using the clustered binders to check if similarities existed in average slope as well.

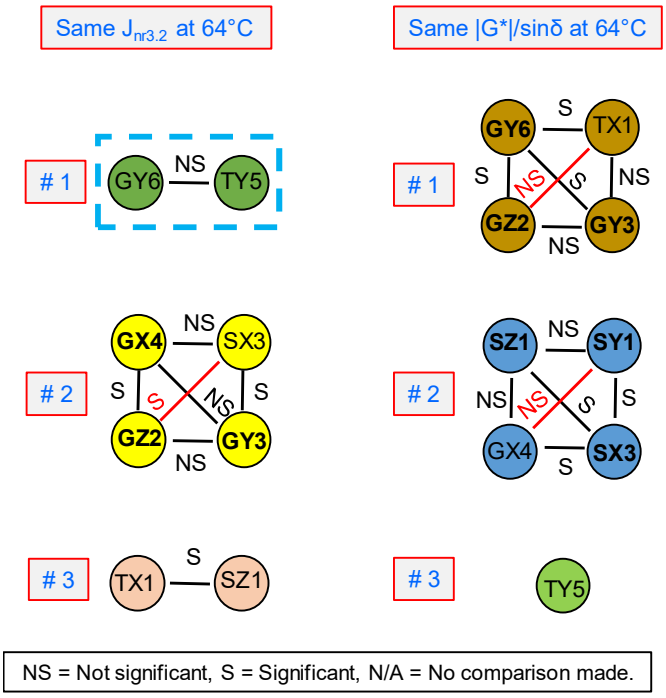

Figure 6-12 The Significance Testing Output for RLPD Average Slope Output from kth Moment Clustering Operation for $J_{nr3.2}$ and $|G^*|/\sin\delta$ at 64°C.

The results from t-test are shown in Figure 6-12. It is to be noted that the mixture pairs sharing the same aggregate type have been highlighted in bold in Figure 6-12. The inferences based on such mixtures pairs can be considered to have higher degree of accuracy, given that they share the same aggregate. To understand the outcomes of this analysis and its significance, consider the comparison between GY6 and TY5 (shown outlined in a blue dashed box for easy identification), which has same $J_{nr3.2}$ at 64°C. As per the results from the t-test, at 95% confidence level, there is no statistically significant difference in rutting among the two mixtures, is indicated in the figure using the abbreviation "NS". This means that for the pair under consideration, $J_{nr3.2}$ is a good indicator

of rutting. Vice-versa if there is a statistically significant difference abbreviation "S" is used. This exercise was repeated for all pairs shown in Figure 6-12.

Based on the above assessment, when comparing mixtures with the same binder property it is seen that both $J_{nr3.2}$ and $|G^*|/\sin\delta$ are equally good indicators as both possessed 50% of mixture pairs that had similar rutting, four out of eight in same $J_{nr3.2}$ category and six out of twelve in same $|G^*|/\sin\delta$ category. However when comparing same binder property and same aggregate source, it is found that $J_{nr3.2}$ better identifies mixtures with the same rutting than does $|G^*|/\sin\delta$. Under the similar $J_{nr3.2}$ category there were three pairs highlighted in bold in Figure 6-12 which had similar $J_{nr3.2}$ and shared the same aggregate type. Out of these three mixture pairs there were two pairs (67%), whose mixtures possessed similar rutting. Likewise, under the similar $|G^*|/\sin\delta$ category there are also three pairs which had similar $|G^*|/\sin\delta$ and shared the same aggregate type. However, out of these three mixture pairs there were only one pair (33%) whose mixtures possessed similar rutting. It is believed that the above assessment, supports the conclusion that $J_{nr3.2}$ and $|G^*|/\sin\delta$ are good indicator of rutting for Arizona mixtures.

6.9.5 Effect of Aging on Relationship between Asphalt Binder Parameters and Asphalt Mixture Rutting

The analysis shown in Chapter 5 found that the binder aging occurs when a mixture is short-term conditioned in a forced draft oven for 4 hours at 135°C per AASHTO R 30 generally exceeds the aging that occurs in the short-term binder aging procedures. This finding is very important for the study herein. In this section, it will be considered in the analysis for evaluating the impact of the rutting correlation between binder and asphalt mixture.

One of the main goals of this chapter was to compare the binder rutting parameters $|G^*|/\sin\delta$, and $J_{nr3.2}$ to mixture rutting. In the literature review presented in Chapter 2, this relationship has been shown by first plotting the two rutting parameters against rut depth; then fitting the relationship to a linear function, and finally inferring upon the suitability of one parameter over the other based on the goodness of fit or the R^2 value. This type of analysis was applied to the test data in this study as shown in Figure 6-13, which uses the Group 1 and Group 2 binder property data at 64°C and mixture rut depth at 50°C. If a linear regression function is used to fit the data presented in Figure 6-13, mixture rutting is found to better correlate to $J_{nr3.2}$ than $|G^*|/\sin\delta$ (R^2 of 0.63 versus 0.19, respectively).

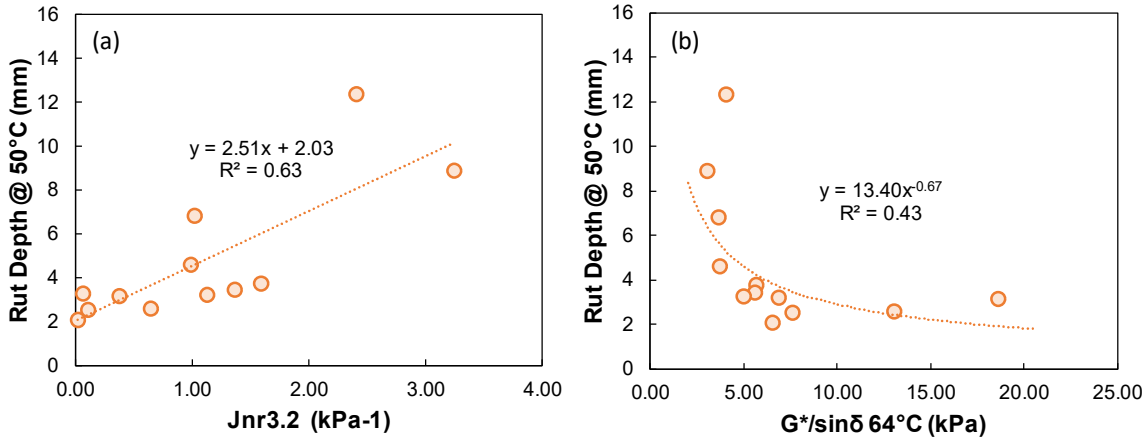

Figure 6-13 Comparison between Binder Rutting Parameters at 64°C and Mixture Rutting at 50°C for Group 1 & 2 Binders (a) $J_{nr3.2}$ vs Rutting and (b) $|G^*|/\sin\delta$ vs Rutting

An improved linear fit is ideal because it would be easier to interpret what a change in binder rutting parameter means to mixture rutting. However, a low R^2 value based on a linear fit is not a guarantee than one parameter is a "better" than another. In this case it might not be a good representation of the true potential of $|G^*|/\sin\delta$ in relating to mixture rutting since non-linear functional relationships may also be acceptable for a specification parameter. Thus,

using a linear regression fit may unfairly penalize the $|G^*|/\sin\delta$, since the relationship in Figure 6-13 (b) appears closer to a power law fit than a linear fit. Therefore, a power law regression function is used to fit the correlation between mixture rutting and $|G^*|/\sin\delta$. Based on the power law fit, the R^2 is better than the linear fit (R^2 of 0.43).

However, when establishing the correlation RTFO used for binder property versus short term aging for mixture rutting. For these conditions, there is considerable scatter and the mixture rutting prediction is also biased. It is possible to calibrate to the mean of mixture rutting effect, but not the scatter effect. If it is assumed that the true binder property related to permanent strain accumulation is intimately related to modulus then the results from Chapter 5 may be used to reasonably correct. To have a better understanding of these relationships and to make an informed decision about improving the correlations, the aging study was performed to assess the scatter and evaluate the suitable binder rutting parameter.

The ratio between STOA aging ratio and RTFO aging ratio (AR_{STOA}/AR_{RTFO}) will be applied using binders for which extracted and recovered the binder are available and thus there is a high confidence that the binder tested represents what exists in the mixture. These values measured at 64°C for the extracted and recovered binders and reported latter in Table 6-7. For the other seven binders, the calibrated simplified global model is used in the section 5.5.2 to back calculate the $|G^*|$ values of STOA condition at 21.1°C, 37.8°C, and 54.4°C. A frequency of 6.0 Hz was used for the calculation of STOA aging to simulate HWT speed. On the other hand, the $|G^*|$ of original and RTFO aging condition were estimated from the master curve at the same three temperatures and same frequency. The relationship of the three temperatures and $|G^*|$ for original, RTFO, and STOA aging condition were plotted for

each binder. A power law regression function is used to fit the correlation between temperature and |G^*|. Figure 6-14 and Figure 6-15 show the correlation between temperature and |G^*| of Z_2 binder for arithmetic logarithmic Scales respectively.

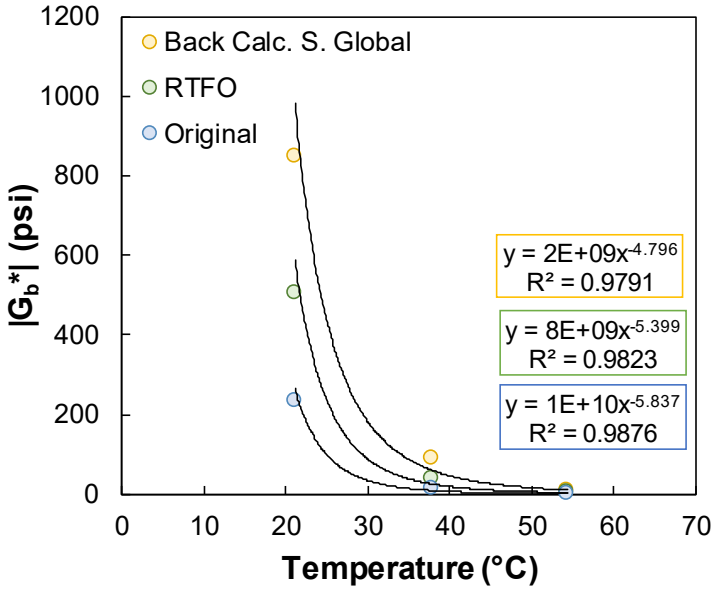

Figure 6-14 Correlation between Temperature & |G^*| of Z_2 Binder Used Arithmetic Space

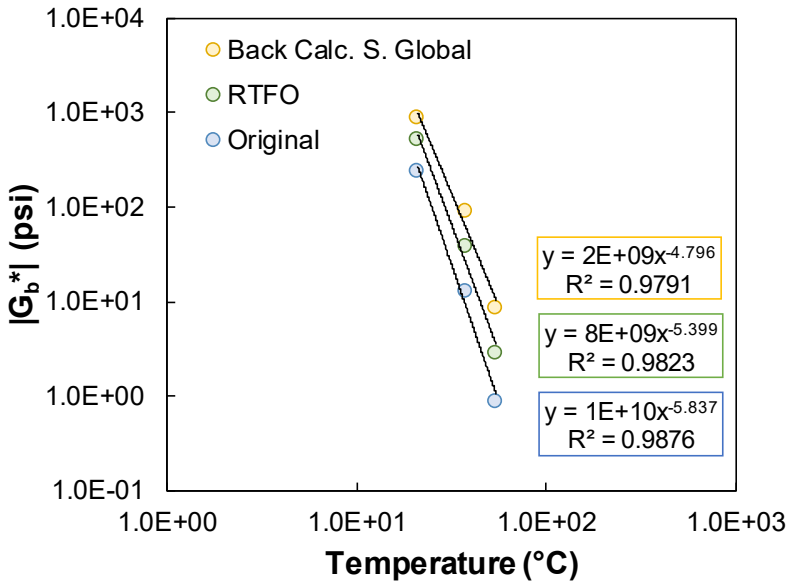

Figure 6-15 Correlation between Temperature and |G^*| of Z_2 Binder Used Logarithmic Scales

Very high R^2 value based on a power law fit is shown in the figures for the three conditions. All the binders are fitted by power law fit functions and the fit parameters are shown along with R^2 reported in Table 6-6. As noted, all the fitted function had very good fit with excellent R^2. These correlation used to estimate the $|G^*|$ at 64°C to use in the aging analysis.

Table 6-6 Power Law Fitting Parameters along with R^2 for All Study Binders

Mixture	Original			RTFO			S. Global (STOA)		
	a	b	R^2	a	b	R^2	a	b	R^2
GX4	2.1E+08	-4.95	0.99	1.1E+09	-5.19	0.98	1.1E+08	-4.25	0.98
GX5	5.7E+09	-5.55	0.99	1.4E+10	-5.61	0.99	4.5E+09	-5.00	0.99
GY3	7.2E+09	-5.68	0.99	5.5E+09	-5.40	0.98	5.0E+08	-4.39	0.99
GY4	1.3E+11	-6.13	0.99	6.4E+10	-5.73	0.98	3.3E+10	-5.24	0.98
GY6	2.6E+08	-4.84	0.99	1.7E+09	-5.17	0.98	6.5E+07	-3.88	0.99
GZ2	1.4E+10	-5.84	0.99	8.3E+09	-5.40	0.98	2.2E+09	-4.80	0.98
SX3	2.2E+08	-4.96	0.99	9.6E+08	-5.14	0.98	5.6E+08	-4.97	0.98
SY1	2.2E+10	-6.13	0.99	3.4E+10	-5.63	0.98	1.3E+10	-5.54	0.95
SZ1	2.8E+10	-6.13	0.99	4.1E+10	-5.93	0.98	1.1E+10	-5.48	0.99
TX1	2.7E+11	-6.54	0.99	1.9E+11	-6.17	0.98	1.3E+10	-5.15	0.97
TY5	1.3E+09	-5.29	0.99	3.8E+09	-5.42	0.98	2.4E+07	-3.71	0.99
TZ4	1.2E+10	-5.59	0.99	4.0E+09	-5.03	0.99	1.7E+09	-4.53	0.97

The aging ratio of STOA and RTFO aging condition was estimated by dividing the $|G^*|$ values of each condition by the $|G^*|$ values of original condition for all Group 1 and Group 2 binders. The ratio between back calculated STOA aging ratio and RTFO aging ratio (AR_{STOA}/AR_{RTFO}) at the same frequency and temperature was calculated for Group 1 and Group 2 binders as shown in Table 6-7.

Table 6-7 AR_{STOA}/AR_{RTFO} for Group 1and Group 2 Binders at 64°C

Mixture	AR_{RTFO}	AR_{STOA}	AR_{STOA}/AR_{RTFO}
GX4	1.9	9.8	5.2
GX5	2.0	7.7	3.9
GY3	2.4	15.0	6.1
GY4	2.5	10.4	4.1
GY6	1.7	13.5	8.1
GZ2	3.6	11.8	3.3
SX3	2.1	2.4	1.1
SY1	12.4	6.8	0.5
SZ1	3.3	6.0	1.8
TX1	3.3	15.0	4.6
TY5	1.7	13.3	7.8
TZ4	3.5	11.4	3.3

After the ratio between STOA aging ratio and RTFO aging ratio (AR_{STOA}/AR_{RTFO}) at 64°C estimated for all study binders were applied directly to adjust rutting binder parameters. The J_{nr} values divided by AR_{STOA}/AR_{RTFO} ratio for all binders and plotted again against the rut depth at 50°C; then fitting the relationship to a linear function as shown in Figure 6-16 (a).

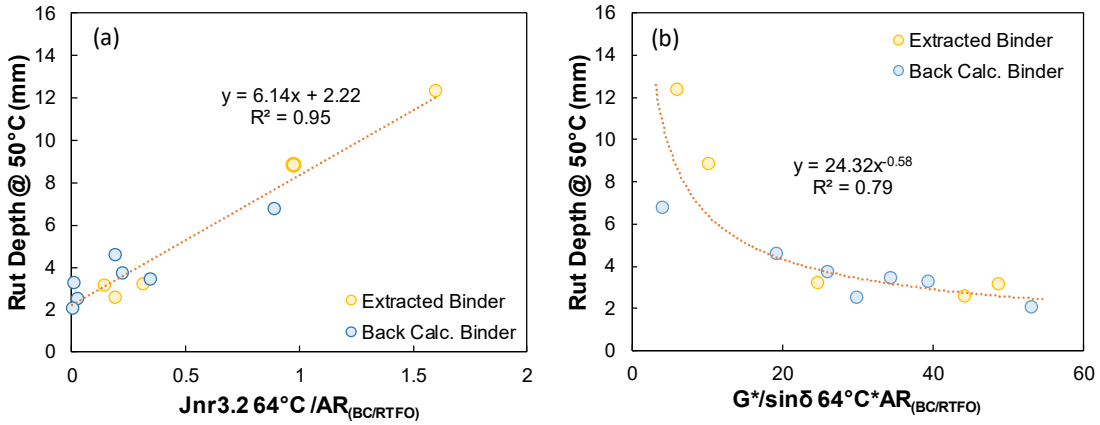

Figure 6-16 Comparison between Adjusted Binder Rutting Parameters at 64°C and Mixture Rutting at 50°C for Group 1 & 2 Binders (a) Adjusted $J_{nr3.2}$ vs Rutting and (b) Adjusted |G*|/sinδ vs Rutting

The mixture rutting is found to better correlate to adjusted $J_{nr3.2}$ than $J_{nr3.2}$ as shown in Figure 6-13 (a) (R^2 of 0.63 versus 0.95, respectively). This is a very good finding and improving the fitting relationship and it will provide a better mixture rutting prediction.

Also, the |G*|/sinδ values are multiplied by AR_{STOA}/AR_{RTFO} ratio for all binders and plotted again against the rut depth at 50°C. Finally, the results are fitted to a power function as shown in Figure 6-16 (b). The mixture rutting is found to better correlate to adjusted |G*|/sinδ than |G*|/sinδ as shown in Figure 6-13 (b) (R^2 of 0.43 versus 0.79, respectively). The aging study assessed the scatter issue in the data. In addition, it help to develop a better mixture rutting prediction by using the binder rutting parameter. This result means; basically that it is possible to find relationships between binder and mixture rutting using binder properties that are not precisely what it find in the mixture because the initial hypothesis that linear properties and even J_{nr} are themselves highly related to the real rutting related behavior of apshalt binder. Correcting to the right condition makes this clearer.

6.10 Conclusions

The following conclusions are made from this study;

- For non-polymer modified asphalts, there is a very strong correlation between $|G^*|/\sin\delta$ and $J_{nr3.2}$ regardless of binder type or grade.
- For polymer modified asphalts, where the base binder, modifier, and cross-linking agents (PPA and sulfur) are all identical, there is a strong correlation between $|G^*|/\sin\delta$ and $J_{nr3.2}$. However, where the base binder, modifier, and any potential other admixtures differ, the correlation varies greatly.

- A good correlation with a R^2 value of 0.69 was obtained between the rut depth at 50°C from the HWTT test and the slope of the secondary region of the RLPD test at 50°C. And a better correlation with a R^2 value of 0.79 was obtained between the rut depth from HWTT test and the flow number from RLPD test. No systematic bias with respect to this correlation and polymer-modified asphalts was observed.
- When correlating the rut depth from the HWTT to both $|G^*|/\sin\delta$ and $J_{nr3.2}$, in the case of the relationship with $|G^*|/\sin\delta$, the function is found to be better described using a power law function. In the case of the relationship with $J_{nr3.2}$, a linear function is found to best describe the relationship.
- Overall, the rut depth from the HWTT has low correlation coefficient to both $|G^*|/\sin\delta$ and $J_{nr3.2}$ relationships, but pairwise comparisons demonstrate that $J_{nr3.2}$ is more consistent at segregating mixture performance.
- When correlating the average slope from RLPD tests to both $|G^*|/\sin\delta$ and $J_{nr3.2}$, the binder parameters relate better to RLPD results than HWTT results. The correlation with respect to $J_{nr3.2}$ is much greater than the correlation with $|G^*|/\sin\delta$.
- When correlating the binder rutting parameters $|G^*|/\sin\delta$, and $J_{nr3.2}$ to mixture rutting, the tested asphalt binder in the laboratory should represent what exists inside the mixture for better coronation.
- The study shows that the better way to ensure the binder test properties reflect the condition of the binder during the mixture test is to run the binder tests by extracting and recovery the same tested asphalt mixture sample.

6.11 Study Limitations and Future Work

The following are the limitations of this study:

1. The study was conducted only using aggregates sourced from the state of Arizona. So, the relationship has not been investigated/validated with different aggregates types from states outside Arizona.
2. The study used, only the most widely used binders in the state of Arizona, which included PG 64-22, PG 70-10, PG 76-16, PG 70-16, and related polymer-modified asphalt.
3. Though aggregates were sourced from three different locations in Arizona, the aggregate gradation was very similar among the three sources. The three different aggregate gradations are dense graded mix. The study has not investigated the correlation with different mix types.

As part of the future work, the developed relationships should be checked with aggregates vastly different from those available in AZ. One such aggregate type to be considered for future testing is limestone. As mentioned above, the investigation did not include any binders with high temperature PG grades lower than 64°C. The addition of these binders would add credibility to the overall work. Lastly, the mixtures were fine graded mixtures, thereby future investigations should involve coarse, open graded and gap graded mixtures also.

Chapter 7. EFFECT OF MSCR PERCENT RECOVERY ON PERFORMANCE OF POLYMER MODIFIED ASPHALT MIXTURES

7.1 Abstract

The AASHTO M332 specification includes a relationship between the non-recoverable creep compliance at 3.2 kPa ($J_{nr3.2}$) and the percent of elastic recovery ($R_{3.2}$) from the multiple stress creep and recovery (MSCR) test. Justification for the exact position of this curve based on binder performance is largely undocumented in the technical literature as is the singular effect of higher or lower $R_{3.2}$ values on mixture performance. In this study, nine binders were tested to evaluate the effect of $R_{3.2}$ on the performance of asphalt mixtures. Binders with similar $J_{nr3.2}$ and varying MSCR $R_{3.2}$ were divided into four groups based on their $J_{nr3.2}$ value. Comparisons were made based on results obtained from the dynamic modulus test, Hamburg Wheel Tracking test, and axial fatigue test. Based on these tests, it was shown that $R_{3.2}$ had a strong relationship to the dynamic modulus of asphalt mixtures especially at intermediate and high temperatures. Binders with lower $R_{3.2}$ had a higher dynamic modulus but showed no correlation to phase angle. Both modulus and phase angle of the mixture correlated to the binder shear modulus and phase angle. Binders with high $R_{3.2}$ had a greater fatigue resistance and the effect is quite noticeable. However, $R_{3.2}$ was shown to have little to no effect on the rutting resistance of the asphalt mixtures for the

---

The parts of this chapter are accepted for publication as: Salim, R., Gundla, A, Underwood, B.S., and K. E. Kaloush, (2019). Effect of MSCR Percent Recovery on Performance of Polymer Modified Asphalt Mixtures. *Journal of the Transportation Research Board*, TRB, National Research Council. Washington, D.C. [135]

temperatures tested in this study. Finally, an alternative $J_{nr3.2}$ vs $R_{3.2}$ relationship based on this study results are also presented.

7.2 Introduction

According to statistics compiled by the Asphalt Institute, nearly 94% of the roadways in the United States are surfaced with asphalt concrete [136]. Rutting and fatigue cracking are the predominant distress types for these pavements. Rutting, permanent deformations in the form of surface depressions in the wheel path, can severely impact ride quality and can also negatively affect safety since the depressions can allow water accumulation that may result in vehicle hydroplaning [137]. Cracking can negatively impact the load carrying capacity of a pavement and accelerate losses in ride quality and ultimate longevity of the pavement [137]. Engineers must carefully make their design and materials selection decisions to balance these two distresses to deliver the best performing, longest lasting, and lowest cost pavement infrastructure. There are many factors that ultimately affect the long-term pavement performance with respect to these two distresses, but one that is critical is the selection and specification of asphalt binder. The asphalt binder used in any given application must be carefully selected because grades that are too stiff for the climate and traffic are likely to crack and those that are too soft will likely experience rutting.

The AASHTO M320 specification was developed during SHRP to guide state agencies in selecting and specifying asphalt binders. However, this specification was developed using experimental data on asphalts that were common in the late 1980's to early 1990's, and did not include many modern technologies including chemical and polymer modification [138]. Agencies have begun to make extensive use of modified asphalts

because they lead to better performing, and thus less costly asphalt pavements over the pavement's life cycle [139,140]. The increased usage of modified asphalts has highlighted certain limitations in the AASHTO M320 parameters and the development of the Multiple Stress Creep and Recovery (MSCR) test (AASHTO T 350 and ASTM D7405) to evaluate rutting susceptibility of asphalt binder and the release of AASHTO M332, which separates climate and traffic factors are two responses to these shortcomings. The MSCR test itself finds its merit because it subjects binders to larger deformations than the AASHTO T315 experiment. At these deformations the polymer network is activated and clearer differences between polymer and non-polymer modified asphalts emerge. Various researchers have demonstrated that the material properties measured from the MSCR test provide better correlation to rutting behavior than the current stiffness measure incorporated into AASHTO M320 [141-145]

The primary test parameter resulting from the AASHTO and ASTM MSCR experiment is the non-recoverable creep compliance, J_{nr}, which relates the strain response of the sample to the applied stress. A material that deforms by a large amount under a prescribed load has a high J_{nr} (e.g., it is more compliant), while one that deforms very little has a low J_{nr}. For specification, low J_{nr} asphalts would be used for high value applications (interstates, US routes, etc.), higher J_{nr} asphalts would be used for less critical and lower traffic volume applications, and very high J_{nr} asphalts would be avoided altogether. Another important parameter that is characterized in the MSCR test is the percentage of total strain that is recovered when the applied stress is removed, R. More elastic asphalts will recover

more of the total strain and thus have high *R* values, while more viscous asphalts will recover less and have low *R* values.

The *R* value is used to confirm the presence of polymer additives using a function to relate the *R* after the 3.2 kPa stress level in the MSCR test, $R_{3.2}$, to the J_{nr} after the 3.2 kPa stress level, $J_{nr3.2}$. In theory, at the same J_{nr}, polymer modified asphalt will demonstrate a considerably higher level of recovery than unmodified asphalt due to the elasticity imparted by the polymer network. In the AASHTO M332 standard the relationship shown in Figure 7-1 is provided for verifying the presence of polymer modification. Note that Figure 7-1 shows two functions, one truncated to 55% recovery at a $J_{nr3.2}$ of 0.1 kPa^{-1} and the other that continues to 100% recovery. The continuing function was originally proposed based on experimental data on the degree of cross-linking observed in asphalt binders at different polymer modification levels with the level of $R_{3.2}$. However, only data until $J_{nr3.2}$ of 0.1 kPa^{-1} was used and some have proposed to eliminate the extrapolation, hence the truncated curve [146]. Both are shown here and in subsequent figures because as of this writing there exists no firm consensus on the best method to use and some agencies choose to extrapolate the function at lower J_{nr} values and some choose to truncate at 0.1 kPa^{-1}. Also note that this relationship has only been observed when J_{nr} is between 2 kPa^{-1} and 0.1 kPa^{-1}.

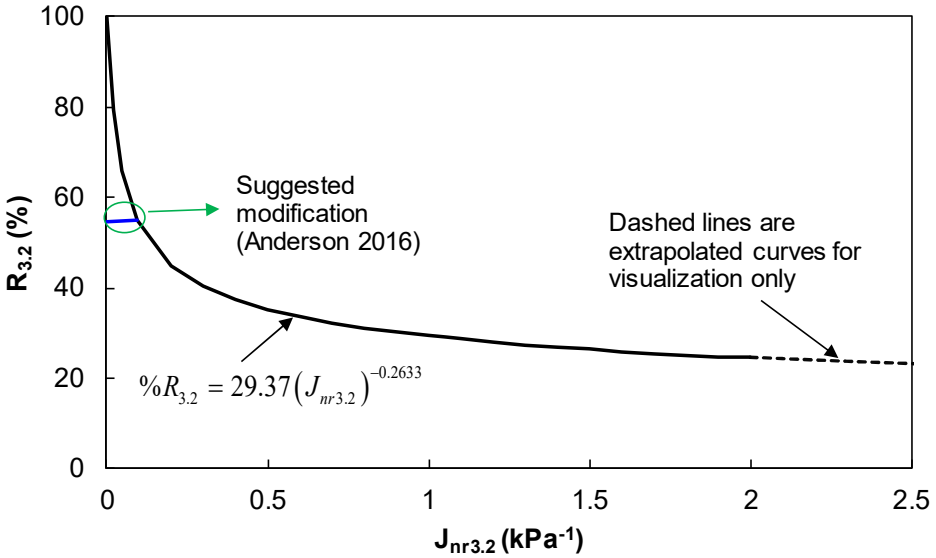

Figure 7-1 AASHTO M332 $R_{3.2}$ Line for Identifying Modified and Non-modified Asphalt.

7.3 Objective

The main objective of this paper is to identify how the $R_{3.2}$ value alone relates to the performance of asphalt concrete mixtures.

7.4 Materials

7.4.1 Asphalt Binders

In this study, nine polymer modified binders were used; seven of those were lab blended asphalts, and two asphalt binders were sourced from two asphalt suppliers in Arizona. The seven polymer modified asphalts were prepared at the Arizona State University laboratory using a high shear mixer. The polymer lab-blended asphalts were prepared by blending a base asphalt binder, PG 58-28, with various dosages of SBS polymer, sulfur, and polyphosphoric acid (PPA). The linear SBS polymer was blended with the base binder at a temperature range of 195-200°C for 1.5 hours using a high shear mixer at 6000 rpm. After

1.5 hours, the temperature was lowered to 178°C, and the mixing speed reduced to 3300 rpm. At this point sulfur was added and the blending was continued for 1.0 hour. Next, PPA was added, and the blending was continued for yet another 30 minutes. If PPA or sulfur were not blended, then the process stopped after the 1.5 hour blending at 6200 rpm. At the end of the blending, the samples were poured into smaller tins for storage to be used for asphalt mixture preparation. The speed for the mixing process, was chosen such that no vortex formed while shearing, as this occurrence could result in oxidation of the asphalt. To confirm that the mixing process itself did not introduce any aging effects, the entire process was performed with just PG 58-28 binder (e.g., without adding SBS, sulfur or PPA). Samples were taken at various time intervals throughout the mixing process, and in each case no increase in stiffness was observed. For the supplier provided asphalts the letter designation conveys the supplier and the number has no significance to the current study. The naming convention adopted for the lab blended asphalts conveys the SBS dosage rate (the number) and whether PPA was included (A = 0%, B = 0.5%, C= 1%, and D = 1.5%). Also, there exist two binders which have a suffix "B" attached to their binder designation. These binders were sampled after adding sulfur and shearing for 0.5 hr. There is no PPA in these binders.

Initial trials showed that it was impossible to create asphalts with precisely the same $J_{nr3.2}$ and varying recovery so asphalts were divided into four groups, J, K, L, and M based on the similarity of their $J_{nr3.2}$ value at 64°C. The ranges of $J_{nr3.2}$ for the four groups were (J) $J_{nr3.2} < 0.1$; (K) $0.1 < J_{nr3.2} < 0.5$; (L) $0.5 < J_{nr3.2} < 1.5$ and (M) $1.5 < J_{nr3.2} < 2$. The

asphalts, their compositions, binder grades, notations, and $J_{nr3.2}$, $R_{3.2}$, shear modulus, $|G^*|$, and phase angle, δ, values at 64°C are listed in Table 7-1.

Table 7-1 Characteristics of Polymer Modified Asphalts Used in the Study

Group	Notation	Weight Percentage (%)				PG Grade		$J_{nr3.2}$ (kPa^{-1})	$R_{3.2}$ (%)	$\|G^*\|$ (kPa)	δ (°)
		Asphalt	SBS	Sulfur	PPA	AASHTO M320	AASHTO M332				
J	Y5	Provided by Supplier				PG 70-16	PG 70H-16	0.06	92.46	4.21	56.95
	B5	94.417	5.0	0.083	0.5	PG 82-28	PG 76V-28	0.08	73.83	13.94	50.38
K	B2	97.433	2.0	0.067	0.5	PG 70-28	PG 70H-28	0.50	51.60	6.18	63.18
	D0.5	97.983	0.5	0.017	1.5	PG 70-28	PG 70H-28	0.41	41.60	8.22	61.10
L	X3	Provided by Supplier				PG 64-22	PG 64H-22	1.03	47.00	3.29	65.40
	A3-B	96.925	3.0	0.075	0.0	PG 70-28	PG 70S-28	0.84	35.50	5.04	66.35
	A4	96.000	4.0	0.000	0.0	PG 70-28	PG 70S-28	0.86	21.40	6.63	69.70
M	A2-B	97.933	2.0	0.067	0.0	PG 64-22	PG 64H-22	1.70	23.40	6.98	70.41
	A3	97.000	3.0	0.000	0.0	PG 64-22	PG 64H-22	1.90	6.80	4.40	75.53

7.4.2 Mixture

The asphalt mixtures manufactured in the study were prepared as per ADOT's 417 Superpave mix design criteria. The aggregates were sourced from Tucson Arizona and had a nominal maximum aggregate size of 19 mm. In Arizona, it is standard practice to use portland cement as an anti-stripping admixture at 1% by aggregate mass; this was duly added to aggregate before preparation of the mixture. The overall gradation was fine and largely plotted above the maximum density line as shown in Figure 7-2. The ADOT 417 mixture design process was performed on all mixtures and yielded asphalt contents in the range of 5.7-5.8%. The samples for dynamic modulus and axial fatigue were compacted to

an air void content of 6±0.5% and the samples prepared for the Hamburg Wheel Tracking test were compacted to an air void content of 7±1%.

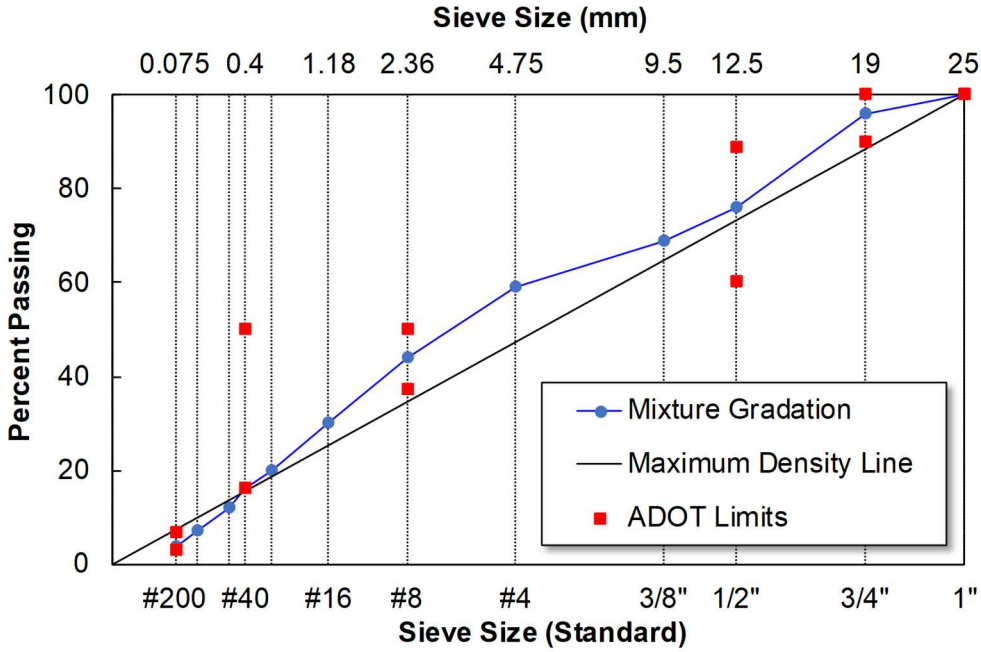

Figure 7-2 Gradation of Study Mixture.

7.5 Experiments

The experimental program for the current study is summarized in Figure 7-3, which includes tests on asphalt binders and asphalt mixtures. Summaries of the most relevant aspects of the test methods as they apply to this study are given below. Though not shown explicitly in Figure 7-3, the other binder tests required for AASTHO M320 and M332 grading (bending beam rheometer and 8-mm dynamic shear modulus testing) were also conducted according to the applicable standards.

7.5.1 Asphalt Binder Experiments

As Table 7-1 demonstrates, the asphalt binder experiments conducted in this study utilized the dynamic shear rheometer (DSR) for determining high temperature linear and non-linear viscoelastic properties of the asphalts. Figure 7-3 also shows that testing has been conducted on asphalt binder at different age conditions. Unaged asphalts were only subjected to initial heating to separate the asphalt from the as-delivered 5-gallon pails into test quantities. For short-term aging AASHTO T240 (Rolling Thin Film Oven, RTFO) has been carried out.

7.5.1.1 Percent Recovery and Non-Recoverable Creep Compliance

The MSCR test was conducted according to AASHTO T350 at RTFO age condition. A sample of asphalt 25 mm in diameter and 1 mm thick is situated between two parallel plates mounted to a DSR; the sample was conditioned to a fixed and specified temperature and loaded repeatedly with a series of square shaped stress-rest pulses (1 second loading and 9 seconds rest) at 0.1 kPa and 3.2 kPa. For each loading cycle the initial strain (ε_0), maximum strain at the end of the loading (ε_c), and strain at the end of the recovery portion (ε_r) were recorded. These values were used to calculate four parameters, the non-recoverable creep compliance at 0.1 kPa and 3.2 kPa ($J_{nr0.1}$ and $J_{nr3.2}$), the percentage of difference between these two quantities (J_{nrdiff}), and the percent of strain recovery during the 3.2 kPa loading, $R_{3.2}$. The equations used to calculate these parameters and the averaging process are detailed in the standard. The tests were conducted at the AASHTO M320 high temperature grade of the asphalt and at ±6°C, except for the PG 76-XX asphalts, which were tested at 76, 70, and 64°C.

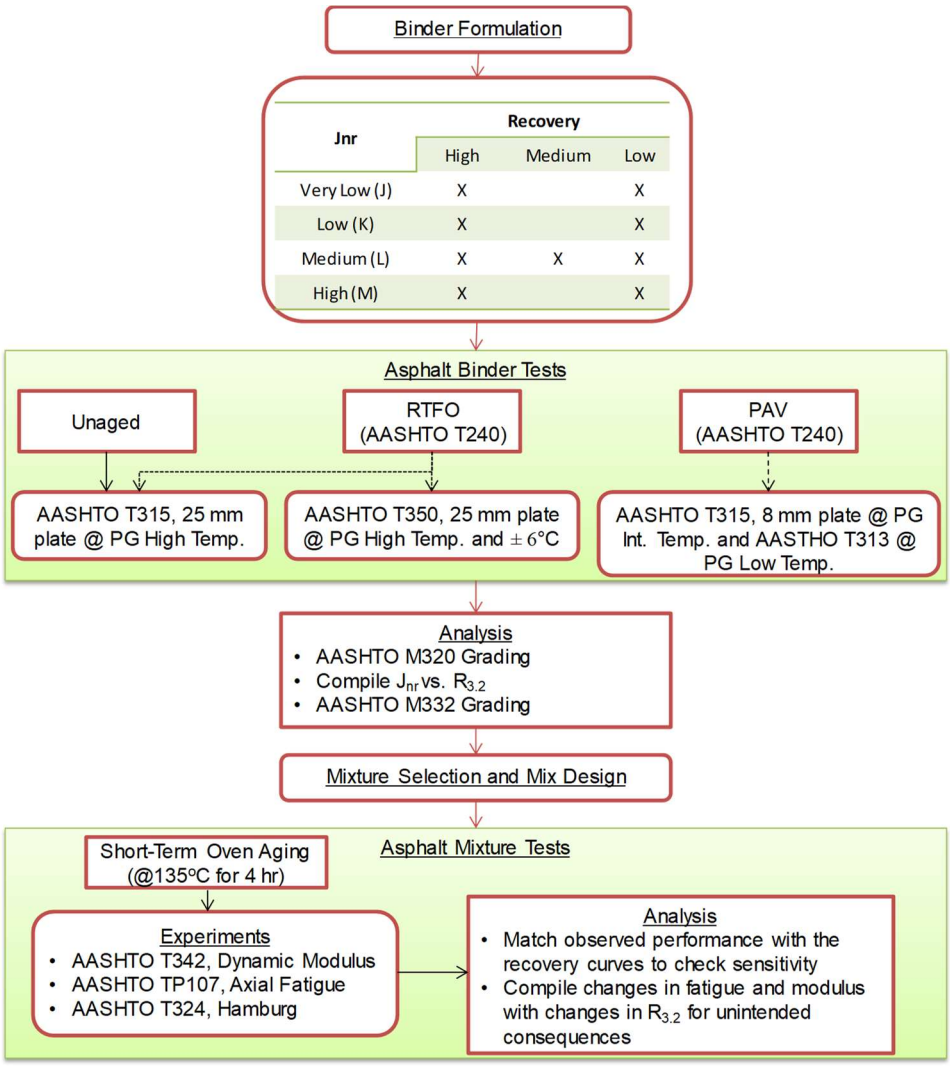

Figure 7-3 Flowchart of the Experimental Program of the Study for the Selected Asphalts.

7.5.2 Asphalt Mixture Experiments

Figure 7-3 shows that AASHTO T342 (dynamic modulus test), AASHTO TP107 (axial fatigue test), and AASHTO T324 (Hamburg wheel tracking test) were carried out on all mixtures. These tests were used to respectively identify the ability of the mixtures to resist deformation, their ability to resist fatigue, and their ability to resist rutting. The sections below highlight the specific details of each test as it is most relevant to the current study.

7.5.2.1 Dynamic Modulus

The axial dynamic modulus, $|E^*|$, test is performed using a servo-hydraulic testing machine and involves repeated sinusoidal loading of a cylindrical specimen along its symmetrical axis. In this study, the protocol given in AASHTO T342 was followed. Test specimens were subjected to cyclic compression loading at frequencies of 25, 10, 5, 1, 0.5, and 0.1 Hz and at temperatures of -10, 4.4, 21.1, 37.8, and 54°C. Tests were conducted in an increasing order of temperature and in a decreasing order of loading frequency. The load was varied with temperature and frequency so that the on-specimen strains remain in the range of 40-60 micro-strains. As per the standard, $|E^*|$ was calculated by sinusoidal regression of the stress and strain responses of the last five cycles of each temperature and frequency combination.

7.5.2.2 Axial Fatigue

The uniaxial fatigue test was conducted according AASHTO TP107 and involves the repeated sinusoidal displacement of a cylindrical sample until it fails. The cylindrical specimen in this study was 150 mm tall and 75 mm in diameter. The test temperature for all mixtures in this study was 18°C. All test results presented in this paper are the result of experiments that failed in within the instrumented region of the specimen. The uniaxial fatigue test was run until a sudden decrease in phase angle was observed.

The tests were conducted at four strain levels, which were estimated such that the material failed in less than 10,000 cycles, between 10,000 - 50,000 cycles, between 50,000 – 100,000 cycles and greater than 100,000 cycles. The fatigue test data was analyzed using simplified viscoelastic continuum damage (S-VECD) theory and model, which is not

repeated here, but is available elsewhere [147,148]. The result of the S-VECD model is the damage characteristic curve or the C vs. S curve. The curves were fitted to a power function shown in Equation (7-1).

$$C = 1 - C_{11} S^{C_{12}} \tag{7-1}$$

While the C vs. S damage curves are good indicators of performance, they alone cannot be considered for the fatigue performance of the asphalt mixtures. For this purpose, fatigue performance simulations were carried out to estimate the strain level that the sample needs to be tested at to fail in 10,000, 100,000, and 1,000,000 cycles. The model form shown in Equation (7-2) was used for this purpose.

$$N_{failure} = \frac{(f)\left(2^{3\alpha}\right) S_{failure}^{\alpha - \alpha C_{12} + 1}}{(\alpha - \alpha C_{12} + 1)(C_{11} C_{12})^{\alpha} \left[(\beta + 1)\left(\varepsilon_{0.pp}\right)\left(|E^*|_{LVE}\right)\right]^{2\alpha} K_1} \tag{7-2}$$

Where:

$N_{failure}$ = predicted cycles to failure,

f = frequency of loading,

$|E^*|$ = dynamic modulus at the frequency and temperature of loading simulated,

α = viscoelastic damage rate (characterized from the dynamic modulus mastercurve),

β = load form factor, taken as 0 in this work to simulate reversed sinusoidal loading,

$\varepsilon_{0.pp}$ = the peak-to-peak strain magnitude for the simulated loading history,

K_1 = loading shape factor, and

$S_{failure}$ = damage level at failure (defined from the experimental results).

7.5.2.3 Hamburg Wheel Tracker

The Hamburg wheel-track (HWT) test, AASHTO T324, is a test method to evaluate the rutting and moisture susceptibility of asphalt mixtures. The equipment consists of a reciprocating wheel, which simulates a moving concentrated load. Test specimens were compacted using the Superpave gyratory compactor and have a diameter of 150 mm. Following ADOT and AASHTO protocols, all tests were performed at a loading frequency of 52 ± 2 passes per minute and for a maximum of 20,000 passes. Each asphalt mixture was tested at a minimum of two temperatures, based on the effective temperature where the asphalt is typically used in Arizona. The effective temperature, T_{eff}, was estimated using the method of El-Basyouny and Jeong with a loading frequency of 10 Hz [149]. Other parameters necessary to estimate T_{eff} by the El-Basyouny and Jeong method were obtained from Pavement Design ME climate files. For the Arizona conditions, these calculations yielded T_{eff} for locations where binders with a high temperature PG grade of 64 is used of between 50 and 44°C, for PG 70 locations T_{eff} was between 50 and 56°C, and for PG 76 locations T_{eff} between 56 and 60°C. It is worth noting that ADOT has been conducting its HWT tests at 50°C, irrespective of the binder grade. So, in line with ADOT practice, mixtures with PG 76S-XX asphalt were also tested at 50°C when possible.

Note that the fact that T_{eff} is not equal to the binder grading temperature reflects an inconsistency in binder characterization and mixture testing. Reasons for this inconsistency are too numerous and detailed to discuss in this paper. Though too detailed to discuss in this paper, it is the authors' opinion that it is important to recognize these differences exist in

order to properly interpret the test results. The approach adopted here is to "match" the binder test results at a given temperature to the appropriate HWT test temperature. The general T_{eff} correlation given earlier is used for this matching effort and suggests the following equivalencies between binder test temperature and mixture test temperature;

- Binder test temperature = 58°C, HWT test temperature = 44°C
- Binder test temperature = 64°C, HWT test temperature = 50°C
- Binder test temperature = 70°C, HWT test temperature = 56°C
- Binder test temperature = 76°C, HWT test temperature = 62°C

7.5.2.4 Specimen Fabrication

All test specimens were compacted using a Servopac Superpave Gyratory compactor. The ram pressure, gyration angle, and gyration speed are 600 kPa, 1.16°, and 30 gyrations per minute respectively. All specimens were compacted with a diameter of 150 mm. Hamburg tests were conducted on the as-compacted samples while dynamic modulus and axial fatigue tests were cut and cored to their final testing geometry. After obtaining specimens of the appropriate dimensions, air void measurements were taken via the AASHTO T166 method, and specimens were stored until testing. During storage, specimens were sealed in bags and placed in an unlit cabinet to reduce aging effects. Furthermore, no test specimens were stored for longer than 2 weeks before testing.

7.6 Results, Discussion and Analysis

7.6.1 Binder

The AASHTO M320 and AASTHO M332 grade of the asphalts were determined using the data obtained from the above-mentioned tests and are summarized in Table 7-1. Figure 7-4 shows the $J_{nr3.2}$ and $R_{3.2}$ values for the binders at 64°C and 70°C. The groupings described earlier are more clearly observed in this figure. Their alignment differs slightly between 64°C and 70°C, but the groupings still align into similar ranges in both.

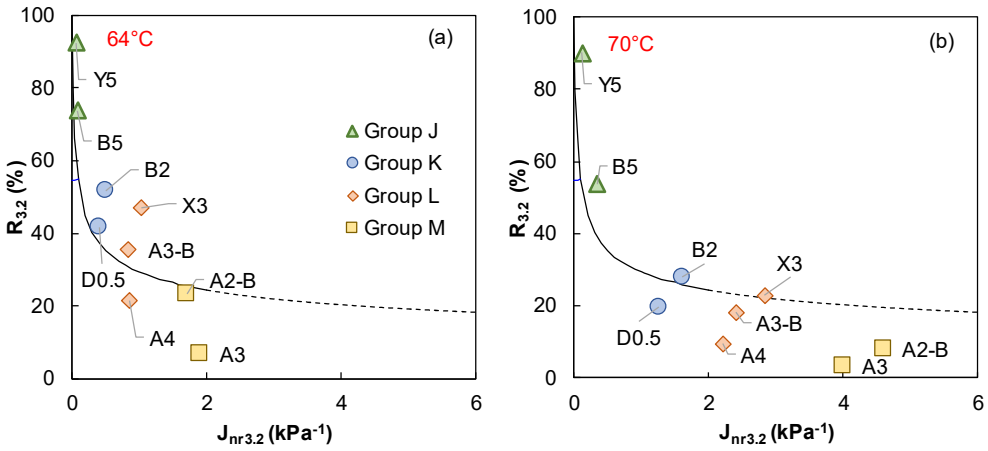

Figure 7-4 Position of the Binders in the $J_{nr3.2}$ vs $R_{3.2}$ at; (a) 64°C and (b) 70°C.

7.6.2 Mixture

7.6.2.1 Dynamic Modulus Test

The results of the dynamic modulus testing are shown in Figure 7-5. These results are labeled with a prefix "T" to indicate that the mixtures were from the Tucson aggregate source and are so named to clearly distinguish mixture test results from binder test results. The binders have been color coded to reflect the group they belong to and the change in the series from solid to dotted line indicates the decreasing level of $R_{3.2}$.

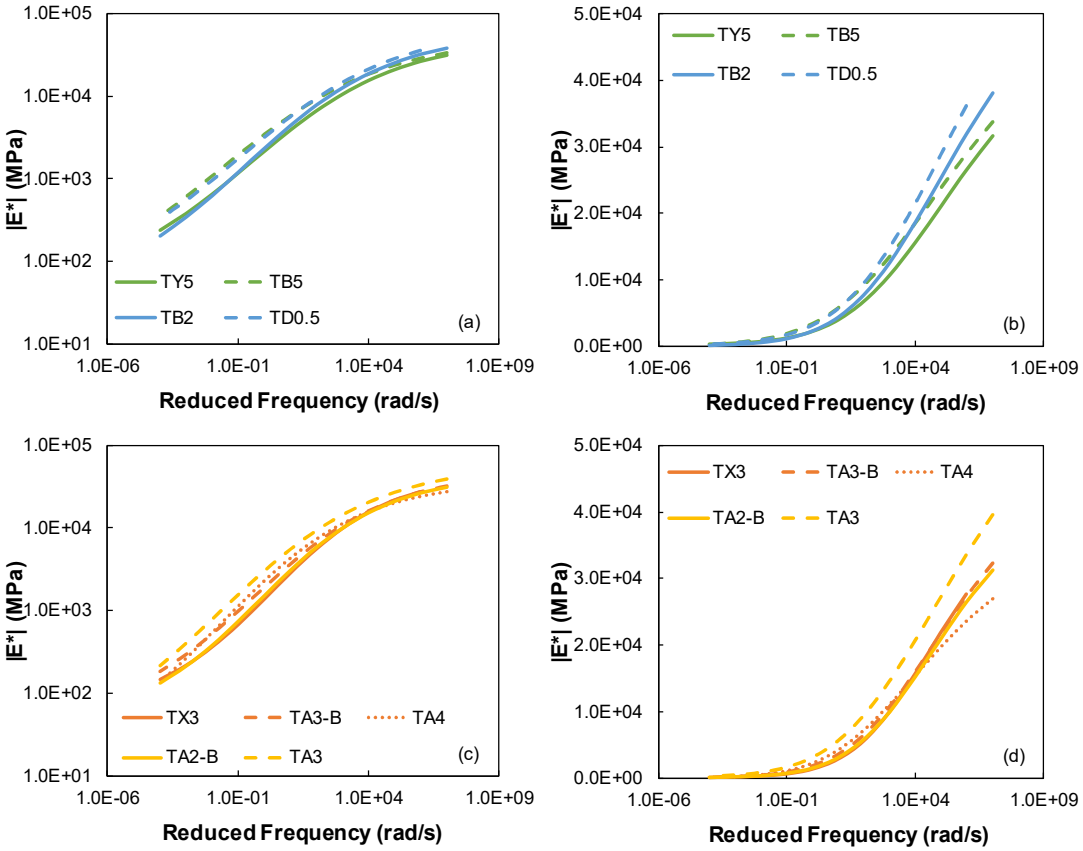

Figure 7-5 Dynamic Modulus Mastercurves for Asphalt Mixtures Prepared Using; (a) Group J and K Asphalt Binders in log-log Scale and (b) in semi-log Scale, (c) Group L and M Asphalt Binders in log-log Scale and (d) semi-log Scale.

Consistent trends across all groups emerge from this analysis. Examining the Group J asphalts as an example, it is seen that TB5 has a higher modulus than TY5 at all temperatures and frequencies. These differences were checked for statistical significance by performing a two-tail t-test at 95% significance level at all five test temperatures at the test frequency of 10 Hz. It was found that the modulus of the two mixtures are only statistically different at intermediate and high temperatures but not at low temperatures, 4.4°C, and -10°C. With regard to the influence of MSCR recovery, a lower $|E^*|$ occurred for the mixtures with higher $R_{3.2}$, as seen with binder Y5, and its corresponding mixture. In all asphalt groups a

statistically significant difference in the high temperature modulus is observed as are correlations between lower moduli and larger $R_{3.2}$. Correlation does not equate to causation, and similar trends emerge when comparisons are made with respect to the linear viscoelastic dynamic modulus, $|G^*|$, measured from the AASHTO T315 protocol. Better correlation between the mixture phase angle (see Figure 7-6) and the linear viscoelastic phase angle are observed than for the $R_{3.2}$ parameter. This is not a surprising finding as the strain levels in the dynamic modulus are low and may not invoke sufficient binder strain to activate the polymer network.

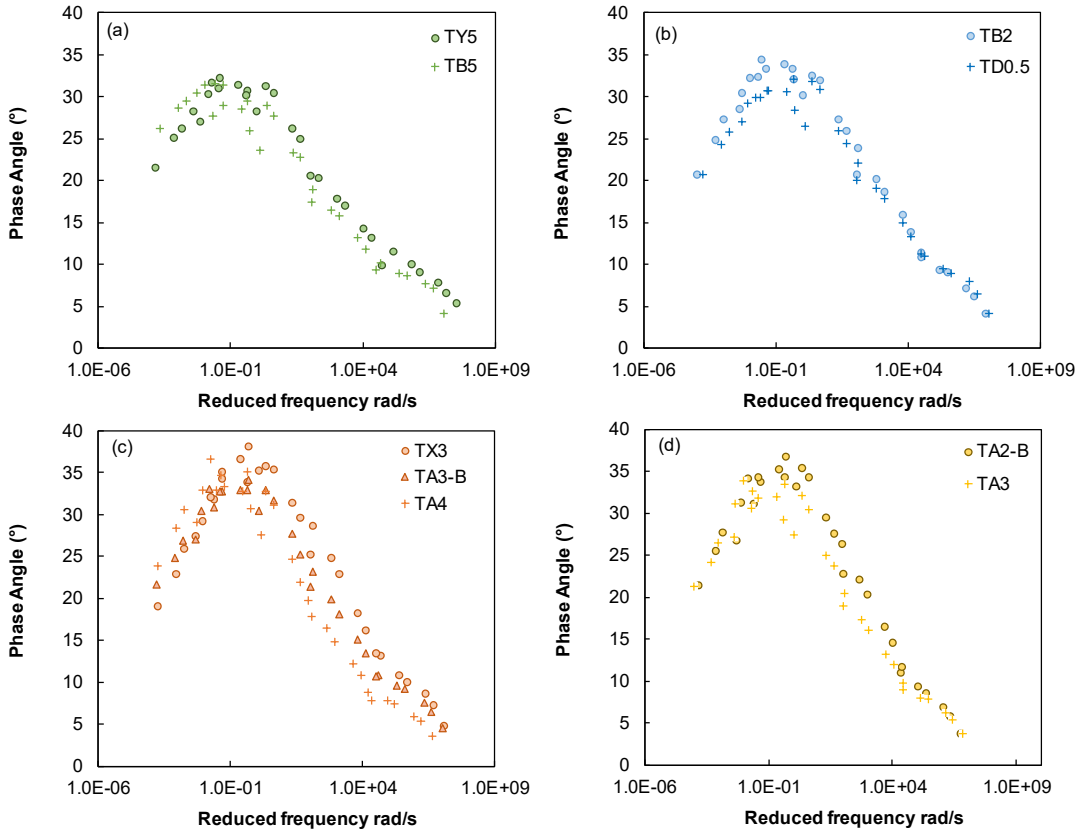

Figure 7-6 Phase Angle Mastercurves for Asphalt Mixtures Prepared Using; (a) Group J Asphalt Binders, (b) Group K Asphalt Binders, (c) Group L Asphalt Binders, and (d) Group M Asphalt Binders.

7.6.2.2 Hamburg Wheel Tracking Test

The rut depths for all nine binders at their corresponding test temperatures are presented in Figure 7-7. Note that for TB5 the test results at 50°C are not shown. Data for this condition was not captured since the rutting at 56°C and 62°C was so small. Binders in group J consisted of two asphalt binders, Y5 and B5. The rut depths at 50°C and 56°C for these asphalts are presented in Figure 7-7 (a) and (b). The error bars shown in the figure correspond to the rut depths achieved at the left wheel and the right wheel and the marker shows the average of these two values.

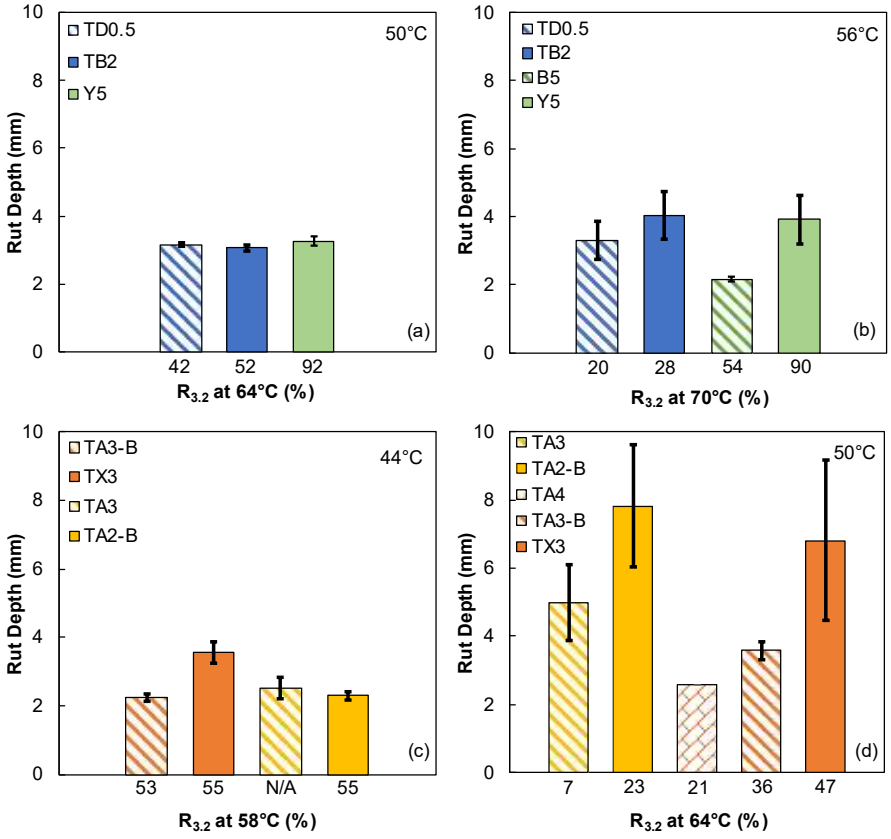

Figure 7-7 (a) and (b) Rut Depth at 50°C and 56°C for Asphalt Mixtures Prepared with Group J and K Binders Respectively, (c) and (d) Rut Depth at 44°C and 50°C for Asphalt Mixtures Prepared with Group L and M Binders Respectively.

For these low compliance asphalts, it is seen that the recovery has little impact on the rut depth that is achieved or does not positively correlate to observed differences in performance. For example, based on the HWT at 56°C, the recovery for Y5 was 92% versus 74% for B5, but the rut depth for Y5 was greater and 3.92 mm versus 2.16 mm. However, a two-tailed t-test shows that there exists no statistically significant difference between the rut depths of the two mixtures.

Further evidence can be obtained in comparing the binders in Group K (B2 versus D0.5). In this case B2 has a higher recovery than D0.5 (52% versus 42% at 64°C and 90% versus 54% at 70°C), but the rut depths of mixtures TB2 and TD0.5 are very similar at both 50°C and 56°C, Figure 7-7 (a) and (b). Statistically there no significant difference between the two rut depths. Similar trends emerge in the Group L asphalts. Notably for these asphalts the HWT tests at 50°C show a reversed correlation, higher $R_{3.2}$ equating to higher rut depths. However, again, there is no statistically significant difference between the mixtures. It is worth pointing here that though the difference between TX3 and TA4 is high, the inherent variability of TX3 is causing the difference to be statistically insignificant. A better repeatability in TX3, will likely make the difference statistically significant.

7.6.2.3 Axial Fatigue Test

The results from the axial fatigue test are summarized in Figure 7-8 in terms of the damage characteristic curve and the predicted fatigue performance. These results are evaluated with respect to $R_{3.2}$ at 64°C to determine whether there exists any evidence that $R_{3.2}$ correlates to the fatigue performance.

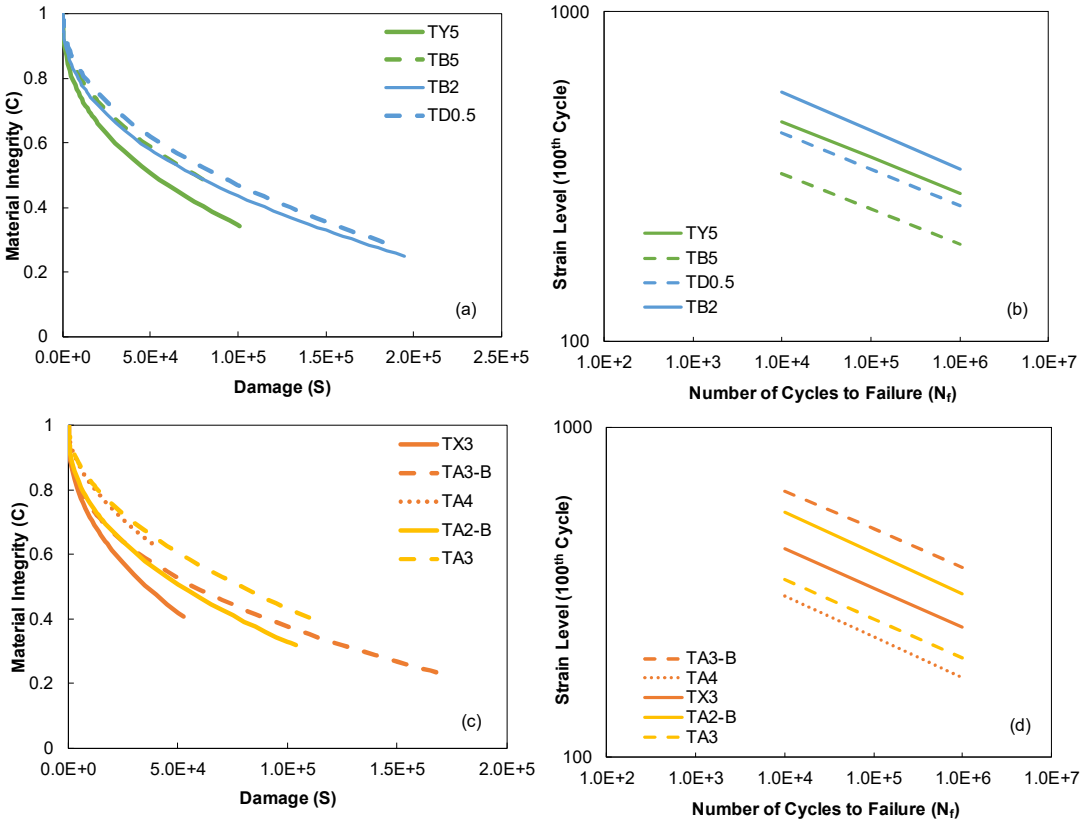

Figure 7-8 (a) and (c) Material Integrity (*C*) vs. Damage (*S*) Damage Curves for Mixtures Prepared with Group J, K and L, M Binders Respectively, and (c), (d) Simulated Fatigue Failure Envelopes for Mixtures Prepared with Group J, K and L, M Binders Respectively.

It is recognized that there exists little intuitive reason why the rheological behaviors of the binder at such high temperatures should relate to the performance of the mixture at intermediate temperatures. It is more intuitive that rheological indices and parameters binder at intermediate temperatures would relate to the mixture fatigue performance. However, it is the objective of this paper to identify whether the $R_{3.2}$ parameter can be shown as an indicator of performance and assess the validity of its use in the binder specification. Based on the results presented thus far with respect to the HWT results, it is not evident that the $R_{3.2}$ parameter and associated threshold value have any direct relevance to load associated

performance. If the same is found with respect to fatigue, then the utility of the threshold function shown in Figure 7-1 may be questionable. Binders in Group J consisted of two binders Y5 and B5. The C vs. S damage characteristic curves, and the fatigue envelopes for the binders in this group are presented in Figure 7-8 (a) and (b). From this figure it can be seen that Y5, which has the highest $R_{3.2}$, also has the best fatigue resistance. Binders in the remaining groups share this same basic trend as is seen in the remaining parts to Figure 7-8. In Group L the trend is not entirely consistent (A3-B shows the highest fatigue performance despite having the second highest $R_{3.2}$). This situation shows the importance of the crosslinking mechanism. Among the three asphalts, the composition of TX3 is not known but TA4 has four percent polymer, and TA3-B has three percent. However, TA4 was not modified with any crosslinking agent, where TA3-B was modified with sulfur. While the exact composition of TX3 is not known, it is known that it has both sulfur and PPA. Overall, even in this group of asphalts the positive effect of MSCR recovery is encountered, and what is more clearly seen is the effect of polymer crosslinking on the performance of these mixtures.

7.6.3 Evaluation of $R_{3.2}$ to $J_{nr3.2}$ Relationship

The experimental results suggest that while the $R_{3.2}$ parameter does not provide a singular indicator of rutting resistance, it does differentiate (for the asphalts in this study) between materials that perform well in fatigue and those that do not. However, it appears that the specific sensitivity of fatigue performance to $R_{3.2}$ varies by $J_{nr3.2}$. To better understand this phenomenon, the S-VECD model was first used to predict the fatigue life at 400 με. There was no particular significance to this number, and the decision to use 400 με has little impact

on the conclusions drawn from the analysis since, as the data in Figure 7-8 (b) and (d) show the fatigue failure curves are largely parallel for the study mixtures. Then, the distance between the observed $R_{3.2}$ and the AASHTO M332 function (see Figure 7-1) was calculated. For this calculation the continuous curve was adopted. This distance was subsequently compared against fatigue life and the results are shown in Figure 7-9. The data shows that in general as the $R_{3.2}$ value gets further from the curve, there is a positive impact on fatigue performance. However, this distance is not a unique function of $J_{nr3.2}$, and in fact the sensitivity in fatigue life to distance shows no obvious trend with respect to the $J_{nr3.2}$ value. Based on the data, the mixtures in the $J_{nr3.2}$ range of 0.1 – 0.5 and 1.5 to 2.0 kPa^{-1} are the most sensitive to changes. In short, while the distance from the existing curve does offer some insight, it alone does not appear to provide enough information to assess if and how any modifications to the curve should be carried out.

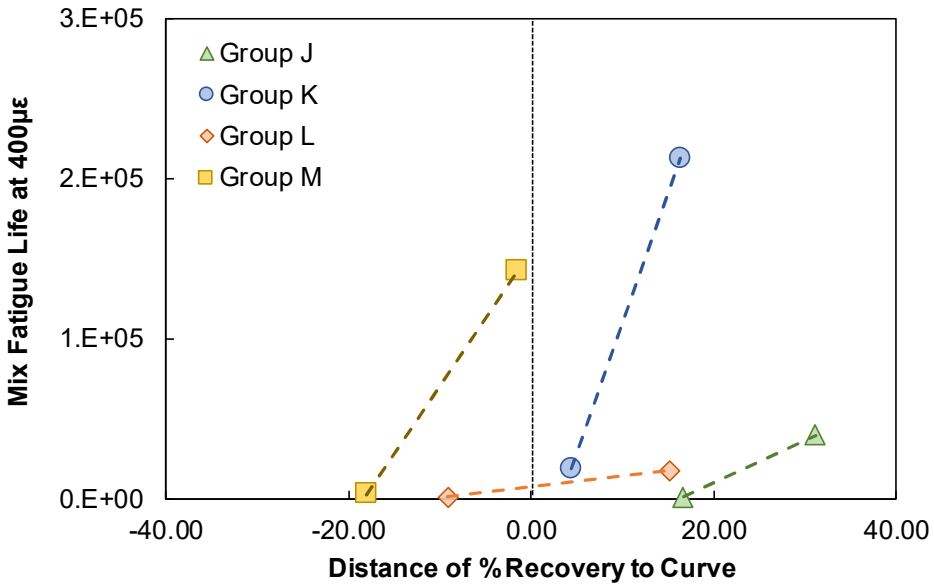

Figure 7-9 Relationship between Mixture Fatigue Life and Distance of $R_{3.2}$ Value of Binders from the $J_{nr3.2}$ vs $R_{3.2}$ Curve.

Next, the typical behaviors for Arizona asphalts in the $J_{nr3.2} - R_{3.2}$ domain are examined as shown along with the AASHTO M332 threshold curve in Figure 7-10. These results are obtained from quality control tests on binders supplied to the state and were conducted by ADOT at the AASHTO M320 high test temperature (e.g., PG 76-22TR+ was tested at 76°C). This data is referred to as the historical database and the details can be found elsewhere [150]. The PG 76-22 TR+ and PG 70-22 TR+ are polymer modified asphalts while the others contain no polymer additives.

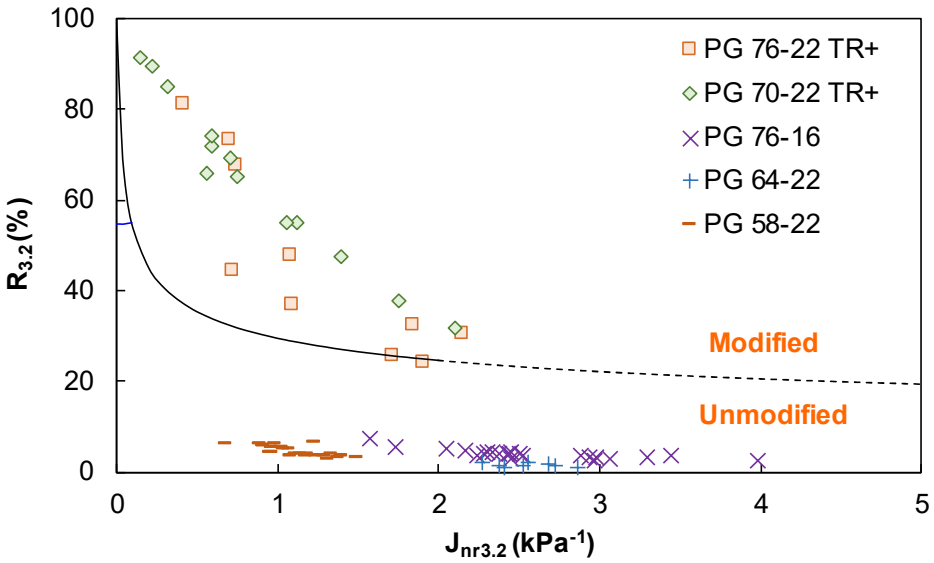

Figure 7-10 AASHTO M332 $R_{3.2}$ Line with Modified and Non-modified Arizona Asphalt.

It is very apparent from this figure that the polymer modified asphalts demonstrate considerably higher $R_{3.2}$ values than their non-polymer modified counterparts. It should be mentioned, that in Arizona polymer modified asphalts are specified based on the content of SBS (2% minimum), an elastic recovery test conducted at 10°C, and a minimum required phase angle at the high PG temperature. It is also evident from this graph that many of the asphalts currently purchased by ADOT have $R_{3.2}$ values located well-above the threshold

curve. Given the data shown above, this distance raises the possibility that adoption of the relationship as given in AASHTO M332 might lead to the acceptance of asphalt binders that are inferior to what the agency is currently obtaining.

Figure 7-11 supplements what is shown in Figure 7-10, by including results from many recently tested ADOT binders as well as the data from the historical database, and by segregating the test results by temperature and grade [150]. The recently tested ADOT binders were tested according to the same protocols explained earlier in this paper and are labeled in the figure according to their as supplied grade and the generic supplier designation (X, Y, or Z) in parenthesis. To differentiate the data sources in these figures those obtained from the historical database are labeled with HD in the figure legend. The data shows that like the historic database, most polymer modified binders that are supplied, or might be supplied, under an AASHTO M332 system currently plot well above the threshold curve regardless of the temperature. There are two additional pieces of information to discuss with this figure. First, is the existence of a second line (colored in light gray), which will be discussed in the coming paragraphs and is shown here to reduce duplication of figures. The second item to note from Figure 7-11 (b) is the behavior of the HD_PG 76-16 data series. In this figure, the $J_{nr3.2}$ and $R_{3.2}$ are those measured at 64°C and demonstrate how non-polymer-modified binders can be positioned nearer to the threshold by reducing the test temperature. Although not shown in detail here, the PG 76-16 asphalts shown in the graph would grade as PG 64E-16 asphalts. The experimental results in this paper suggest that even though the binder would be graded as an “E” grade it would likely not perform as well in fatigue as another asphalt with the same $J_{nr3.2}$ value, but higher $R_{3.2}$.

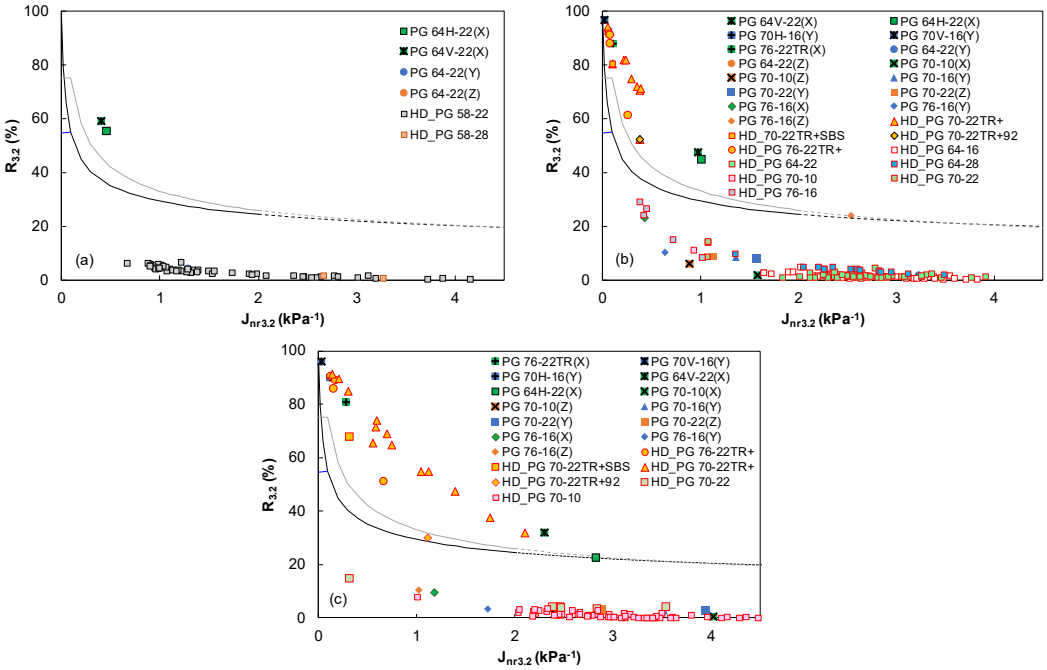

Figure 7-11 Comparison of Study Binders and Historical Data in the Modified $J_{nr3.2}$ vs $R_{3.2}$ Space at; (a) 58°C, (b) 64°C, and (c) 70°C.

To summarize the totality of the observations thus far;

1. The published $R_{3.2}$ threshold limit was established with studies demonstrating the formation of distinct structures in polymer modified asphalts.
2. In this study and historically, currently supplied asphalts lie above the published $R_{3.2}$ line and often well-above the curve.
3. Higher $R_{3.2}$ correlates to better fatigue resistance. The improvement in fatigue resistance increased with higher $R_{3.2}$.
4. This relationship is specific to J_{nr} values, meaning that there is no fixed $R_{3.2}$ for all binders at all J_{nr} values. Asphalts with lower J_{nr} values required greater $R_{3.2}$ to show similar fatigue performance benefits.

5. Parallel to these issues it is also found that non-polymer-modified binders tested at a temperature resulting in a "low" J_{nr} may have high $R_{3.2}$. This can occur when testing non- polymer-modified binders at a low temperature in combination with PPA or possibly other modifiers. Thus, the positioning of the $R_{3.2}$ line should be reasonably high to avoid such circumstances. Asphalt suppliers do not reveal their specific formulations but do acknowledge that some asphalts in the database here do use PPA.

With these issues in mind, it is believed that there may exist a different and alternative function that would better account for the performance benefits of higher $R_{3.2}$. While the data available is informative it cannot be used exclusively to define this curve because the spacing of $R_{3.2}$ values is limited (only two or three values per J_{nr} value). Thus, a rational approach based on the preponderance of data along with consideration of the issues identified above is adopted to define a potential alternative function. The changes should certainly consider the experimental results above, they should also consider a workable specification that suppliers could meet (for example expecting 100% recovery at all $J_{nr3.2}$ values would be unreasonable), that there is no greater potential for falsely identifying a non-polymer modified asphalt as modified, and that the changes do not undermine the original morphological observations made when establishing the curve that is presented in the AASHTO M332 standard. The rationale adopted here to define such a revised curve is to set the limit such that the binder with the lowest recovery within each group just meets the modified specification. Two exceptions were made. For Group L binders, A3-B is used as the lowest recovery binder as A4 is already below the existing specification. For Group

M binders, since both A2-B and A3 are already below the existing specification, effort was made to match the modified curve to the existing curve for this range of $J_{nr3.2}$ onwards. Even though the performance of the A2-B asphalt was good, it was felt that the proposed curve should not go below the existing function to prevent non-polymer modified asphalts, which are tested at lower than normal temperatures and/or are modified with PPA from passing the limit.

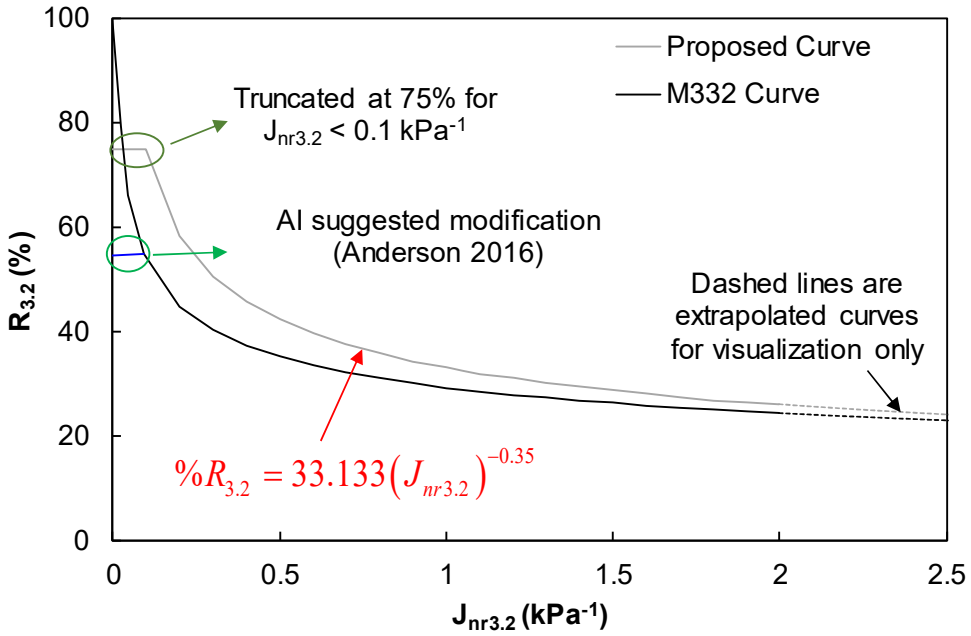

Figure 7-12 Modified $J_{nr3.2}$ Versus $R_{3.2}$ Curve.

Another question is how to handle data at J_{nr} values smaller than the observed dataset. While the curve for low $J_{nr3.2}$ asphalts can be extended to 100%, this would eliminate many asphalt binders that have purportedly good performance, see Figure 7-10 and Figure 7-11. Thus, the alternative curve is truncated based on the adjusted curve value at $J_{nr3.2}$ equal to 0.1. This value is 74%, which based on the evidence in Figure 7-9, it can be confirmed that binder

having $R_{3.2}$ less than 74% will see an increase in fatigue performance. For convenience, this value was extended slightly and a truncation value of 75% was adopted. The suggested function is shown, along with the one currently included in the AASHTO M332 specification in Figure 7-12. The modified curve is also shown against the historical database and the recently tested binders in Figure 7-11, which shows that the modified curve still permits passing of most modified asphalt binders. Again, it is noted that these asphalts have a history of good performance. The authors believe that this curve better balances the need for assessment of binder modification with the desire to ensure asphalts that are currently available continue to perform as expected.

7.7 Conclusions

The following conclusions are made from this study;

- The mixture dynamic modulus and phase angle are proportional to the binder $|G^*|$ and δ.
- The mixture |E*| is inversely proportional to $R_{3.2}$ provided two binders have a similar $J_{nr3.2}$ while the phase angle of the mixture shows no relationship with $R_{3.2}$.
- There is no statistically significant difference to suggest that $R_{3.2}$ has an effect on rutting performance. Instead, the rutting resistance of the above mixtures was more closely related to $J_{nr3.2}$ and $|G^*|/\sin\delta$ of the binder.
- The $R_{3.2}$ value shows a direct proportionality to the fatigue resistance of asphalt mixtures, with the precise impact being dependent upon the value of $J_{nr3.2}$.

- Many current and likely future polymer modified asphalts have $R_{3.2}$ values that are positioned substantially higher than the current AASHTO M332 relationship between $R_{3.2}$ and $J_{nr3.2}$.

Based on these experimental conclusions, a modified $R_{3.2}$ to $J_{nr3.2}$ function was presented. This modified function represents a slight adjustment to the published version and is believed to better reflect the currently observed benefits of polymer modification. The goal for the modification is to set the limits so that there are no obvious likelihoods that binder performance will be negatively affected by adoption, while at the same time creating a realistic limit that can be met.

Chapter 8. HMA LABORATORY FATIGUE AND EQUIVALENT METHODS TO ESTIMATE ASPHALT BINDER FATIGUE IN THE LAB.

In the previous two chapters, the results and the relationship between asphalt rutting binder parameters and asphalt mixture rutting tests were discussed. In this chapter, the results and connections between the binder fatigue parameters and axial fatigue test will be addressed. The discussions have been segmented into three main parts. The first part deals with the fatigue binder properties of the study asphalts deduced from the temperature-frequency test are and linear amplitude sweep (LAS). In the second part, the axial fatigue test was performed to assess the resistance of the current Arizona asphalt mixtures to fatigue damage. Also displayed in this part the fatigue test data results for all the mixtures using simplified viscoelastic continuum damage theory (S-VECD) formulation. Finally, different binder fatigue predictive methods will be used and a detailed discussion on the relationship between the mixture fatigue and fatigue binder parameters are presented.

8.1 Background

The binder fatigue parameter, $|G^*|\sin\delta$ introduced during the SHRP work is based on small strain rheology and does not consider damage resistance. Therefore, the Linear Amplitude Sweep Test (LAS) was proposed in order to reflect a performance-based assessment of binder fatigue resistance and to act as a surrogate to the time sweet test, which is a conventional fatigue test with repeated cyclic loading at constant strain amplitudes. One of the drawbacks of the time sweep test, which prevents it from being considered for specification, is the uncertainty in test duration. The linear amplitude sweep (LAS) test is a strain controlled cyclic torsion test conducted on a dynamic shear rheometer at a fixed

frequency, loading cycles and incrementally increasing strain levels [151]. The test is run at 10 Hz, with 1% strain increments from 0% to 30%) and a total of 3000 cycles are applied, this means the test is essentially completed in five minutes. The uncertainty in duration with the time sweep test was overcome with the LAS test, which has fixed loading cycles. The damage characterization conducted in the LAS test is in the AASHTO similar to the time sweep test which considers simplified viscoelastic continuum damage (S-VECD) formulation. The S-VECD fatigue model was reviewed at the beginning of this study, but it was difficult to use the model to correlate binder test data to fatigue performance of asphalt mixtures having a wide range of stiffnesses and being tested at multiple strain levels and failure criteria than the one used for Mixture fatigue. The NCHRP 9-59 research team discovered a new approach for asphalt binder fatigue analysis called the general failure theory for asphalt binders (GFTAB). The theory will be explained in detail in the analysis section. The LAS data was analyzed as a fatigue test, using GFTAB.

8.2 Methodology and Testing

This study was divided into three main phases as follows:

Phase 1: Binder fatigue performance of the study asphalt binders will be investigated conducting the LAS test along with evaluating $|G^*|\sin\delta$ parameter.

Phase 2: Mixture fatigue performance was investigated using Axial Fatigue test and analyzed considering simplified viscoelastic continuum damage (S-VECD).

Phase 3: In order to investigate the correlation between the binder and mixture fatigue performance. Group 1 and Group 2 mixtures were used in the analysis herein. These mixtures were produced using neat binders and polymer modified binders as shown in the

Chapter 3. The optimum binder contents were obtained using super pave mix design with a target air void of 5%. The optimum binder content of the study mixtures was within the range of 5.2%–5.8%. The Axial Fatigue specimens were compacted at their corresponding optimum binder contents using a gyratory compactor. All of the specimens had an air void content within the range of 6.5% ± 0.5%.

8.2.1 $|G^*|\sin\delta$ parameter

According to AASHTO T315 [55], the $|G^*|\sin\delta$ parameter is evaluated using the Dynamic Shear Rheometer (DSR) at the frequency of 10 rads (1.6 Hz). An 8-mm-diameter plate with a 2-mm testing gap or a 25-mm-diameter plate with a 1-mm testing gap is utilized in this test. The selection of the testing geometry is based on the operational conditions, so that generally the 25-mm plate geometry is being used at high temperatures (46–82°C) and the 8-mm plate geometry is being used at low and intermediate temperatures (13–31°C). According to AASHTO T315, to control the fatigue cracking of asphalt binder, $|G^*|\sin\delta$ should be less than 5000 kPa for aged binder obtained from Rolling Thin Film Oven (RTFO) and Pressure Age Vessel (PAV) tests. This test has been done for all study binders.

8.2.2 The LAS test

8.2.2.1 Performing LAS Test

The LAS test evaluates the ability of asphalt binder to resist fatigue damage. Basically, this test is an oscillatory strain sweep test that generates damage to the binder by applying linearly increasing load amplitudes. The LAS test consists of two steps: first, a frequency

Sweep is performed in order to get information about undamaged material properties and evaluate the rheological characteristics of the binder. Second, the damage characteristics of the binder is measured employing a linear amplitude strain sweep test.

In this study, frequency sweeps were conducted at a strain amplitude of 0.1% with a range of frequencies from 0.2 to 30 Hz according to AASHTO TP101 [56]. Amplitude sweep test was done at a constant frequency of 10 Hz. The testing protocol consisted of applying a linearly increasing load from zero to 30% over 3100 cycles of loading. All tests were conducted using DSR device with an 8-mm diameter parallel plate and a 2-mm gap. The test was carried out on PAV aged binders at 18^{o}C in accordance with study by Safaei and Castorena 2015. The study concluded that the test temperatures should be selected such that linear dynamic shear moduli falls within the range of 12 and 60 MPa to avoid the confounding effects of flow or adhesion loss. [57]. Two replicates were performed for each binder.

8.2.2.1 LAS Test Analysis

There are two way to analysis LAS Test; using simplified viscoelastic continuum damage (S-VECD) formulation (AASHTO TP 101-12) or general failure theory for asphalt binders (GFTAB) method (suggested by NCHRP 9-59 research). The analysis for both methods will be reviewed herein, but the LAS data was analyzed using GFTAB. For the reason, it was difficult to use the S-VECD model to correlate binder test data to fatigue performance of asphalt mixtures.

8.2.2.1.1 LAS Test Analysis by S-VECD Formulation

To determine the number of cycles till fatigue failure, Eq. (8-1) is used. The fatigue failure in the LAS test occurs when the initial stiffness is reduced by 35% [58].

$$N_f = A(\gamma_{max})^B \tag{8-1}$$

Where: A and B: Material characteristics dependent coefficients of the VECD model. A is the ability of the material to maintain its integrity during loading cycles and due to accumulated damage. This parameter is associated with the storage modulus. It decreases with the decrease of the storage modulus during loading cycles. From Eq. (8-1), when the strain level is equal to 1, the fatigue life will be equal to A parameter, hence, A parameter can be considered as the fatigue life of the binder at a strain level of 1 (100%). The sensitivity of the asphalt binder to strain level change is described by B parameter. Higher absolute values of B parameter indicates that the fatigue life decreases at a higher rate when strain level amplitude increases. In general, more fatigue resistant binders tend to have higher a values and lower absolute B values [59].

8.2.2.1.1 General Failure Theory for Asphalt Binders (GFTAB) Method

The GFTAB model relies on the failure of the material rather than its damage accumulation [152]. This is due to the fact that pavement failure, for design purposes, is more critical than its damage accumulation. Using this concept, the number of cycles till fatigue failure is determined from the fatigue strain capacity (FSC) value, which is defined as the fatigue life at the maximum strain level, as shown in Equation (8-2). In this equation, the average binder strain inside the blend, is estimated by the ratio of the strain to the effective binder content.

$$N_{failure} = \left(\frac{(FSC)(VBE/100)}{\varepsilon_t} \right)^{k_1(90/\delta)} \quad (8\text{-}2)$$

Where:

FSC = binder fatigue strain capacity, %

VBE = mixture effective binder content, volume %

ε_t = mixture maximum tensile strain, %

k_1 = fatigue exponent coefficient

δ = binder phase angle, degrees

The general model explained in Equation (8-2) was used later to relate binder fatigue to mixture fatigue. Equation (8-2) also indicates that the material failure occurs when the measured binder strain is equal to the fatigue strain capacity, which means, the material will fail in one cycle. According to Christensen [152].

> *"In practical terms, this means that FSC should be closely related to measures of binder failure strain. However, the binder inside the mixture, is severely confined and also contains numerous flaws and stress concentrations, so it is possible that FSC and failure strain might be highly correlated but significantly different in magnitude."*

Equation (8-2) can be rearranged to tackle a number of issues in the evaluation of asphalt binder and mixture fatigue and fracture data, as shown in Equation (8-3).

$$FSC = N_f^{k_1/2(90)} \left(\varepsilon_t \frac{100}{VBE} \right) \quad (8\text{-}3)$$

Where the parameters as was defined above in Equation (8-2). For a certain fatigue test where the strain is held constant, Equation (8-3) can be used to estimate the value of *FSC*. When the applied strain level is not constant, the following damage function is used:

$$D=\sum_{i=1}^{n} N_i \left(\frac{\left(\varepsilon_t\right)_i}{FSC_i} \times \left(VBE/100\right) \right)^{2(90/\delta)} \tag{8-4}$$

Where

i: loading segments where the values of ε_t and *FSC* are approximately equal.

At failure, When the damage using Equation (8-4) = 1, Equation (8-5) is used to determine *FSC*.

$$FSC=\left(\sum_{i=1}^{n_f} N_i \left[\frac{\left(\varepsilon_t\right)_i}{\left(VBE/100\right)} \right]^{2(90/\delta)} \right)^{\delta/2(90)} \tag{8-5}$$

Where

n_f : the total loading cycles to failure.

8.2.2.1.1 LAS Test Analysis by GFTAB Method

Equations (8-3) through (8-5) can be utilized to calculate *FSC* values for linear amplitude sweep (LAS) tests.by replacing the term (*VBE/100*) to be equal to one. Thus, Equation (8-5) can be re-written as indicated in Equation (8-6).

$$FSC=\left(\sum_{i=1}^{n_f} N_i \left[\left(\varepsilon_t\right)_i \right]^{2(90/\delta)} \right)^{\delta/2(90)} \tag{8-6}$$

Under a range of different temperatures and loading rates, the plot of FSC as a function of binder modulus is a well-defined failure envelope. This relationship was reported in the

literature by Heukelom, and supported with measured data later in NCHRP 9-59 [152]. Figure 8-1 shows the Heukelom's proposed failure envelope, using data from both Heukelom's and NCHRP 9-59 studies. In addition, other binder direct tension data from different research projects are used. The typical FSC values -as used to define the general failure envelope- are denoted as FSC* and should be estimated using Equation (8-7).

$$Typical\ FSC^{*} = \frac{1}{\left(6.56\times10^{-3}\,S(T,t)^{0.0482} + 1.35\times10^{-9}\,S(T,t)^{1.10}\right)} \tag{8-7}$$

Where

$S(T,t)$ = Initial stiffness of the asphalt material.

FSC^{*} = Typical failure envelope.

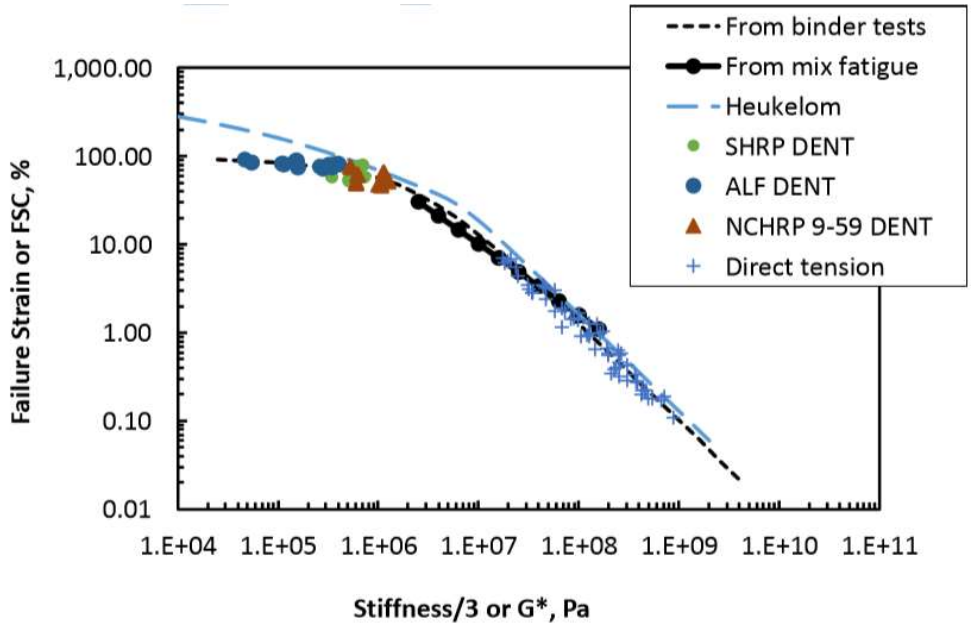

Figure 8-1 Binder Failure Envelopes as Proposed by Heukelom (1966) and as Found during NCHRP 9-59, Using Various Binder Tensile Tests, along with the data gathered in other research projects [152].

Not all binders have an FSC values with the expected binder failure envelope. For example, many polymer-modified binders have *FSC* values higher than the typical binders [152]. The rheology of the binder also affects the *FSC* value significantly. The fracture/fatigue performance ratio (*FFPR*) is defined by the deviation of a particular binder from this typical failure envelope as shown in Equation (8-8).

$$FFPR = \frac{FSC_{binder}}{FSC_{Typical}} = \frac{FSC}{FSC^{*}} \tag{8-8}$$

Where:

FFPR = defined as the ratio of observed to expected failure strain.

FSC = Binder fatigue strain capacity value calculated for a specific binder.

*FSC** = Binder fatigue strain capacity value for typical failure envelope.

When *FFPR* is greater than one, the binder will have a good fatigue performance, and when it is lower than one, the binder will have a poor performance.

The LAS data was analyzed as a fatigue test, using a variation of Equation (8-9). This equation was formulated by substituting Equation (8-6) in Equation (8-8).

$$FFPR = \frac{1}{4.8 \times FSC^{*}} \left(\sum_{i=1}^{n_f} N_i \left[\gamma_i \right]^{K_1/(\delta/90)} \right)^{\delta/2(90)} \tag{8-9}$$

Where the variables are as described for equations above, except that shear strain γ is now used rather than extension strain ε. Equation (8-9) was divided by 4.8, to account for the conversion of shear strain to extensional strain (factor of 3), and a LAS test geometry calibration factor (1.6).

Defining material failure under fatigue loading is always challenging. Ideally, fatigue failure must be defined based on physical characteristics of intensity and distribution of damage within the material body. On the other hand, it is unrealistic, if not impossible at all, to capture and monitor material's internal physical state during loading. Researchers and practitioners have commonly adopted the alternative definition from phenomenological perspective. One of the fatigue failure definition is the drop of phase angle, which adopted herein to analyze both binder and mixture fatigue.

8.2.2.1 LAS Test Results

For group 1 binders the test was performed at 18ºC by using AASHTO TP 101-12 for PAV aging condition. However, the LAS data was analyzed using GFTAB method described above. The frequency sweep and LAS parameters are tabled in Table 8-1. From the table, it is noted that all FFPR value of Group 1 are less than one. This is an indication of poor fatigue or fracture performance for all Group 1. The relationship between both FFPR and FCS^* with the initial complex sheer modulus at 10 Hz and 18ºC was graphed in Figure 8-2. As observed from the figure that the strain capacity decreases substantially with increased modulus, which can also result in decreased fatigue life at higher strain levels. In general FFPR is lower than one for all Group 1 binders.

Table 8-1 Frequency Sweep and LAS Parameters for Group 1 Binder

Mixture		Frequency Sweep at 10 Hz and 18°C		FCS*	$FFPR_f$	FCS
		Complex Modulus (G*) [Pa]	Phase Angle [°]			
X1	S1	6.5E+07	29.61	1.838	0.882	1.620
	S2	6.4E+07	29.56	1.864	0.856	1.595
Y1	S1	3.2E+07	31.93	3.890	0.583	2.269
	S2	3.2E+07	31.75	3.925	0.566	2.221
Y3	S1	3.0E+07	31.43	4.206	0.621	2.613
	S2	2.9E+07	31.14	4.250	0.631	2.683
Y4	S1	7.0E+07	27.49	1.696	0.829	1.406
	S2	6.9E+07	27.38	1.711	0.812	1.389
Z2	S1	3.3E+07	29.96	3.757	0.518	1.944
	S2	3.2E+07	29.96	3.830	0.513	1.966
Z4	S1	4.6E+07	29.27	2.621	0.742	1.944
	S2	4.6E+07	29.34	2.625	0.741	1.946
Z1	S1	3.7E+07	29.35	3.330	0.650	2.163
	S2	3.7E+07	29.23	3.365	0.641	2.155

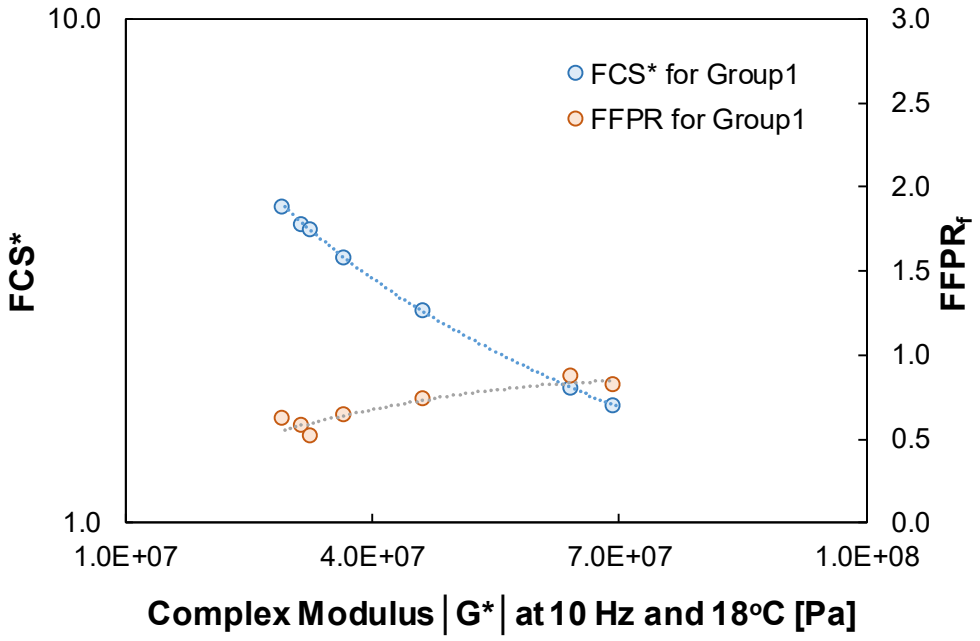

Figure 8-2 Relationship of FFPR and FCS* with the Initial Complex Sheer Modulus at 10 Hz and 18°C for Group 1 Binder

Furthermore, the same analyses were repeated for the extracted binders from Group one binder. The frequency sweep and LAS parameters are tabled in Table 8-2 for the extracted binders. Also, the relationship between both FFPR and FCS^* with the initial complex shear modulus at 10 Hz and 18ºC was graphed in Figure 8-3.These data will be used later in the chapter to study the effect of aging in the binder to mixture fatigue correlation.

Table 8-2 Frequency Sweep and LAS Parameters for Group 1 Extracted Binders

Mixture		Frequency Sweep at 10 Hz and 18ºC		FCS*	$FFPR_f$	FCS
		Complex Modulus (G*) [Pa]	Phase Angle [°]			
Y1- E	S1	1.8E+07	39.67	6.958	0.600	4.173
	S2	1.8E+07	39.70	7.065	0.608	4.295
Y4 -E	S1	6.7E+07	28.39	1.774	0.829	1.470
	S2	6.8E+07	28.42	1.733	0.871	1.510
Z2-E	S1	2.8E+07	33.35	4.392	0.570	2.501
	S2	2.7E+07	33.42	4.569	0.562	2.567
Z4-E	S1	4.6E+07	30.87	2.672	0.727	1.943
	S2	4.3E+07	31.22	2.809	0.721	2.026
Z1-E	S2	9.6E+06	41.94	12.618	0.427	5.384
	S3	9.5E+06	41.98	12.739	0.422	5.380

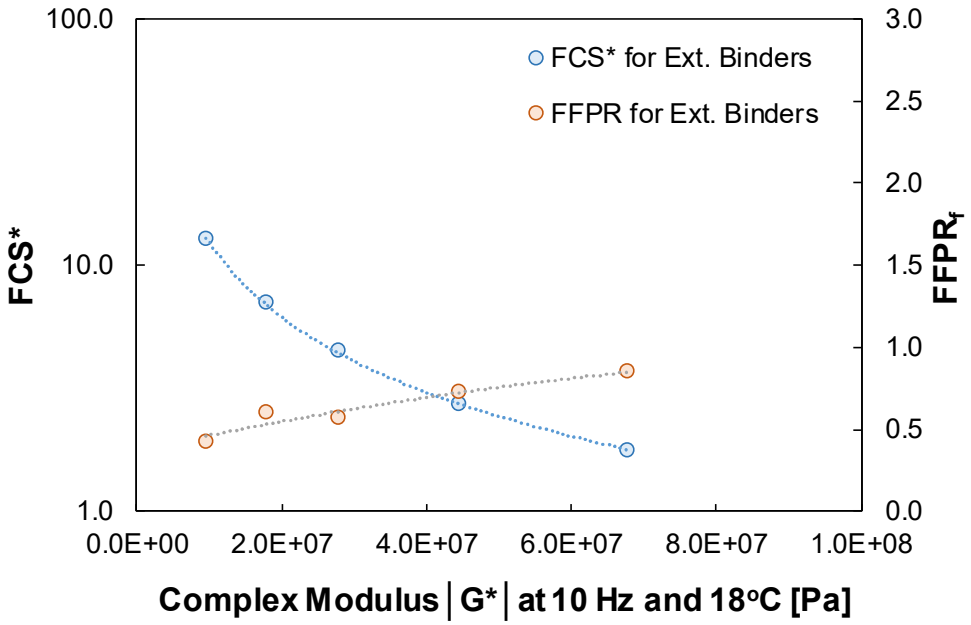

Figure 8-3 Relationship of FFPR and FCS* with the Initial Complex Sheer Modulus at 10 Hz and 18°C for the Extracted Binders.

The main advantage of using FFPR to characterize fatigue performance is that it eliminates the effect of modulus on fracture and fatigue properties. As noted from the graph that the strain capacity decreases substantially with increased modulus, which can also result in decreased fatigue life at higher strain levels. This can complicate comparing fatigue and fracture tests among mixtures and binders with different modulus values. The applied strain can also affect the fatigue life of a mixture. Even though it is very easy to manage strain in some mixture fatigue tests, evaluating tests outcomes at different strains can be difficult, and binder tests and mixtures tests are not often carried out at similar strain levels. FFPR presents a way of likening fatigue and fracture performance mostly impartial of the effects of modulus and strain.

8.2.3 Axial Fatigue Test Results for Group1 and Group 2 Mixtures:

The axial fatigue test was performed to assess the resistance of the asphalt mixtures to fatigue damage. The test was performed at an intermediate temperature of 18°C and were run at four strain levels. The strain levels were estimated such that the material fails in less than 10,000 cycles, between 10,000 - 50,000 cycles, between 50,000 – 100,000 cycles and greater than 100,000 cycles. The fatigue test data was analyzed using simplified viscoelastic continuum damage theory (S-VECD) formulation as was explained in Appendix A. The first step in this approach is to establish the damage characteristic (*C* vs. *S*) curve. *C* represents the integrity of the material, which decreases as the material is repeatedly loaded, and S represents the damage accumulated, by the material during the test. The *C* vs. *S* curve is a unique relationship to a given asphalt concrete mixture and it is independent of test conditions. These test conditions include strain levels, temperatures, mode of loading, and loading history. The *C* vs. *S* curve for the study mixtures are shown in Figure 8-4. One of the fatigue failure definition is the drop of phase angle, which is adopted herein to analyze mixture fatigue. The *C* vs. *S* curves for each individual mixture at different strain levels, along with on-specimen strain at cycle 80 are summarized in Appendix C.

The interpretation of the figure can be explained using an example. Consider two mixtures, SX3, and SY1. At failure, SY1 suffered a loss in material integrity which dropped to around 0.5 (50%) and accumulated a damage of around 7×10^4. On the other hand, SX3 could resist failure until its material integrity dropped to around 0.15 (15%), and in the process accumulated damaged more than 1.5×10^5. While SX3 accumulates more damage, it resists

failure until its material integrity drops to 15%. If all other factors are the same, then this characteristic would make SX3 a superior material in fatigue resistance than SY1.

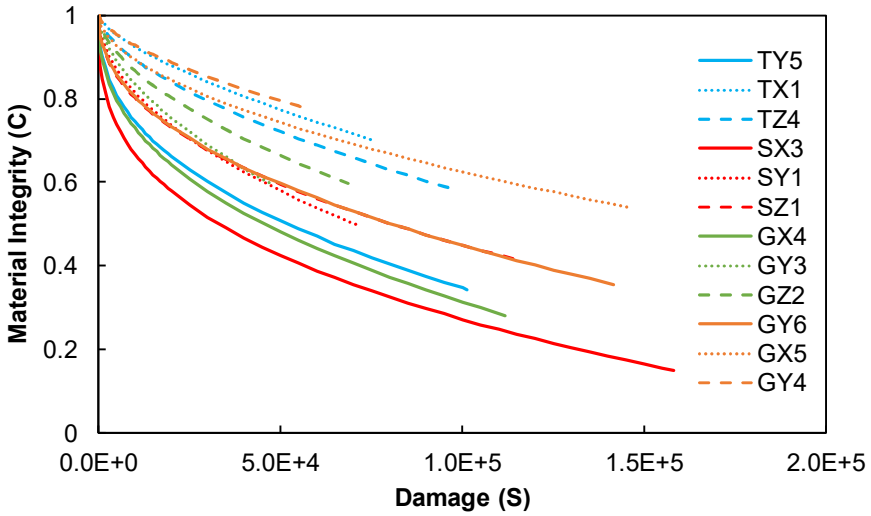

Figure 8-4. C (Material Integrity) vs S (Damage) Curves for the Study Asphalt Mixtures.

While the *C* vs. *S* damage curves are good indicators of performance, they alone cannot be considered for the fatigue performance of the asphalt mixtures. Simulations are carried out using Equation (7-2) to estimate the strain level that the sample needs to be tested at to fail in 10,000, 100,000, and 1,000,000 cycles. The result of these simulations are fatigue failure envelopes as shown in Figure 8-5. In simpler terms, the vertical positioning of the line indicates the performance of the mixture in fatigue. The higher the vertical position, the better the fatigue resistance. So, for the example SX3 has a higher vertical position than SY1 and thus SX3 has better fatigue resistance than SY1.

Among all the mixtures used in the study, the mixture prepared with the X3 binder provided the greatest amount of fatigue resistance. It is observed from Figure 8-5 that five of the top six best performing mixtures are polymer modified. For ease of observation, the *C* vs *S*

curves in Figure 8-4 and fatigue failure envelopes in Figure 8-5 are seperated by aggregate type and presented in Figure 8-6 through Figure 8-8. It can be seen in Figure 8-6 through Figure 8-8 that the best performing mixtures in each aggregate type are polymer modified mixtures.

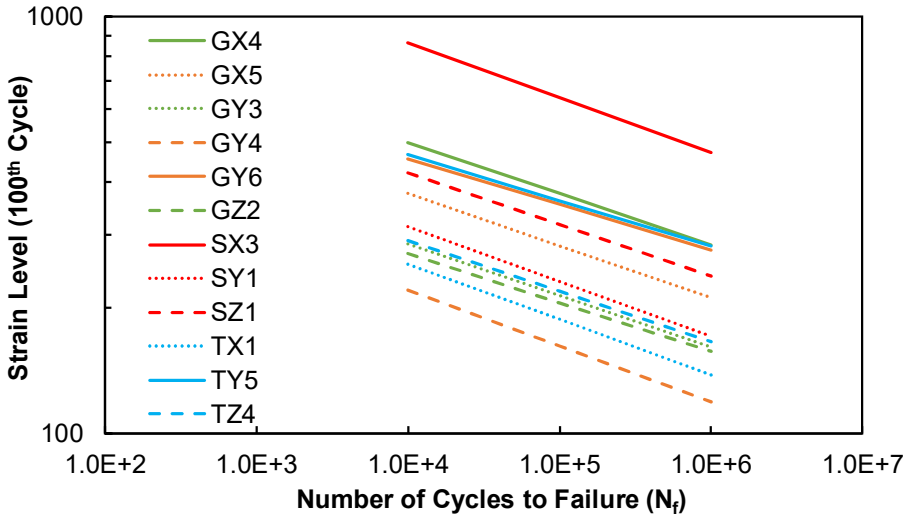

Figure 8-5. Simulated Fatigue Failure Envelopes for the Study Asphalt Mixtures.

To quantify and compare the differences observed in fatigue behavior of the asphalt mixtures, the fatigue life for all 12 mixtures was estimated at 400 με using the failure envelopes shown in Figure 8-5. The results shown in Table 8-3 is a re-affirmation of the trends seen in Figure 8-5. It is seen that SX3 which is a polymer modified mixture possesses the highest number of cycles to failure. Among the top six mixtures with the highest number of cycles to failure, five are polymer modified asphalt mixtures. These mixtures are highlighted in Table 8-3

Table 8-3. A mixture to mixture comparison with the same aggregate source is performed in the following paragraphs. Overall, it is seen that, irrespective of the source of the aggregate, polymer modified mixtures are more fatigue resistant. To put the statement into perspective of numbers, the average N_f value for the five polymer modified mixtures across three aggregate sources was 728,166 in comparison to 2,702, which is the average value from the seven non-polymer modified asphalt mixtures. The increase in fatigue life from polymer modified mixtures is 26,853%. The large average N_f value of the polymer modified mixtures is due to the high fatigue resistance offered by SX3. Even without SX3, if only the four polymer modified asphalts were to be averaged, the average N_f is 34,428 which is 1,174% more that the average N_f value of the non-polymer modified mixtures.

Table 8-3. Simulated Fatigue Life for Study Asphalt Mixtures at 400 με.

Mixture	N_f
GX4	59512
GX5	6073
GY3	631
GY4	116
GY6	32186
GZ2	360
SX3	3503118
SY1	1537
SZ1	2426
TX1	334
TY5	39941
TZ4	699

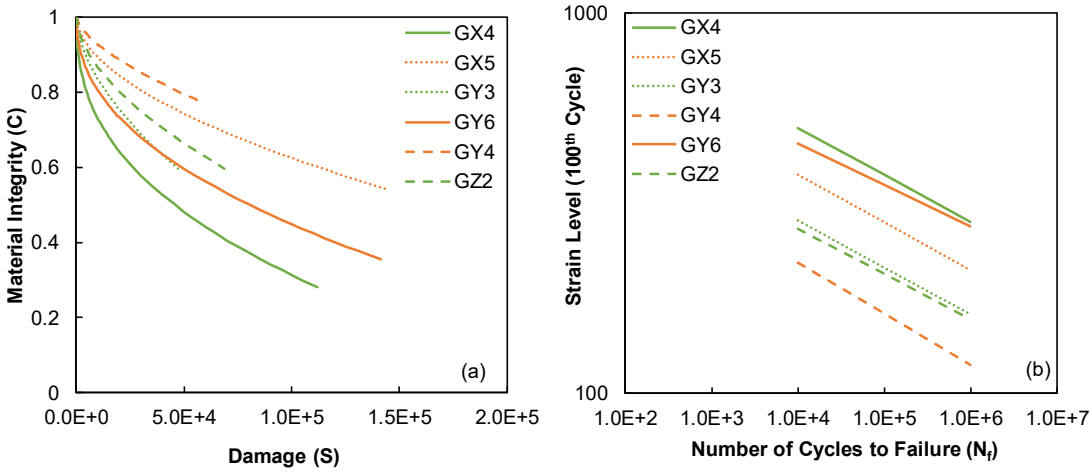

Figure 8-6. (a) C vs S Damage Characteristic Curves (b) Simulated Fatigue Failure Envelopes for Asphalt Mixtures Prepared with Globe Aggregate.

The mixtures prepared with Globe aggregate contain three polymer modified asphalts, X4, X5 and Y6. It can be seen from Figure 8-6 that the mixtures prepared with these asphalts rank 1, 3, and 2 respectively in terms of fatigue resistance. The mixture GX4 which is the best performing mixture with an overall improvement of 9,337% over the best performing non-polymer modified mixture, GY3 and an improvement of 85% over the next best performing polymer modified asphalt which is GY6.

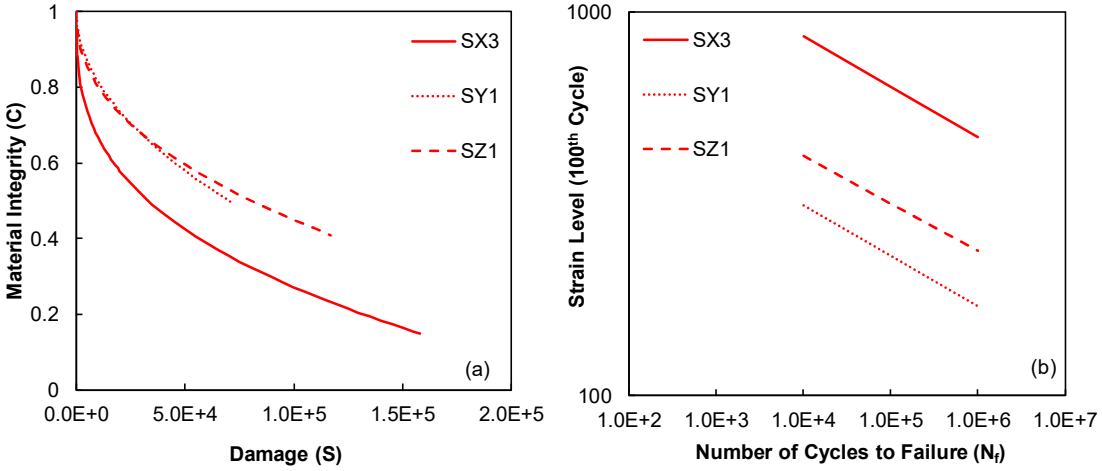

Figure 8-7. (a) C vs S Damage Characteristic Curves (b) Simulated Fatigue Failure Envelopes for Asphalt Mixtures Prepared with Snowflake Aggregate.

The mixtures prepared with Snowflake aggregate contain one polymer modified asphalt, X3. The mixture prepared with X3 ranks best in fatigue resistance not only among the Snowflake mixtures but among all twelve mixtures tested in this study. The mixture SX3 has an improvement of 22,895% over SZ1.

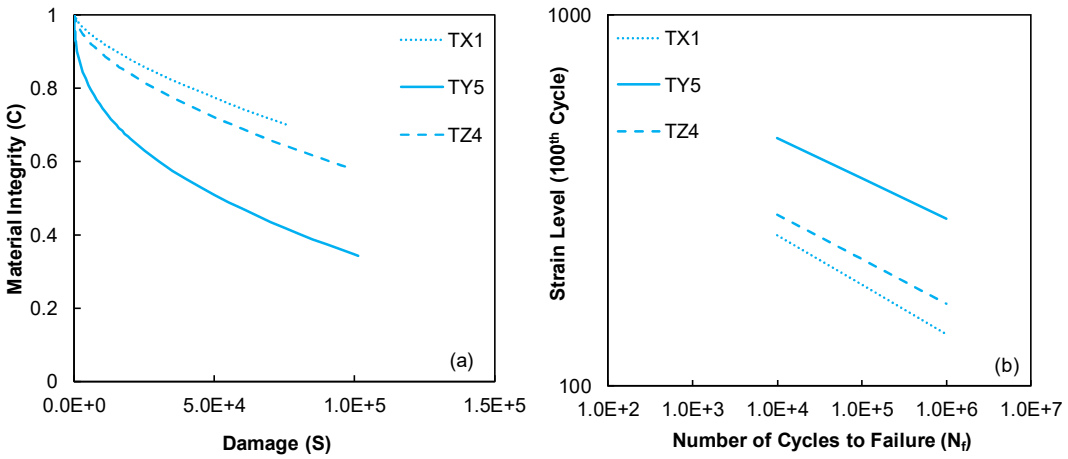

Figure 8-8. (a) C vs S Damage Characteristic Curves (b) Simulated Fatigue Failure Envelopes for Asphalt Mixtures Prepared with Tucson Aggregate.

The mixtures prepared with Tucson aggregate contain one polymer modified asphalt, Y5. The mixture prepared with Y5 ranks best in fatigue resistance among the Tucson mixtures and third overall. In Figure 8-8, the mixture TY5 has an improvement of 5,614% over TZ4.

8.2.4 Axial Fatigue Test Results for Group 3 Mixtures:

The fatigue tests were conducted at an intermediate temperature of 18°C and were run at four strain levels, which were estimated such that the material fails in less than 10,000 cycles, between 10,000 - 50,000 cycles, between 50,000 – 100,000 cycles and greater than 100,000 cycles. The fatigue test data was analyzed using simplified viscoelastic continuum

damage theory (S-VECD) formulation as explained in Appendix A. The result of the S-VECD model is the damage characteristic curve or the C vs. S curve. The curves were fitted to a power function shown in Equation (8-10). Figure 8-9 shows the C vs. S curves that were developed for all nine binders.

$$C = 1 - aS^b \tag{8-10}$$

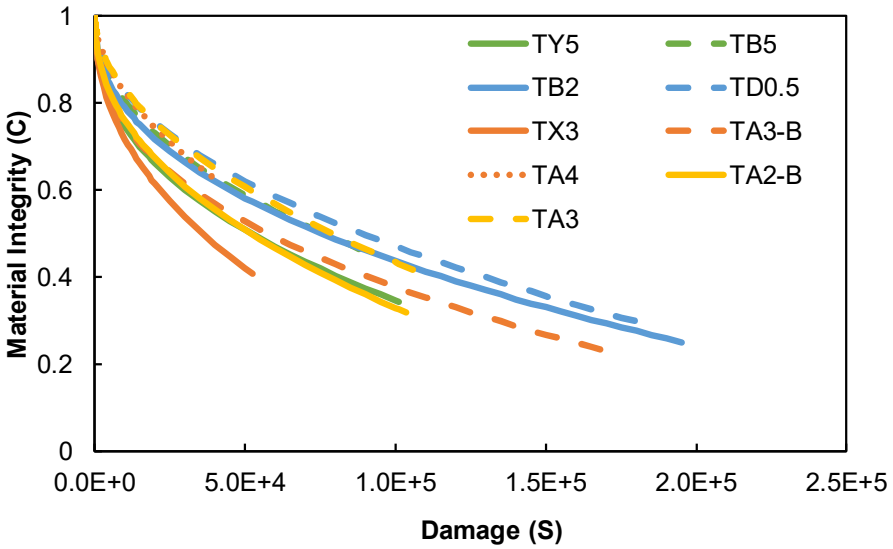

Figure 8-9. Material Integrity (C) vs. Damage (S) Damage Curves Developed Using Data from Axial Fatigue Test.

The interpretation of the figure can be explained using an example. Consider two mixtures, TA3, and TA3-B. At its failure TA3 suffered a loss in material integrity which dropped to around 0.4 (40%) and accumulated a damage of around 1E+5. On the other hand, TA3-B could resist failure until its material integrity dropped to around 0.2 (20%), and in the process accumulated damaged more than 1.5E+5. While TA3-B accumulates more damage, it resists failure until its material integrity drops to 20%. This makes it a superior material in fatigue resistance than TA3, which has accumulated less damage but fails at a higher material integrity (40%).

While the C vs. S damage curves are good indicators of performance, they alone cannot be considered for the fatigue performance of the asphalt mixtures. Simulations are carried out to estimate the strain level that the sample needs to be tested at to fail in 10,000, 100,000, and 1,000,000 cycles. The result of these simulations are fatigue failure envelopes as shown in Figure 8-10. In simpler terms, the vertical positioning of the line indicates the performance of the mixture in fatigue. The higher the vertical position, the better the fatigue resistance. So for the example in the previous paragraph, TA3-B has a higher vertical position than TA3, thus TA3-B has a better fatigue resistance. More specifically, at a fixed strain level asphalt mixture prepared with binder A3-B can resist more of cycles before failure than A3. Among all binders prepared for the study, A3-B has the best resistance to fatigue, and A4 has the worst resistance to fatigue.

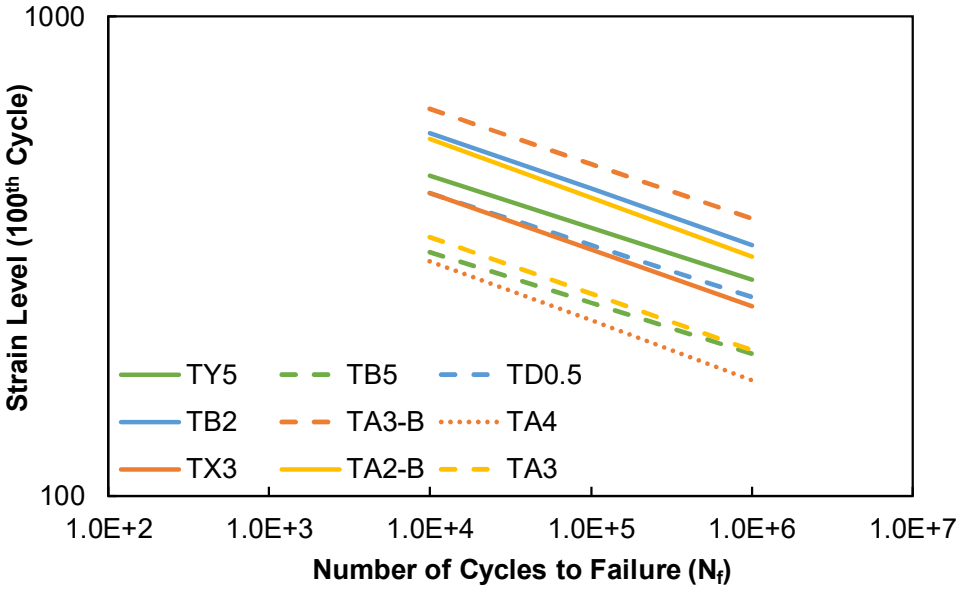

Figure 8-10. Simulated Fatigue Failure Envelopes for the Study Mixtures.

8.3 Studying the Relation between the Binder Fatigue Parameters with Asphalt Mixtures Fatigue.

This chapter focusses on estimating the binder fatigue parameters and axial fatigue test for asphalt mixtures. Also, studying the results and the connections between the relative merits of these two parameters. The first task is already discussed early in this chapter for all the study binders; Frequency sweep test for the asphalt binder was performed which estimated the linear viscoelastic binder fatigue parameter ($|G^*| \sin\delta$). Also, LAS was performed and the nonlinear viscoelastic binder fatigue parameter was calculated. Then, the axial fatigue test to assess the resistance of asphalt mixtures to fatigue damage was completed. In addition, the fatigue test results for all the mixtures using simplified viscoelastic continuum damage theory (S-VECD) formulation were displayed. This subtask will be correlating the binder fatigue parameters to axial fatigue test for asphalts:

8.3.1 $|G^*|sin\delta$ Parameter

The number of cycles to failure of asphalt mixture at 400 με and 18°C were related to $|G^*|\sin\delta$ at 18°C and the results are presented in Figure 8-11. Historically, the relationship between this binder parameter and mixture fatigue parameter is fit to a linear function and the correlation is reported to be poor. However, in this research the function is found to be better described using a power law function. Overall, the relationship have low correlation coefficients. The correlation between $|G^*|\sin\delta$ parameter and the axial fatigue test was weak, for this reason, the $|G^*|\sin\delta$ parameter does not perform to be a good indicator of asphalt mixture's fatigue performance.

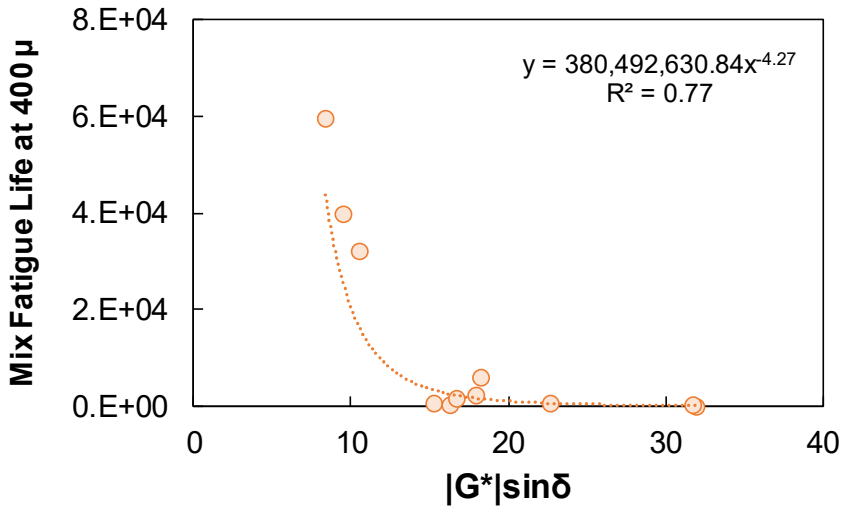

Figure 8-11 $|G^*|\sin\delta$ Results at Intermediate Temperatures 18°C.

8.3.2 The LAS Test

This subtask will be correlating the binder fatigue using LAS test to axial fatigue test for asphalts by using the GFTAB predictive method. The general model based on Equation (8-2) was used herein to relate binder fatigue to mixture fatigue. The final following model was used to predict number of cycles to failure:

$$\hat{N}_f = \left(\frac{(FFPR_i)(FSC^*)(VBE/100)}{\varepsilon_t} \right)^{k_1(90/\delta)} \tag{8-11}$$

Where:

$\hat{N}_f$ = Predicted cycles to failure

$FFPR_i$ = fatigue/fracture performance ratio for *i*th binder

FSC^* = typical binder fatigue strain capacity, %

= Equation (8-7) where the $|G^*|$ is the modulus (Pa) for the binder of interest at the

test temperature and a frequency of 10 Hz 6

VBE = mixture effective binder content, volume %

k_1 = fatigue exponent coefficient and will be estimated from the data.

ε_t = mixture maximum tensile strain, %, and

δ = binder phase angle (degrees) for the binder of interest at the test temperature and a frequency of 10 Hz

Simulations are carried out using Equation (7-2) to estimate the number of cycles to failure of asphalt mixture at three different strain levels. The strain level was selected to be within the range of strain levels used to run the axial fatigue testing. The selected levels are 300 με, 350 με, and 400 με as shown in Table 8-4. The result of these simulations are number of cycles to failure that are used herein to build the correlation and estimate K_1.

Table 8-4 Number of Cycles to Failure of Asphalt mixture along with the Binder Parameters for Group 1 Binder

Mixture	N_f mix at			*VBE* %	Phase Angle [°]	*FCS** %	$FFPR_f$
	300 με	350 με	400 με				
X1	2916	914	334	11.28	29.59	1.851	0.869
Y1	13816	4260	1537	10.93	31.84	3.908	0.575
Y3	6512	1864	631	9.57	31.29	4.228	0.626
Y4	998	315	116	9.77	27.44	1.704	0.820
Z2	4121	1116	360	9.54	29.96	3.794	0.515
Z4	7566	2111	699	11.38	29.31	2.623	0.741
Z1	24861	7145	2426	11.39	29.29	3.347	0.645

In performing the analysis, Microsoft Excel Solver was used to determine the model coefficient. Preliminary analyses showed that the coefficient in the fatigue exponent (k_1) had a value of 1.44. Figure 8-12 shows predicted and observed cycles to failure in arithmetic space for Group 1 fatigue data used in this analysis. The R^2 value for the data is slightly low

and data is systematically different from the observed cycles to failure (bias), which is probably because the use of the STOA aging increased the variability in the mixture properties. Figure 8-13 shows predicted and observed cycles to failure in a logarithmic space for Group 1. The bias was more clear and obvious in this figure. As noted, it was clearly related to the mixture tensile strain level that was used in the analysis. This means that k_1 is correlated to the tensile strain level. So, on Equation (8-11) replaced by k_2 which equal to:

$$k_2 = \left(\frac{k_1}{\varepsilon_t} \right) \tag{8-12}$$

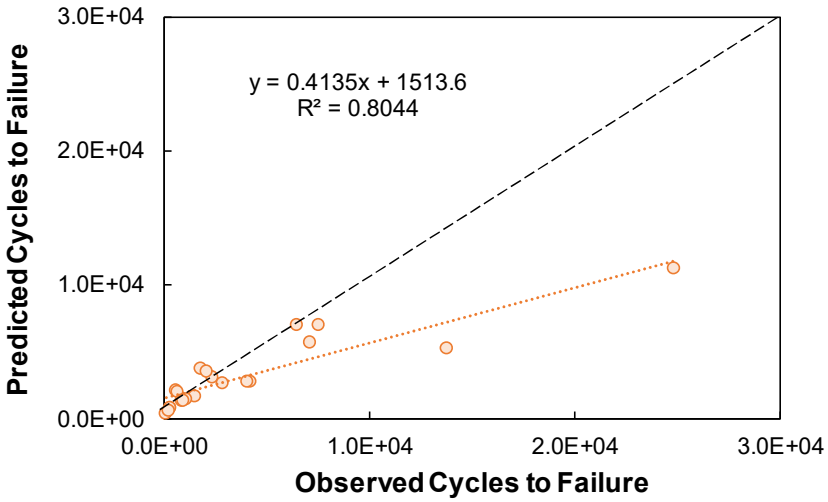

Figure 8-12 Predicted and Observed Cycles to Failure for Group 1 Asphalt Mixtures in Arithmetic Scales

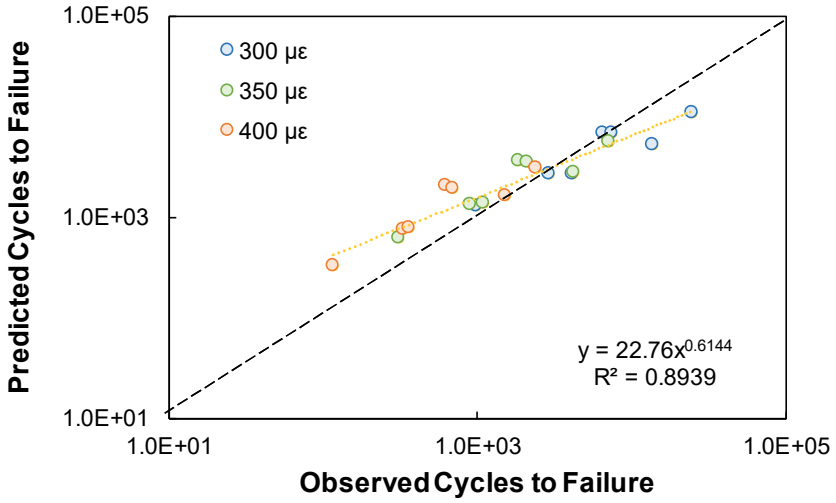

Figure 8-13 Predicted and Observed Cycles to Failure for Group 1 Mixtures in Logarithmic Scales

The final model used to predict mixture fatigue cycles to failure from binder fatigue is Equation (8-12)

$$\hat{N}_f = \left(\frac{(FFPR_i)(FSC^*)(VBE/100)}{\varepsilon_t} \right)^{\left(\frac{k_1}{\varepsilon_t}\right)^{(90/\delta)}} \tag{8-13}$$

The variables are as described for Equation (8-11) above. The analysis was performed one more time by using Equation (8-13) with Microsoft Excel Solver to determine the model coefficient k_1. The analyses showed that the coefficient in the fatigue exponent (k_1) had a value of 4.75. Figure 8-14 shows predicted and observed cycles to failure in arithmetic space for Group 1 fatigue data by using Equation (8-13). After using the new model, the R^2 value for the data is still low but the data points are along the line of quality. So, introducing k_2 the date was less bias. Figure 8-15 shows predicted and observed cycles to failure in logarithmic space for Group 1 fatigue data by using Equation (8-13).

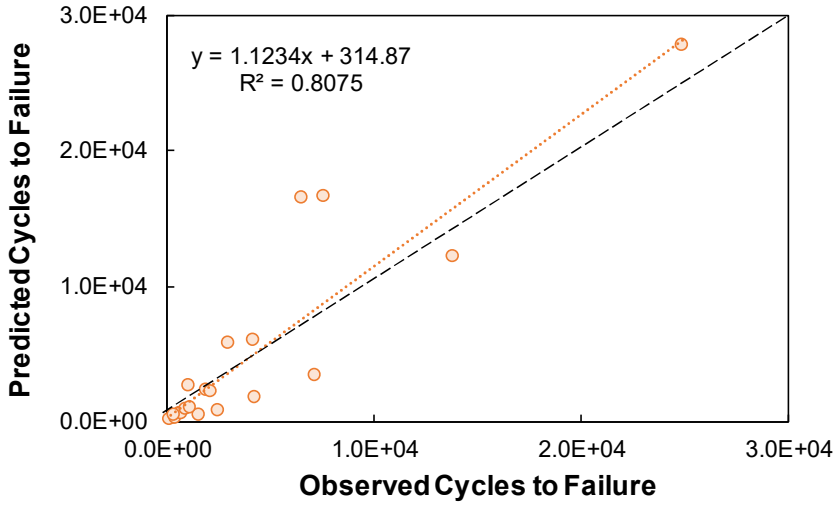

Figure 8-14 Predicted and Observed Cycles to Failure for Group 1 Mixtures in Arithmetic Scales Using Equation (8-13)

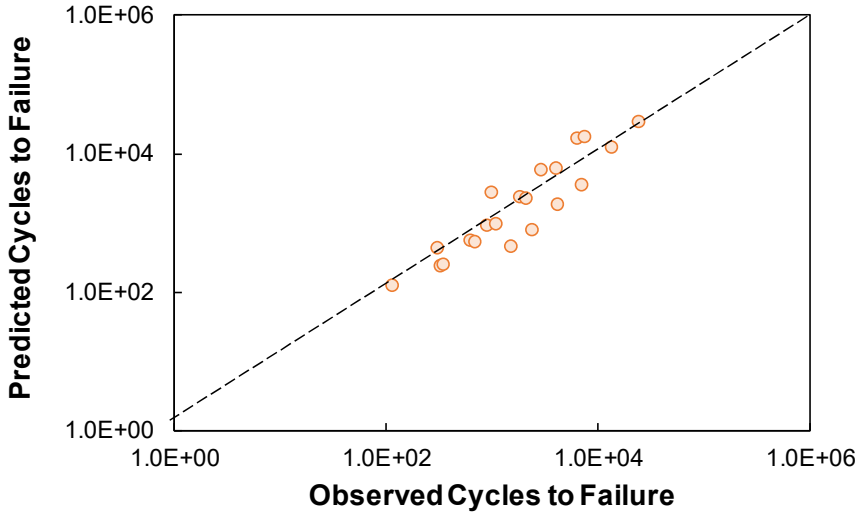

Figure 8-15 Predicted and Observed Cycles to Failure for Group 1 Mixtures in Logarithmic Scales Using Equation (8-13)

The other issue with the data is significant scatter from the line of quality as noted from Figure 8-15. This occurs probably because of inequivalent aging condition used in the binder to the mixture aging condition. This issue was discussed in detail in Chapter 5. The GFTAB method is applied using binders which has been extracted and recovered, and it can be confidently stated that the tested binder represents what exists in the mixture.

The theory is not perfect so the model can be calibrated in a better way. When this calibrated model is applied to PAV versus short term for other conditions, there is considerable scatter and the mean prediction is off. It is possible to calibrate to the mean effect, but not the scatter effect. The scatter exists, because unlike in rutting where the binder property related to permanent strain accumulation is so closely tied to modulus and it could reasonably corrected or evaluated, in the case of binder fatigue because there are three distinct phenomenon that occur; 1) resistance to deformation, 2) damage resistance, and 3) damage tolerance.

The analysis is more complicated herein. Also, probably because the use of STOA aging increased variability in the mixture properties. For this reason, the decision was taken to run LAS test one more time for the extracted binders from Group 1 and compare the result with the previous analysis that has done above for PAV aging condition using Equation (8-13). The same three strain levels (300 με, 350 με, and 400 με) were used herein for the extracted binders from Group 1. The number of cycles to failure of asphalt mixture along with the binder parameters for Group 1 extracted binders tabled in Table 8-5.

Table 8-5 Number of Cycles to Failure of Asphalt mixture along with the Binder Parameters for Group 1 Extracted Binders

Mixture	N_f mix at			*VBE* %	Phase Angle [°]	*FCS* %*	$FFPR_f$
	300 με	350 με	400 με				
Y1- E	13816	4260	1537	10.93	39.69	7.012	0.604
Y4 -E	998	315	116	9.77	28.41	1.753	0.850
Z2-E	4121	1116	360	9.54	33.39	4.480	0.566
Z4-E	7566	2111	699	11.38	31.05	2.740	0.724
Z1-E	24861	7145	2426	11.39	41.96	12.678	0.425

The result of these simulations are the number of cycles to failure that is used to build the correlation and estimate K_1. The analyses showed that the coefficient in the fatigue exponent (k_1) had a value of 4.67. Figure 8-16 shows predicted and observed cycles to failure in arithmetic space for Group 1 fatigue data by using Equation (8-13). After using the new model, the R^2 value for the data is still low but the data point along with line of quality. Therefore, introducing k_2 the date was less bias. Figure 8-16 and Figure 8-17 illustrate predicted and observed cycles to failure in arithmetic and logarithmic space for extracted Group 1 fatigue data by using Equation (8-13).

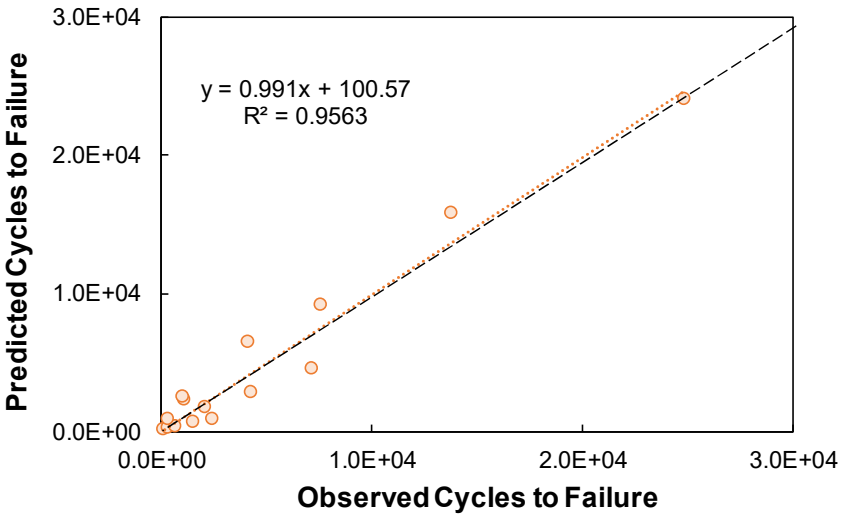

Figure 8-16 Predicted and Observed Cycles to Failure for Extracted Group 1 Mixtures in Arithmetic Scales Using Equation (8-13)

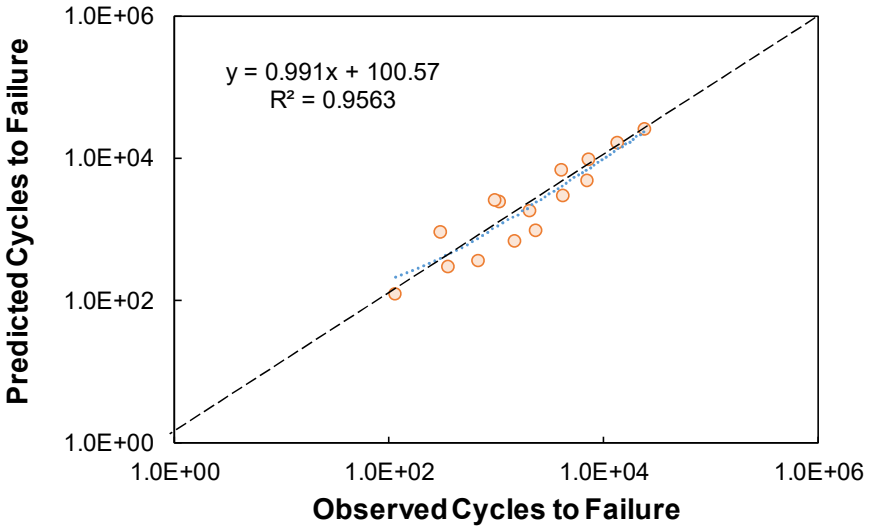

Figure 8-17 Predicted and Observed Cycles to Extracted Failure for Group 1 Mixtures in Logarithmic Scales Using Equation (8-13)

In both, the correlation between predicted and observed cycles to failure is very good with R^2 = 96%, in the range typically seen for asphalt mixture fatigue models. Comparing the analysis from PAV aging condition and extracted STOA, it is clear that there is effect of aging (the R^2 improved from 80% to 96%). Because of the high inherent variability of mixture fatigue tests, it is probably not possible to achieve R^2 values much higher than this, so the criteria for evaluating the GFTAB model has been met by using the final predicted model to estimate mixture fatigue cycles to failure from binder fatigue is Equation (8-14)

$$\hat{N}_f = \left(\frac{(FFPR_i)(FSC^*)(VBE/100)}{\varepsilon_t} \right)^{\left(\frac{4.67}{\varepsilon_t}\right)^{(90/\delta)}} \quad (8\text{-}14)$$

Where:

$\hat{N}_f$ = Predicted cycles to failure

$FFPR_i$ = fatigue/fracture performance ratio for ith binder

FSC^* = typical binder fatigue strain capacity, %

= Equation (8-7) where the $|G^*|$ is the modulus (Pa) for the binder of interest at the test temperature and a frequency of 10 Hz 6

VBE = mixture effective binder content, volume %

ε_t = mixture maximum tensile strain, %, and

δ = binder phase angle (degrees) for the binder of interest at the test temperature and a frequency of 10 Hz

8.4 Conclusions

The following conclusions are made from this study;

- Polymer modification has a profound impact on the fatigue performance of asphalt mixtures. Within each aggregate type, the best performing polymer modified mixture had an average improvement of 12,615% over the best non-polymer modified mixture with a range of 5,614% to 22,895%.
- The differences are significant and warrant further investigation, which is unfortunately outside the scope of the current work. One key observation believed to be responsible for these differences is related to the observed failure mechanisms in the polymer versus non-polymer modified mixtures. In the case of the polymer modified mixtures, failure was consistently cohesive (i.e., in the asphalt film) evidenced by the fact that the failure surface was black in color. However, also the non-polymer modified asphalts consistently showed mixed adhesion/cohesion

failure, which was evidenced by the presence of thinly coated aggregate particles on the failure surface.

- The $|G^*|\sin\delta$ parameter does not perform to be a good indicator of asphalt mixture's fatigue performance.
- The GFTAB model for fatigue and fracture failure of asphalt binders performs to be practically precise in comparing the fatigue behavior of asphalt mixtures with binder fatigue.
- The GFTAB model is generally valuable in linking the fatigue behavior of asphalt mixtures with binder fatigue and fracture test results.
- The strain capacity of asphalt binders is mainly a function of modulus with higher modulus values being associated with lower failure strains.
- It is quite evident that if mixture fatigue tests had been done at a significantly lower modulus range and/or using less aggressive laboratory aging methods, will increase the variability in comparing the fatigue behavior of asphalt mixtures with binder fatigue.

Chapter 9. SUMMARY AND FUTURE WORK

9.1 Summary and Conclusions

Through the literature reviewed for this dissertation, there was a wealth of data on the linear and non-linear viscoelastic behaviors of asphalt mixture and binders. In addition, the relationship between the laboratory mixture short-term aging and the binder aging conditions were studied, characterized and analyzed. However, the literature lacked information on the relationship between the non-recoverable creep compliance at 3.2 kPa ($J_{nr3.2}$) and the percent of elastic recovery ($R_{3.2}$) from the multiple stress creep and recovery (MSCR) test, which is included in the AASHTO M332 specification. The justification for the exact position of the $J_{nr3.2}$ versus $R_{3.2}$ curve based on binder performance is largely undocumented in the technical literature, as is the singular effect of higher or lower $R_{3.2}$ values on mixture performance. The novel contribution of this research is the utilization of dynamic modulus test, Hamburg Wheel Tracking test, and axial fatigue test to develop an alternative $J_{nr3.2}$ vs $R_{3.2}$ relationship; this was done by preparing nine binders with similar $J_{nr3.2}$ and varying MSCR $R_{3.2}$ to evaluate the effect of $R_{3.2}$ on the performance of asphalt mixtures. Recall, the main objective of this study was to relate the linear viscoelastic properties and non-linear viscoelastic behaviors of asphalt mixture and the corresponding binders. As a first step in achieving this goal, changes in dynamic modulus $|E^*|$ as a function of changes the linear viscoelastic parameters (binder shear modulus $|G^*|$), mixture volumetric properties, and aggregate gradation were evaluated. However, more work needs to be performed to apply the predictive relationships identified by the research team in the

analysis herein are: Original Witczak Equation (NCHRP 1-37A), Modified Witczak |G^*| Equation (NCHRP 1-40D), Hirsch Model, and Simplified Global Model.

Furthermore, estimating and studying the relative merits of the HMA laboratory rutting and equivalent binder rutting parameters in the lab. More specifically, performing AASHTO M320 for the asphalt binder, estimating the linear viscoelastic binder rutting parameter (ratio of dynamic modulus to the sine of the phase angle, $|G^*|/\sin\delta$), performing AASHTO M332, and estimating the nonlinear viscoelastic binder rutting parameter (which uses the non-recovered creep compliance, J_{nr} for this purpose). As a result, the two binder rutting parameters were correlated to both mixture rutting tests (Hamburg wheel and flow number).

Another aging study was performed including different binder aging methods and short-term oven aging on asphalt mixtures. In this study, the propensity to oxidize measured by calculating the aging ratio of RTFO, PAV, and STOA aged conditions were gathered for analysis. The focus of the analysis was to ensure that the binder tests properties reflect the condition of the binder during the mixture test when evaluating binder-to-mixture properties.

Finally, the research ended up with a study to estimate the linear viscoelastic and non-linear viscoelastic properties of the binder fatigue parameters and to study the links between the relative merits of these two parameters with asphalt mixtures fatigue.

9.1.1 Findings for Relating Linear Viscoelastic Properties of Binder and Asphalt Mixture

- For all study binders at three aging levels, i.e. original, RTFO, and PAV, the modulus increases with aging level.

- The vertical spread between aged and original conditions is greater in non-polymer modified asphalt than polymer modified asphalt. These visual observations can be quantified using the aging ratio parameter.
- The mixture's dynamic modulus results rank and go hand-in-hand with the binder's modulus results $|G^*|$.
- The polymer modified mixtures predominantly had lower moduli than non-polymer modified mixtures.
- The Al-Khateeb model displayed a significant bias relative to the other existing models and, therefore, the model dropped from future ageing analysis.
- Both of Witczak models had less goodness of fit statistics compared to the other models; both of them had two variables (phase angle and binder shear modulus) and can't be used to back calculate the binder shear modulus. Therefore, they were excluded from the models list.
- The statistical measurements for the simplified global and Hirsch models indicate an excellent fit with high correlation. Both of the models performed very well and showed the least scatter with the least bias overall.

9.1.2 Conclusions from Aging Study

- The main conclusion from the comparison of aging ratios of binders of the same grade was that the oxidative properties of the binders are source and formulation dependent. Similar PG grade does not necessarily equate to similar oxidative properties as was evidenced by the different aging ratio (*AR)* values.

- The *AR* based analysis clearly showed that the polymer modified asphalts have a lower propensity to aging. However, at intermediate temperatures the aging ratios of the unmodified and polymer modified binders were very similar with the latter having a lower aging ratio. Furthermore, at higher temperatures, the polymer modified asphalts had a noticeably lower aging ratio than the neat binder.
- The binder aging that occurs when a mixture is short-term conditioned in a forced draft oven for 4 hours at 135°C per AASHTO R30 generally exceeds the aging in the short-term binder aging procedures. The difference was noted to be higher at high temperatures, and lower-high temperature PG grade binders. This finding was very important for this study, because it may possibly have negative impacts on any rutting correlation that would be established between binder and asphalt mixture.
- The AR_{PAV}/ AR_{STOA} ratio values varied by temperature and PG grade. This ratio increased with increase in temperature for most binders. The AR_{PAV}/ AR_{STOA} ratio found to be stable for the higher-high temperature PG grade binders between 1.0 to 1.5 times, and inconsistence for lower-high temperature PG grade binders. This difference was important especially at mid temperatures when fatigue correlation will be formulated between binder and asphalt mixture.

9.1.3 Relationship between Asphalt Binder Parameters and Asphalt Mixture Rutting

- For non-polymer modified asphalts, there was a very strong correlation between $|G^*|/\sin\delta$ and $J_{nr3.2}$ regardless of binder type or grade.

- For polymer modified asphalts, where the base binder, modifier, and cross-linking agents (PPA and sulfur) are all identical, there was a strong correlation between $|G^*|/\sin\delta$ and $J_{nr3.2}$. However, where the base binder, modifier, and any potential other admixtures differed, the correlation varied greatly.
- A good correlation with a R^2 value of 0.69 was obtained between the rut depth at 50°C from the HWTT test and the slope of the secondary region of the RLPD test at 50°C. And a better correlation with a R^2 value of 0.79 was obtained between the rut depth from HWTT test and the flow number from RLPD test. No systematic bias with respect to this correlation and polymer-modified asphalts was observed.
- When correlating the rut depth from the HWTT to both $|G^*|/\sin\delta$ and $J_{nr3.2}$, in the case of the relationship with $|G^*|/\sin\delta$, the function was found to be better described using a power law function. In the case of the relationship with $J_{nr3.2}$, a linear function was found to best describe the relationship.
- Overall, the rut depth from the HWTT had low correlation coefficient to both $|G^*|/\sin\delta$ and $J_{nr3.2}$ relationships, but pairwise comparisons demonstrate that $J_{nr3.2}$ was more consistent at segregating mixture performance.
- When correlating the average slope from RLPD tests to both $|G^*|/\sin\delta$ and $J_{nr3.2}$, the binder parameters related better to RLPD results than HWTT results. The correlation with respect to $J_{nr3.2}$ was much greater than the correlation with $|G^*|/\sin\delta$.
- When correlating the binder rutting parameters $|G^*|/\sin\delta$, and $J_{nr3.2}$ to mixture rutting, the tested asphalt binder in the laboratory should represent that of the mixture for better correlation.

- The study showed that the better way to ensure the binder test properties reflect the condition of the binder during the mixture test, was to run the binder tests by extracting and recovery the same tested asphalt mixture sample.

9.1.4 Effect of MSCR Percent Recovery on Performance of Polymer Modified Asphalt Mixtures

- The mixture dynamic modulus and phase angle were proportional to the binder $|G^*|$ and δ.
- The mixture |E*| is inversely proportional to $R_{3.2}$ provided two binders have a similar $J_{nr3.2}$, while the phase angle of the mixture shows no relationship with $R_{3.2}$.
- There was no statistically significant difference to suggest that $R_{3.2}$ had an effect on rutting performance. Instead, the rutting resistance of the above mixtures was more closely related to $J_{nr3.2}$ and $|G^*|/\sin\delta$ of the binder.
- The $R_{3.2}$ value showed a direct proportionality to the fatigue resistance of asphalt mixtures, with the precise impact being dependent upon the value of $J_{nr3.2}$.
- Many current (and likely future polymer modified asphalts) had $R_{3.2}$ values that are positioned substantially higher than the current AASHTO M332 relationship between $R_{3.2}$ and $J_{nr3.2}$.
- Based on these experimental conclusions, a modified $R_{3.2}$ to $J_{nr3.2}$ function was presented. This modified function represents a slight adjustment to the published version and is believed to better reflect the currently observed benefits of polymer modification. The goal for the modification was to set the limits so that there are no

obvious likelihoods that binder performance will be negatively affected by its adoption, while at the same time creating a realistic limit that can be met.

9.1.5 Comparing the Fatigue Behavior of Asphalt Mixtures with Binder Fatigue.

- Polymer modification had a profound impact on the fatigue performance of asphalt mixtures. Within each aggregate type, the best performing polymer modified mixture had an average improvement of 12,615% over the best non-polymer modified mixture with a range of 5,614% to 22,895%.
- The differences were significant and warrant further investigation, which is unfortunately outside the scope of the current work. One key observation believed to be responsible for these differences was related to the observed failure mechanisms in the polymer versus non-polymer modified mixtures. In the case of the polymer modified mixtures, failure was consistently cohesive (i.e., in the asphalt film) evidenced by the fact that the failure surface was black in color. However, also the non-polymer modified asphalts consistently showed mixed adhesion/cohesion failure, which was evidenced by the presence of thinly coated aggregate particles on the failure surface.
- The $|G^*|\sin\delta$ parameter does not perform to be a good indicator of asphalt mixture's fatigue performance.
- The GFTAB model for fatigue and fracture failure of asphalt binders was practical in comparing the fatigue behavior of asphalt mixtures with binder fatigue.

- The GFTAB model was generally valuable in linking the fatigue behavior of asphalt mixtures with binder fatigue and fracture test results.
- The strain capacity of asphalt binders was mainly a function of modulus; with higher modulus values being associated with lower failure strains.
- It was quite evident that if mixture fatigue tests had been done at a significantly lower modulus range and/or using less aggressive laboratory aging methods, it will increase the variability in comparing the fatigue behavior of asphalt mixtures with binder fatigue.

9.2 Study Limitations and Future Work

The following are limitations of this study:

- It is highly recommended developing a better laboratory aging procedures than the one in AASHTO R30 to harmonize the binder and mixture aging conditions, and harmonize these with in-service aging conditions. This is viewed as an important finding from the study; this is needed and even articulated in existing NCHRP project 9-36.
- The study also suggested improving Jnr3.2 vs R3.2 curve in AASHTO M332. Therefore, the modified Jnr3.2 vs R3.2 curve proposed herein will limit the possibility of inferior binders in advent of transition to AASHTO M332 based specification.

- The study was conducted only using aggregates sources from Arizona. So, the relationship has not been investigated/validated with different aggregates types from other states.
- It is noted that this study only used binders in Arizona, which included PG 64-22, PG 70-10, PG 76-16, PG 70-16, and related polymer-modified asphalt.
- The aggregate gradation was very similar among the three Arizona sources. The three different aggregate gradations are dense graded mix. The study has not investigated the correlation with different mix types.
- As part of the future work, the developed relationships should be confirmed with aggregates vastly different from those used in this study. One such aggregate type to be considered for future testing is limestone. As mentioned above, the investigation did not include any binders with high temperature PG grades lower than 64°C. The addition of these binders would validate findings in this study. Lastly, the mixtures were fine graded mixtures, thereby future investigations should involve coarse, open graded and gap graded mixtures.

REFERENCES

1. Hot mix asphalt materials, mixture design and construction. National Center for Asphalt Technology; 1996.

2. Kliewer JE, Bell CA, Sosnovske DA. Investigation of the relationship between field performance and laboratory aging properties of asphalt mixtures. ASTM STP 1995;1265:3–20.

3. Bishara SW, McReynolds RL. Laboratory aging and annealing of asphalt binder by microwave radiation. Transport Res Rec: J Transport Res Board 1996;1535:98–107.

4. Elseifi MA, Flintsch GW, Al-Qadi IL. Quantitative effect of elastomeric modification on binder performance at intermediate and high temperatures. J Mater Civ Eng, ASCE 2003;15:32–40.

5. Huang S-C, Tia M, Ruth BE. Laboratory aging methods for simulation of field aging of asphalts. J Mater Civ Eng, ASCE 1996:147–52.

6. Liang RY, Lee SH. Short-term and long-term aging behavior of rubber modified asphalt paving mixture. Transport Res Rec: J Transport Res Board 1996;1530:11–7.

7. Mihai OM, Arindam B. Stiffness m-value and the low temperature relaxation properties of asphalt binders. Road Mater Pav Des 2004;5(1):121–31.

8. Ove LB, Ivar H. The influence of filler materials on rheology and ageing of filler bitumen mixes. Road Mater Pav Des 2003;4(4):455–69.

9. Soon-Jae Lee, Serji N. Amirkhanian, Kwang W. Kim. Laboratory evaluation of the effects of short-term oven aging on asphalt binders in asphalt mixtures using HP-GPC. Construction and Building Materials, ISSN: 0950-0618, Vol: 23, Issue: 9, Page: 3087-3093Publication Year: 2009.

10. David A. Anderson, Ramon Bonaquist. Investigation of Short-Term Laboratory Aging of Neat and Modified Asphalt Binders. NCHRP Project 09-36.

11. Advanced Research Associates. 2002 Design Guide: Design of New and Rehabilitated Pavement Structures. NCHRP 1-37A Project, National Cooperative Highway Research Program. National Research Council. Washington, D.C (2004).

12. Andrei, D., M. W. Witczak, and M. W. Mirza. Development of a Revised Predictive Model for the Dynamic (Complex) Modulus of Asphalt Mixtures. Inter Team

Technical Report prepared for the NCHRP 1-37A Project. Department of Civil Engineering, University of Maryland, College Park, MD. (1999).

13. Bari, J. Development of a New Revised Version of the Witczak E* Predictive Models for Hot Mix Asphalt Mixtures. Ph.D. Dissertation. Arizona State University (2005).

14. Dongré, R., L. Myers, J. D'Angelo, C. Paugh, and J. Gudimettla. Field Evaluation of Witczak and Hirsch Models for Predicting Dynamic Modulus of Hot-Mix Asphalt. *Journal of the Association of Asphalt Paving Technologists* (AAPT), Vol. 74 (2005).

15. Christensen, Jr., D. W., T. K. Pellinen, and R. F. Bonaquist. Hirsch Model for Estimating the Modulus of Asphalt Concrete. *Journal of the Association of Asphalt Paving Technologists* (AAPT), Vol. 72(2003).

16. Al-Khateeb, G., A. Shenoy, N. Gibson, T. Harman. A New Simplistic Model for Dynamic Modulus Predictions of Asphalt Paving Mixtures. Association of Asphalt Paving Technologists Annual Meeting. Paper Preprint CD (2006).

17. Donald W. Christensen & Ramon Bonaquist. Improved Hirsch model for estimating the modulus of hot-mix asphalt, Road Materials and Pavement Design, 16:sup2, 254-274, DOI: 10.1080/14680629.2015.1077635 (2015).

18. Dickinson, E.J., and Witt, H.P. "The Dynamic Shear Modulus of Paving Asphalts as a Function of Frequency," Transactions of the Society of Rheology, vol. 18, no. 4, pp. 591-606. 1974.

19. Christensen, D. W., and D. A. Anderson. "Interpretation of dynamic mechanical test data for paving grade asphalt cements (with discussion)." Journal of the Association of Asphalt Paving Technologists 61. 1992.

20. Stastna, J., L. Zanzotto, and J. Berti. "How Good Are Some Rheological Models of Dynamic Material Functions of Asphalt? (With Discussion)." Journal of the Association of Asphalt Paving Technologists 66 (1997).

21. Minnesota Department of Transportation. *Asphalt Binder Multiple Stress Creep Recovery Overview*. Saint Paul, MN: Minnesota Department of Transportation: 2015.

22. D'Angelo, J., R. Kluttz, R. Dongre, K. Stephens, and L. Zanzotto. "Revision of the Superpave High Temperature Binder Specification: The Multiple Stress Creep Recovery Test." *Journal of Association of Asphalt Paving Technologists* 76. 2007: 123-162.

23. Zhang, J., L.F. Walubita, A.N.M Faruk, P. Karki, and G.S. Simate. "Use of the MSCR test to characterize the asphalt binder properties relative to HMA rutting performance – A laboratory study." *Construction and Building Materials* 94. 2015: 218-227.

24. Laukkanen, O. V., H. Soenen, T. Pellinen, S. Heyrman, and G. Lemoine. "Creep-Recovery Behavior of Bituminous Binders And its Relation to Asphalt Mixture Rutting." *Materials and Structures*, 48(12). 2015: 4039-4053.

25. Leahy, R.B, E. T. Harrigan, and H.V. Quintus. 1994. *Validation of Relationships Between Specification Properties and Performance*. Report no. SHRP-A-409. Washington DC. Strategic Highway Research Program, National Research Council. 1994.

26. Bouldin, M., G. Row, J. Souse, and J. Shamrock . "Mix Rheology - a tool for predicting the high performance of hot mix asphalt." *Proceedings, Association of Asphalt* Paving Technologies, 63 (1994), 218-227.

27. DuBois, E., Mehta, Y., & Nolan, A. Correlation between multiple stress creep recovery (MSCR) results and polymer modification of binder. *Construction and Building Materials*, *65.* (2014), 184-190.

28. M.J.Ayazi, A. Moniri, P. Barghabany, Moisture susceptibility of warm mixed reclaimed asphalt pavement containing Sasobit and Zycotherm additives, Pet. Sci. Technol. 35 (2017) 890–895.

29. H. Behbahani, M.J. Ayazi, A. Moniri, Laboratory investigation of rutting performance of warm mix asphalt containing high content of reclaimed asphalt pavement, Pet. Sci. Technol. 35 (2017) 1556–1561.

30. H. Ziari, R. Babagoli, M. Ameri, A. Akbari, Evaluation of fatigue behavior of hot mix asphalt mixtures prepared by bentonite modified bitumen, Constr. Build. Mater. 68 (2014) 685–691.

31. H. Ziari, A. Amini, A. Goli, D. Mirzaeiyan, Predicting rutting performance of carbon nano tube (CNT) asphalt binders using regression models and neural networks, Constr. Build. Mater. 160 (2018) 415–426.

32. F. Haddadi, M. Ameri, M.H. Mirabimoghadam, H.R.A. Hosseini, Validation of a simplified method in viscoelastic continuum damage (VECD) model developed for flexural mode of loading, Constr. Build. Mater. 95 (2015) 892–897.

33. A. Kavussi, P. Barghabany, Investigating fatigue behavior of nanoclay and nano hydrated lime modified bitumen using LAS test, J. Mater. Civ. Eng. 28 (2015) 04015136.

34. H. Ziari, M. Nakhaei, A. Akbari Nasrekani, A. Moniri, Characterization of rutting resistance of EBS-modified asphalt mixtures, Pet. Sci. Technol. 34 (2016) 1107–1112.
35. H.U. Bahia, D. Hanson, M. Zeng, H. Zhai, M. Khatri, R. Anderson, NCHRP Report 459: Characterization of modified asphalt binders in superpave mix design, Transportation Research Board, 2001.

36. M. Ameri, S. Nowbakht, M. Molayem, M.H. Mirabimoghaddam, A study on fatigue modeling of hot mix asphalt mixtures based on the viscoelastic continuum damage properties of asphalt binder, Constr. Build. Mater. 106 (2016) 243–252.

37. D. Anderson, Y. Hir, M. Marasteanu, J.-P. Planche, D. Martin, G. Gauthier, Evaluation of fatigue criteria for asphalt binders, Transp. Res. Rec.: J. Transp. Res. Board (2001) 48–56.

38. H. Ziari, A. Moniri, R. Imaninasab, M. Nakhaei, Effect of copper slag on performance of warm mix asphalt, Int. J. Pavement Eng. (2017) 1–7.

39. F. Zhou, W. Mogawer, H. Li, A. Andriescu, A. Copeland, Evaluation of Fatigue Tests for Characterizing Asphalt Binders, J. Mater. Civ. Eng. 25 (2012) 610–617.

40. W. Martono, H.U. Bahia, J. D'angelo, Effect of testing geometry on measuring fatigue of asphalt binders and mastics, J. Mater. Civil Eng. 19 (2007) 746–752.

41. K. Bonnetti, K. Nam, H. Bahia, Measuring and defining fatigue behavior of asphalt binders, Transp. Res. Rec.: J. Transp. Res. Board (2002) 33–43.

42. J.-P. Planche, D. Anderson, G. Gauthier, Y. Le Hir, D. Martin, Evaluation of fatigue properties of bituminous binders, Mater. Struct. 37 (2004) 356–359.

43. C. Johnson, Evaluation of Accelerated Procedures for Fatigue Characterization of Asphalt Binders, ph.D, Wisconsin, 2010.

44. C. Hintz, R. Velasquez, C. Johnson, H. Bahia, Modification and validation of linear amplitude sweep test for binder fatigue specification, Transp. Res. Rec.: J. Transp. Res. Board 2207 (2011) 99–106.

45. H.-J. Lee, Y.R. Kim, Viscoelastic constitutive model for asphalt concrete under cyclic loading, J. Eng. Mech. 124 (1998) 32–40.

46. H. Lee, Y. Kim, S. Lee, Prediction of asphalt mix fatigue life with viscoelastic material properties, Transp. Res. Rec.: J. Transp. Res. Board (2003) 139–147.

47. J.S. Daniel, W. Bisirri, Y.R. Kim, fatigue evaluation of asphalt mixtures using dissipated energy and viscoelastic continuum damage approaches, J. Assoc. Asphalt Paving Technol. 73 (2004) 557–583.

48. J.S. Daniel, Y.R. Kim, Development of a simplified fatigue test and analysis procedure using a viscoelastic continuum damage model, J. Assoc. Asphalt Paving Technol. 71 (2002) 619–650.

49. S.W. Park, Y.R. Kim, R.A. Schapery, A viscoelastic continuum damage model and its application to uniaxial behavior of asphalt concrete, Mech. Mater. 24 (1996) 241–255.

50. M. Sabouri, Y. Kim, Development of a failure criterion for asphalt mixtures under different modes of fatigue loading, Transp. Res. Rec.: J. Transp. Res. Board (2014) 117–125.

51. M. Sabouri, T. Bennert, J.S. Daniel, Y.R. Kim, Fatigue and rutting evaluation of laboratory-produced asphalt mixtures containing reclaimed asphalt pavement, Transp. Res. Rec.: J. Transp. Res. Board (2015) 32–44.

52. A. Norouzi, M. Sabouri, Y. Richard Kim, Fatigue life and endurance limit prediction of asphalt mixtures using energy-based failure criterion, Int. J. Pavement Eng. 18 (2017) 990–1003.

53. C. Clopotel, R. Velasquez, H. Bahia, F. Pérez-Jiménez, R. Miró, R. Botella, Relationship between binder and mixture damage resistance at intermediate and low temperatures, Transp. Res. Rec.: J. Transp. Res. Board (2012) 39–47.

54. M. Sabouri, D Mirzaiyan, A Moniri, Effectiveness of Linear Amplitude Sweep (LAS) asphalt binder test in predicting asphalt mixtures fatigue performance, Constr. Build. Mater. 171 (2018) 281–290.

55. T. AASHTO, 315 Standard Method of Test for Determining the Rheological Properties of Asphalt Binder Using a Dynamic Shear Rheometer (DSR), American Association of State Highway and Transportation Officials, Washington, DC (2012 R2016).

56. A. TP101, Standard method of test for estimating fatigue resistance of asphalt binders using the linear amplitude sweep, American Association of State Highway and Transportation Officials, Washington, DC, 2012.

57. T. AASHTO, 240-09 Effect of Heat and Air on a Moving Film of Asphalt Binder (Rolling Thin-Film Oven Test), AASHTO Standard Specifications for Transportation Materials and Methods of Sampling and Testing, 2011.

58. C. Hintz, R. Velasquez, C. Johnson, H. Bahia, Modification and validation of linear amplitude sweep test for binder fatigue specification, Transp. Res. Rec.: J. Transp. Res. Board 2207 (2011) 99–106.

59. M. Ameri, S. Nowbakht, M. Molayem, M.H. Mirabimoghaddam, A study on fatigue modeling of hot mix asphalt mixtures based on the viscoelastic continuum damage properties of asphalt binder, Constr. Build. Mater. 106 (2016) 243–252.

60. S. Shen, S. Carpenter, Development of an asphalt fatigue model based on energy principles, J. Assoc. Asphalt Paving Technol. 76 (2007) 525–573.

61. AASHTO. Standard method of test for determining the fatigue life of compacted asphalt mixtures subjected to repeated flexural bending. AASHTO T 321, 2014, Washington D.C.

62. G.M. Rowe, P. Blankenship, M.J. Sharrock, T. Bennert. The fatigue performance of asphalt mixtures in the four point bending beam fatigue test in accordance with AASHTO and ASTM analysis methods. Presented at the 5th Eurasphalt & Eurobitume Congress, June 13-15th 2012, Istanbul. http://www.h-a-d.hr/pubfile.php?id=667.

63. C. Wang, C. Castorena, J. Zhang, Y.R. Kim, Unified failure criterion for asphalt binder under cyclic fatigue loading, J. Assoc. Asphalt Paving Technol. 84 (2015) 269–299.

64. U.A. Mannan, M.R. Islam, R.A. Tarefder, Effects of recycled asphalt pavements on the fatigue life of asphalt under different strain levels and loading frequencies, Int. J. Fatigue 78 (2015) 72–80.

65. C.M. Johnson, Estimating Asphalt Binder Fatigue Resistance Using an Accelerated Test Method Ph.D. Dissertation, University of Wisconsin- Madison, Madison, WI, 2010.

66. AASHTO. Standard method of test for estimating fatigue resistance of asphalt binders using the Linear Amplitude Sweep. AASHTO TP 101, 2016, Washington D.C.

67. M. Sabouri, Y.R. Kim, Development of a failure criterion for asphalt mixtures under different modes of fatigue loading, Transp. Res. Rec. 2447 (2014) 117–125.

68. M. Sabouri, T. Bennert, J.S. Daniel, Y.R. Kim, Fatigue and rutting evaluation of laboratory-produced asphalt mixtures containing reclaimed asphalt pavement, Transp. Res. Rec. 2506 (2015) 32–44.

69. W. Cao, A. Norouzi, Y.R. Kim, Application of viscoelastic continuum damage approach to predict fatigue performance of Binzhou perpetual pavements, J. Traffic Transp. Eng. 3 (2016) 104–115.

70. F. Safaei, C. Castorena, Y.R. Kim, Linking asphalt binder fatigue to asphalt mixture fatigue performance using viscoelastic continuum damage modeling, Mech. Time-Depend. Mater. 20 (2016) 299–323.

71. W. Cao, C. Wang. A new comprehensive analysis framework for fatigue characterization of asphalt binder using the Linear Amplitude Sweep test. Construction and Building Materials 171 (2018) 1–12

72. Wang, Y., and Y. R. Kim. Development of a Pseudo Strain Energy-Based Fatigue Failure Criterion for Asphalt Mixtures. International Journal of Pavement Engineering, 2017, DOI: 10.1080/10298436.2017.1394100.

73. Van der Poel, C. *A General System Describing Visco-Elastic Properties of Bitumens and Its Relation to Routine Test Data*. Journal of Applied Chemistry, Vol. 4, Part 5, pp. 221-236, and Shell Bitumen Reprint No 9, 1954.

74. François Olard & Hervé Di Benedetto. *General "2S2P1D" Model and Relation Between the Linear Viscoelastic Behaviours of Bituminous Binders and Mixes, Road Materials and Pavement Design*, (2003). 4:2, 185-224.

75. Bonaquist, R. *Wisconsin mixture characterization using the Asphalt Mixture Performance Tester (AMPT) on historical aggregate structures* (WHRP 09-03). Madison, WI: Wisconsin Department of Transportation (2010).

76. Rowe, G. M., King, G., and Anderson, M., "*The Influence of Binder Rheology on the Cracking of Asphalt Mixes in Airport and Highway Projects*", Journal of Testing and Evaluation, 2014, Vol. 42, No. 5.

77. Johnson CM. *Estimating asphalt binder fatigue resistance using an accelerated test method*. PhD thesis, University of Wisconsin–Madison; 2010.

78. AASHTO R 30, *Standard Practice for Mixture Conditioning of Hot Mix Asphalt AASHTO*, Washington, D.C. (2012)

79. Heithaus, J. J. and R. W. Johnson "A Microviscometer Study of Road Asphalt Hardening in the Field and Laboratory." Journal of the Association of Asphalt Paving Technologists, (1958). Vol. 27, pp. 17–34.

80. Traxler, R. N. "Relation Between Asphalt Composition and Hardening by Volatization and Oxidation." Journal of the Association of Asphalt Paving Technologists, (1961) Vol. 27, pp. 359–377.

81. Chipperfield, E. H. and T. R. Welch. "Studies on the Relationships Between the Properties of Road Bitumens and Their Service Performance." Journal of the Association of Asphalt Paving Technologists, (1967).Vol. 36, pp. 421–488.

82. Lund, J. W. and J. E. Wilson "Evaluation of Asphalt Aging in Hot Mix Plants." Journal of the Association of Asphalt Paving Technologists, (1984). Vol. 53, pp. 1–18.

83. Lund, J. W. and J. E. Wilson. "Field Validation of Asphalt Aging in Hot Mix Plants." Journal of the Association of Asphalt Paving Technologists, (1986), Vol. 55, pp. 92–119.

84. Topal, A. and B. Sengoz. "Effect of SBS Polymer Modified Bitumen on the Ageing Properties of Asphalt." Proceedings of the 4th Eurasphalt and Eurobitume Congress, Copenhagen, Denmark. European Asphalt Pavement Association (2008).

85. Zhao, D., M. Lei, and Z. Yao "Evaluation of Polymer-Modified Hot-Mix Asphalt: Laboratory Characterization." Journal of Materials in Civil Engineering, (2009). Vol. 21, No. 4, pp. 163–170.

86. Morian, N., E. Y. Hajj, C. J. Glover, and P. Sebaaly "Oxidative Aging of Asphalt Binders in Hot-Mix Asphalt Mixtures." Transportation Research Record: Journal of the Transportation Research Board, No. 2207, Transportation Research Board, Washington, D.C. (2011), pp. 107–116.

87. Rashwan, M. H. and R. C. Williams "An Evaluation of Warm Mix Asphalt Additives and Reclaimed Asphalt Pavement on Performance Properties of Asphalt Mixtures." 91st Annual Meeting of the Transportation Research Board Compendium of Papers DVD, Transportation Research Board, Washington, D.C. (2011).

88. Mogawer, W., T. Bennert, J. S. Daniel, R. Bonaquist, A. Austerman, and A. Booshehrian "Performance Characteristics of Plant Produced High RAP Mixtures." Journal of the Association of Asphalt Paving Technologists, (2012). Vol. 80, pp. 403–439.

89. Daniel, J. S., T. Bennert, Y. R. Kim, and W. Mogawer "TPF 5(230): Evaluation of Plant-Produced RAP Mixtures in the Northeast." Pooled Fund Phase I Interim Report, Federal Highway Administration. (2014).

90. ASTM. Effect of heat and air on a moving film of asphalt (rolling thin film oven test). Standard D2872-88 (reapproved 1995). Philadelphia, Pa: American Society for Testing and Materials; 1995.

91. Aschenbrener, T. and N. Far "Short-Term Aging of Hot Mix Asphalt." Colorado Department of Transportation Public Report No. CDOT-DTD-R-94-11. (1994).

92. Epps Martin, A., E. Arambula, F. Yin, L. Garcia Cucalon, A. Chowdhury, R. Lytton, J. Epps, C. Estakhri, and E. S. Park NCHRP Report 763: Evaluation of the Moisture Susceptibility of WMA Technologies. Transportation Research Board, Washington, D.C. (2014).

93. Newcomb, D., A. E. Martin, F. Yin, E. Arambula, E. S. Park, A. Chowdhury, R. Brown, C. Rodezno, N. Tran, E. Coleri, and D. Jones. NCHRP Report 815: Short-Term Laboratory Conditioning of Asphalt Mixtures. Transportation Research Board of the National of Academies. Washington, D.C. (2015).

94. Pellinen, T.K. Investigation of the Use of Dynamic Modulus as an Indicator of HotMix Asphalt Performance, Ph.D. dissertation, Arizona State University, Tempe, AZ. (2001).

95. Schwartz, C. W. "Evaluation of the Witczak dynamic modulus prediction model." Proc., the 84th Annual Meeting of the Transportation Research (CD-ROM), Transportation Research Board, Washington, D.C, (2005).

96. D'Angelo, J., Paugh, C., and Gudimettla, J. "Field evaluation of Witczak and Hirsch models for predicting dynamic modulus of hot-mix asphalt." Journal of the Association of Asphalt Paving Technologists, (2005). 74 (CD-ROM).

97. Bari, J. and Witczak, M.W. "Development of a new revised version of the Witczak E* predictive model for hot mix asphalt mixtures." Journal of the Association of Asphalt Paving Technologists, (2006). 75, 381- 423.

98. Al-Khateeb, G., Shenoy, A., Gibson, N., and Harman, T. "A new simplistic model for dynamic modulus predictions of asphalt paving mixtures." Journal of the Association of Asphalt Paving Technologists, (2006). 75 (CD-ROM).

99. Azari, H., Al-Khateeb, G., Shenoy, A., and Gibson, N. "Comparison of simple performance test |E*| of accelerated loading facility mixtures and prediction |E*|: use of NCHRP 1-37A and Witczak's mew equations." Transportation Research Record, (2007). No.1998, pp. 1-9.

100. LYTTON, R.L., UZAN, J., FERNANDO, E.G., ROQUE, R., HILTUNEN, D., STOFFELS, S.M., "Development and Validation of Performance Prediction Models and Specifications for Asphalt Binders and Paving Mixes", SHRP-A-357, Strategic Highway Research Program , National Research Council, Washington, DC, 1993.

101. FRANKEN, L., VANELSTRAETE, A., "Relation between mix stiffness and binder complex modulus", The Rheology of Bituminous Binders, European Workshop, Brussels, 5-7 April 1995.

102. ZENG, M., BAHIA, H.U., ZHAI, H., ANDERSON, M.R., TURNER, P., "Rheological modeling of modified asphalt binders and mixtures", Annual Meeting of the Association of Asphalt paving Technologists, 2001.

103. Ceylan, H., Kim, S., and Gopalakrishnan, K. "Hot mix asphalt dynamic modulus prediction models using neural network approach." Proc., ANNIE 2007, ASME, New York. (2007).

104. TRB Circular. "Use of artificial neural networks in geomechanical and pavement systems." Number E-C012, Transportation Research Board, National Research Council, Washington, D.C.

105. Tsoukalas, L. H., and Uhrig, R. E. Fuzzy and neural approaches in engineering, Wiley, New York. (1997).

106. H. Ceylan, C.W. Schwartz, S. Kim, K. Gopalakrishnan Accuracy of predictive models for dynamic modulus of hot-mix asphalt Journal of Materials in Civil Engineering, 21 (2009), pp. 286-293

107. Kim YR, Underwood BS, Sakhaei Far M, Jackson N, Puccinelli J. LTPP computed parameter: dynamic modulus. Final report for project: DTFH61-02-D-00139, Washington, D.C.: Federal Highway Administration; 2009.

108. Singh D, Zaman M, Commuri S. Inclusion of aggregate angularity, texture, and form in estimating dynamic modulus of asphalt mixes. Road Mater Pavement Des 2012;13:327–44.

109. Dai Q. Prediction of dynamic modulus and phase angle of stone-based composites using a micromechanical finite-element approach. ASCE J Mater Civ Eng 2010;22:618–27.

110. You Z, Buttlar WG. Micromechanical modeling approach to predict compressive dynamic moduli of asphalt mixtures using the distinct element method. J Transport Res Rec 2006;1970:73–83.

111. Sakhaeifar, M.S., Richard Kim, Y. and Kabir, P., 2015. New predictive models for the dynamic modulus of hot mix asphalt. Construction and Building Materials, 76, 221–231.10.1016/j.conbuildmat.2014.11.011

112. Jemison, H. B., B. L. Burr, R. R. Davison, J. A. Bullin, and C. J. Glover. "Application and use of the ATR, FT-IR method to asphalt aging studies." Fuel Science &Technology International, 1992.10(4-6): 795-808.

113. Petersen, J. Claine, and Ronald Glaser. "Asphalt oxidation mechanisms and the role of oxidation products on age hardening revisited." Road Materials and Pavement Design, (2011).12(4): 795-819.

114. Huang, Y. H. *Pavement Analysis and Design*. New Jersey: Pearson Education Inc. 2004.

115. Bouldin, M., G. Row, J. Souse, and J. Shamrock. Mix Rheology - a tool for predicting the high performance of hot mix asphalt." 1994. *Asphalt Paving Technology*, 63, 218-227.

116. D'Angelo, J., R. Kluttz, R. Dongre, K. Stephens, and L. Zanzotto. Revision of the Superpave High Temperature Binder Specification: The Multiple Stress Creep Recovery Test. *Journal of Association of Asphalt Paving* Technologists. 2007. 76: 123-162.

117. Minnesota Department of Transportation. *Asphalt Binder Multiple Stress Creep Recovery Overview*. Saint Paul, MN: Minnesota Department of Transportation: 2015.

118. Zhang, J., L.F. Walubita, A.N.M Faruk, P. Karki, and G.S. Simate. Use of the MSCR test to characterize the asphalt binder properties relative to HMA rutting performance – A laboratory study. 2015. *Construction and Building Materials* 94: 218-227.

119. Laukkanen, O. V., H. Soenen, T. Pellinen, S. Heyrman, and G. Lemoine. Creep-Recovery Behavior of Bituminous Binders And its Relation to Asphalt Mixture Rutting. *Materials and Structures*, 2015. 48(12): 4039-4053.

120. Leahy, R.B, E. T. Harrigan, and H.V. Quintus. *Validation of Relationships Between Specification Properties and Performance*, *SHRP-A-409*. Washington DC. Strategic Highway Research Program, National Research Council. 1994.

121. DuBois, E., Y. Mehta, and A. Nolan. Correlation between Multiple Stress Creep Recovery (MSCR) Results and Polymer Modification of Binder. *Construction and Building Materials*, 2014. *65*, 184-190.

122. Domingos, M.D.I., A.L. Faxina, and L.L.B Bernucci. Characterization of the rutting potential of modified asphalt binders and its correlation with the mixture's rut resistance. *Construction and Building Materials,* 2017. 207-213.

123. American Association of State Highway Transportation Officials. 2012. *Standard Method of Test for Determining the Rheological Properties of Asphalt Binder Using DSR*. AASHTO T 315. Washington D.C.: American Association of State Highway Transportation Officials: 2012.

124. American Association of State Highway Transportation Officials. 2014. *Standard Method of Test for Muliple Stress Creep Recovery (MSCR) Test of Asphalt Binder Using a Dynamic Shear Rheometer (DSR)*. AASHTO T 350. Washington D.C.: American Association of State Highway Transportation Officials: 2014.

125. American Association of State Highway Transportation Officials. 2016. *Standard Method of Test for Bulk Specific Gravity (Gmb) of Compacted Hot Mix Asphalt (HMA) Using Saturated Surface-Dry Specimens* AASHTO T166. Washington D.C.: American Association of State Highway Transportation Officials: 2016.

126. Moulthrop, J., and M. Witczak. *NCHRP report 704: A Performance-Related Specification for Hot-Mixed Asphalt*." Transportation Research Board, Washington, D.C. 2011.

127. El-Basyouny, M., and M. Jeong. Effective temperature for analysis of permanent deformation and fatigue distress on asphalt mixtures. *Transportation Research Record: Journal of the Transportation Research Board*. 2009. 2127: 155–163.

128. American Association of State Highway Transportation Officials. 2017. *Standard Method of Test for Determining the Dynamic Modulus and Flow Number for Asphalt Mixtures Using the Asphalt Mixture Performance Tester (AMPT)*. AASHTO T 378. Washington D.C.: American Association of State Highway Transportation Officials: 2017.

129. Mohseni, A. and M. Symons, Improved AC Pavement Temperature Models from LTPP Seasonal Data, Presented at 77th Annual TRB Conference, Washington D.C., 1998.

130. Mohseni, A., S. Carpenter and J. D'Angelo. Development of SUPERPAVE High-Temperature Performance Grade (PG) Based on Rutting Damage (with discussion and closure). *Journal of the Association of Asphalt Paving Technologists*, 2005. 74.

131. J. P. Hallin. *Development of the 2002 Guide for the Design of New and Rehabilitated Pavement Structures: Phase II*. National Cooperative Highway Research Program, Transportation Research Board, 2004.

132.Stevens, R., J. Stempihar, B. S. Underwood, and P. Pal. Evaluation of Multiple Stress Creep and Recovery (MSCR) Data for Arizona. *International Journal of Pavement Research and Technology*. 2015. 8(5): 337-345.

133.J.R. Donoghue. Variable Screening for Cluster Analysis. *ETS Research Report Series* 1994. No. 2 (1994): I-55.

134.Salim, R., Gundla, A., Zalghout A, Underwood, B.S., and K. E. Kaloush, Relationship between Asphalt Binder Parameters and Asphalt Mixture Rutting. *Transportation Research Record: Journal of the Transportation Research Board*, TRB, National Research Council. Washington, D.C. (2019).

135.Salim, R., Gundla, A, Underwood, B.S., and K. E. Kaloush, Effect of MSCR Percent Recovery on Performance of Polymer Modified Asphalt Mixtures. *Journal of the Transportation Research Board*, TRB, National Research Council. Washington, D.C. (2019).

136.Asphalt Institute (AI). "How Many U.S. Roads are Paved with Asphalt?" Online. http://asphaltmagazine.com/how-many-u-s-roads-are-paved-with-asphalt/. Accessed July 2018.

137.Huang, Y. H. *Pavement Analysis and Design*. New Jersey: Pearson Education Inc. 2004.

138.Anderson, D.A., D.W. Christensen, H.U. Bahia, R. Dongre, M.G. Sharma, C.E. Antle, J. Button. 1994. *Binder Characterization and Evaluation, Volume 3: Physical Characterization*. Strategic Highway Research Program. Report SHRP-A-369, Washington, D.C. Strategic Highway Research Program, National Research Council. 1994.

139.Buncher, M., and C. Rosenberger. Understanding the True Economics of Using Polymer Modified Asphalt through Life Cycle Cost Analysis. *Asphalt*, 20(2), 2005. 28-30.

140.Sargand, S.M., and S.S. Kim.. "Performance evaluation of polymer modified and unmodified Superpave mixes." In *Second International Symposium on Maintenance and Rehabilitation of Pavements and Technological Control*, 2001. Alabama, 01-147.

141.Bouldin, M., G. Row, J. Souse, and J. Shamrock. "Mix Rheology - a Tool for Predicting the High Performance of Hot Mix Asphalt." *Proceedings, Association of Asphalt* Paving Technologies, 1994. 63, 218-227.

142.D'Angelo, J., R. Kluttz, R. Dongre, K. Stephens, and L. Zanzotto. Revision of the Superpave High Temperature Binder Specification: The Multiple Stress Creep Recovery Test. *Journal of Association of Asphalt Paving Technologists*, 2007. 76: 123-162.

143.Minnesota Department of Transportation. *Asphalt Binder Multiple Stress Creep Recovery Overview*. Saint Paul, MN: Minnesota Department of Transportation: 2015.

144.Zhang, J., L.F. Walubita, A.N.M Faruk, P. Karki, and G.S. Simate. Use of the MSCR test to characterize the asphalt binder properties relative to HMA rutting performance – A laboratory study. *Construction and Building Materials*, 2015. 94: 218-227.

145.Laukkanen, O.V., H. Soenen, T. Pellinen, S. Heyrman, and G. Lemoine. Creep-Recovery Behavior of Bituminous Binders And its Relation to Asphalt Mixture Rutting. *Materials and Structures*, 2015. 48(12): 4039-4053.

146.Anderson, R.M. "Implementation of the MSCR Test and Specification." Presented *at the AMAP Annual Meeting,* 2016.

147.Underwood, B.S. Kim, Y.R. and M.N. Guddati. Improved Calculation Method of Damage Parameter in Viscoelastic Continuum Damage Model. *International Journal of Pavement Engineering*, 2010. 11(6), 459-476.

148.Underwood, B.S., C. Baek, and Y.R. Kim. Simplified Viscoelastic Continuum Damage Model as Platform for Asphalt Concrete Fatigue Analysis. *Transportation Research Record: Journal of the Transportation Research Board*, 2012.

149.El-Basyouny, M., and M. Jeong. Effective Temperature for Analysis of Permanent Deformation and Fatigue Distress on Asphalt Mixtures. *Transportation Research Record: Journal of the Transportation Research Board*, 2009. 2127: 155–163.

150.Stevens, R., J. Stempihar, B.S. Underwood, and P. Pal. 2015. Evaluation of Multiple Stress Creep and Recovery (MSCR) Data for Arizona. *International Journal of Pavement Research and Technology*, 2015. 8(5): 337-345.

151.C. Hintz, H.U. Bahia, Simplification of Linear Amplitude Sweep test and specification parameter, Transp. Res. Rec. 2370 (2013) 10–16.

152.Christensen, Jr., D. W., and N. Tran. Relationships between Mixture Fatigue Performance and Asphalt Binder Properties. *Journal of the Association of Asphalt Paving Technologists* (AAPT) (2019).

153.Gundla. A. Understanding Viscoelastic Behavior of Asphalt Binders through Molecular Structure Investigation. Ph.D. Dissertation. ASU (2018).

APPENDIX A

TESTS ON ASPHALT BINDER AND MIXTURES

AASHTO T240 and R28 for conditioning asphalt binder samples

AASHTO T240 (Rolling Thin Film Oven) is used to replicate short term aging of asphalt binder and AASHTO R28 (Pressure Aging Vessel aging) is used to replicate long term aging. In the AASHTO T240 procedure the Rolling Thin Film Oven (RTFO), Figure A-1a and b, is first set at 163 ± 1°C to attain thermal equilibrium. For sample preparation, 35 ± 0.5 g of the unaged asphalt binder is poured into a specially designed glass bottle, Figure A-1c. The poured asphalt is allowed to cool for a minimum of 1 hour and a maximum of 3 hours after which the bottles are inserted into the rotating rack of the RTFO. A maximum of eight bottles can be inserted in one cycle. Inside the oven, the bottles rotate with a speed of 15 rotations per minute. The unaged binders are subjected to an air flow of 4 liters/min at a constant temperature of 163 ± 1°C for a period of 85 minutes. Subsequently, the aged material is scraped from inside the bottle using a specially designed tool and is stored for future testing or transferred to a pan for further conditioning via AASHTO R28.

Figure A-1. (a) Overview of RTFO, (b) Inside the RTFO, and (c) RTFO Bottle.

In AASHTO R28, the pressurized aging vessel (PAV), Figure A-2. a, is first set to the desired testing temperature plus 5°C and allowed to equilibrate. For the sample preparation, 50 ± 0.5 g of the RTFO aged material is poured onto each of the specially designed PAV pans. These pans are then stacked in a holder, Figure A-2. b, which is inserted into the vessel. Up to 10 pans can be stacked in the holder. However, there is no specified minimum or maximum number to use during the process. The decision is based on judgment as to how much amount would be required for DSR and BBR testing. For the current project, five to six pans were used during any given test. After placing the pan holder inside the vessel, the vessel is first allowed to heat to the required temperature. When the vessel is within 5°C of the desired aging temperature it is pressurized in 0.2 MPa increments starting with 0.1

MPa until 2.1 MPa is reached. When both the desired aging temperature and aging pressure are achieved, the asphalt binder is conditioned for 20 hours ± 10 minutes. Subsequently, the vessel is depressurized and the material is scraped from the pans and stored in tins for future testing.

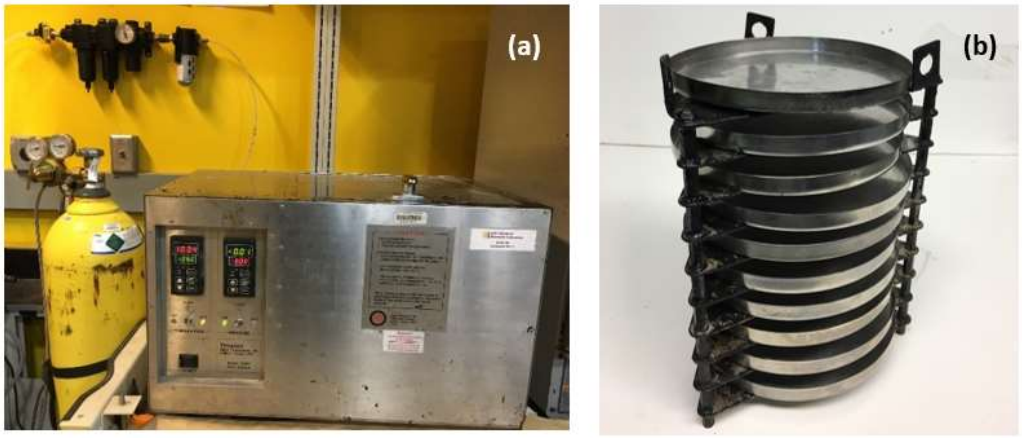

Figure A-2. (a) Overview of PAV and (b) PAV Pan and Pan Holder.

AASHTO TP101-Estimating Fatigue Resistance of Asphalt Binders Using the Linear Amplitude Sweep

The LAS test evaluates the ability of asphalt binder to resist fatigue damage. This test is basically an oscillatory strain sweep test that generates damage to the binder by applying linearly increasing load amplitudes. The LAS test consists of two steps: first, a frequency sweep is performed in order to get information about undamaged material properties and evaluate the rheological characteristics of the binder. Second, the damage characteristics of the binder is measured employing a linear amplitude strain sweep test.

Asphalt binder is first aged using T 240 (RTFOT) to represent short-term aging of asphalt pavements. The binder may be further aged using R 28 (PAV) prior to testing in order to simulate long-term aging of asphalt pavements. A sample is prepared according to T 315 (DSR) using the 8-mm parallel plate geometry with a 2-mm gap setting. The sample is tested in shear using a frequency sweep to determine its rheological properties. The sample is then tested using a series of oscillatory load cycles at systematically increasing amplitudes at a constant frequency to cause accelerated fatigue damage. The continuum damage approach is used to calculate the fatigue resistance from the rheological properties and amplitude sweep results.

Frequency sweeps were conducted at a strain amplitude of 0.1% with a range of frequencies from 0.2 to 30 Hz according to AASHTO TP101. Amplitude sweep test was done at a constant frequency of 10 Hz. The testing protocol consisted of applying a linearly increasing load from zero to 30% over 3100 cycles of loading. Two replicates were run for each binder.

The number of cycles to failure was calculated using Eq. (1). The failure definition in the LAS test is defined as 35% reduction in the initial modulus.

$$N_f=A(\gamma_{max})^B \quad (1)$$

where A and B are VECD model coefficients that depend on the material characteristics. Details of A and B parameters formulations can be found elsewhere [AASHTO TP101]. A parameter represents the materials ability to keep its integrity during loading cycles and due to accumulated damage. This parameter is directly related to the storage modulus. In other words, by decreasing the storage modulus thorough loading cycles, the A parameter decreases, which indicates the low binder resistance in maintaining its integrity during loading and due to accumulated damage. From Eq. (1), when the strain level is equal to 1, the fatigue life will be equal to A parameter, hence, A parameter can be considered as the fatigue life of the binder at a strain level of 1 (100%).

The sensitivity of the asphalt binder to strain level change is described by B parameter. Higher absolute values of B parameter indicates that the fatigue life decreases at a higher rate when strain level amplitude increases. In general, more fatigue resistant binders tend to have higher A values and lower absolute B values.

AASHTO T315 – Dynamic Shear Rheometer

AASHTO T315 uses a dynamic shear rheometer (DSR) to apply an sinusoidally oscillating and constant displacement angle to an asphalt binder sample. Encompassing the geometry setup is an environmental chamber used for maintaining the desired temperature during the test. The DSR used for the current project is a TA Instruments AR 2000 EX as shown in Figure A-3. The loading is applied via parallel plates either 25 mm with a 1 mm gap or 8 mm with a 2-mm depending on the aging level of the sample being tested. The parallel plate geometry consists of a fixed lower plate and an upper plate, which is attached to a rotating shaft / spindle. During the test the DSR equipment tracks and records the displacement angle and applied torque. These values are used to calculate the maximum applied shear stress and shear strain according to Equations (1) and (2). Additional and proprietary algorithms internal to the DSR equipment then apply additional corrections for the machine inertia, geometry inertia, bearing friction, and others. AASHTO T315 requires calculation of the dynamic shear modulus, $|G^*|$ (reported to three significant figures), the phase angle, δ (reported to the nearest 0.1 degree), and either $|G^*|/\sin\delta$ (to the nearest 0.01 kPa) or $|G^*|\sin\delta$ (to the nearest whole number). The software that controls these instruments automatically calculates these parameters and report them to the user.

$$\tau = \frac{2T}{\pi r^3} \tag{1}$$

$$\gamma = \frac{\theta r}{h} \tag{2}$$

where;

τ = shear stress;

T = torque;

r = sample radius (25 mm or 8 mm);

γ = shear strain;

θ = rotational angle; and

h = testing gap (1 mm or 2 mm).

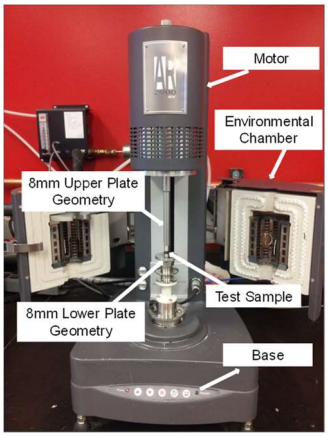

Figure A-3. Dynamic Shear Rheometer at Arizona State University.

The sample preparation for the AASHTO T315 procedure starts with pouring the asphalt binder into silicon molds, which have a designated size according to the required diameter of the sample i.e. 8 mm or 25 mm. For testing, the parallel plates are first preheated and then the sample is detached from the molds and placed between the plates. The parallel plates are then brought within 50 µm of the final testing gap for trimming. Once trimming is complete the final gap is set to obtain the desired bulge in the sample. After the test gap is set, the asphalt binder samples are conditioned at the desired testing temperature so that thermal equilibrium is achieved prior to testing. During the test, the upper geometry applies a torque commensurate to the desired strain / stress and frequency values input in the test procedure.

AASHTO T313 – Bending Beam Rheometer

AASHTO T313 evaluates the resistance of asphalt binders to low temperature cracking by measuring the material's creep stiffness and relaxation properties at low temperatures. Creep stiffness, *S*, is a measure of thermal stresses in the asphalt binder, which might build up as a result of thermal contraction. If these stresses are too high the pavement will crack. Higher values of creep stiffness are thus undesirable. Another important characteristic for asphalt binders to possess is the ability to relax the stresses quickly. When an extreme cooling event occurs, stresses build up quickly, and if not relaxed, they will exceed the critical point and cause cracks to occur.

During an AASHTO T313 test a bending beam rheometer (BBR), Figure A-4, is used to apply a constant center point load to a beam of asphalt that is 6.35 ± 0.05 mm thick, 12.7 ± 0.5 mm wide, and 127 ± 2.0 mm long (see Figure A-5). The beam is submerged in coolant ethyl alcohol in the experiments for this study, which is circulated through a chilling apparatus to maintain temperature. During the test the load and center point deflection of the asphalt beam is monitored for a period of 240 seconds. These values are used to calculate the creep stiffness according to Equation (3). The stress relaxation properties are determined by calculating the log-log slope of the creep stiffness as a function of time, Equation (4). These values are automatically computed by the BBR software. Specification parameters from the test are the creep stiffness (reported to three significant digits) and m-value (reported to the nearest 0.001) at 60 seconds. Post completion of the test, AASHTO T 313 requires reporting of creep stiffness to three significant figures and the m-value to the nearest 0.001.

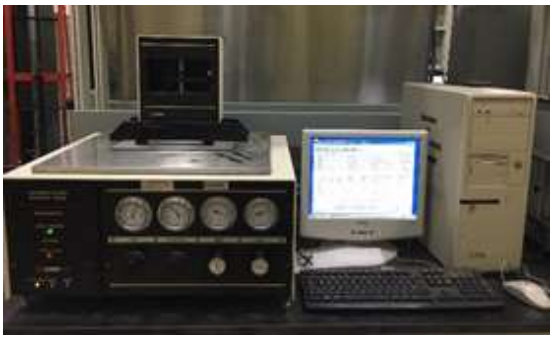

Figure A-4. Bending Beam Rheometer at Arizona State University.

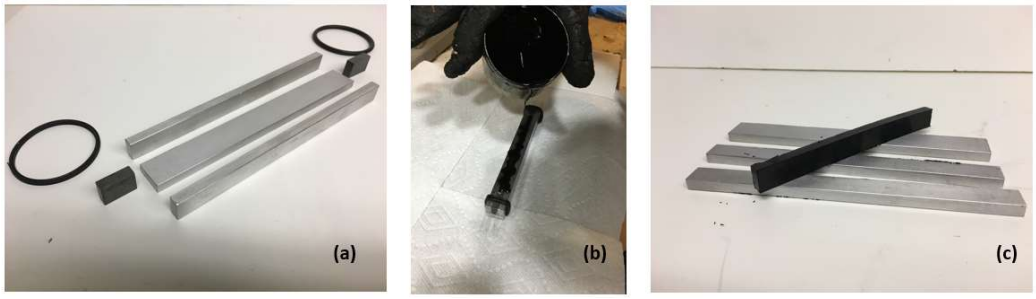

Figure A-5. (a) Disassembled BBR Mold, (b) Pouring Asphalt into Mold, and (c) Demolded Test Specimen.

$$S(t) = \frac{PL^3}{4bh^3\delta(t)} \tag{3}$$

$$m(t) = \frac{d\log S(t)}{d\log t} \tag{4}$$

As per the AASHTO M320 and M332 standards, BBR tests are performed at 10°C lower than the ultimate low temperature performance grade of the asphalt binder. The test is conducted on PAV aged residue. To cast the test specimens the asphalt is first heated to 155 to 165°C depending upon he grade of the binder and poured into molds of the appropriate dimensions, Figure A-5. After trimming and cooling the sample is demolded and placed into the instrument for testing. The test load applied as per AASHTO T313 was 980 ± 50 mN.

AASHTO T350 – Multiple Stress Creep and recovery

The Multiple Stress Creep and Recovery (MSCR) test is standardized by both the American Association of State Highway and Transportation Officials (AASHTO) and the American Society of Test Methods (ASTM): AASHTO T 350 and ASTM D7405 respectively. The essential elements in both standards are the same: a sample of asphalt 25 mm in diameter and 1 mm thick is situated between two parallel plates mounted to a DSR; the sample is conditioned to a fixed and specified temperature; the sample is loaded repeatedly with a series of square shaped stress-rest pulses (1 second loading and 9 seconds rest) at 0.1 kPa and 3.2 kPa; and quantities relating the stress input to the strain response are calculated. A typical strain response from the 10, 3.2 kPa loading cycles are shown in Figure A-6.

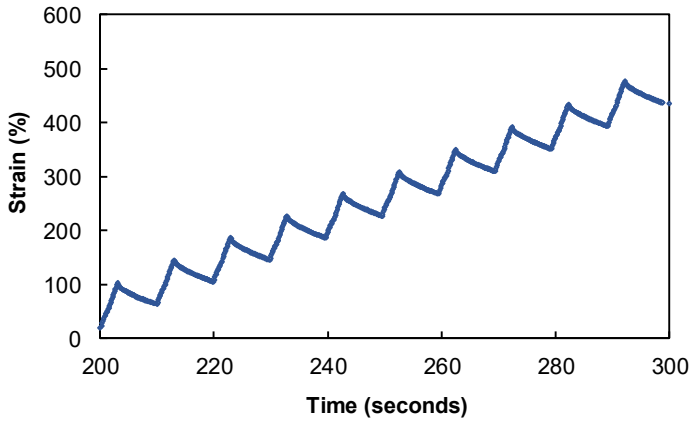

Figure A-6. Typical MSCR Strain Response During 3.2 kPa Stress Cycles.

These two standards have gone through several iterations since their first publication, but trace their beginnings to developmental work performed through the National Cooperative Highway Research Program (Bahia et al. 2001) and the Federal Highway Administration (FHWA) (D'Angelo et al. 2007). In the case of AASHTO T350, the method began as a provisional standard (TP70) in 2009, was refined in 2010, 2012, and 2013, and achieved full standard status in 2014. At ASTM, the first version of D7405 was 2008, and was refined

in 2010 and 2015. The current versions of these two standards are identical, except for the fact that the current ASTM standard provides precision and bias estimates but the AASHTO standard does not. During the test, 20 total cycles are applied at 0.1 kPa, but only the last 10 are used for analysis. Immediately following the end of the 0.1 kPa loading, 10 creep and recovery cycles are applied at the stress level of 3.2 kPa and all 10 are used for calculating the required test parameters.

Figure A-7 shows the strain response for a single cycle and identifies the parameters that are extracted from each cycle. For each loading cycle the initial strain (ε_0), maximum strain at the end of the loading (ε_c), and strain at the end of the recovery portion (ε_r) are recorded. These values are used to calculate two parameters, the non-recoverable creep compliance at 0.1 kPa and 3.2 kPa ($J_{nr0.1}$ and $J_{nr3.2}$) and the percentage of maximum strain recovered after 3.2 kPa loading ($R_{3.2}$). The equations used to calculate these parameters and the averaging process are detailed in the standard and in Equations (5) - (15). The J_{nr} values are reported to two significant digits and the difference between the $J_{nr3.2}$ and $J_{nr0.1}$, J_{nrdiff}, is reported to the nearest 0.1 percent.

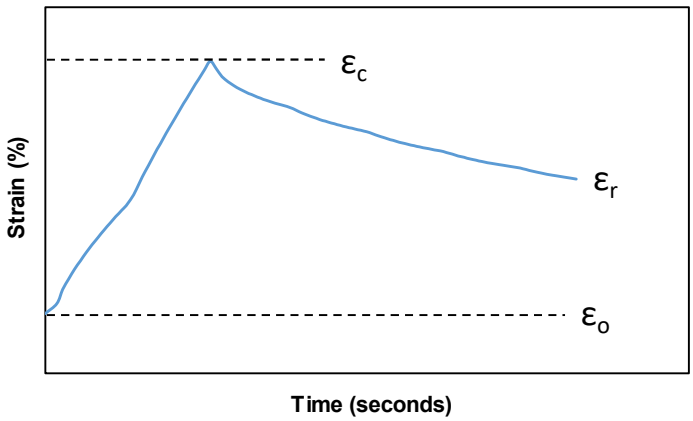

Figure A-7. Location of Strain Values During a Creep/Recovery Cycle.

$$\varepsilon_1 = \varepsilon_c - \varepsilon_0 \tag{5}$$

$$\varepsilon_{10} = \varepsilon_r - \varepsilon_0 \tag{6}$$

$$\varepsilon_r(0.1, N) = \frac{(\varepsilon_1 - \varepsilon_{10}) \times 100}{\varepsilon_1} \text{ For cycles } N\text{=1 through } N\text{=10} \tag{7}$$

$$\varepsilon_r(3.2, N) = \frac{(\varepsilon_1 - \varepsilon_{10}) \times 100}{\varepsilon_1} \text{ For cycles } N\text{=1 through } N\text{=10} \tag{8}$$

$$R_{0.1} = \frac{SUM[\varepsilon_r(0.1, N)]}{10} \tag{9}$$

$$R_{3.2} = \frac{SUM[\varepsilon_r(3.2, N)]}{10} \tag{10}$$

$$J_{nr}(0.1, N) = \frac{\varepsilon_{10}}{0.1} \tag{11}$$

$$J_{nr}(3.2, N) = \frac{\varepsilon_{10}}{3.2} \tag{12}$$

$$J_{nr0.1} = \frac{SUM[J_{nr}(0.1, N)]}{10} \tag{13}$$

$$J_{nr3.2} = \frac{SUM[J_{nr}(3.2, N)]}{10} \tag{14}$$

$$J_{nrdiff} = \frac{[J_{nr3.2} - J_{nr0.1}] \times 100}{J_{nr0.1}} \tag{15}$$

Fourier Transform Infrared Spectroscopy

For many years Fourier Transform Infrared (FT-IR) spectroscopy has been used as a tool to study the structure of materials. The application of the FT-IR technique in the field of asphalt science has been mainly for chemical characterization of asphalt and for oxidation studies (Jemison et al. 1992, Petersen and Glaser 2011). The advent of attenuated total reflectance (ATR) methods has made FT-IR a rapid technique that requires minimal sample preparation and training of the operators. The advantages of the ATR method over conventional transmission methods are quick and easy sample preparation, natural state analysis, and clean and reproducible spectra (Jemison et al. 1992). ATR-FTIR is a technique whereby the sample is placed in contact with the sensing element, and a spectrum is recorded as a result of that contact. Unlike other sampling techniques, radiation is not transmitted through the sample; consequently, the sample does not have to be thin enough for the radiation to be transmitted (Griffiths and de Haseth 2007). Figure A-8 shows the FT-IR instrument at Arizona State University that was used in the current study.

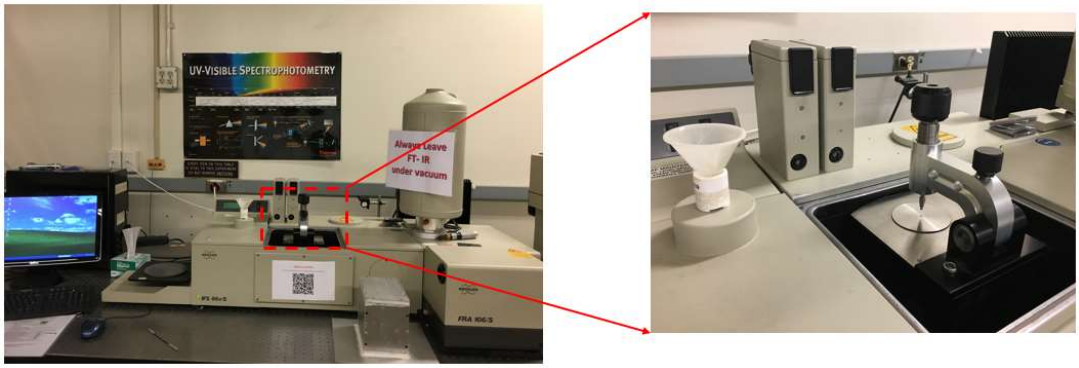

Figure A-8. Fourier Transform Infrared Spectroscopy Instrument at Arizona State University.

A typical FT-IR spectrum for asphalt binder is shown in Figure A-9. The figure also points out the dominant peaks in the spectrum, along with the bonds that those peaks represent. The two peaks that are of interest are the sulfoxide and the carbonyl peaks. Asphalt oxidation studies (Jemison et al. 1992, Petersen and Glaser 2011) have shown that the level of oxidation can be linked directly to the area under the sulfoxide and carbonyl peaks. A graphical representation of how the area is calculated is presented in Figure A-10. A program was specifically developed for the purpose of calculation of carbonyl and sulfoxide areas. A step by step procedure which conveys the implementation process of the program is presented below. It is noted that this program is currently used for the NCHRP 9-54 study and the calculation steps were established based on discussions and input from researchers at the Western Research Institute, which has more than 30 years of experience in analyzing FTIR data.

i. The data are sorted by wavenumber and the absorbance values corresponding to the Carbonyl region (1650 to 1820 cm^{-1}), the Sulfoxide region (1000 to 1050 cm^{-1}), and the wavenumber used to calculation the absorbance adjustment factor (1375 cm^{-1}) are extracted.
ii. The user then enters in the normalization factor if known. If this value is not known, then the default of 0.1 is used. The normalization factor is the value that the absorbance should have at the wavenumber used for normalization. The spectrograph adjustment factor is determined by dividing the normalization factor by the measured absorbance at the normalization wavelength. This adjustment process is a common technique used to correct spectrographs for known variations in FTIR scans (detector

inconsistencies, pathway differences, etc.) and essentially involves forcing the spectrograph for a number of replicates to have a certain fixed value at a pre-defined wavenumber.

iii. This adjustment factor is then multiplied to the absorbance values at all other wavenumbers.

iv. The normalized peak values of Carbonyl and Sulfoxide are extracted from the spectrograph. Depending on the data collection details, this process may require linear interpolation of the raw data at precisely 1702 cm^{-1} (Carbonyl) and 1032 cm^{-1} (Sulfoxide). The total Carbonyl+Sulfoxide peak value is calculated by summing the individual Carbonyl and Sulfoxide peak values.

v. The Carbonyl area (CA) is determined by numerical integration (Trapezoidal rule) of the normalized spectrograph between wavenumbers of 1650 and 1820 cm^{-1}.

vi. The Sulfoxide area (SA) is determined by numerical integration (Trapezoidal rule) of the normalized spectrograph between wavenumbers of 1000 and 1050 cm^{-1}).

vii. The Carbonyl+Sulfoxide Area (C+SA) is determined by adding the CA and SA.

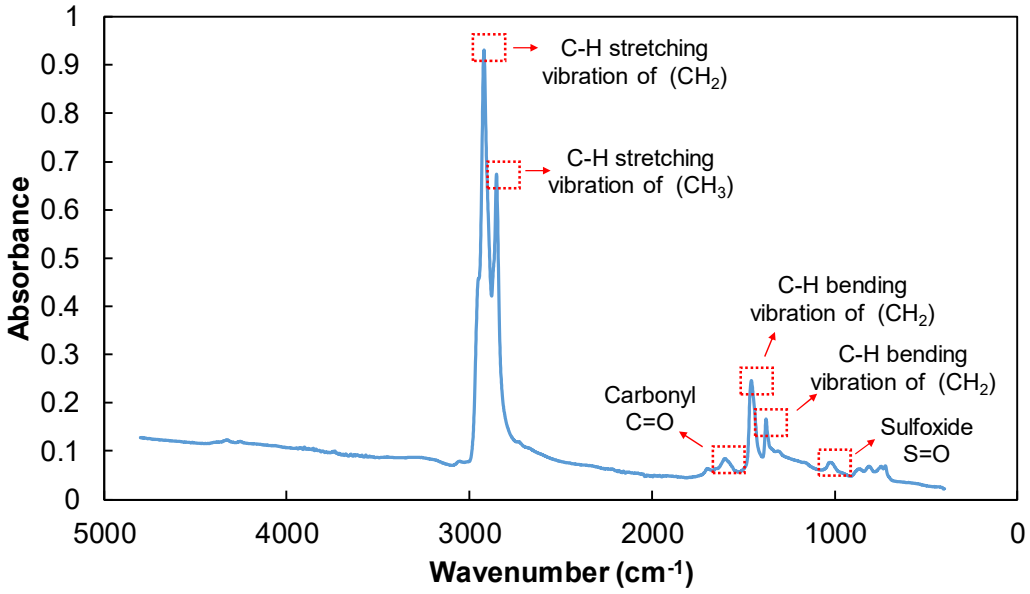

Figure A-9. Typical FT-IR Spectrum of Asphalt Binder with Dominant Peaks and the Bonds They Represent.

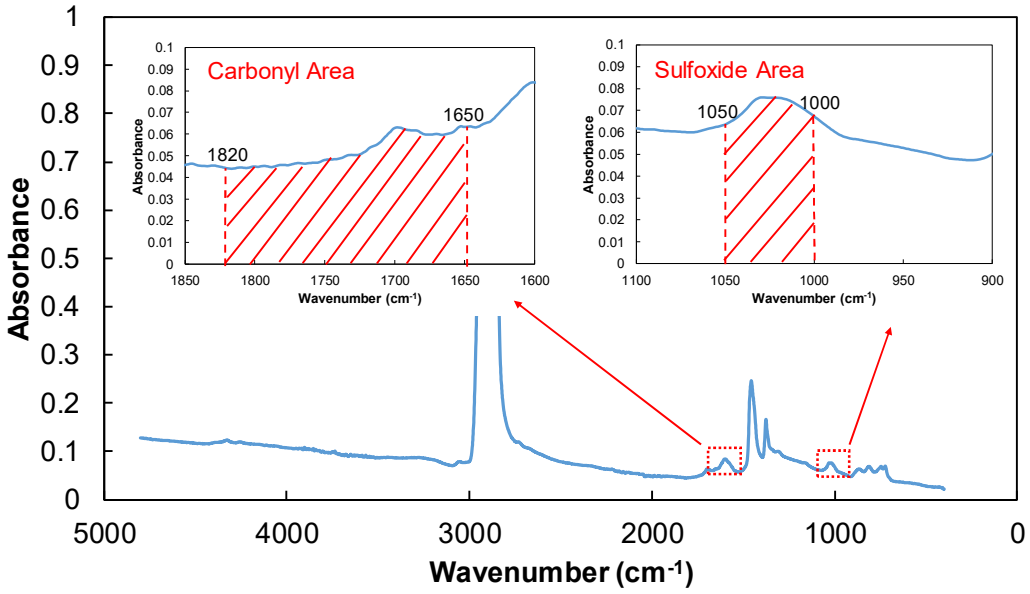

Figure A-10. Graphical Representation of Carbonyl and Sulfoxide Area Calculation.

AASHTO T 342 – Dynamic Modulus Test

Dynamic modulus, $|E^*|$, tests are performed according to AASHTO T342 using a servo-hydraulic testing machine. There are many different manufacturers and models for this type of equipment, but the one used at Arizona State University (ASU) is an Industrial Process Controls (IPC) Universal Testing Machine-25 (UTM-25), Figure A-11. The load frame capacity is 25 kN in both static and dynamic loading and testing is conducted inside a thermally controlled chamber. The temperature control system is able to provide temperatures in the range of -15 to 60°C, and for extended periods. The loading frequencies and test temperatures used in this study are 25, 10, 5, 1, 0.5, and 0.1 Hz and -10, 4.4, 21.1, 37.8, and 54°C respectively. Tests are conducted in an increasing order of temperature and in a decreasing order of loading frequency. This temperature-frequency sequence is carried out to minimize any potential damage to the specimen before the next sequential test. The load is varied with temperature to keep the specimen response in the range of 40-80 micro-strains. The number of cycles applied varies by frequency as shown in Table A- 1.

Table A- 1. Number of Loading Cycles at Each Frequency in Dynamic Modulus Experiment, AASHTO T342.

Frequency (Hz)	Number of Cycles
25	200
10	200
5	100
1	20
0.5	15
0.1	15

A continuous haversine wave shape, as shown in Figure A-12, is applied and measured through a load cell. Prior to testing the sample diameter is measured and used to calculate the stresses applied to the sample from the measured forces. At the same time as the load is being monitored and controlled, the deformations are measured using three spring-loaded Linear Variable Differential Transducers (LVDTs) mounted every 120° directly to the surface of the test sample. The LVDTs are secured in-place using brackets and studs glued onto the specimens. The studs are glued using a specially designed apparatus to ensure proper placement and alignment. Guide rods are added to the instrumentation to ensure good alignment. Likewise, the LVDT gauge length is used to calculate the strain from the measured displacements. Prior to the initiation of the testing program, the load cell, LVDTs, and temperature probes are calibrated and verified. The dynamic modulus test setup at Arizona State University is shown in Figure A-11.

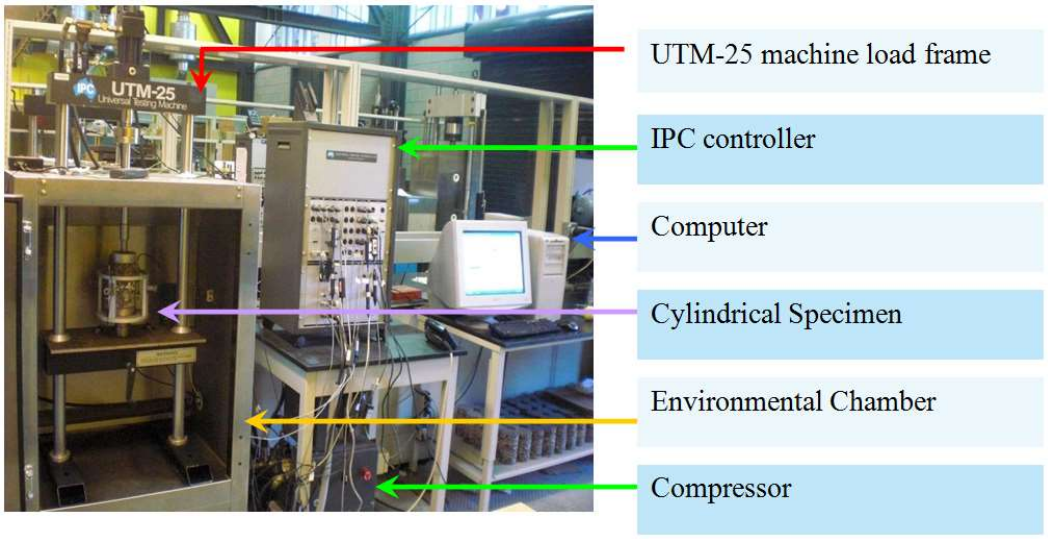

Figure A-11. Dynamic Modulus Test Setup at Arizona State University.

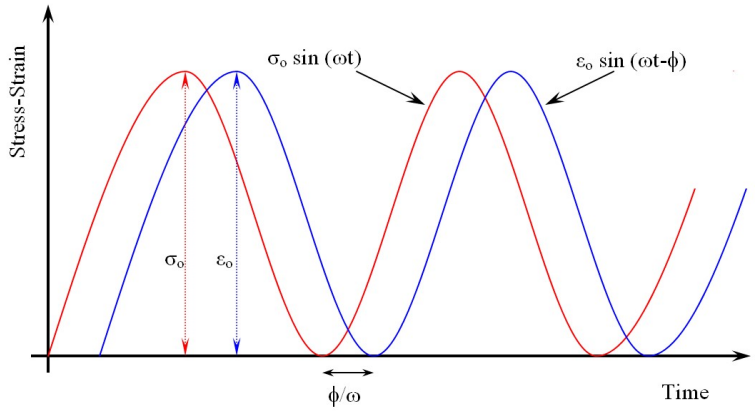

Figure A-12. Applied Stress and Strain Wave Shapes.

The $|E^*|$ is calculated by taking the ratio of the stress magnitude to the strain magnitude, Equation (16), while the phase angle, δ is calculated by using the time delay (Δt) between the peak of stress and the peak of strain, Equation (17). These magnitudes and time delay are determined based on sinusoidal regression of the last five cycles of the stresses and strains at each temperature and frequency combination. The equations used for this regression are provided in AASHTO T342 and are handled internally through the UTM25 control software.

$$\left|E^*\right| = \frac{\sigma_0}{\varepsilon_0} \tag{16}$$

$$\delta = 2\pi f \Delta t \tag{17}$$

The $|E^*|$ and δ for each temperature and frequency combination (a total of 30 points) are analyzed based on the principle of time-temperature superposition to construction mastercurves. The basis of these curves is the sigmoidal function, Equation (18), the coefficients of which are identified using an optimization approach.

$$\log|E^*| = \delta + \frac{\alpha}{1 + \frac{1}{e^{\beta+\gamma(\log f_r)}}} \tag{18}$$

where:

f_r = reduced frequency of loading (Hz);

δ = minimum logarithmic value of $|E^*|$;

$\delta+\alpha$ = maximum logarithmic value of $|E^*|$; and

β, γ = parameters describing the shape of the sigmoidal function.

The reduced frequency is the product of the test frequency and the time-temperature shift factor, a_T, which is a temperature, T, dependent value that quantifies the amount of horizontal shift necessary to create a continuous mastercurve. T_R here is the reference temperature (21.1°C For this study). Multiple analytical representations exist for the time-temperature shift factor and in this research the 2nd order polynomial expression with coefficients α_1 and α_2, Equation (17) is adopted. The values of δ, α, β, γ, α_1, and α_2 are optimized to minimize the sum of the squared error between the measured and predicted dynamic modulus. Figure A-13 demonstrates the process by first showing an example of the measured data in physical frequency domain, Figure A-13(a), and then showing the resultant shifted data and mastercurve function in reduced frequency domain, Figure A-13(b).

$$\log(a_T) = \alpha_1 (T - T_R)^2 + \alpha_2 (T - T_R) \tag{19}$$

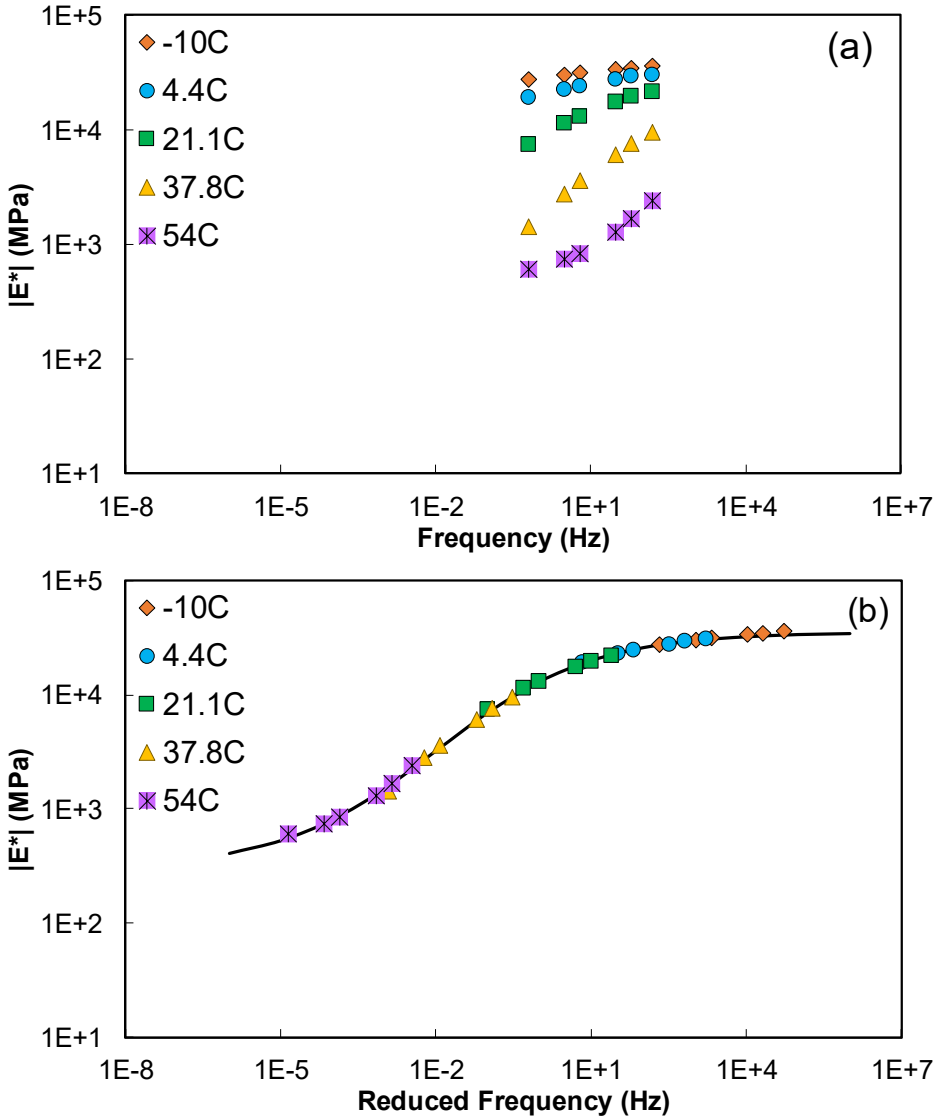

Figure A-13. (a) Measured Dynamic Modulus in Physical Frequency Domain; and (b) Dynamic Modulus in Reduced Frequency Domain.

AASHTO TP107 – Axial Fatigue Test

The uniaxial fatigue test applies a repeating sinusoidal load or deformation along the long axis of a cylindrical test specimen until it fails. The test may be performed on multiple specimens and at different temperatures and deformation/load levels. The test itself is standardized in AASHTO TP107 and uses a closed-loop servo hydraulic testing machine in a temperature controlled environment, Figure A-14. This machine applies a continuous sinusoidal loading pattern based on load, actuator displacement, or output from the on-specimen LVDTs. In this study the actuator displacement control method is adopted as is required in AASHTO TP107.

The test specimens are cored and cut from the center of 150 mm diameter and 180 mm tall gyratory compacted plugs to obtain the appropriate test geometry. The ASU testing has been conducted on 75 mm diameter and 150 mm tall samples. After coring and cutting samples, the air voids are measured according to AASHTO T166 and samples are glued to steel end plates using Devcon 10240 steel putty and the jig shown in Figure A-14. This jig ensures that the sample and end plates are axially aligned thus eliminating loading eccentricities. Next, the samples are instrumented with four loose core LVDTs that monitor the on-specimen deformation. The same stud and bracket system used in $|E^*|$ testing is used for this purpose. At each loading cycle, the software calculates the $|E^*|$ and δ plus the stress and the strain values from the actuator and the four LVDTs. The fatigue test is run until a sudden decrease in phase angle is observed. This pattern indicates that a crack has localized and that failure has occurred.

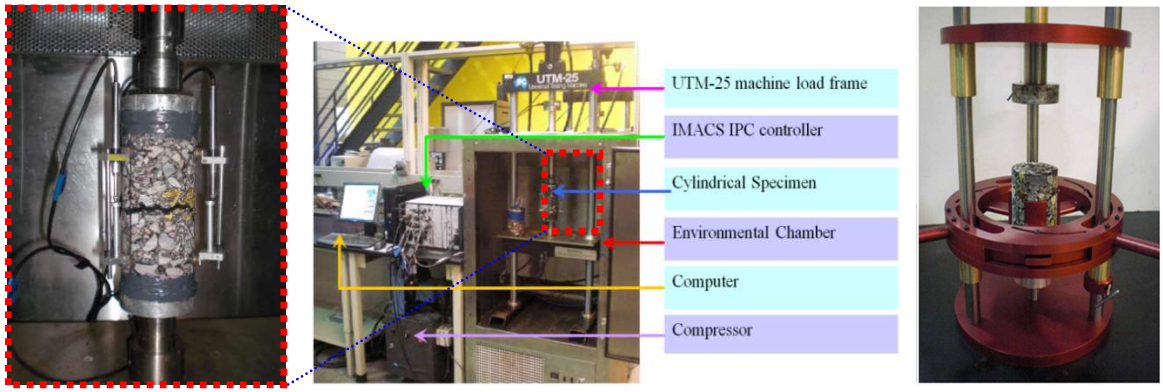

Figure A-14. Uniaxial Fatigue Test Setup and Gluing Jig.

The test results are analyzed using the simplified viscoelastic continuum damage (S-VECD) approach to characterizing fatigue behavior. The first step in that approach is to establish the damage characteristic (*C*-*S*) curve. The *C*-*S* curve is a relationship unique to a given asphalt concrete mixture that is independent of test conditions including strain levels, temperatures, mode of loading (stress controlled or strain controlled), and loading history. This unique function exists as a fundamental characteristic of the material and is characterized by employing the work potential theory as incorporated into the S-VECD formulation and summarized in the following equations.

$$C = \begin{cases} \dfrac{\sigma}{\varepsilon^R \times DMR} & first\ cycle \\ \dfrac{\sigma}{\varepsilon_{0,ta}^R \times DMR} & rest\ of\ cycles \end{cases} \tag{20}$$

$$\varepsilon^R = \frac{1}{E_R} \int_0^t E(t-\tau) \frac{d\varepsilon}{d\tau} d\tau \tag{21}$$

$$\left(\varepsilon_{0,ta}^R\right)_i = \frac{1}{E_R} \times \frac{\beta+1}{2} \left(\left(\varepsilon_{0,pp}\right)_i \times \left|E^*\right|_{LVE} \right) \tag{22}$$

$$DMR = \frac{|E^*|_{fp}}{|E^*|_{LVE}} \tag{23}$$

$$S_{N+1} = S_N + \left[-\frac{DMR}{2}(C_N - C_{N-1})(\varepsilon^R)^2 \right]^{\frac{\alpha}{(1+\alpha)}} (\Delta\xi_i)^{\frac{1}{(1+\alpha)}} (K_1)^{\frac{1}{(1+\alpha)}} \tag{24}$$

$$\alpha = \frac{1}{1+m} \tag{25}$$

$$K_1 = \frac{1}{\xi_f - \xi_i} \int_{\xi_i}^{\xi_f} \left(f(\xi) \right)^{2\alpha} d\xi \tag{26}$$

where:

C = normalized pseudo stiffness indicating the material integrity;

S = internal state variable denoting the internal damage in the material;

σ = measured stress;

ε^R = pseudo strain;

DMR = dynamic modulus ratio;

$\varepsilon^R_{0,ta}$ = tensile pseudo strain tension amplitude;

E_R = reference modulus;

$E(t)$ = relaxation modulus and creep compliance, respectively;

t = elapsed time from specimen fabrication and time of interest;

τ = time when loading began;

ε = measured strain;

$\varepsilon_{0,pp}$ = peak-to-peak strain amplitude;

β = stress wave shape factor (1 tension, 0 tension-compression, and -1 compression);

$|E^*|_{fp}$ = fingerprint dynamic modulus;

$|E^*|_{LVE}$ = linear viscoelastic dynamic modulus of the material;

N = number of loading cycle;

$\Delta\xi_1$ = change in the average reduced time between analysis cycles;

K_1 = developed functional parameter to account for the analysis of cyclic data;

α = material property;

m = slope in the central part of the dynamic modulus master curve for the log $E(t)$-log(t);

ξ_i = reduced starting time; and

ξ_f = reduced ending time.

The C-S relationship generally follows an exponential or power-law decay form as shown in Figure A-15 . At small levels of damage the material integrity is high (close to 1), but as damage increases the material integrity is lost until eventually failure will occur. Thus, from characterization of this function two factors are important, the overall position of the C-S curve and also the material integrity level at which failure occurs, $C_{failure}$. All other factors being the same, materials with lower $C_{failure}$ values will exhibit superior fatigue performance. Once characterized, the C-S relationship can be fitted to an analytical form represented by Equation (27), where C_1 and C_2 are regression coefficients.

$$C(S) = 1 - C_1(S)^{C_2} \tag{27}$$

In order to gain useful information on fatigue cracking, simulated predictions of the fatigue life at specific conditions of interest can be performed using theoretically derived formulas for predicting the material response to fully reversed constant stress and constant strain loadings as shown in the following formulations:

$$N_{failure} = \frac{\left(f_r\right)\left(2^{3\alpha}\right)S_{failure}^{\alpha-\alpha C_2+1}}{\left(\alpha-\alpha C_2+1\right)\left(C_1C_2\right)^{\alpha}\left[\left(\varepsilon_{0.pp}\right)\left(\left|E^*\right|_{LVE}\right)\right]^{2\alpha}K_1} \tag{28}$$

$$N_{failure} = \frac{f_r * 2^{3\alpha}\left|E^*\right|^{2\alpha}}{\left[\left(\sigma_{0,pp}\right)\right]^{2\alpha}K_1}\int_0^{\hat{S}_{failure}}\left(\frac{\left(1-\hat{C}_1\left(\hat{S}\right)^{C_2}\right)^2}{\hat{C}_1C_2\hat{S}^{C_2-1}}\right)^{\alpha}\left(d\hat{S}\right) \tag{29}$$

$$\hat{S}_{failure} = \frac{S_{failure}}{\left|E^*\right|^{2\alpha/\alpha+1}} \tag{30}$$

$$\hat{C}_{11} = C_{11}\left(\left|E^*\right|^{2\alpha/\alpha+1}\right)^{C_{12}} \tag{31}$$

where:

$N_{failure}$ = predicted cycle number of cycles to failure;

f_r = reduced frequency for the condition being simulated;

$|E^*|$ = dynamic modulus for the condition being simulated;

$\varepsilon_{0,pp}$ = peak-to-peak strain level for simulation;

$\sigma_{0,pp}$ = peak-to-peak stress level for simulation; and

$S_{failure}$ = damage level at failure.

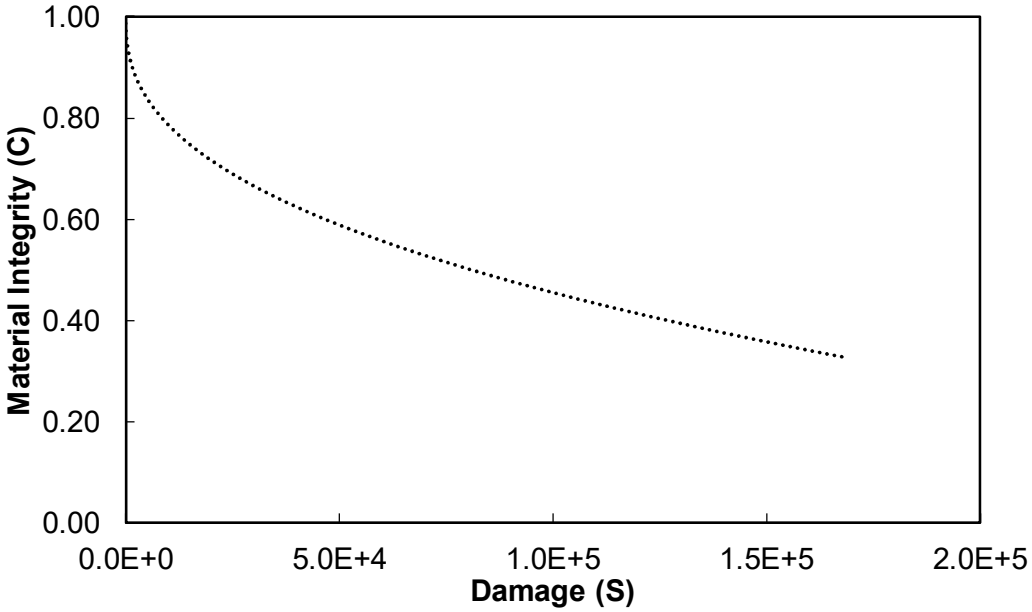

Figure A-15. Damage Characteristic Curve.

Figure A-16 shows the typical relationship between the total cumulative plastic strain and the number of load cycles during a flow number test. This relationship is generally defined by three regions: primary, secondary, and tertiary. In the primary region, permanent deformations accumulate rapidly. The incremental permanent deformations decrease reaching a constant value in the secondary region. Finally, the incremental permanent deformations again increase, and permanent deformations accumulate rapidly in the tertiary region. The starting point, or cycle number, at which tertiary flow occurs, is referred to as the Flow Number (FN).

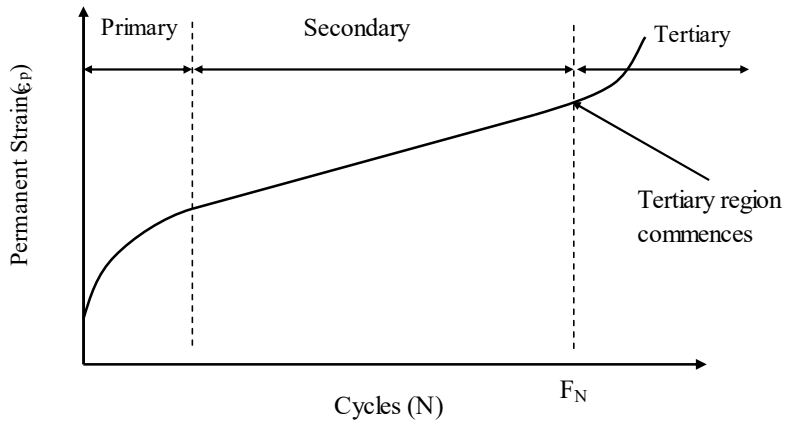

Figure A-16. Typical relationship between total cumulative plastic strain and number of load cycles.

Two basic analyses are performed with the data in these tests; (1) identifying the FN and (2) establishing strain accumulation coefficients for structural performance assessment. To identify the FN value, a statistical analysis technique, the Franken model, is often utilized. This model structure, shown in Equation (31), has been selected because it

combines both a power function, which characterizes the primary and secondary regions, and an exponential function that fits the tertiary region.

$$\varepsilon_p(N) = AN^B + C\left(e^{DN} - 1\right) \tag{32}$$

where:

$\varepsilon_p(N)$ = permanent deformation or permanent strain;

N = number of loading cycles; and

A, B, C and D = regression constants.

In this study, the average slope for the secondary region was estimated and used to investigate correlations between the binder parameters and mixture permanent deformation resistance. It is recognized that multiple indices could be used, but the slope of the secondary region was adopted due to research that relates this slope to the rate of rutting accumulation in asphalt pavements. The average slope for the secondary region was defined by first identifying the FN cycle using after optimizing the Franken model to the measured permanent strain data. This cycle was taken to be the end of the secondary region. Then, the beginning of the secondary region was estimated as the cycle that was 50% of the FN cycle, Finally, the average slope of the Franken model fitting between these two cycles was calculated.

AASHTO T324 – Hamburg wheel track test

The Hamburg Wheel Track Test (HWTT) equipment, shown in Figure A-17, consists of a reciprocating wheel, which simulates a moving concentrated load. The test provides information about the rate of permanent deformation when an asphalt mixture slab or cylinder is loaded. The compacted cylindrical specimens obtained from the Superpave gyratory compactor which have a diameter of 150 mm are used for testing. The thickness of the cylinder ranges from 38 mm to 100 mm. The test requires two compacted cylinders mounted on high density polyethylene (HDPE) molds over which the test wheel will reciprocate. Prior to mounting the cylindrical test samples have to be cut along the secant such that when joined together in the molds there is minimal gap between the cut edges. As per AASHTO T324 this gap should be no greater than 7.5 mm. The air void content of the cut specimens is 7 ± 1 percent. Figure A-18, shows the specimen mounting system.

Figure A-17. Hamburg wheel tracking device (Texas Transportation Institute 2007).

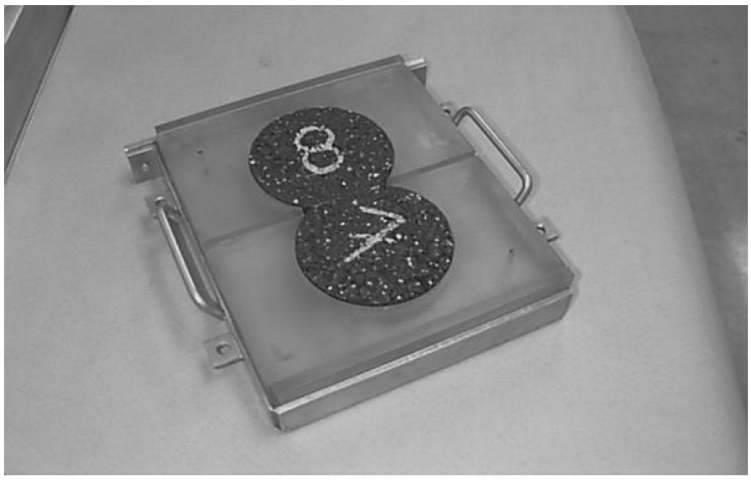

Figure A-18. Cylindrical Specimen Mounting System for the Hamburg Wheel Tracking Test (AASHTO T324 2014).

After mounting the sample into the equipment, rut depth is measured continuously with a series of LVDTs on the sample. Hamburg wheel tracking test results can be used to evaluate resistance to rutting and stripping. Figure A-19 shows a typical plot from a Hamburg wheel tracking test and the key plot parameters. These parameters are explained as follows:

- Creep slope: The inverse of the rutting slope after post-compaction consolidation but before the stripping inflection point. Creep slope is used to evaluate rutting potential instead of rut depth because the number of load cycles at which moisture damage begins to affect rut depth varies between HMA mixtures and cannot be conclusively determined from the plot.
- Stripping inflection point: The point at which the creep slope and stripping slope intercept. This can be used to evaluate moisture damage potential. If the stripping inflection point occurs at a low number of load cycles (e.g., less than 10,000), the HMA mixture may be susceptible to moisture damage.

- Stripping slope: A measure of the accumulation of moisture damage. As with flow time and flow number, this portion of the plot may contain tertiary flow as well, however it is not possible to separate out moisture damage from tertiary viscous flow.

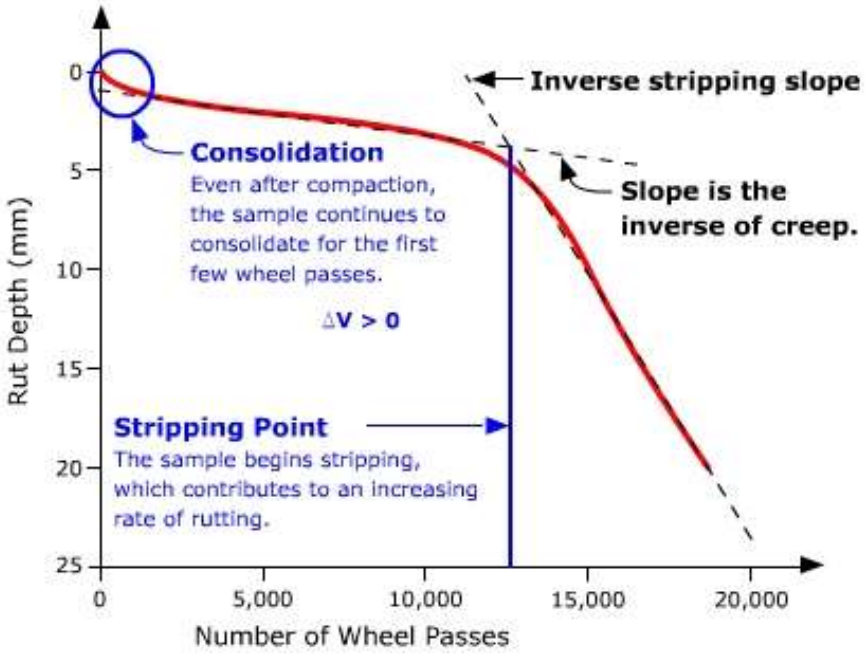

Figure A-19. Typical Plot from a HWTD Test and the Key Plot Parameters (Source: www.pavementinteractive.org).

LABORATORY PREPARATION OF POLYMER MODIFIED ASPHALTS

To prepare laboratory blended polymer modified asphalts, a non-modified PG 58-28 was used. Preparation was performed using batches of approximately 2000-2300 g and 1-gallon cans. The following steps were followed to prepare a batch of polymer modified asphalt. These steps were completed using a Ross LSK-high shear mixer with a round hole disintegrating shear head, and a Glas-Col heating mantle, capable of heating one-gallon containers. Figure A-20 shows the high-speed mixer and components.

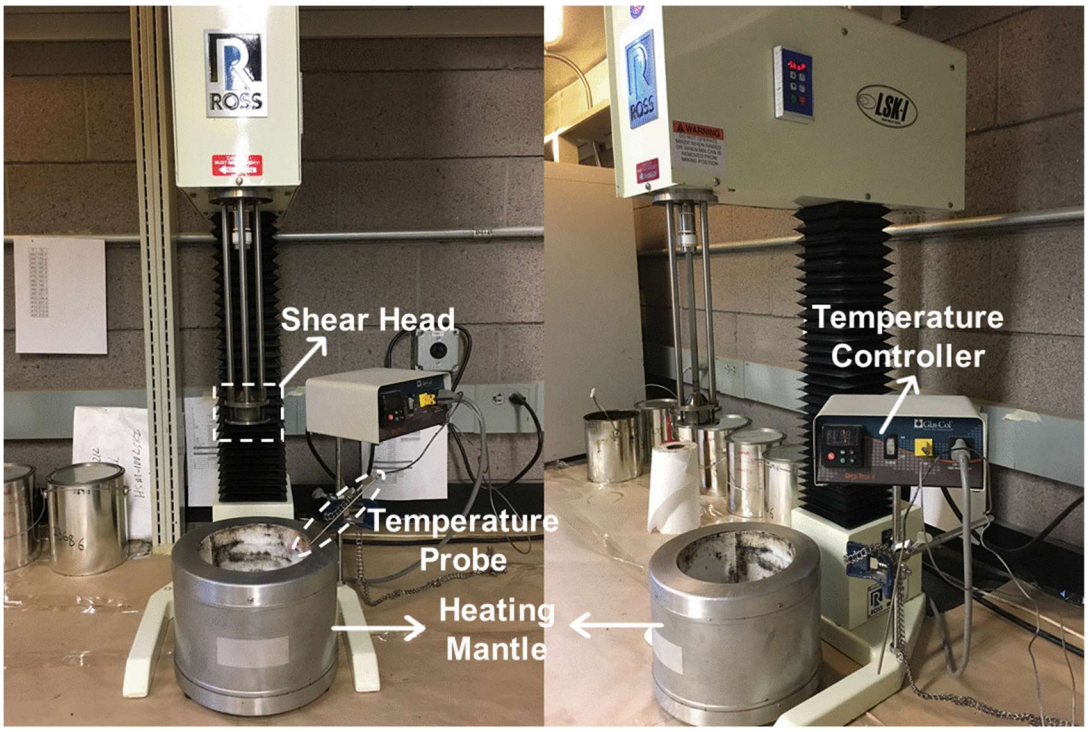

Figure A-20. High Shear Mixer and its Components Used for the Binder Preparation.

1. If the separated binder containers were stored at room temperature, heat the containers at 150°C for 1.5 hours.
2. Place the heated container in the heating mantle and the thermocouple into the container. Set temperature in the controller to 178°C.
3. Lower the shaft of the high shear mixer into container and make sure that the bottom of the shearing head is within ½" from the bottom of the container. This will eliminate settlement of polymer at the bottom of the container.
4. Turn on the shear mixer. The mixer will initially be at its slowest speed, 494 rpm. Gradually increase the speed to 3000 rpm over a period of one minute.
5. Once the temperature reaches 178°C (usually 15 to 20 minutes), increase the rpm to 4500 rpm over a period of 30 seconds. This will create just enough disturbance to

avoid stagnation of polymer on the surface of the asphalt binder. Care should be taken in this step, as a larger disturbance will create a vortex which will drive oxygen into the binder and there is a chance for oxidation.

6. Slowly add the calculated amount of polymer over a period of 5 to 10 minutes. While the polymer is being added, ensure that all polymer is being disturbed into the container where the shear head is located and that none remains on the surface or adhering to the walls. If this occurs use a popsicle stick or a coffee stirrer to push the polymer towards the center, so that it gets sucked in.
7. After all the polymer is added, it can be observed from the reading on the temperature controller that the temperature in the asphalts has increased about 5 to 10°C. This is due to the heat generated during the shearing mechanism in the 10-minute period.
8. Turn off the temperature controller and increase the speed to 8000 rpm. Maintain this speed for about five minutes. Turn on the controller to check the temperature. If the temperature of the asphalt is less than 197°C, keep shearing at the same speed until the temperature is between 197 – 200°C. The temperatures increases very quickly at such high speeds, so it is recommended to check the temperature every minute after the first five minute period. If the temperature exceeds 200°C, but is no more 210°C bring the speed down to 5000 rpm and wait until the temperature comes down to 197 – 200°C. If the temperature exceeds 210°C, discard the batch as it is highly likely that the polymer might have been damaged.

9. Once the temperature is in the range of 197 – 200°C, turn off the temperature controller and lower the speed to 6000-6200 rpm. It is very important that the temperature controller is turned off. This will ensure that no external heat is supplied, and the only heat generated is from the shearing action, which is sufficient for the breaking down of polymer and its dispersion. At this condition, the temperature of the asphalt will be maintained at 195 - 200°C.
10. The polymer should be sheared for a period of 90 minutes. The countdown starts from when the speed was increased to 8000 rpm.
11. After the 90 minutes shearing is completed, turn on the temperature controller. It should be remembered that the set point is still at 178°C, while the actual temperature is between 195 - 200°C. Increase the set point to 187°C and lower the speed to 3300 rpm. Leave the temperature controller on and the speed at 3300 rpm for the remainder of the preparation process. The temperature will gradually reduce to the set point i.e. 187°C over a period of 5 – 10 minutes.
12. Once the temperature reaches 187°C, add the calculated amount of sulfur and continue the shearing for 60 minutes.
13. After 60 minutes, add the calculated amount of polyphosphoric acid, and continue the shearing for additional 30 minutes.
14. At the end of 30 minutes, turn off the temperature controller, and lower the speed of the shaft to 494 rpm (default speed) over a period of one minute and eventually turn off the shear controller.

15. Once the shearing stops, raise the shearing head and take the container out of the mantle. Stir the contents of the container manually using a stirring rod. Use a small cut-out portion of a screen mesh as a filter while transferring the contents into smaller containers for storage and future use. Use of a filter ensures that the polymer granules that did not break down during the shearing process can be filtered out.

The polymer modified asphalt binders prepared for Chapter 7 and their respective compositions are as listed below. It should be noted that not all polymer modified asphalts blended for the study have cross linking agents, sulfur and PPA. For such asphalts, the preparation process stops at Step 10.

Table A- 2. Composition of the Polymer Modified Asphalts Blended for Subtask 3.4

Group	**Sample**	**Weight Percentage (%)**			
		Asphalt	**SBS**	**Sulfur**	**PPA**
$J_{nr3.2} < 0.5$	Y5	Provided by Supplier			
	B5	94.417	5.000	0.083	0.500
	D0.5	97.983	0.500	0.017	1.500
$0.5 < J_{nr3.2} < 1$	B2	97.433	2.000	0.067	0.500
	A3-B	96.925	3.000	0.075	0.000
	A4	96.000	4.000	0.000	0.000
$1 < J_{nr3.2} < 2$	X3	Provided by Supplier			
	A2-B	97.933	2.000	0.067	0.000
	A3	97.000	3.000	0.000	0.000

So, for the binders which have just the SBS polymer, the mixing conditions were 1.5 hours at 195°C - 200°C using a shearing speed of 6000-6200 rpm. For binders which have SBS and sulfur, the mixing conditions before adding sulfur were same as mentioned above. After addition of sulfur, the mixing conditions were 0.5 hours at 187°C using a shearing speed of 3300 rpm. For binders which have SBS, sulfur, and PPA, the mixing conditions before

adding sulfur were same as mentioned above. After addition of sulfur, the mixing conditions were 1 hour at 187°C using a shearing speed of 3300 rpm. Same temperature and shearing speed was maintained for additional 0.5 hour after addition of PPA.

REFERENCES

Bahia, H.U., D. Hanson, M. Zeng, H. Zhai, M. Khatri, and R. Anderson. 2001. *Characterization of Modified Asphalt Binders in Superpave Mix Design*. Final Report, NCHRP Project 9–10. Washington, D.C. National Cooperative Highway Research Program, National Research Council: 2001.

D'Angelo, J., R. Kluttz, R. Dongre, K. Stephens, and L. Zanzotto. 2007. "Revision of the Superpave High Temperature Binder Specification: The Multiple Stress Creep Recovery Test." *Journal of Association of Asphalt Paving Technologists* 76: 123-162.

Griffiths, Peter, R. and de Haseth, James, A. 2007. *Fourier Transform Infrared Spectroscopy, Second Edition*. New Jersey: John Wiley and Sons Inc..

Yildrim, Y., P. W. Jayawickrama, M.S. Hossain, A. Alhabshi, C. Yildrim, A.F. Smit, and D. Little. 2007. *Hamburg Wheel-Tracking Database Analysis*. Final Report, FHWA/TX-05/0-1707-7. Austin, Texas. Texas Transportation Institute: 2007.

APPENDIX B

DYNAMIC MODULUS MASTERCURVES OF ALL STUDY ASPHALT BINDERS

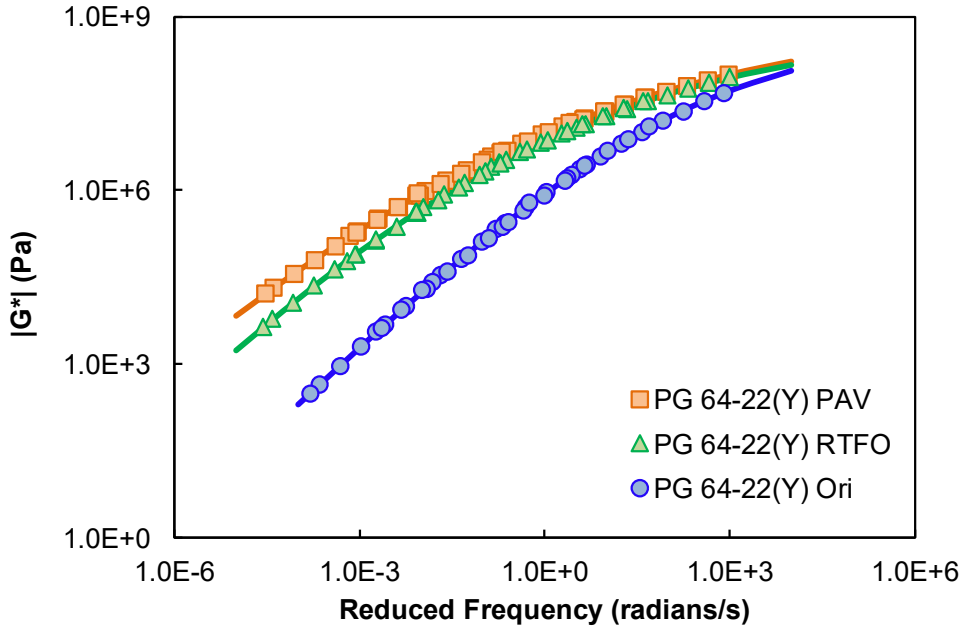

Figure B-1: Dynamic Modulus Mastercurves for Asphalt PG 64-22(Y) at All Three Aging Conditions.

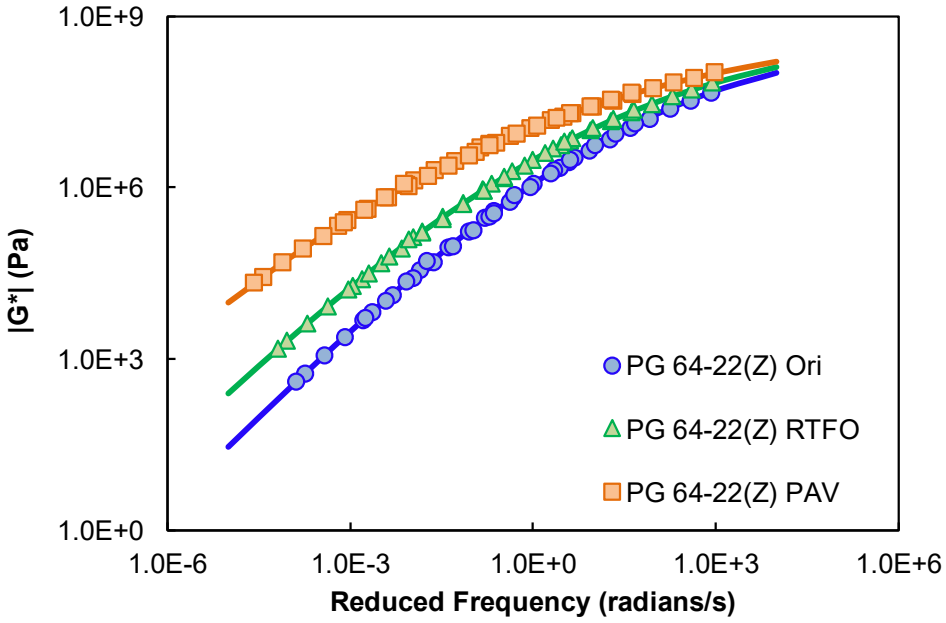

Figure B-2: Dynamic Modulus Mastercurves for Asphalt PG 64-22(Z) at All Three Aging Conditions.

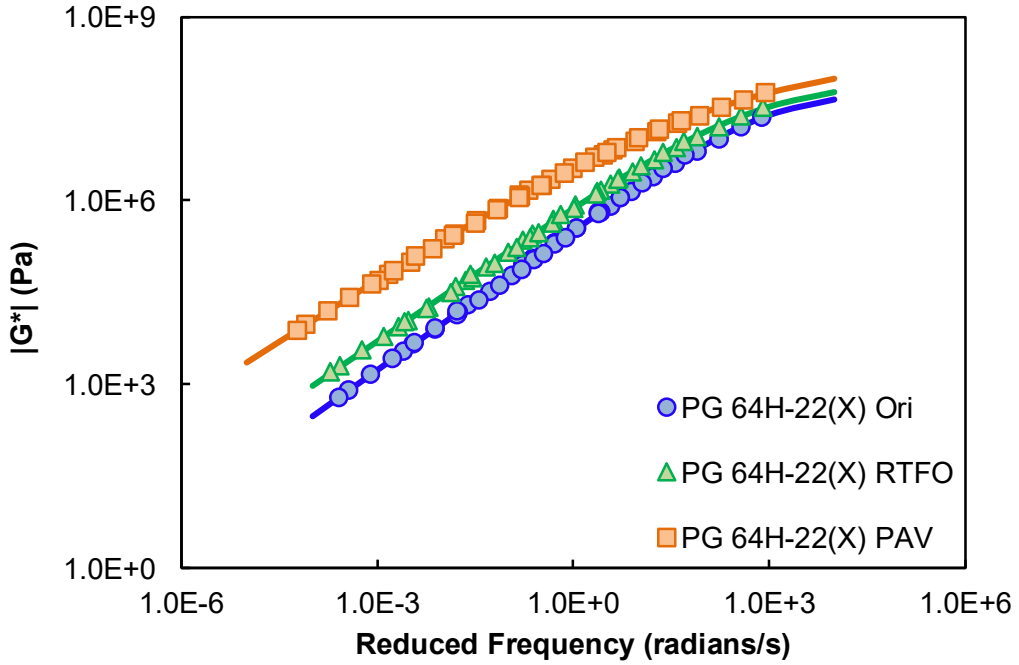

Figure B- 3: Dynamic Modulus Mastercurves for Asphalt PG 64H-22(X) at All Three Aging Conditions

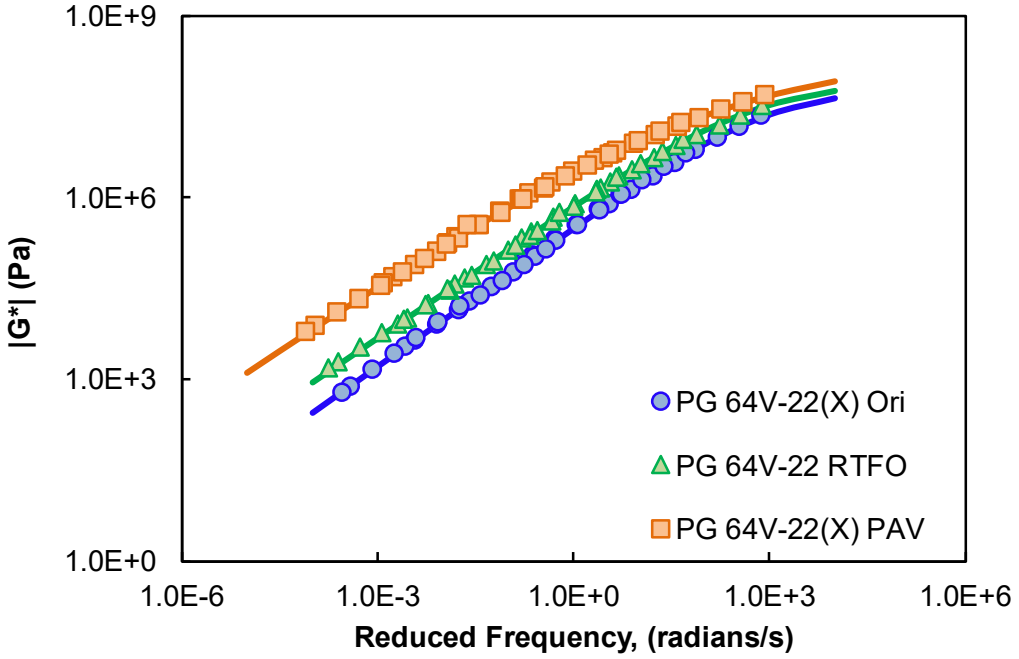

Figure B- 4: Dynamic Modulus Mastercurves for Asphalt PG 64V-22(X) at All Three Aging Conditions

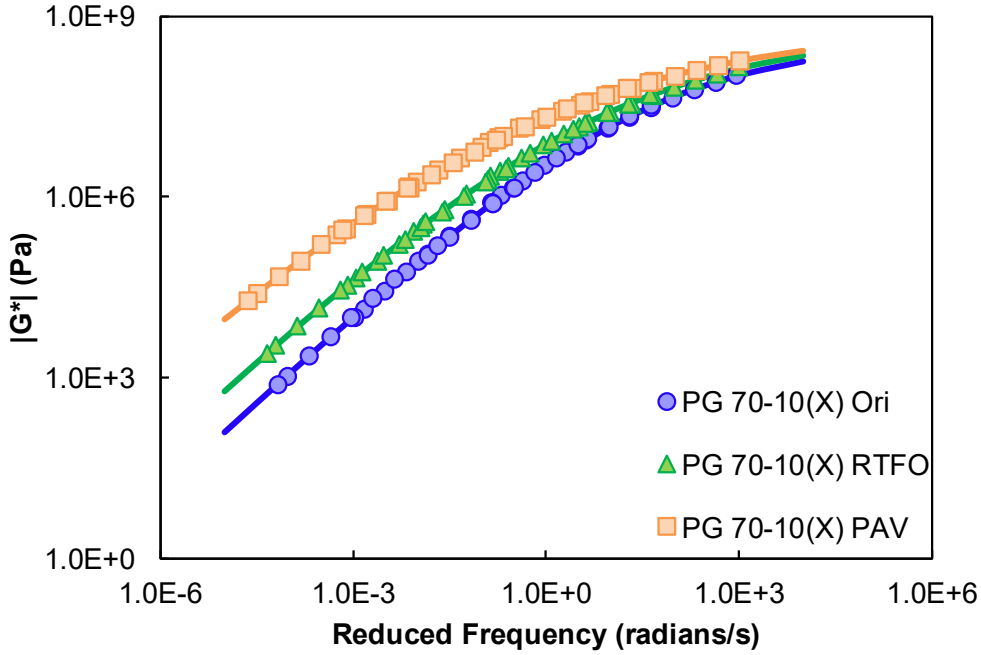

Figure B- 5: Dynamic Modulus Mastercurves for Asphalt PG 70-10(X) at All Three Aging Conditions

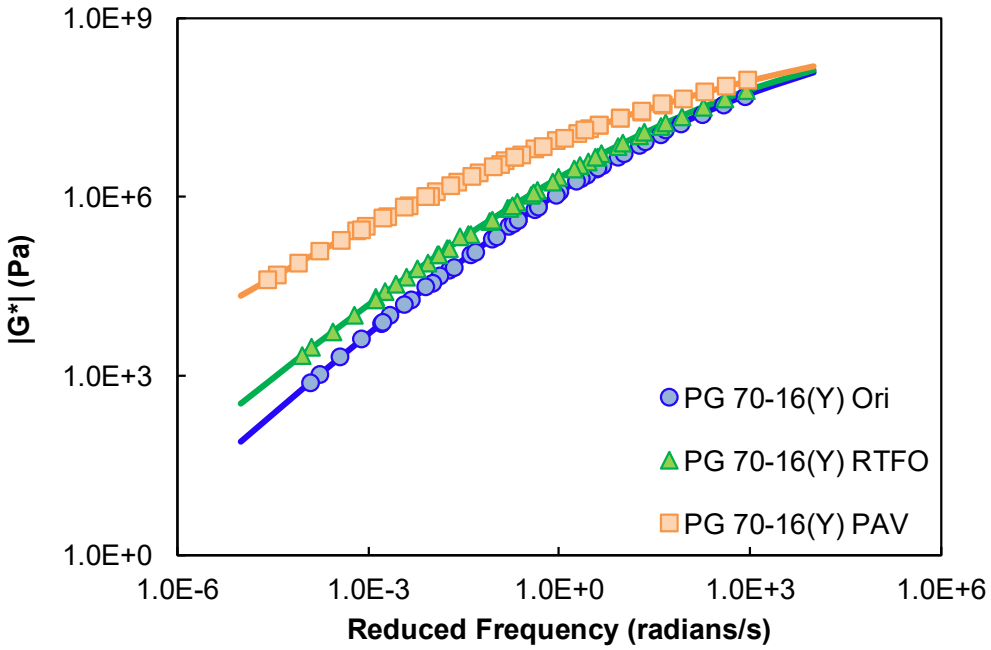

Figure B- 6: Dynamic Modulus Mastercurves for Asphalt PG 70-16(Y) at All Three Aging Conditions

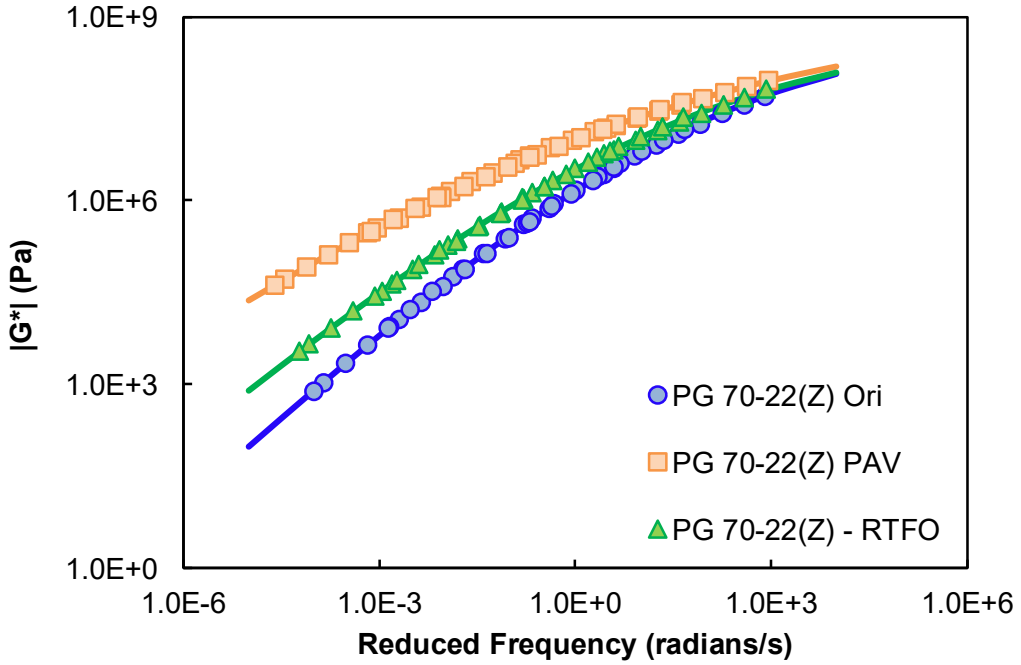

Figure B- 7: Dynamic Modulus Mastercurves for Asphalt PG 70-22(Z) at All Three Aging Conditions

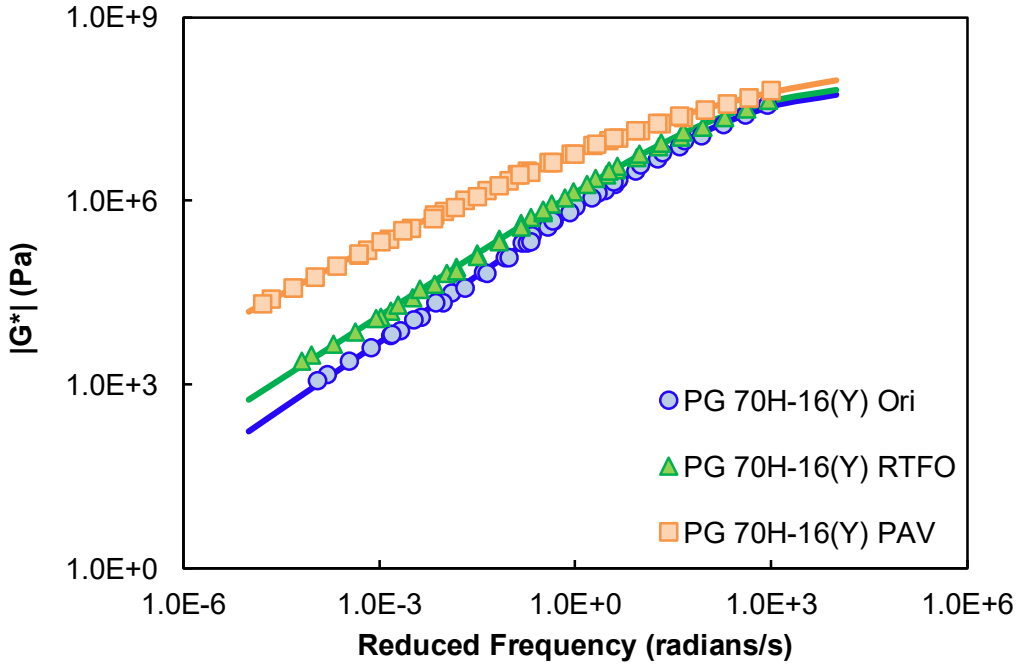

Figure B- 8: Dynamic Modulus Mastercurves for Asphalt PG 70H-16(Y) at All Three Aging Conditions

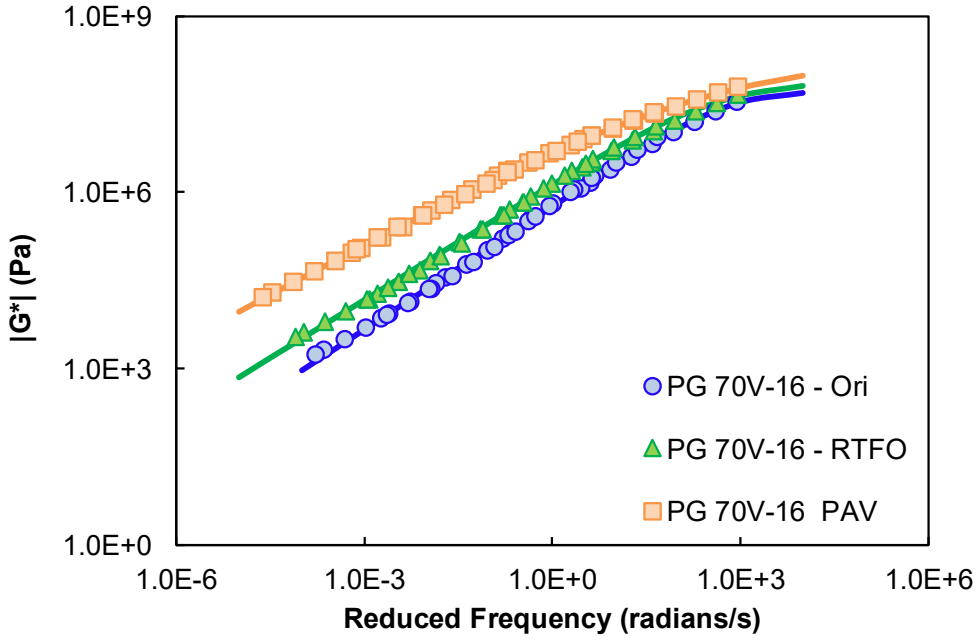

Figure B- 9: Dynamic Modulus Mastercurves for Asphalt PG 70V-16(Y) at All Three Aging Conditions

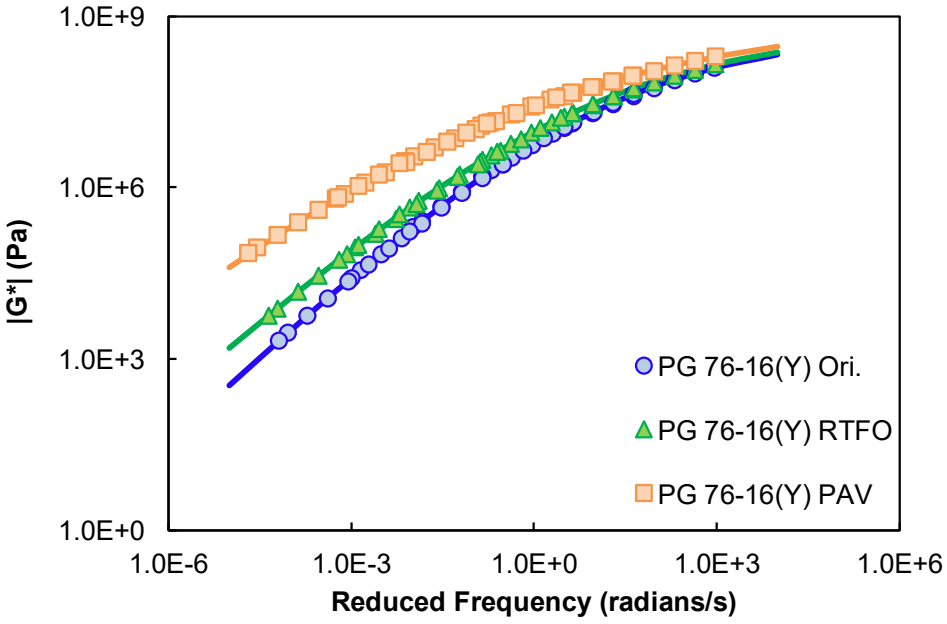

Figure B- 10: Dynamic Modulus Mastercurves for Asphalt PG 76-16(Y) at All Three Aging Conditions

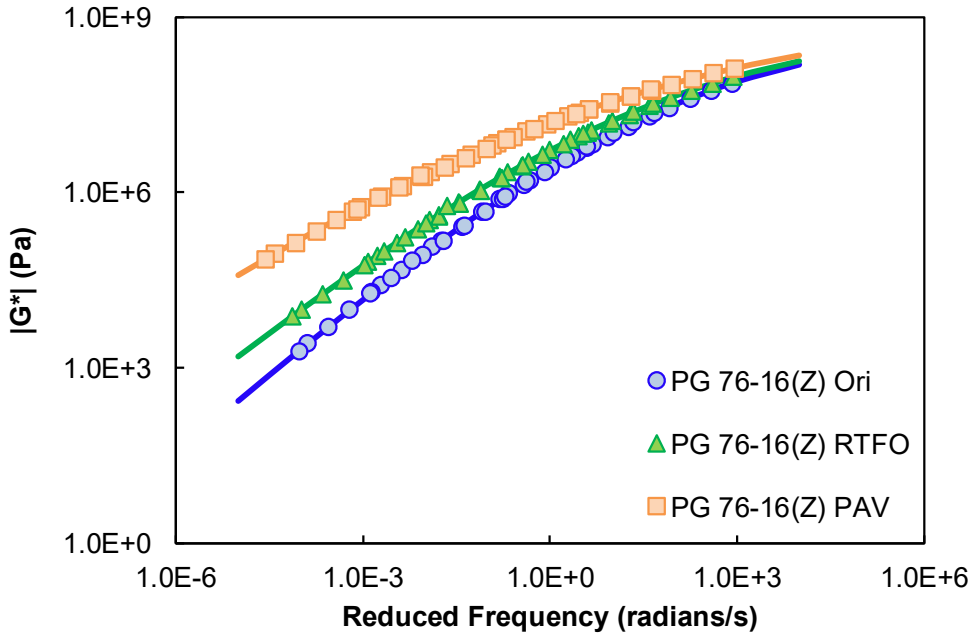

Figure B- 11: Dynamic Modulus Mastercurves for Asphalt PG 76-16(Z) at All Three Aging Conditions

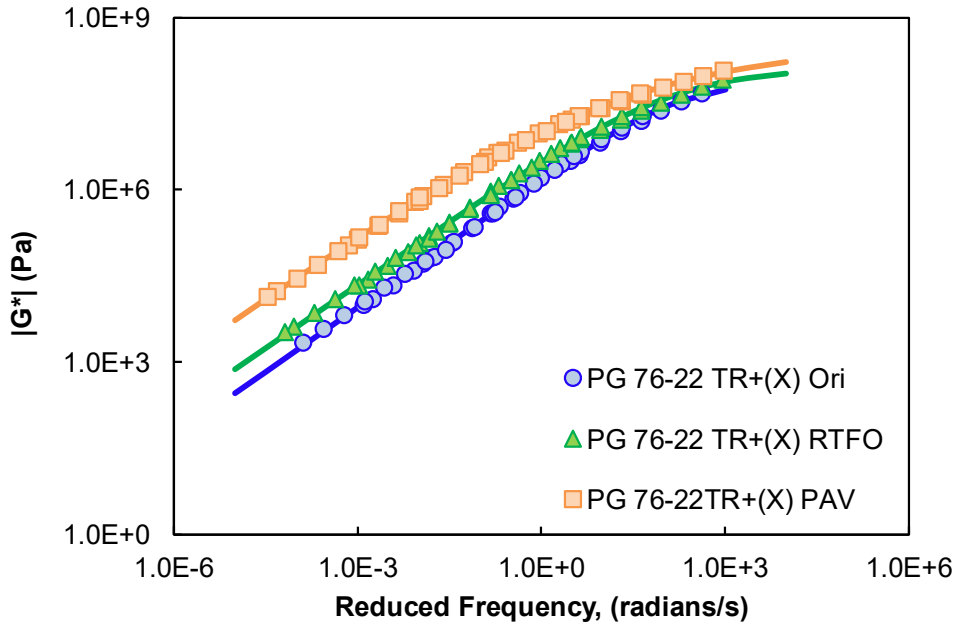

Figure B- 12: Dynamic Modulus Mastercurves for Asphalt PG 76-22TR+(X) at All Three Aging Conditions

APPENDIX C

MECHANICAL TESTING OF ASPHALT MIXTURES

Aggregate Gradation and Mixture Volumetric Properties

In this table, the aggregate gradation that required as an input for dynamic modulus |E*| predictive models in Chapter 4 was presented.

Table C- 1. Asphalt Mixtures Aggregate Gradation Input Requirement for Different Dynamic Modulus |E*| Predictive Models

Source	Mixture	% Passing				
		3/4"	3/8"	No. 4	No. 30	No. 200
Globe	GX4	98.0	76.00	54.0	17.0	4.500
	GX5	98.0	76.00	54.0	17.0	4.500
	GY3	98.0	76.00	54.0	17.0	4.500
	GY4	98.0	76.00	54.0	17.0	4.500
	GY6	98.0	76.00	54.0	17.0	4.500
	GZ2	98.0	76.00	54.0	17.0	4.500
Snowflake	SX3	98.0	72.00	51.0	17.0	4.100
	SY1	98.0	72.00	51.0	17.0	4.100
	SZ1	98.0	72.00	51.0	17.0	4.100
Tucson	TX1	96.0	69.00	59.0	20.0	3.700
	TY5	96.0	69.00	59.0	20.0	3.700
	TZ4	96.0	69.00	59.0	20.0	3.700
	Y5	96.0	69.00	59.0	20.0	3.700
	B5	96.0	69.00	59.0	20.0	3.700
	B2	96.0	69.00	59.0	20.0	3.700
	D0.5	96.0	69.00	59.0	20.0	3.700
	X3	96.0	69.00	59.0	20.0	3.700
	A3-B	96.0	69.00	59.0	20.0	3.700
	A4	96.0	69.00	59.0	20.0	3.700
	A2-B	96.0	69.00	59.0	20.0	3.700
	A3	96.0	69.00	59.0	20.0	3.700
	C3	96.0	69.00	59.0	20.0	3.700

The prefix “T”, “S”, and “G” to the binder notation in the table below indicates the source of the aggregate, which is Tucson, Snowflake, and Globe respectively.

Table C- 2. Mix Design Properties of Arizona Asphalt Mixtures Used in the Study.

Source	Mixture	Mix Design Property						
		Asphalt Binder (%), Pb	Eff. Asphalt content (%), Pbe	% VMA	% VFA	Dust Proportion	Gsb	Gse
Globe	**GX4**	5.2	4.32	14.6	65.9	0.84	2.567	2.628
	GX5	5.4	4.43	14.8	66.2	0.82	2.567	2.634
	GY3	5.3	4.25	14.4	65.3	0.85	2.567	2.643
	GY4	5.3	4.34	14.6	65.8	0.83	2.567	2.636
	GY6	5.3	4.31	14.6	65.7	0.84	2.567	2.634
	GZ2	5.3	4.23	14.4	65.3	0.86	2.567	2.640
Snowflake	**SX3**	5.6	5.18	17.8	64.1	0.91	2.580	2.610
	SY1	5.5	4.94	17.3	63.0	0.96	2.580	2.621
	SZ1	5.3	5.19	17.8	64.1	0.91	2.580	2.586
Tucson	**TX1**	5.8	5.12	17.5	63.5	0.73	2.583	2.633
	TY5	5.5	4.98	17.6	63.6	0.75	2.583	2.618
	TZ4	5.8	5.04	17.5	63.5	0.74	2.583	2.636
	Y5	5.5	4.98	17.6	63.6	0.75	2.583	2.618
	B5	5.8	4.80	17.2	62.8	0.77	2.583	2.647
	B2	5.8	4.80	17.2	62.8	0.77	2.583	2.647
	D0.5	5.8	4.80	17.2	62.8	0.77	2.583	2.647
	X3	5.8	4.80	17.2	62.8	0.77	2.583	2.647
	A3-B	5.8	4.80	17.2	62.8	0.77	2.583	2.647
	A4	5.8	4.80	17.2	62.8	0.77	2.583	2.647
	A2-B	5.8	4.80	17.2	62.8	0.77	2.583	2.647
	A3	5.8	4.80	17.2	62.8	0.77	2.583	2.647
	C3	5.80	4.82	17.2	62.8	0.77	2.583	2.650

Dynamic Modulus Data

Presented below is the dynamic modulus data for all the Group 1and Group 2 asphalt mixtures. The data in Figure C- 1 through Figure C- 12 below is graphical representation of the replicate data and the mastercurve, computed using the average of the replicates. The dynamic modulus and phase angle data for all mixtures and their corresponding replicates is also presented in a tabular format in Table C- 3. through Table C- 14..

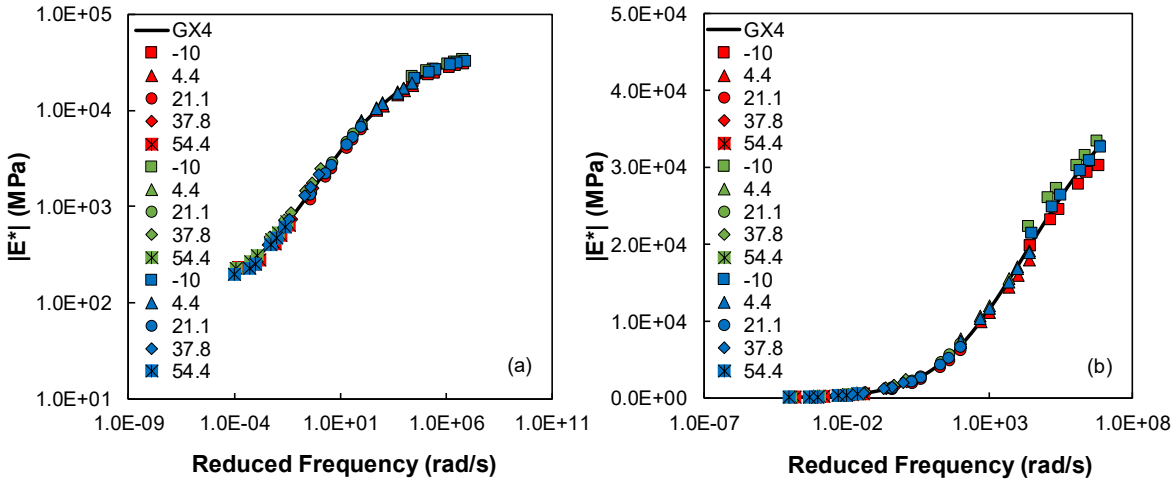

Figure C- 1. Dynamic Modulus Replicate Data and Mastercurve for Mixture GX4 in (a) log-log space and (b) semi-log space.

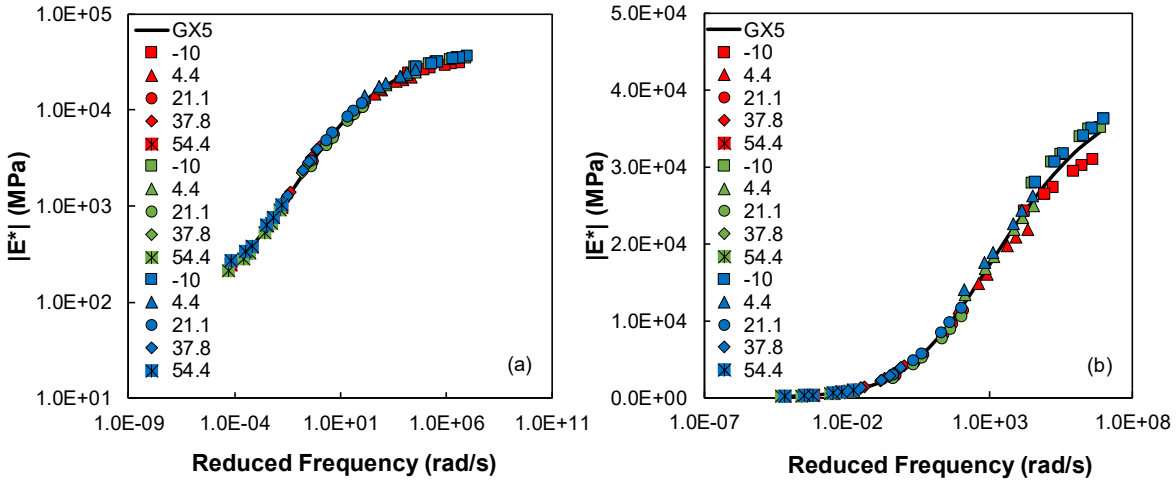

Figure C- 2. Dynamic Modulus Replicate Data and Mastercurve for Mixture GX5 in (a) log-log space and (b) semi-log space.

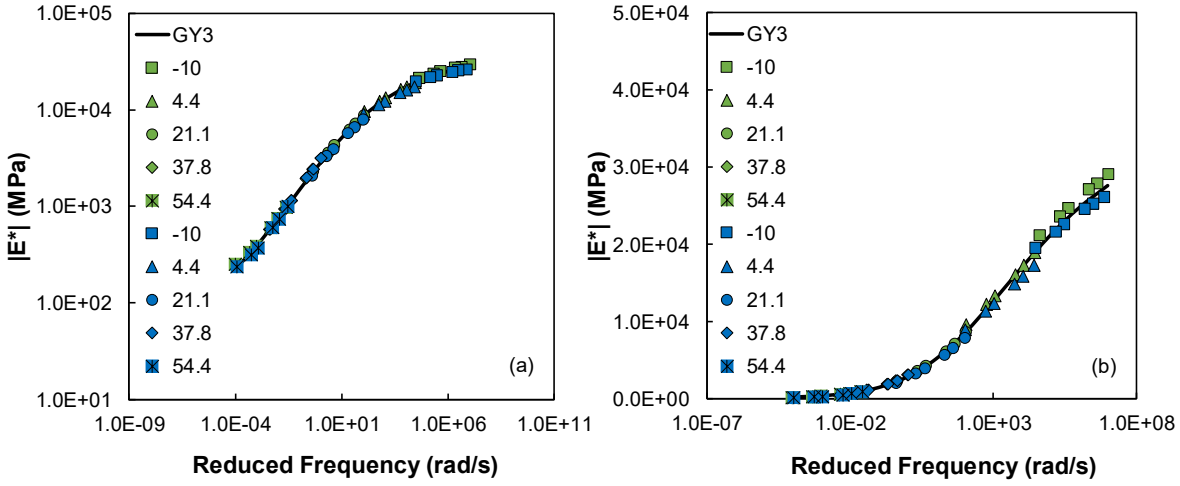

Figure C- 3. Dynamic Modulus Replicate Data and Mastercurve for Mixture GY3 in (a) log-log space and (b) semi-log space.

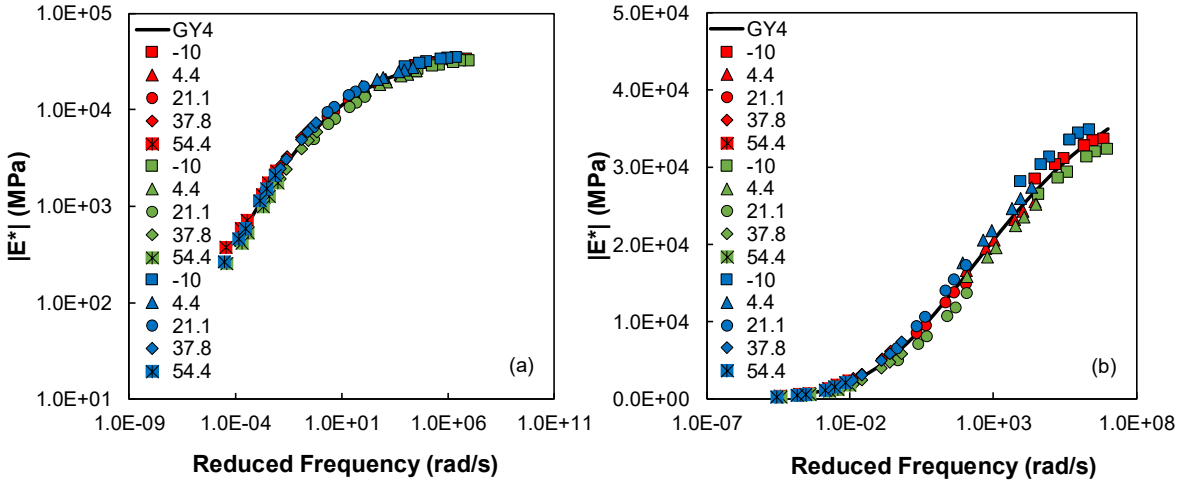

Figure C- 4. Dynamic Modulus Replicate Data and Mastercurve for Mixture GY4 in (a) log-log space and (b) semi-log space.

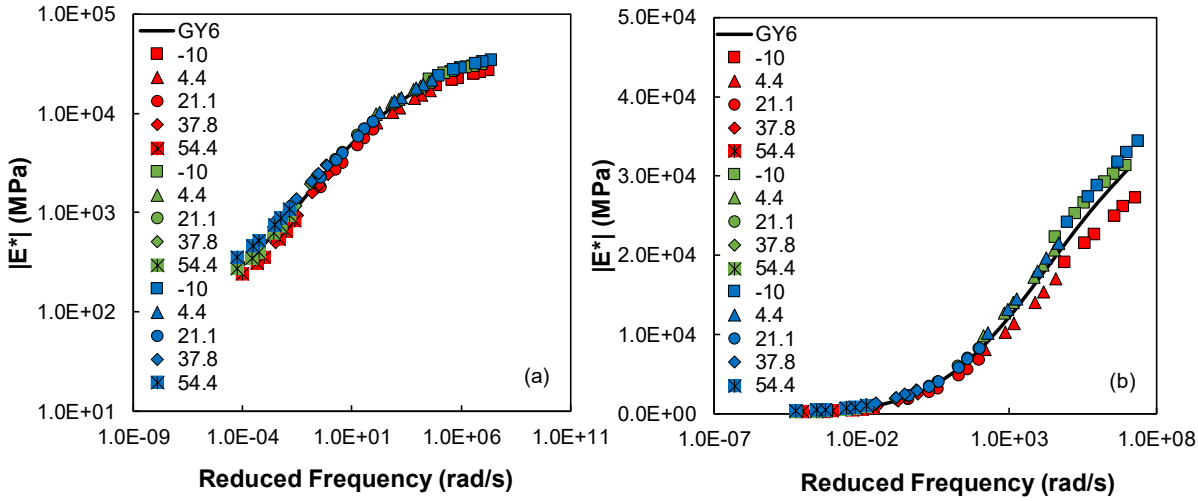

Figure C- 5. Dynamic Modulus Replicate Data and Mastercurve for Mixture GY6 in (a) log-log space and (b) semi-log space.

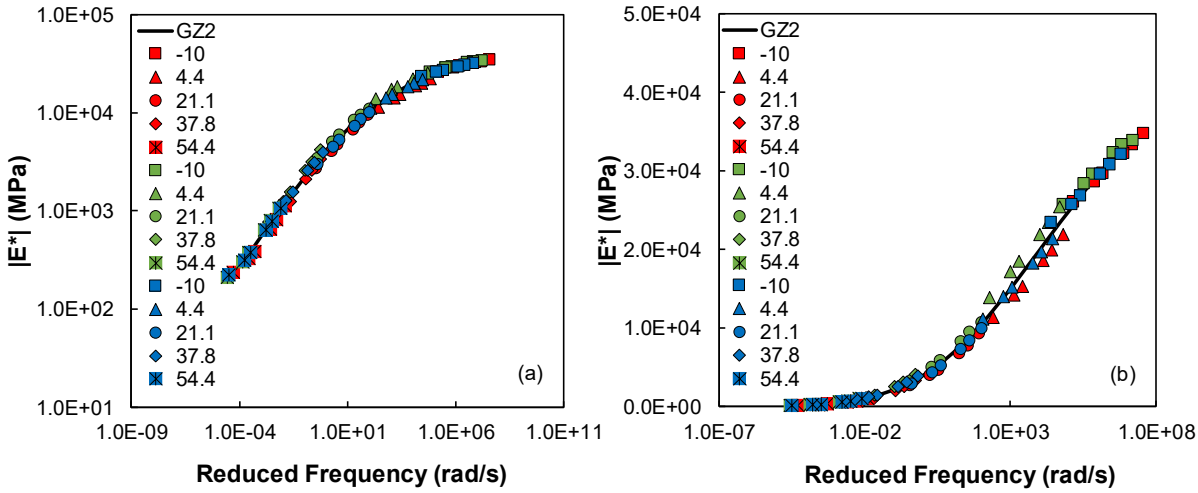

Figure C- 6. Dynamic Modulus Replicate Data and Mastercurve for Mixture GZ2 in (a) log-log space and (b) semi-log space.

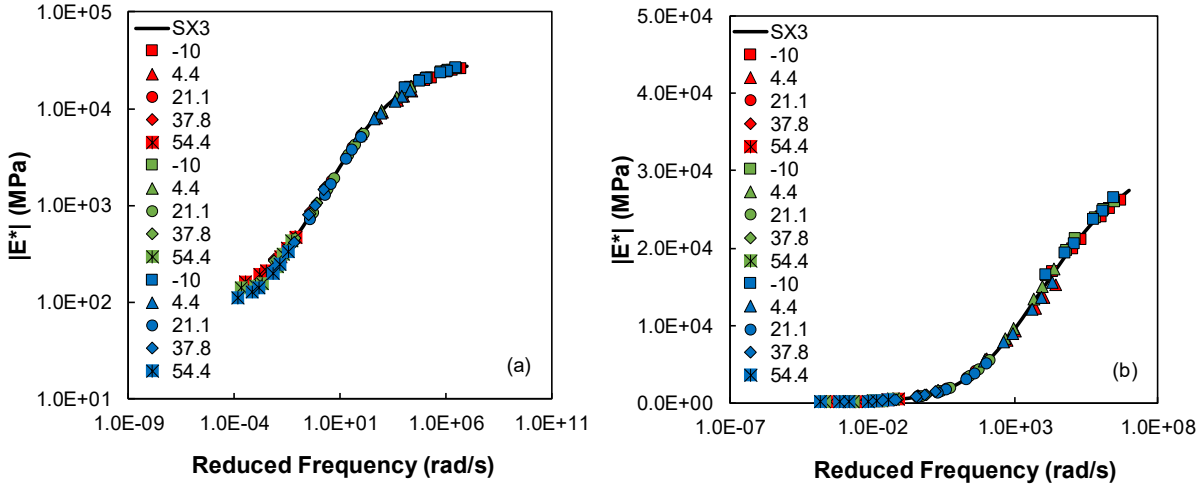

Figure C- 7. Dynamic Modulus Replicate Data and Mastercurve for Mixture SX3 in (a) log-log space and (b) semi-log space.

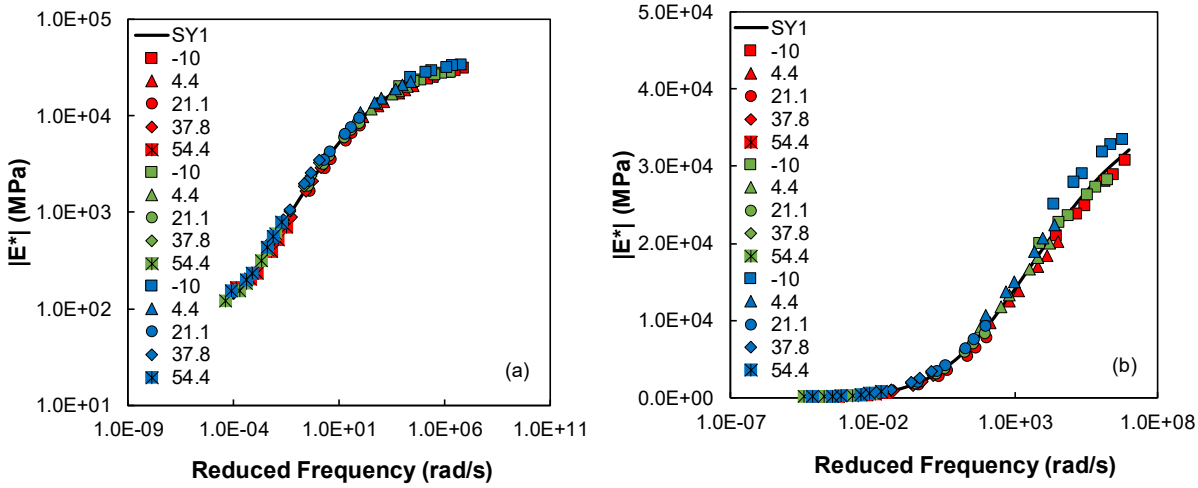

Figure C- 8. Dynamic Modulus Replicate Data and Mastercurve for Mixture SY1 in (a) log-log space and (b) semi-log space.

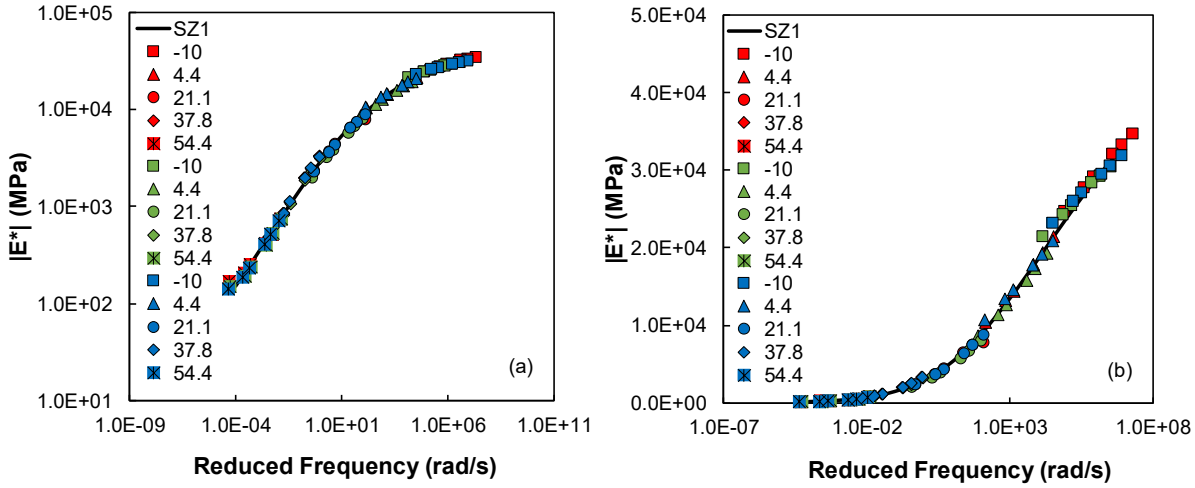

Figure C- 9. Dynamic Modulus Replicate Data and Mastercurve for Mixture SZ1 in (a) log-log space and (b) semi-log space.

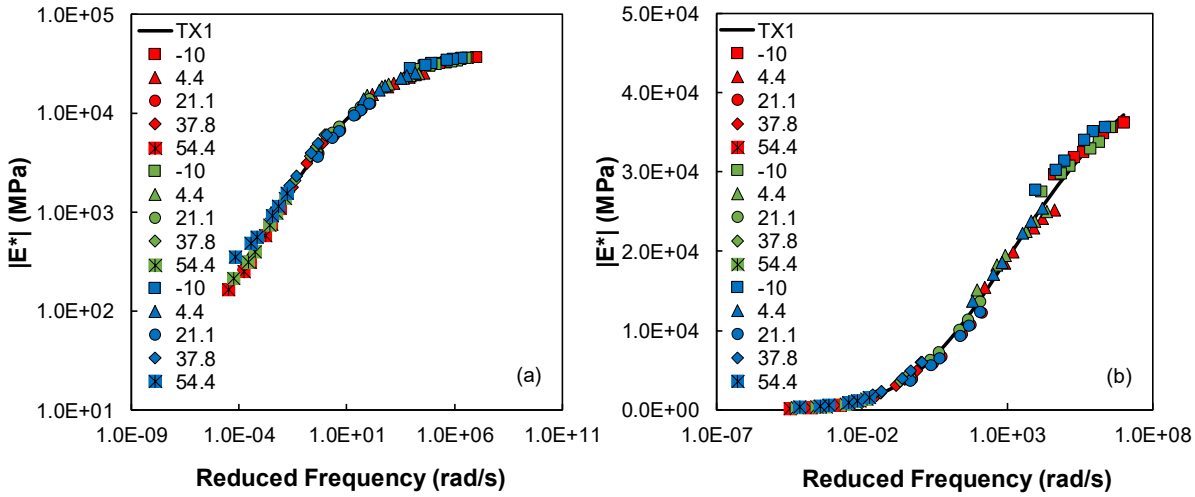

Figure C- 10. Dynamic Modulus Replicate Data and Mastercurve for Mixture TX1 in (a) log-log space and (b) semi-log space.

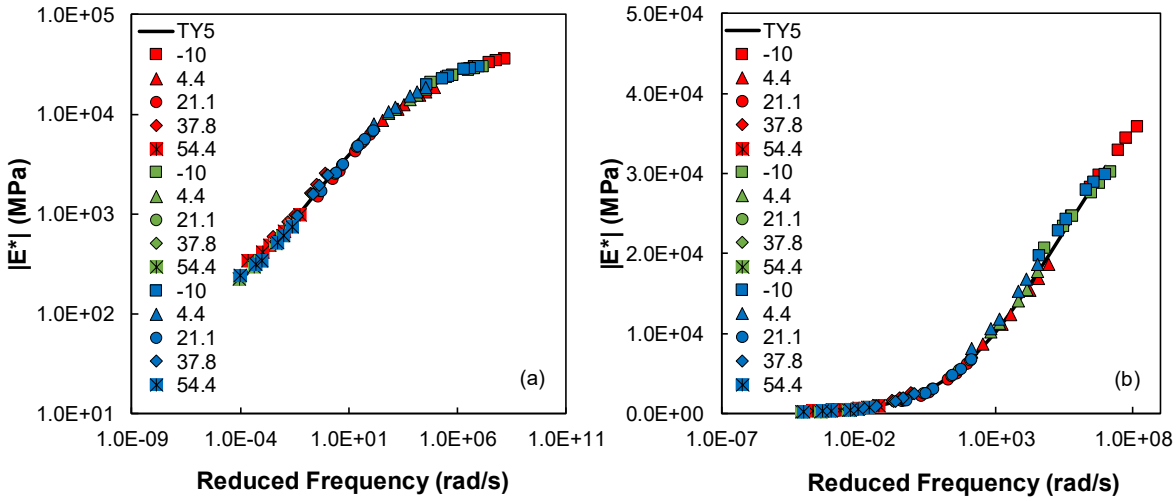

Figure C- 11. Dynamic Modulus Replicate Data and Mastercurve for Mixture TY5 in (a) log-log space and (b) semi-log space.

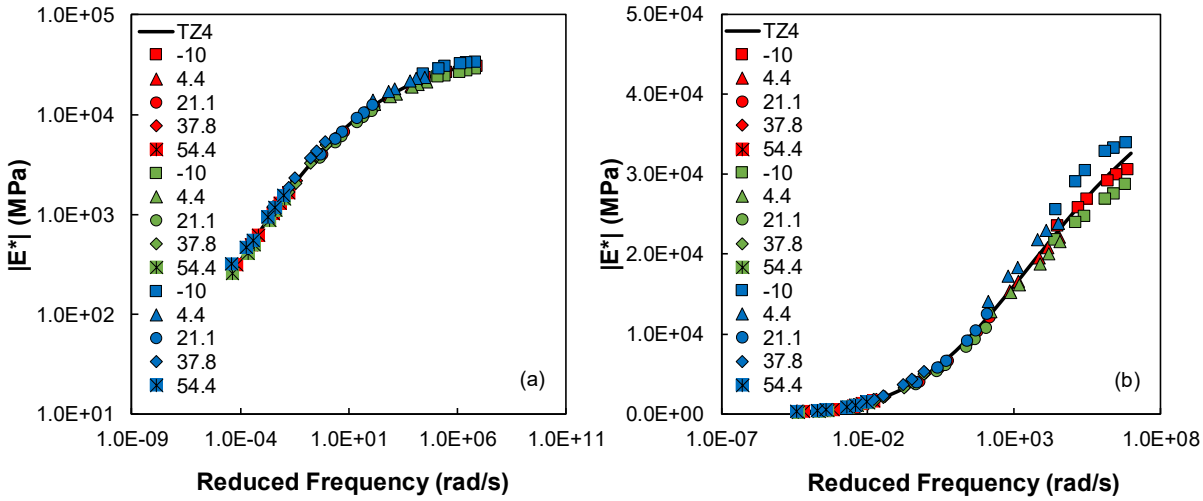

Figure C- 12. Dynamic Modulus Replicate Data and Mastercurve for Mixture TZ4 in (a) log-log space and (b) semi-log space.

Table C- 3. Dynamic Modulus and Phase Angle Replicate Data for Mixture GX4.

Temp (°C)	Freq. (Hz)	Dynamic Modulus, |E*|			Phase Angle, φ		
		Repl. 1 (MPa)	Repl. 2 (MPa)	Repl. 3 (MPa)	Repl. 1 (Deg.)	Repl. 2 (Deg.)	Repl. 3 (Deg.)
-10.0	25	30348	33477	32761	4.8	4.9	5.8
	10	29374	31603	30910	7.2	6.3	7.4
	5	27900	30336	29644	8.3	8.6	7.8
	1	24620	27288	26407	9.9	9.6	9.7
	0.5	23302	26080	24978	10.3	10.1	10.0
	0.1	19823	22378	21487	12.3	12.1	12.5
4.4	25	18024	19163	19039	10.4	10.0	13.3
	10	16002	17138	16936	14.0	13.2	15.0
	5	14503	15586	15156	16.0	15.6	16.9
	1	11168	12125	11796	19.0	19.0	20.2
	0.5	9965	10746	10418	21.7	20.4	22.4
	0.1	7200	7847	7518	25.7	24.6	26.2
21.1	25	6311	7104	6659	22.4	21.5	21.5
	10	4901	5712	5229	27.6	26.3	26.6
	5	4014	4687	4381	28.5	28.8	28.7
	1	2495	2866	2709	33.9	32.7	33.3
	0.5	2009	2305	2208	34.5	34.0	34.5
	0.1	1185	1386	1324	33.1	32.9	32.8
37.8	25	2183	2492	2135	33.4	32.5	33.3
	10	1571	1772	1576	36.5	36.2	35.5
	5	1279	1466	1299	36.7	36.1	37.7
	1	745	864	743	36.6	33.2	35.1
	0.5	619	717	605	36.0	33.9	34.1
	0.1	410	483	399	32.4	31.0	30.1
54.4	25	634	699	611	37.6	35.5	39.6
	10	499	531	473	36.3	34.8	41.0
	5	409	456	402	35.4	32.2	38.8
	1	277	306	254	31.7	29.9	31.5
	0.5	253	269	229	29.4	27.4	28.8
	0.1	231	226	200	28.3	25.9	27.7

Table C- 4. Dynamic Modulus and Phase Angle Replicate Data for Mixture GX5.

Temp (°C)	Freq. (Hz)	Dynamic Modulus, |E*|			Phase Angle, φ		
		Repl. 1 (MPa)	Repl. 2 (MPa)	Repl. 3 (MPa)	Repl. 1 (Deg.)	Repl. 2 (Deg.)	Repl. 3 (Deg.)
-10.0	25	31032	35245	36280	2.0	2.1	3.2
	10	30301	35001	35159	5.8	4.3	5.3
	5	29535	34042	34171	6.2	5.5	5.6
	1	27425	31658	31827	7.9	6.6	7.0
	0.5	26514	30715	30662	7.9	6.9	6.9
	0.1	24313	27999	28033	8.7	7.8	8.2
4.4	25	21941	24950	26260	6.6	7.0	7.6
	10	20870	23461	24448	11.3	8.9	9.9
	5	19817	21950	22675	12.1	10.0	11.2
	1	16131	18373	18989	15.9	14.1	13.9
	0.5	14824	16887	17667	16.8	14.3	14.6
	0.1	11675	13451	14084	20.6	18.3	18.9
21.1	25	11372	10565	11709	17.2	16.9	16.4
	10	9569	8970	9777	20.7	21.0	20.2
	5	8271	7677	8439	23.4	23.7	22.3
	1	5593	5140	5779	30.8	29.9	29.2
	0.5	4683	4254	4816	32.6	32.4	30.8
	0.1	2892	2556	2940	36.0	34.3	33.9
37.8	25	4146	3819	3927	26.0	27.6	26.3
	10	3179	2809	2930	30.5	32.6	30.6
	5	2526	2225	2359	33.6	34.6	34.1
	1	1394	1246	1290	35.5	35.1	35.4
	0.5	1112	984	1017	34.6	34.9	35.0
	0.1	663	589	606	30.1	30.2	30.7
54.4	25	969	908	1042	33.2	36.7	34.8
	10	756	663	769	31.7	36.4	37.6
	5	622	533	633	30.6	32.4	35.4
	1	374	325	385	27.2	28.1	27.6
	0.5	324	282	336	24.0	26.1	25.1
	0.1	245	211	272	19.8	21.5	22.6

Table C- 5. Dynamic Modulus and Phase Angle Replicate Data for Mixture GY3.

Temp (°C)	Freq. (Hz)	Dynamic Modulus, |E*|			Phase Angle, φ		
		Repl. 1 (MPa)	Repl. 2 (MPa)	Repl. 3 (MPa)	Repl. 1 (Deg.)	Repl. 2 (Deg.)	Repl. 3 (Deg.)
-10.0	25	39794	29128	26125	2.3	3.2	1.6
	10	38031	27883	25293	4.1	5.0	3.3
	5	37097	27149	24547	5.6	5.6	4.7
	1	34059	24718	22565	6.4	6.7	6.0
	0.5	32891	23641	21643	6.3	6.9	6.1
	0.1	29478	21210	19594	7.5	7.8	7.0
4.4	25	26667	19040	17386	5.8	7.2	7.3
	10	24570	17390	15950	8.9	10.6	9.8
	5	22810	16155	14940	10.3	11.8	10.8
	1	19358	13428	12404	12.8	13.5	13.4
	0.5	17956	12283	11396	13.8	15.0	13.6
	0.1	14564	9619	8987	16.2	17.4	17.2
21.1	25	11787	8701	7853	16.4	15.7	16.5
	10	9980	7142	6617	21.3	20.3	19.8
	5	8717	6179	5720	22.0	22.5	22.7
	1	6017	4262	3906	27.2	27.2	27.2
	0.5	5098	3578	3282	28.0	29.6	29.2
	0.1	3379	2296	2078	30.1	32.4	30.2
37.8	25	4849	3161	3171	23.5	25.7	24.7
	10	3676	2425	2430	26.3	28.7	27.7
	5	2973	1956	1969	29.8	31.6	29.5
	1	1770	1156	1153	32.7	33.7	32.7
	0.5	1438	933	940	33.4	33.2	32.7
	0.1	883	578	573	31.4	31.2	30.5
54.4	25	1372	982	992	32.8	35.7	33.5
	10	976	747	743	34.9	37.6	34.7
	5	787	608	601	35.4	36.1	34.0
	1	487	389	369	32.8	33.2	29.1
	0.5	406	334	318	30.0	31.6	26.0
	0.1	274	255	238	26.5	26.4	22.4

Table C- 6. Dynamic Modulus and Phase Angle Replicate Data for Mixture GY4.

Temp (°C)	Freq. (Hz)	Dynamic Modulus, |E*|			Phase Angle, φ		
		Repl. 1 (MPa)	Repl. 2 (MPa)	Repl. 3 (MPa)	Repl. 1 (Deg.)	Repl. 2 (Deg.)	Repl. 3 (Deg.)
-10.0	25	33626	32309	34884	1.4	3.8	2.1
	10	33473	32056	34439	3.0	5.1	2.7
	5	32843	31372	33524	3.7	5.9	3.4
	1	31137	29427	31406	5.0	6.6	4.6
	0.5	30376	28596	30374	5.3	6.6	5.0
	0.1	28543	26581	28199	6.2	7.5	5.2
4.4	25	25549	25155	27459	2.6	5.3	3.0
	10	24365	23532	25939	5.4	7.7	6.3
	5	23201	22416	24704	6.7	8.5	7.5
	1	20585	19642	21785	9.0	9.9	9.5
	0.5	19518	18402	20536	10.3	10.4	10.6
	0.1	16647	15810	17577	11.5	12.3	12.2
21.1	25	14914	13648	17329	12.5	11.8	11.7
	10	13769	11838	15379	16.3	15.2	14.8
	5	12413	10693	14005	17.8	17.2	16.7
	1	9512	8006	10627	22.7	21.5	21.5
	0.5	8469	7024	9347	25.1	23.8	24.3
	0.1	6098	4964	6489	30.1	28.3	29.1
37.8	25	7276	5855	7343	20.9	21.5	22.3
	10	6159	4768	5898	25.1	25.3	26.2
	5	5173	3956	4958	28.7	28.1	29.4
	1	3245	2412	3102	34.1	34.2	35.2
	0.5	2625	1930	2482	36.1	36.3	36.6
	0.1	1562	1095	1430	36.4	35.7	36.6
54.4	25	2332	1753	2105	33.1	33.5	32.5
	10	1733	1270	1510	37.1	37.1	36.6
	5	1314	987	1141	38.6	39.4	40.1
	1	720	525	582	37.8	37.1	39.0
	0.5	581	416	455	36.2	36.1	37.4
	0.1	373	255	268	31.1	31.5	31.3

Table C- 7. Dynamic Modulus and Phase Angle Replicate Data for Mixture GY6.

Temp (°C)	Freq. (Hz)	Dynamic Modulus, |E*|			Phase Angle, φ		
		Repl. 1 (MPa)	Repl. 2 (MPa)	Repl. 3 (MPa)	Repl. 1 (Deg.)	Repl. 2 (Deg.)	Repl. 3 (Deg.)
-10.0	25	27242	31263	34425	3.4	2.3	5.6
	10	26120	30184	32960	6.9	5.2	7.7
	5	24986	29172	31804	8.0	7.4	9.4
	1	22664	26564	28833	9.7	8.5	10.3
	0.5	21552	25231	27361	9.6	8.5	11.4
	0.1	19112	22275	24201	10.6	9.7	12.7
4.4	25	17042	20626	21545	9.9	7.4	10.3
	10	15412	18814	19660	12.0	11.0	13.4
	5	14082	17232	18022	13.6	12.4	15.1
	1	11391	14002	14507	15.8	14.6	20.1
	0.5	10344	12723	13202	16.3	15.5	20.0
	0.1	8115	9907	10187	18.9	18.3	24.0
21.1	25	6786	8220	8252	19.4	18.2	24.7
	10	5601	6976	6905	23.2	23.5	27.8
	5	4781	6016	5845	24.3	25.8	29.3
	1	3188	4030	3983	28.2	29.4	31.9
	0.5	2695	3429	3345	29.6	30.4	33.0
	0.1	1791	2285	2258	30.6	31.4	31.8
37.8	25	2449	3071	2987	29.1	25.3	27.9
	10	1901	2411	2477	31.4	29.0	29.6
	5	1580	1967	2069	31.5	31.1	31.3
	1	943	1175	1386	32.2	32.8	30.4
	0.5	777	953	1167	31.9	32.6	28.6
	0.1	507	629	820	30.4	30.3	26.2
54.4	25	836	933	1092	31.4	32.6	30.7
	10	658	733	882	32.5	33.4	29.4
	5	545	624	759	30.2	31.5	28.9
	1	353	404	526	28.3	28.1	22.5
	0.5	312	348	463	28.5	26.3	24.2
	0.1	244	272	359	26.1	23.2	22.6

Table C- 8. Dynamic Modulus and Phase Angle Replicate Data for Mixture GZ2.

Temp (°C)	Freq. (Hz)	Dynamic Modulus, |E*|			Phase Angle, φ		
		Repl. 1 (MPa)	Repl. 2 (MPa)	Repl. 3 (MPa)	Repl. 1 (Deg.)	Repl. 2 (Deg.)	Repl. 3 (Deg.)
-10.0	25	34778	33952	32123	3.4	2.0	5.0
	10	33416	33381	30848	5.6	3.1	6.9
	5	32284	32341	29624	6.0	4.2	7.2
	1	29794	29598	26923	7.4	5.7	8.2
	0.5	28617	28488	25853	8.4	5.7	8.7
	0.1	26086	25780	23452	8.3	6.0	9.2
4.4	25	21996	25457	21446	8.0	6.6	5.4
	10	19991	23519	19793	9.8	7.5	8.4
	5	18684	21995	18372	11.0	9.6	9.5
	1	15394	18519	15251	14.0	12.0	12.6
	0.5	14232	17241	14041	15.3	12.8	12.8
	0.1	11444	13955	11202	17.7	14.2	15.2
21.1	25	9384	10784	9968	17.7	17.1	15.3
	10	7801	9504	8463	21.1	19.1	19.1
	5	6763	8296	7326	22.5	21.4	21.9
	1	4755	5939	5219	27.5	25.6	26.9
	0.5	4053	5095	4427	29.2	27.5	28.7
	0.1	2721	3438	2964	32.4	29.7	31.8
37.8	25	3385	4186	3962	24.3	24.2	23.1
	10	2586	3187	3133	26.7	28.1	27.0
	5	2098	2599	2583	30.4	31.0	29.6
	1	1258	1558	1557	32.5	34.5	33.8
	0.5	1069	1256	1274	32.1	34.2	35.1
	0.1	670	771	787	31.1	32.1	33.1
54.4	25	1127	1067	1071	37.8	34.8	33.5
	10	820	808	778	39.7	33.7	35.6
	5	647	645	641	38.5	35.9	37.2
	1	384	380	380	33.4	33.2	34.3
	0.5	329	304	316	30.0	31.2	33.2
	0.1	238	212	224	27.6	26.8	29.5

Table C- 9. Dynamic Modulus and Phase Angle Replicate Data for Mixture SX3.

Temp (°C)	Freq. (Hz)	Dynamic Modulus, |E*|			Phase Angle, φ		
		Repl. 1 (MPa)	Repl. 2 (MPa)	Repl. 3 (MPa)	Repl. 1 (Deg.)	Repl. 2 (Deg.)	Repl. 3 (Deg.)
-10.0	25	26195	26008	26457	3.0	4.1	5.9
	10	25129	24988	24810	7.0	7.6	8.4
	5	23970	23944	23713	8.0	10.0	8.1
	1	21034	21195	20524	9.3	10.9	10.3
	0.5	19875	19690	19392	9.8	11.5	9.8
	0.1	17003	16452	16530	12.4	12.9	11.8
4.4	25	15262	17278	15585	12.1	13.5	12.2
	10	13574	15044	13623	16.2	16.9	16.2
	5	12155	13393	12110	17.5	18.6	18.2
	1	9226	9608	8992	21.3	25.2	22.5
	0.5	8107	8272	7812	23.4	26.8	24.5
	0.1	5642	5551	5338	27.6	30.6	29.2
21.1	25	5262	5521	5053	25.2	25.3	25.4
	10	4027	4248	3793	28.8	28.7	30.6
	5	3174	3371	3031	32.1	31.4	33.5
	1	1806	1910	1672	35.5	36.1	35.9
	0.5	1381	1465	1269	37.0	35.9	36.0
	0.1	775	837	714	33.8	33.1	33.9
37.8	25	1561	1531	1477	34.8	36.7	36.3
	10	1080	1071	1016	35.1	38.9	39.4
	5	877	822	801	35.3	39.9	38.1
	1	479	460	418	31.4	34.6	33.2
	0.5	387	384	333	30.1	32.2	30.4
	0.1	279	269	226	25.6	25.7	24.6
54.4	25	474	435	337	36.7	45.9	32.0
	10	365	316	250	32.3	43.1	30.2
	5	300	233	200	29.3	41.1	27.7
	1	214	156	143	20.8	34.0	23.0
	0.5	194	147	128	19.5	32.6	20.2
	0.1	163	141	111	17.9	33.3	17.0

Table C- 10. Dynamic Modulus and Phase Angle Replicate Data for Mixture SY1.

Temp (°C)	Freq. (Hz)	Dynamic Modulus, |E*|			Phase Angle, φ		
		Repl. 1 (MPa)	Repl. 2 (MPa)	Repl. 3 (MPa)	Repl. 1 (Deg.)	Repl. 2 (Deg.)	Repl. 3 (Deg.)
-10.0	25	30739	28283	33489	3.2	4.8	4.2
	10	28944	27273	32809	5.6	6.8	5.8
	5	27999	26281	31868	6.2	7.8	6.6
	1	24905	23645	29038	7.7	8.6	8.0
	0.5	23815	22725	27927	8.0	8.6	8.2
	0.1	20937	20063	25057	9.3	9.4	9.0
4.4	25	20202	20007	22385	7.9	7.0	7.8
	10	18434	18200	20631	10.9	11.0	10.7
	5	17021	16665	18899	12.5	12.7	12.0
	1	13816	13316	15035	15.2	17.4	16.2
	0.5	12562	11744	13747	16.6	17.5	16.5
	0.1	9693	9121	10702	19.1	20.4	19.5
21.1	25	7728	8298	9301	20.2	21.9	19.6
	10	6462	6992	7529	23.9	27.3	23.3
	5	5414	5916	6392	26.5	29.9	26.1
	1	3483	3801	4209	32.3	34.2	31.5
	0.5	2812	3133	3439	32.8	35.9	34.6
	0.1	1640	1835	2068	34.8	36.3	36.5
37.8	25	2867	3255	3406	29.7	30.6	29.3
	10	2095	2376	2526	31.5	33.3	32.8
	5	1633	1863	1979	35.8	38.0	34.7
	1	883	1023	1059	36.5	38.8	38.7
	0.5	689	768	825	36.3	38.6	38.9
	0.1	387	459	475	32.5	33.6	36.6
54.4	25	695	593	790	38.4	40.9	39.4
	10	512	405	559	37.4	41.2	40.2
	5	387	312	427	33.5	37.6	36.6
	1	231	183	230	29.9	31.2	30.7
	0.5	201	151	198	27.5	27.8	28.0
	0.1	165	120	152	23.7	23.4	21.3

Table C- 11. Dynamic Modulus and Phase Angle Replicate Data for Mixture SZ1.

Temp (°C)	Freq. (Hz)	Dynamic Modulus, |E*|			Phase Angle, φ		
		Repl. 1 (MPa)	Repl. 2 (MPa)	Repl. 3 (MPa)	Repl. 1 (Deg.)	Repl. 2 (Deg.)	Repl. 3 (Deg.)
-10.0	25	34628	30388	31804	4.3	4.7	3.3
	10	33181	29246	30459	4.4	7.2	5.2
	5	32063	28286	29468	6.2	8.0	6.2
	1	29073	25390	26986	6.3	9.1	7.6
	0.5	27643	24223	25898	7.5	9.0	8.2
	0.1	24667	21398	23153	8.4	10.3	9.0
4.4	25	21386	19198	20847	8.8	8.2	7.2
	10	19342	17290	19155	10.9	10.4	10.4
	5	17871	15799	17746	12.2	12.6	11.6
	1	14366	12623	14549	15.3	15.2	14.0
	0.5	13117	11296	13362	16.1	17.1	15.3
	0.1	10301	8572	10621	19.1	19.2	18.1
21.1	25	7757	7931	8740	18.2	18.3	17.4
	10	7434	6673	7391	23.4	22.4	21.7
	5	6411	5699	6346	25.2	24.2	24.0
	1	4345	3821	4309	30.3	29.8	28.6
	0.5	3642	3188	3616	31.8	31.1	30.1
	0.1	2312	1988	2281	34.8	32.9	32.3
37.8	25	3289	3146	3265	30.0	27.3	26.8
	10	2453	2326	2503	32.6	29.3	30.6
	5	1988	1843	1990	35.0	32.0	33.2
	1	1108	1069	1119	35.5	35.0	34.9
	0.5	844	820	857	35.8	35.2	35.7
	0.1	469	479	489	32.5	32.6	33.8
54.4	25	746	745	707	37.6	36.6	37.8
	10	516	523	516	39.8	38.3	42.4
	5	414	400	409	38.4	37.4	40.6
	1	250	238	231	30.5	31.2	33.6
	0.5	207	192	187	28.1	29.0	28.5
	0.1	168	151	140	21.0	23.0	24.1

Table C- 12. Dynamic Modulus and Phase Angle Replicate Data for Mixture TX1.

Temp (°C)	Freq. (Hz)	Dynamic Modulus, |E*|			Phase Angle, φ		
		Repl. 1 (MPa)	Repl. 2 (MPa)	Repl. 3 (MPa)	Repl. 1 (Deg.)	Repl. 2 (Deg.)	Repl. 3 (Deg.)
-10.0	25	36115	35609	35612	4.8	5.6	3.6
	10	35666	33732	35124	6.6	3.2	5.5
	5	34860	32899	33964	7.3	3.4	5.6
	1	32450	30770	31426	9.0	4.5	6.5
	0.5	31777	29752	30223	8.5	5.1	7.3
	0.1	29691	27463	27727	9.2	5.7	8.3
4.4	25	25217	24956	25473	6.6	8.2	6.5
	10	24088	23808	23819	9.5	6.0	8.4
	5	22880	22514	22284	10.1	8.2	10.3
	1	19869	19475	18599	12.5	10.7	12.8
	0.5	18524	18211	17099	12.6	11.2	13.4
	0.1	15435	15109	13760	15.0	14.7	16.7
21.1	25	12237	13606	12325	14.6	15.5	15.7
	10	10707	11295	10556	18.0	18.5	20.7
	5	9459	9969	9255	19.8	20.9	22.5
	1	6616	7156	6442	26.2	26.8	27.7
	0.5	5829	6189	5553	29.4	30.1	31.0
	0.1	3839	3999	3589	34.3	35.7	36.2
37.8	25	4950	5966	5975	23.9	26.3	26.8
	10	3862	4540	4877	29.0	30.9	30.0
	5	3077	3619	3932	32.4	33.5	32.8
	1	1777	2080	2286	35.9	38.6	37.6
	0.5	1378	1612	1826	36.4	39.0	38.4
	0.1	749	869	1053	34.1	36.8	34.7
54.4	25	1102	1377	1539	37.7	38.1	37.4
	10	756	976	1136	38.6	39.8	37.0
	5	576	732	908	37.2	39.8	37.1
	1	308	393	561	32.5	35.0	32.1
	0.5	248	314	486	30.3	32.3	26.9
	0.1	164	212	348	24.5	26.8	19.9

Table C- 13. Dynamic Modulus and Phase Angle Replicate Data for Mixture TY5.

Temp (°C)	Freq. (Hz)	Dynamic Modulus, |E*|			Phase Angle, φ		
		Repl. 1 (MPa)	Repl. 2 (MPa)	Repl. 3 (MPa)	Repl. 1 (Deg.)	Repl. 2 (Deg.)	Repl. 3 (Deg.)
-10.0	25	35933	30233	29948	4.3	5.8	6.0
	10	34450	28883	29004	7.1	5.6	7.2
	5	32937	27721	28010	8.0	7.6	7.9
	1	29870	24725	24335	9.4	8.0	9.9
	0.5	28282	23483	22869	9.9	8.8	11.3
	0.1	24702	20761	19757	11.6	10.0	12.8
4.4	25	18624	17826	18622	11.9	9.3	8.5
	10	16899	15563	16828	14.8	11.3	13.3
	5	15399	14167	15334	15.5	13.0	14.1
	1	12372	11293	11813	18.0	15.7	17.4
	0.5	11201	10175	10630	18.4	16.5	18.5
	0.1	8745	7744	8113	21.4	18.8	20.5
21.1	25	6206	6657	6783	22.8	18.9	20.0
	10	5050	5400	5589	27.7	22.7	24.3
	5	4242	4690	4794	29.5	23.7	25.2
	1	2669	3078	3117	33.8	27.0	30.4
	0.5	2246	2542	2570	34.1	28.0	31.7
	0.1	1499	1686	1693	31.7	28.2	32.3
37.8	25	2596	2493	2478	28.8	26.9	29.1
	10	1976	1910	1961	29.0	31.2	30.4
	5	1613	1588	1601	31.8	30.4	32.1
	1	982	970	962	33.0	30.4	33.2
	0.5	833	794	781	32.9	29.6	32.5
	0.1	599	537	527	27.5	26.7	30.7
54.4	25	992	774	744	28.7	30.6	33.7
	10	799	608	615	28.1	31.6	31.3
	5	681	514	517	26.2	28.4	26.3
	1	492	340	344	24.5	25.6	28.5
	0.5	420	297	314	22.5	25.3	27.6
	0.1	340	226	243	19.6	21.7	23.3

Table C- 14. Dynamic Modulus and Phase Angle Replicate Data for Mixture TZ4.

Temp (°C)	Freq. (Hz)	Dynamic Modulus, |E*|			Phase Angle, φ		
		Repl. 1 (MPa)	Repl. 2 (MPa)	Repl. 3 (MPa)	Repl. 1 (Deg.)	Repl. 2 (Deg.)	Repl. 3 (Deg.)
-10.0	25	30600	28795	34004	2.2	5.0	3.8
	10	29977	27555	33284	4.5	4.1	5.3
	5	29189	26875	32847	5.1	4.6	5.8
	1	26882	24756	30486	6.1	5.6	6.5
	0.5	25851	24008	29051	6.4	5.4	7.0
	0.1	23511	21853	25583	7.0	6.5	8.0
4.4	25	22149	21606	23861	5.7	4.8	6.6
	10	20834	20118	23026	7.3	7.9	8.3
	5	19543	18813	21804	8.5	9.0	10.0
	1	16669	16218	18348	10.6	10.1	12.2
	0.5	15476	15251	17234	11.1	10.9	12.5
	0.1	12762	12794	14138	13.3	12.4	14.9
21.1	25	12022	10778	12526	12.9	13.3	16.5
	10	10356	9377	10473	16.8	17.0	19.4
	5	9103	8419	9193	18.1	17.9	21.5
	1	6703	6145	6696	22.0	22.7	25.4
	0.5	5829	5330	5783	24.1	24.5	27.9
	0.1	4036	3707	3979	27.7	28.0	31.1
37.8	25	5119	4971	5362	20.9	19.9	22.5
	10	4132	3940	4349	25.7	25.6	27.9
	5	3462	3298	3689	27.5	26.9	29.5
	1	2199	2081	2311	31.5	29.9	33.5
	0.5	1828	1711	1888	32.4	32.1	34.2
	0.1	1167	1070	1197	32.2	31.7	34.2
54.4	25	1674	1457	1570	30.4	30.6	31.3
	10	1302	1111	1176	31.2	31.7	32.0
	5	1038	873	947	31.8	32.7	33.6
	1	621	498	551	30.2	29.9	32.4
	0.5	497	409	471	29.5	28.2	30.9
	0.1	318	257	324	26.8	25.7	26.8

Dynamic Modulus Data

Presented below is the dynamic modulus data for all Group 3 asphalts used to study the effect of recovery on the performance of asphalt concrete. Each mixture has three replicates, and presented in the Figures below is the replicate data and the mastercurve, computed using the average of the three replicates.

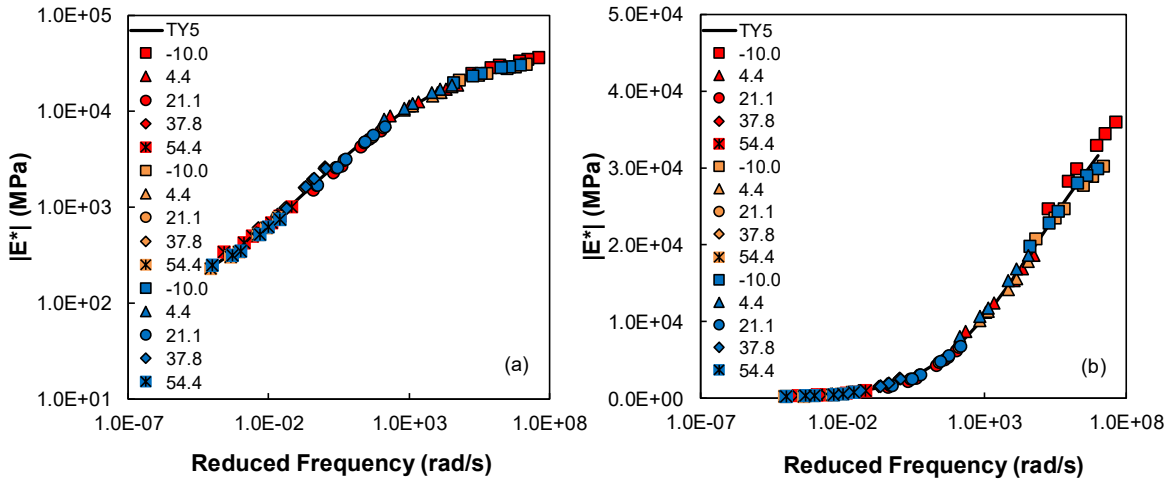

Figure C- 13. Dynamic Modulus Replicate Data for Mixture TY5 in (a) log-log space and (b) semi-log space.

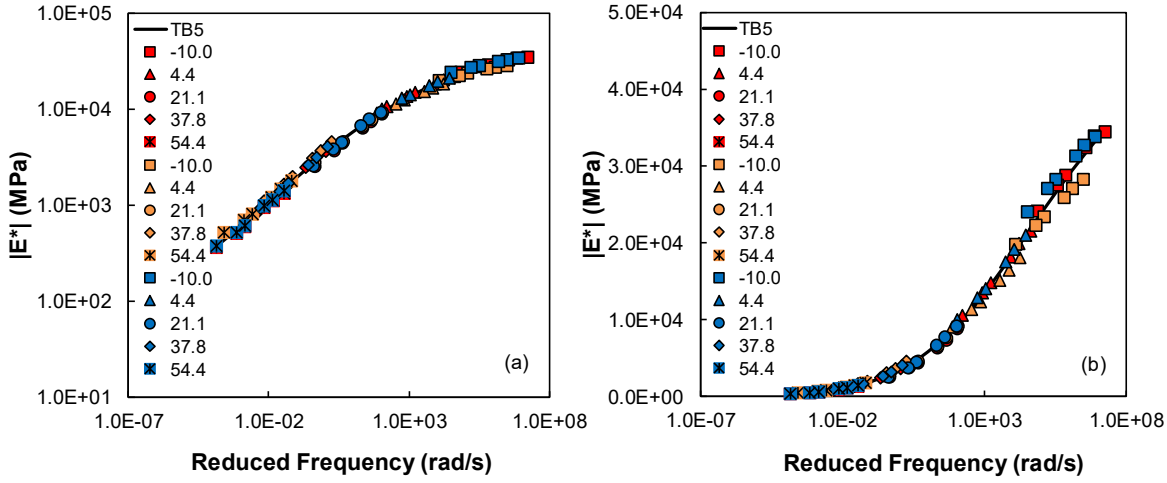

Figure C- 14. Dynamic Modulus Replicate Data for Mixture TB5 in (a) log-log space and (b) semi-log space.

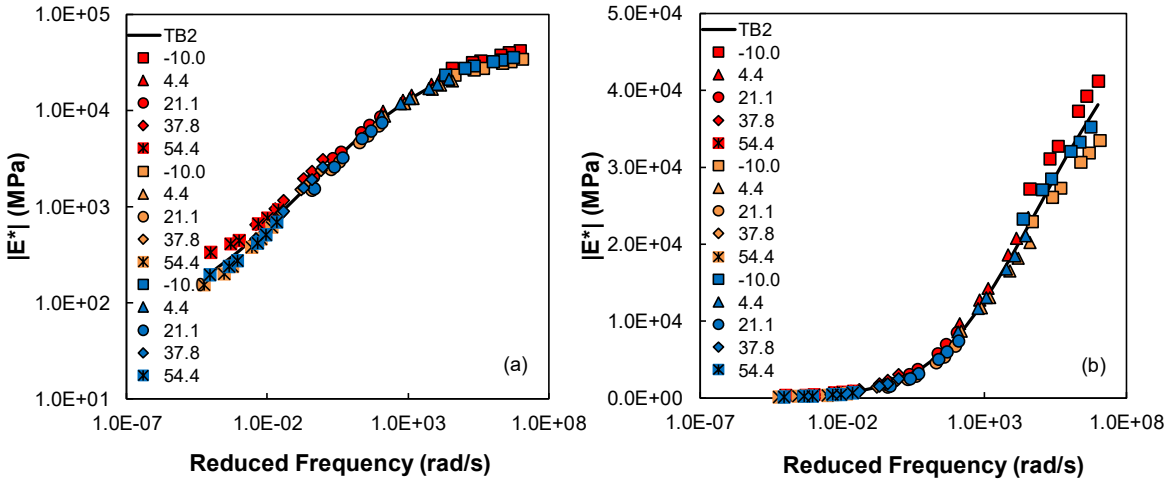

Figure C- 15. Dynamic Modulus Replicate Data for Mixture TB2 in (a) log-log space and (b) semi-log space.

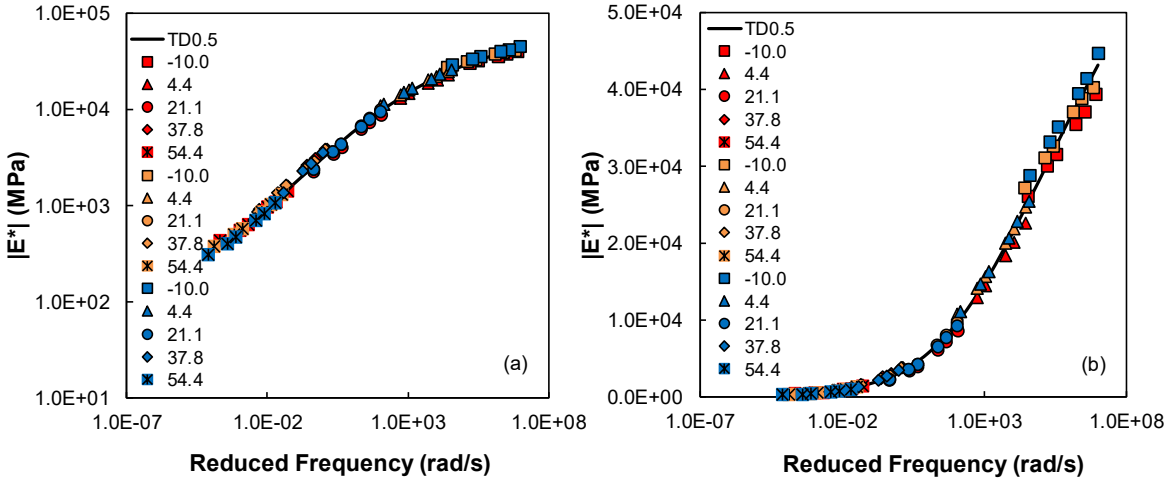

Figure C- 16. Dynamic Modulus Replicate Data for Mixture TD0.5 in (a) log-log space and (b) semi-log space.

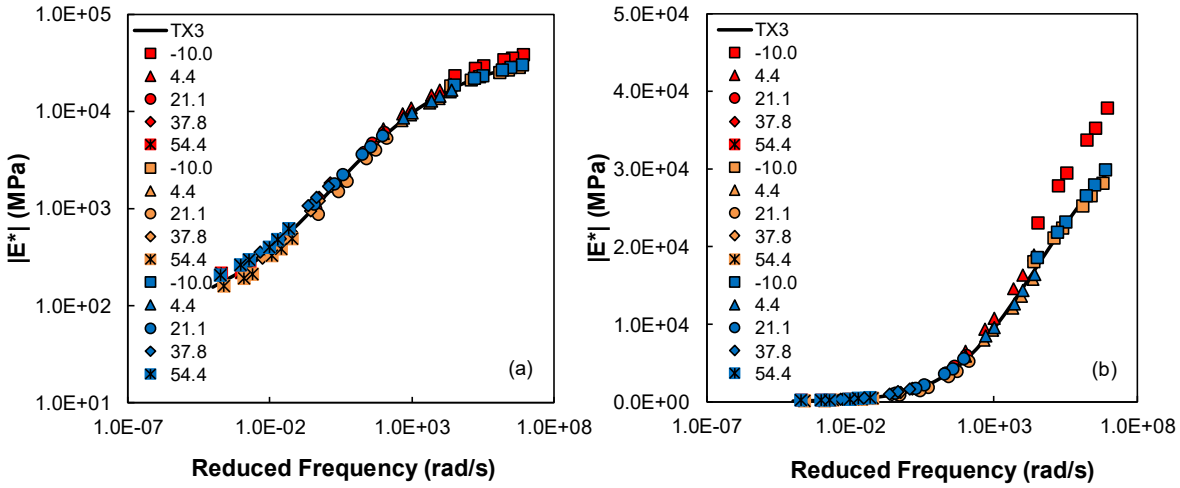

Figure C- 17. Dynamic Modulus Replicate Data for Mixture TX3 in (a) log-log space and (b) semi-log space.

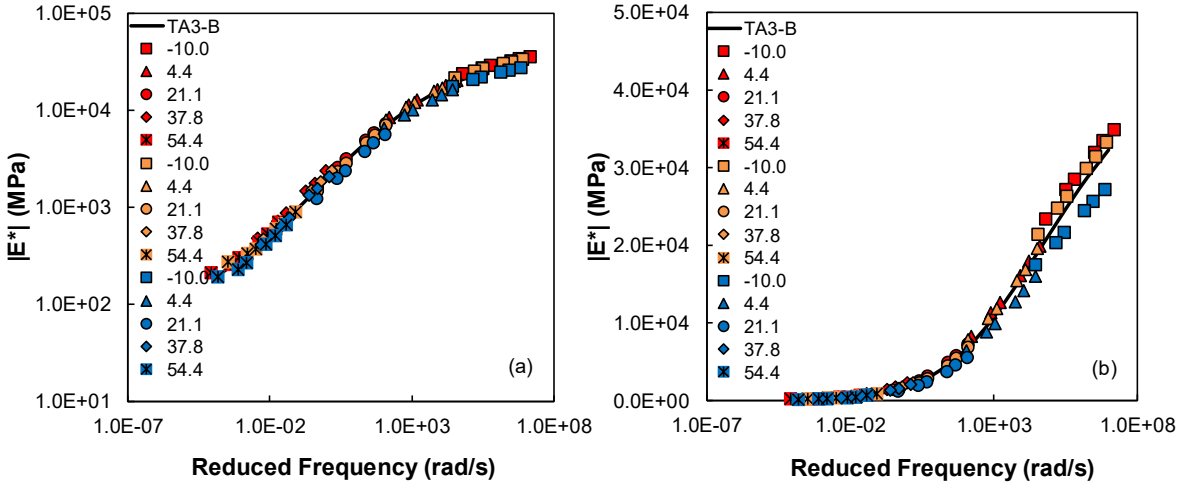

Figure C- 18. Dynamic Modulus Replicate Data for Mixture TA3-B in (a) log-log space and (b) semi-log space.

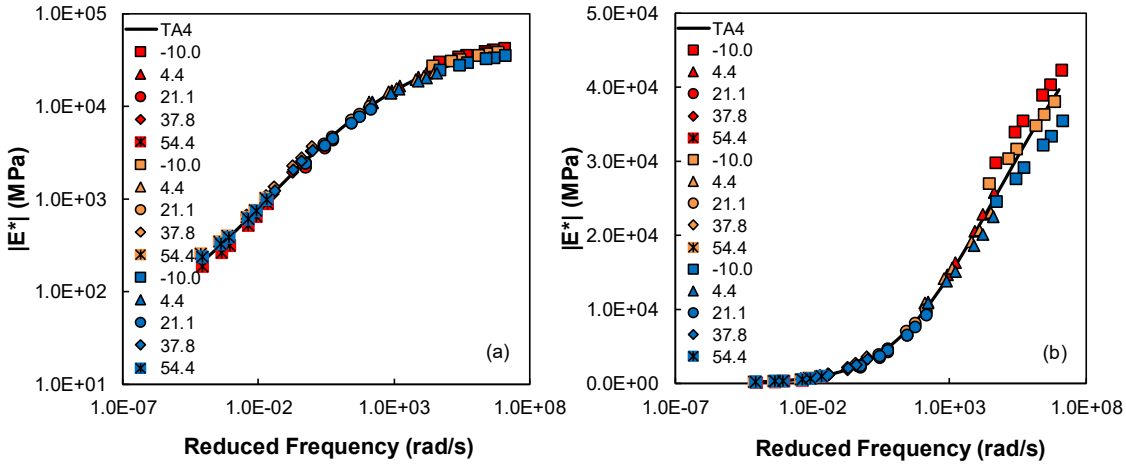

Figure C- 19. Dynamic Modulus Replicate Data for Mixture TA4 in (a) log-log space and (b) semi-log space.

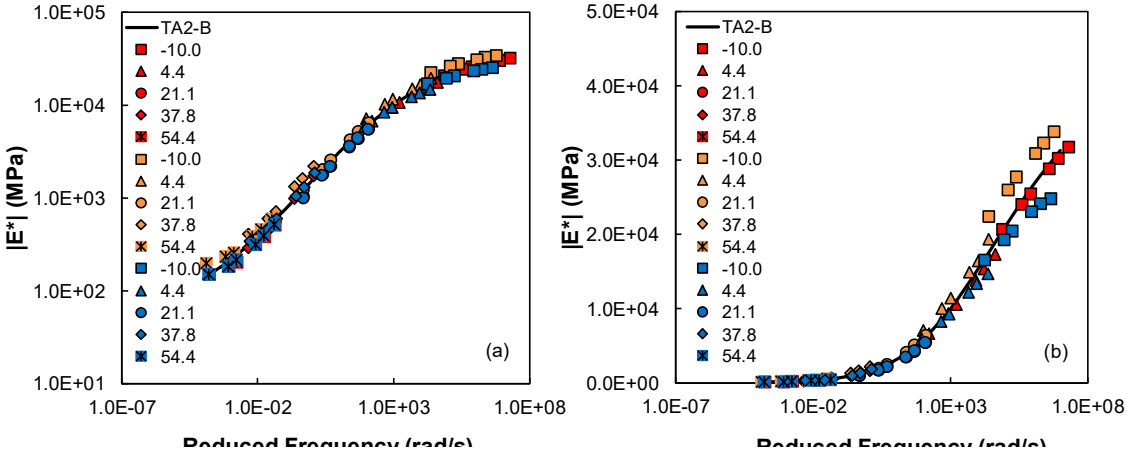

Figure C- 20. Dynamic Modulus Replicate Data for Mixture TA2-B in (a) log-log space and (b) semi-log space.

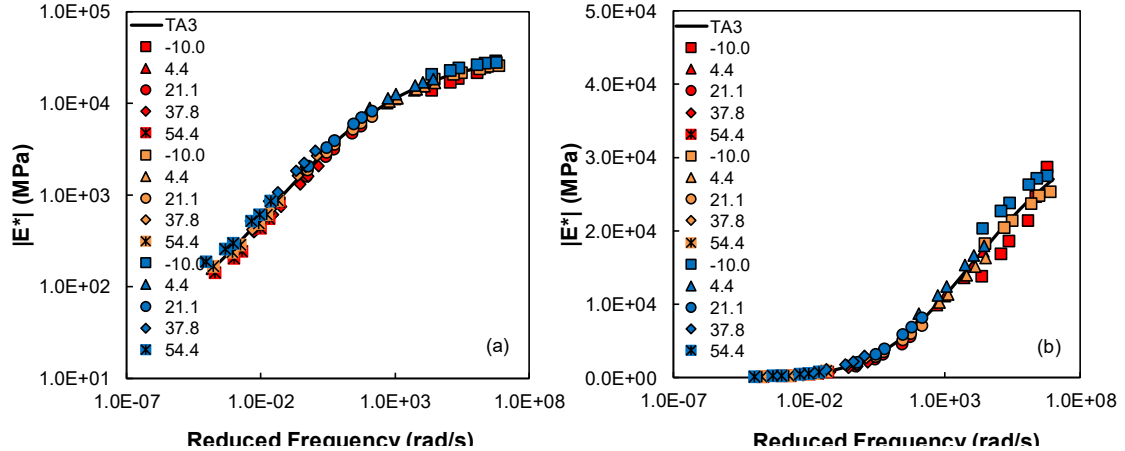

Figure C- 21. Dynamic Modulus Replicate Data for Mixture TA3 in (a) log-log space and (b) semi-log space.

Table C- 15. Dynamic Modulus and Phase Angle Replicate Data for Mixture TY5.

Temp (°C)	Freq. (Hz)	Dynamic Modulus, |E*|			Phase Angle, φ		
		Repl. 1 (MPa)	Repl. 2 (MPa)	Repl. 3 (MPa)	Repl. 1 (Deg.)	Repl. 2 (Deg.)	Repl. 3 (Deg.)
-10.0	25	35933	30233	29948	4.3	5.8	6.0
	10	34450	28883	29004	7.1	5.6	7.2
	5	32937	27721	28010	8.0	7.6	7.9
	1	29870	24725	24335	9.4	8.0	9.9
	0.5	28282	23483	22869	9.9	8.8	11.3
	0.1	24702	20761	19757	11.6	10.0	12.8
4.4	25	18624	17826	18622	11.9	9.3	8.5
	10	16899	15563	16828	14.8	11.3	13.3
	5	15399	14167	15334	15.5	13.0	14.1
	1	12372	11293	11813	18.0	15.7	17.4
	0.5	11201	10175	10630	18.4	16.5	18.5
	0.1	8745	7744	8113	21.4	18.8	20.5
21.1	25	6206	6657	6783	22.8	18.9	20.0
	10	5050	5400	5589	27.7	22.7	24.3
	5	4242	4690	4794	29.5	23.7	25.2
	1	2669	3078	3117	33.8	27.0	30.4
	0.5	2246	2542	2570	34.1	28.0	31.7
	0.1	1499	1686	1693	31.7	28.2	32.3
37.8	25	2596	2493	2478	28.8	26.9	29.1
	10	1976	1910	1961	29.0	31.2	30.4
	5	1613	1588	1601	31.8	30.4	32.1
	1	982	970	962	33.0	30.4	33.2
	0.5	833	794	781	32.9	29.6	32.5
	0.1	599	537	527	27.5	26.7	30.7
54.4	25	992	774	744	28.7	30.6	33.7
	10	799	608	615	28.1	31.6	31.3
	5	681	514	517	26.2	28.4	26.3
	1	492	340	344	24.5	25.6	28.5
	0.5	420	297	314	22.5	25.3	27.6
	0.1	340	226	243	19.6	21.7	23.3

Table C- 16. Dynamic Modulus and Phase Angle Replicate Data for Mixture TB5.

Temp (°C)	Freq. (Hz)	Dynamic Modulus, |E*|			Phase Angle, φ		
		Repl. 1 (MPa)	Repl. 2 (MPa)	Repl. 3 (MPa)	Repl. 1 (Deg.)	Repl. 2 (Deg.)	Repl. 3 (Deg.)
-10.0	25	34488	28245	33791	4.8	4.1	3.5
	10	33937	27115	32697	7.8	6.5	7.2
	5	32370	25926	31331	8.3	7.1	7.5
	1	28838	23337	28295	9.8	7.8	8.3
	0.5	27515	22267	27082	10.1	8.2	8.6
	0.1	24185	19844	24030	11.1	9.1	10.2
4.4	25	21543	18032	20957	9.2	9.7	9.1
	10	19900	16429	19104	11.5	12.3	11.6
	5	18188	15136	17508	12.7	13.6	13.3
	1	14795	12345	14030	16.2	15.2	15.8
	0.5	13503	11329	12827	16.7	15.7	16.8
	0.1	10566	9017	10038	19.0	18.4	19.3
21.1	25	8784	9113	9131	18.0	17.1	17.0
	10	7317	7622	7760	24.3	20.8	23.2
	5	6320	6580	6628	25.0	21.6	23.2
	1	4356	4598	4464	28.9	26.0	28.0
	0.5	3677	3941	3779	30.1	27.0	29.5
	0.1	2485	2748	2561	31.2	27.6	29.6
37.8	25	3577	4556	4046	25.0	22.7	22.9
	10	2909	3637	3137	28.0	24.7	25.0
	5	2464	3041	2624	32.0	26.3	27.4
	1	1536	1975	1675	34.2	29.6	30.3
	0.5	1270	1650	1367	34.9	29.3	30.3
	0.1	841	1107	911	33.9	28.6	28.8
54.4	25	1329	1776	1403	30.0	26.7	29.9
	10	1091	1453	1115	27.9	26.4	28.9
	5	933	1205	969	34.3	29.5	30.3
	1	587	805	600	32.3	27.8	28.4
	0.5	500	689	518	30.9	27.5	27.4
	0.1	361	513	372	28.4	25.3	25.0

Table C- 17. Dynamic Modulus and Phase Angle Replicate Data for Mixture TD0.5.

Temp (°C)	Freq. (Hz)	Dynamic Modulus, |E*|			Phase Angle, φ		
		Repl. 1 (MPa)	Repl. 2 (MPa)	Repl. 3 (MPa)	Repl. 1 (Deg.)	Repl. 2 (Deg.)	Repl. 3 (Deg.)
-10.0	25	39332	40245	44702	2.5	4.8	5.3
	10	37018	38755	41363	5.9	6.6	7.0
	5	35474	37093	39505	7.3	8.1	8.6
	1	31583	32649	35126	8.2	9.0	9.6
	0.5	30029	31122	33138	8.7	9.7	10.2
	0.1	26055	27165	28824	10.1	11.0	11.7
4.4	25	22617	24649	25395	12.6	11.1	9.9
	10	20082	21899	22863	13.6	13.6	12.6
	5	18417	20012	20618	15.0	15.5	14.5
	1	14532	15668	16289	18.0	18.4	17.3
	0.5	13012	14129	14717	19.0	19.8	18.4
	0.1	9819	10789	11165	22.1	22.7	21.3
21.1	25	8584	9750	9285	20.5	19.9	19.7
	10	7184	8033	7795	24.0	25.7	23.4
	5	6105	6718	6568	25.3	27.4	25.1
	1	3941	4317	4267	29.8	32.6	30.0
	0.5	3349	3573	3569	30.9	34.3	30.2
	0.1	2211	2349	2361	31.4	33.8	30.9
37.8	25	3784	3821	3502	27.7	26.5	25.2
	10	3066	2885	2733	30.3	27.6	27.4
	5	2604	2424	2244	32.4	30.0	29.3
	1	1591	1616	1357	32.4	28.6	31.1
	0.5	1311	1347	1092	32.5	27.0	30.2
	0.1	906	852	718	29.0	24.2	27.7
54.4	25	1410	1305	1051	31.6	28.5	32.2
	10	1088	1018	814	33.3	24.8	31.4
	5	957	846	699	33.2	25.2	29.2
	1	625	568	464	30.6	21.6	25.3
	0.5	549	498	394	28.4	20.5	23.8
	0.1	426	374	307	24.6	16.8	20.9

Table C- 18. Dynamic Modulus and Phase Angle Replicate Data for Mixture TA4.

Temp (°C)	Freq. (Hz)	Dynamic Modulus, |E*|			Phase Angle, φ		
		Repl. 1 (MPa)	Repl. 2 (MPa)	Repl. 3 (MPa)	Repl. 1 (Deg.)	Repl. 2 (Deg.)	Repl. 3 (Deg.)
-10.0	25	28687	25354	27491	3.3	4.6	2.5
	10	24664	24752	27151	4.7	6.2	4.9
	5	21474	23738	26276	5.1	6.2	6.3
	1	18629	21426	23815	6.8	8.0	7.3
	0.5	16906	20478	22756	7.2	8.5	7.6
	0.1	13790	18261	20392	8.1	9.4	8.5
4.4	25	17193	16361	17968	7.8	8.7	6.9
	10	15160	15090	16623	10.4	11.4	10.7
	5	13613	13982	15359	12.1	12.0	12.3
	1	11074	11310	12375	14.7	14.7	14.7
	0.5	9956	10267	11219	16.7	16.2	16.1
	0.1	7449	7972	8763	20.3	19.6	19.2
21.1	25	7194	7104	8125	19.1	18.0	16.2
	10	5571	6036	6907	23.0	21.7	21.0
	5	4649	5135	5899	24.4	25.3	24.2
	1	3133	3502	3906	31.9	31.6	29.7
	0.5	2582	2883	3235	33.6	32.8	31.6
	0.1	1587	1844	2052	35.9	35.9	33.3
37.8	25	2061	2655	2982	27.6	28.2	26.6
	10	1577	2004	2223	29.8	32.8	29.3
	5	1299	1609	1818	32.2	33.8	32.0
	1	740	903	1066	32.7	35.5	31.6
	0.5	604	698	844	31.9	35.5	31.0
	0.1	389	416	514	28.0	30.9	28.2
54.4	25	814	858	841	35.4	37.1	31.4
	10	550	609	610	37.6	39.3	32.6
	5	434	486	510	33.8	35.4	29.2
	1	240	281	296	31.0	32.7	28.0
	0.5	202	237	255	29.2	30.1	25.6
	0.1	140	165	187	26.3	25.1	20.0

Table C- 19. Dynamic Modulus and Phase Angle Replicate Data for Mixture TA3-B.

Temp (°C)	Freq. (Hz)	Dynamic Modulus, |E*|			Phase Angle, φ		
		Repl. 1 (MPa)	Repl. 2 (MPa)	Repl. 3 (MPa)	Repl. 1 (Deg.)	Repl. 2 (Deg.)	Repl. 3 (Deg.)
-10.0	25	34843	33279	27191	4.4	5.0	3.9
	10	33458	31388	25646	5.5	7.2	6.4
	5	31985	29908	24433	7.2	7.7	7.5
	1	28493	26296	21606	8.8	9.8	8.8
	0.5	27183	24848	20387	8.6	10.4	9.6
	0.1	23366	21412	17507	9.8	11.8	10.9
4.4	25	19912	19563	15964	10.2	12.6	9.3
	10	17924	16900	14177	12.7	14.2	13.1
	5	16159	15413	12769	14.6	15.8	14.6
	1	12675	11907	9935	17.6	18.8	17.6
	0.5	11323	10606	8816	19.2	20.5	19.8
	0.1	8257	7818	6415	22.5	24.2	22.7
21.1	25	7261	6881	5564	21.4	21.4	21.2
	10	5812	5472	4550	24.4	25.6	25.7
	5	4882	4535	3744	26.1	28.8	28.2
	1	3130	2834	2375	30.4	33.5	31.1
	0.5	2573	2307	1969	31.7	35.0	32.0
	0.1	1596	1460	1214	31.8	34.6	32.1
37.8	25	2353	2366	2064	30.5	32.4	28.3
	10	1734	1804	1543	33.9	35.8	32.4
	5	1457	1482	1306	32.0	35.1	31.3
	1	858	845	762	31.9	35.7	30.5
	0.5	709	693	626	30.1	33.9	28.3
	0.1	471	464	408	26.8	29.4	24.5
54.4	25	691	888	652	31.8	32.9	33.5
	10	522	663	502	32.1	33.3	33.4
	5	442	589	412	28.4	31.5	31.4
	1	300	368	268	24.8	28.1	27.4
	0.5	255	329	228	22.1	26.3	25.8
	0.1	210	270	189	18.9	22.8	23.3

Table C- 20. Dynamic Modulus and Phase Angle Replicate Data for Mixture TB2.

Temp (°C)	Freq. (Hz)	Dynamic Modulus, |E*|			Phase Angle, φ		
		Repl. 1 (MPa)	Repl. 2 (MPa)	Repl. 3 (MPa)	Repl. 1 (Deg.)	Repl. 2 (Deg.)	Repl. 3 (Deg.)
-10.0	25	41207	33460	35230	4.5	3.9	4.1
	10	39228	31874	33239	6.6	6.2	5.7
	5	37284	30652	32057	7.5	6.8	7.3
	1	32699	27331	28512	10.1	8.5	8.7
	0.5	31118	26071	27131	10.0	8.5	9.6
	0.1	27156	22916	23269	11.9	9.9	10.7
4.4	25	23452	20216	21051	11.9	8.9	13.5
	10	20807	18196	18520	15.0	11.6	14.9
	5	18612	16548	16772	17.4	12.9	17.3
	1	14274	13102	13076	21.0	15.7	19.3
	0.5	12772	11761	11656	22.3	17.5	20.9
	0.1	9752	8682	8638	25.8	21.4	24.5
21.1	25	8466	6803	7435	22.3	18.9	20.9
	10	6963	5351	6024	27.7	24.8	25.1
	5	5828	4549	5077	29.1	25.8	26.9
	1	3677	2891	3163	34.4	30.6	30.7
	0.5	3095	2388	2552	34.9	30.7	32.0
	0.1	2017	1464	1525	34.0	30.6	31.6
37.8	25	3041	2344	2551	29.2	29.0	32.3
	10	2301	1774	1893	30.9	32.5	36.5
	5	1913	1487	1542	33.6	31.8	36.1
	1	1136	846	877	33.6	30.7	35.7
	0.5	932	674	715	33.8	29.1	34.3
	0.1	641	424	457	30.1	25.0	30.4
54.4	25	915	600	680	35.1	33.3	34.8
	10	748	453	508	34.7	28.9	33.1
	5	656	373	414	32.1	29.1	30.1
	1	438	234	269	30.2	24.9	26.9
	0.5	405	197	234	26.8	23.5	24.0
	0.1	334	153	192	20.2	18.3	23.5

Table C- 21. Dynamic Modulus and Phase Angle Replicate Data for Mixture TA2-B.

Temp (°C)	Freq. (Hz)	Dynamic Modulus, |E*|			Phase Angle, φ		
		Repl. 1 (MPa)	Repl. 2 (MPa)	Repl. 3 (MPa)	Repl. 1 (Deg.)	Repl. 2 (Deg.)	Repl. 3 (Deg.)
-10.0	25	31727	33818	24797	3.6	3.4	4.3
	10	30187	32290	24110	6.2	4.8	6.3
	5	28859	30839	23018	7.0	6.7	7.0
	1	25432	27701	20416	9.1	8.4	8.3
	0.5	24004	26017	19289	9.8	9.2	9.2
	0.1	20645	22364	16596	11.5	10.7	10.8
4.4	25	17305	19374	14643	10.7	12.5	11.8
	10	15390	16461	13408	15.1	14.4	14.4
	5	13811	14920	12178	16.2	16.6	16.9
	1	10571	11408	9291	20.2	20.3	20.4
	0.5	9367	10073	8237	22.2	22.2	22.2
	0.1	6627	7062	5850	26.0	27.4	25.9
21.1	25	5453	6455	5506	21.4	23.4	23.6
	10	4323	5146	4377	26.5	27.8	28.4
	5	3546	4196	3559	29.2	30.1	29.4
	1	2183	2528	2160	32.3	35.7	35.1
	0.5	1768	2010	1733	33.8	36.7	35.9
	0.1	1044	1221	1005	32.7	35.6	34.9
37.8	25	1702	2194	1865	31.3	34.8	33.7
	10	1215	1611	1284	35.6	37.5	37.3
	5	972	1313	1040	33.6	36.4	35.7
	1	548	713	591	32.4	34.8	34.3
	0.5	437	587	465	30.8	31.1	31.6
	0.1	288	407	337	26.6	26.3	27.5
54.4	25	506	580	518	32.6	34.8	35.5
	10	383	452	389	33.8	34.8	34.2
	5	317	378	314	31.6	31.7	30.5
	1	202	255	212	27.6	28.9	26.8
	0.5	180	233	182	25.7	26.9	24.3
	0.1	149	195	148	20.2	23.4	20.9

Table C- 22. Dynamic Modulus and Phase Angle Replicate Data for Mixture TA3.

Temp (°C)	Freq. (Hz)	Dynamic Modulus, |E*|			Phase Angle, φ		
		Repl. 1 (MPa)	Repl. 2 (MPa)	Repl. 3 (MPa)	Repl. 1 (Deg.)	Repl. 2 (Deg.)	Repl. 3 (Deg.)
-10.0	25	42302	38053	35462	2.4	3.9	5.2
	10	40361	36296	33406	4.9	5.2	6.2
	5	38958	34815	32179	5.7	5.9	7.0
	1	35439	31620	29137	7.3	7.9	8.4
	0.5	33923	30317	27639	7.4	8.0	8.8
	0.1	29753	27005	24594	10.2	9.6	9.7
4.4	25	25815	23009	22543	9.8	8.1	9.0
	10	22818	20695	20145	13.7	11.6	10.7
	5	20609	19120	18564	14.8	12.9	12.2
	1	16348	15527	15102	17.9	15.7	14.9
	0.5	14676	14144	13779	18.7	17.1	16.2
	0.1	11029	10926	10843	22.3	20.8	18.4
21.1	25	9704	9993	9268	20.5	18.4	17.9
	10	7892	8217	7634	26.5	22.4	22.6
	5	6602	7067	6599	26.7	24.8	23.5
	1	4285	4672	4504	33.8	29.4	28.3
	0.5	3528	3916	3754	35.4	31.3	29.6
	0.1	2184	2466	2419	36.3	32.2	32.2
37.8	25	3248	3664	3306	29.0	26.8	26.5
	10	2424	2783	2537	30.6	29.3	28.1
	5	1932	2243	2046	34.2	31.0	30.7
	1	1123	1341	1223	33.4	31.2	30.9
	0.5	895	1073	983	31.7	29.5	30.9
	0.1	556	672	609	28.7	25.7	27.1
54.4	25	888	1014	980	35.0	31.2	32.0
	10	646	749	734	36.6	32.3	32.9
	5	518	628	600	33.2	29.7	30.5
	1	311	393	378	29.4	23.6	26.5
	0.5	262	347	322	26.5	21.6	24.3
	0.1	187	257	235	22.9	16.7	24.4

Table C- 23. Dynamic Modulus and Phase Angle Replicate Data for Mixture TX3.

Temp (°C)	Freq. (Hz)	Dynamic Modulus, |E*|			Phase Angle, φ		
		Repl. 1 (MPa)	Repl. 2 (MPa)	Repl. 3 (MPa)	Repl. 1 (Deg.)	Repl. 2 (Deg.)	Repl. 3 (Deg.)
-10.0	25	37779	28212	29917	4.0	4.3	5.8
	10	35246	26533	27971	7.4	5.8	8.3
	5	33651	25212	26500	8.5	7.3	9.9
	1	29480	22432	23201	10.0	8.5	11.4
	0.5	27858	21076	21854	11.2	9.5	11.8
	0.1	23094	18020	18622	13.9	11.6	13.7
4.4	25	18920	15757	16421	14.4	12.5	13.4
	10	16284	13576	14388	17.1	14.4	16.7
	5	14568	12124	12644	19.6	17.0	17.8
	1	10755	9214	9597	23.9	21.9	22.8
	0.5	9384	8012	8511	26.4	23.0	24.8
	0.1	6503	5584	5897	28.3	28.0	29.5
21.1	25	6060	5238	5521	25.3	24.8	25.4
	10	4627	3983	4285	29.4	29.3	30.0
	5	3702	3244	3572	31.9	31.0	31.3
	1	2111	1873	2228	35.6	35.1	35.4
	0.5	1669	1491	1767	36.1	35.2	36.0
	0.1	984	869	1095	33.7	33.6	34.1
37.8	25	1814	1671	1661	35.3	34.7	35.6
	10	1282	1200	1283	38.5	37.5	38.2
	5	1041	939	1049	37.9	35.2	36.7
	1	573	565	609	35.0	33.7	34.1
	0.5	470	445	485	32.2	31.1	31.8
	0.1	314	306	351	27.6	27.2	27.2
54.4	25	518	481	618	36.4	36.0	32.8
	10	399	383	471	32.7	33.7	29.8
	5	334	323	399	28.9	31.5	26.9
	1	239	211	292	26.5	27.5	23.4
	0.5	219	188	260	24.4	24.0	20.1
	0.1	212	158	205	18.6	19.4	19.0

Table C- 24. Actual Number of Cycles to Failure and the Input Machine Strain on the Sample

Mixture	Input Machine Strain	No. of Cycles to Failure (N_f)	Actual Strain @ 80th Cycle (με)		Mixture	Input Machine Strain	No. of Cycles to Failure (N_f)	Actual Strain @ 80th Cycle (με)
GX4	250 με	122151	218		SX3	300 με	285605	224
	300 με	67931	229			500 με	57165	412
	350 με	16307	259			600 με	19730	429
	400 με	34823	314			650 με	11710	552
GX5	300 με	127534	236		SY1	200 με	203622	165
	400 με	36115	252			300 με	57002	202
	450 με	13506	323			400 με	33733	241
	480 με	7702	282			450 με	3234	400
GY3	200 με	490553	127		SZ1	250 με	83005	191
	250 με	48516	196			300 με	35569	204
	300 με	13706	223			400 με	16355	256
	350 με	8899	248			430 με	3697	371
GY4	250 με	131361	163		TX1	200 με	535573	112
	275 με	47531	151			300 με	122474	184
	300 με	16700	206			350 με	45029	220
	325 με	2698	287			400 με	8502	259
GY6	300 με	142351	238		TY5	250 με	57878	256
	350 με	37103	241			300 με	57355	243
	400 με	15909	343			350 με	18811	319
	450 με	10307	400			400 με	9534	364
GZ2	250 με	20516	164		TZ4	250 με	76507	179
	300 με	43319	192			300 με	42919	215
	350 με	16298	230			400 με	19927	272
	400 με	4898	302			450 με	3713	321

Table C- 25. The regression coefficients C1 and C2 of C-S relationship

Mixture	Coefficients	
	C_1	C_2
GX4	0.0065	0.4051
GX5	0.0007	0.5456
GY3	0.0008	0.5789
GY4	0.0002	0.6465
GY6	0.0031	0.4510
GZ2	0.0007	0.5749
SX3	0.0145	0.3403
SY1	0.0017	0.5101
SZ1	0.0033	0.4443
TX1	0.0001	0.6806
TY5	0.0058	0.4104
TZ4	0.0004	0.5991

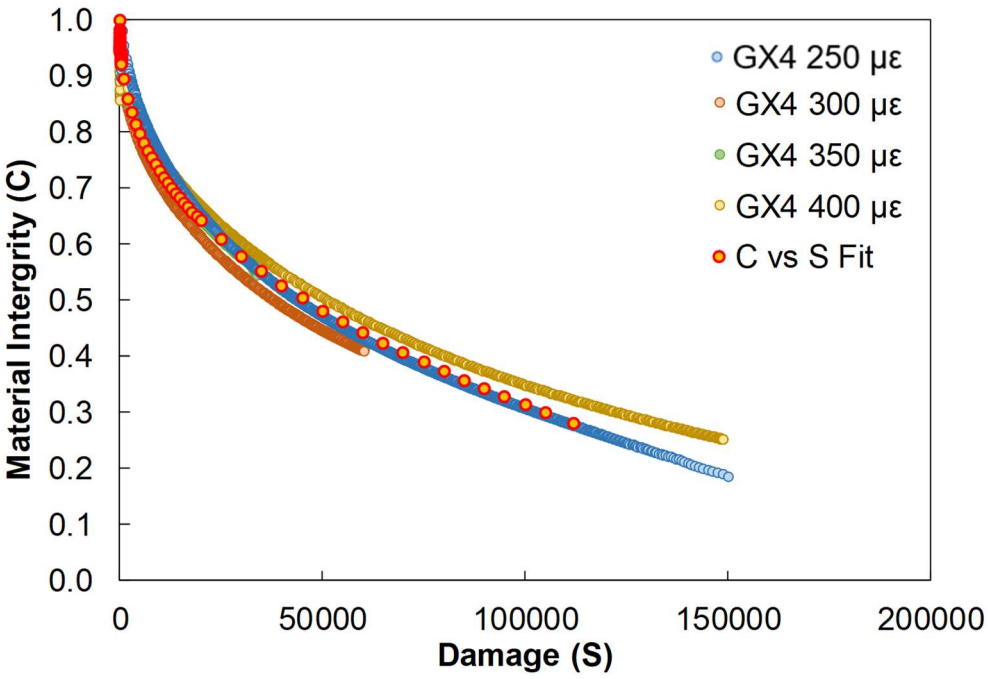

Figure C- 22. C vs S Curve for GX4 with Data at All Strain Levels.

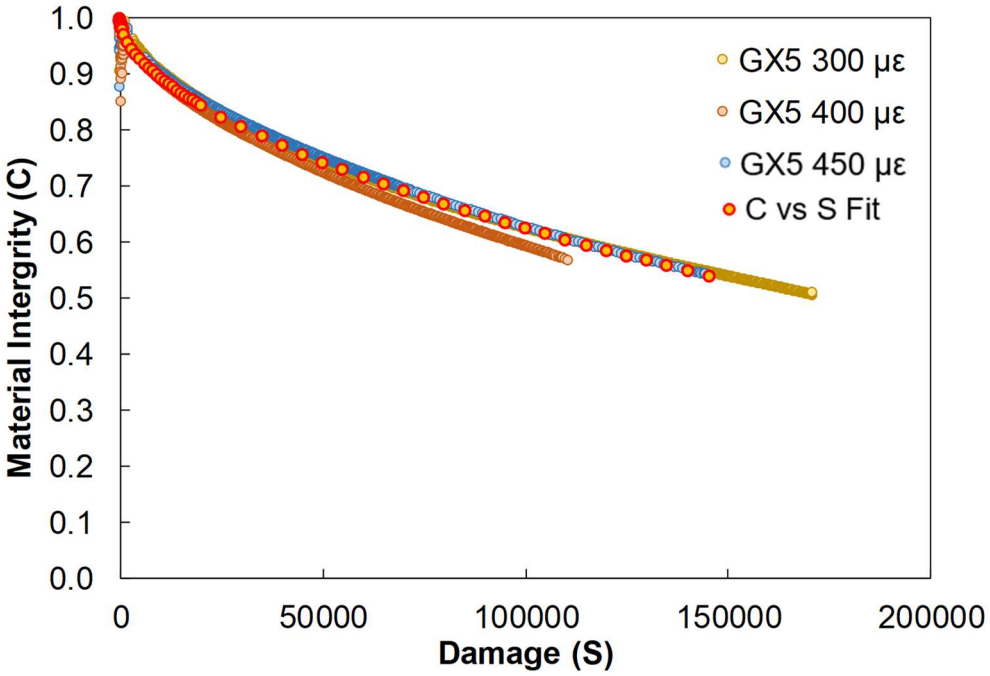

Figure C- 23. C vs S Curve for GX5 with Data at All Strain Levels.

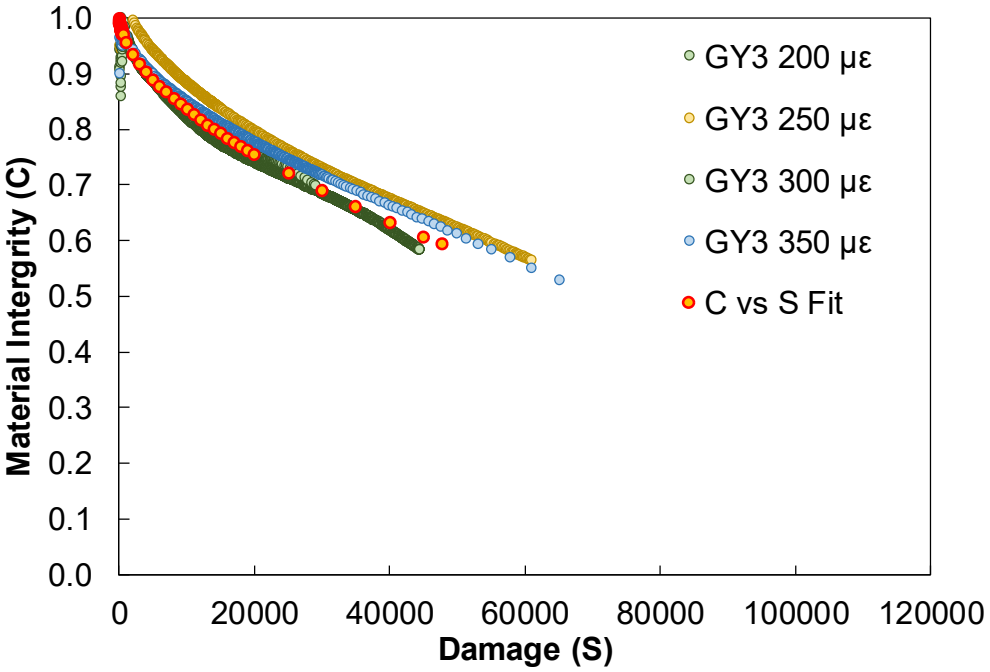

Figure C- 24. C vs S Curve for GY3 with Data at All Strain Levels.

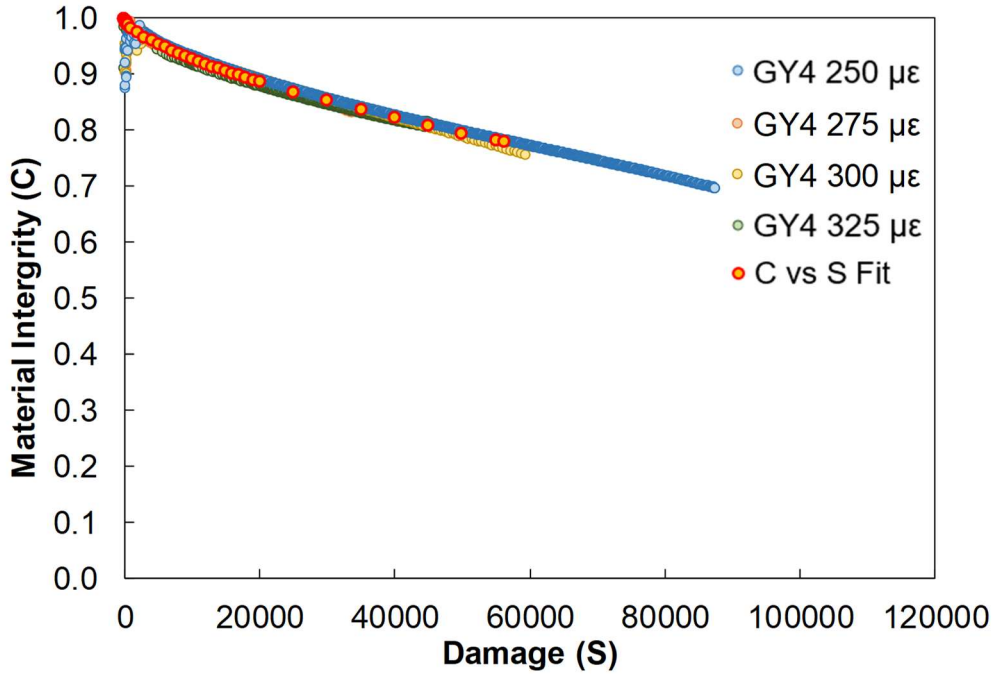

Figure C- 25. C vs S Curve for GY4 with Data at All Strain Levels.

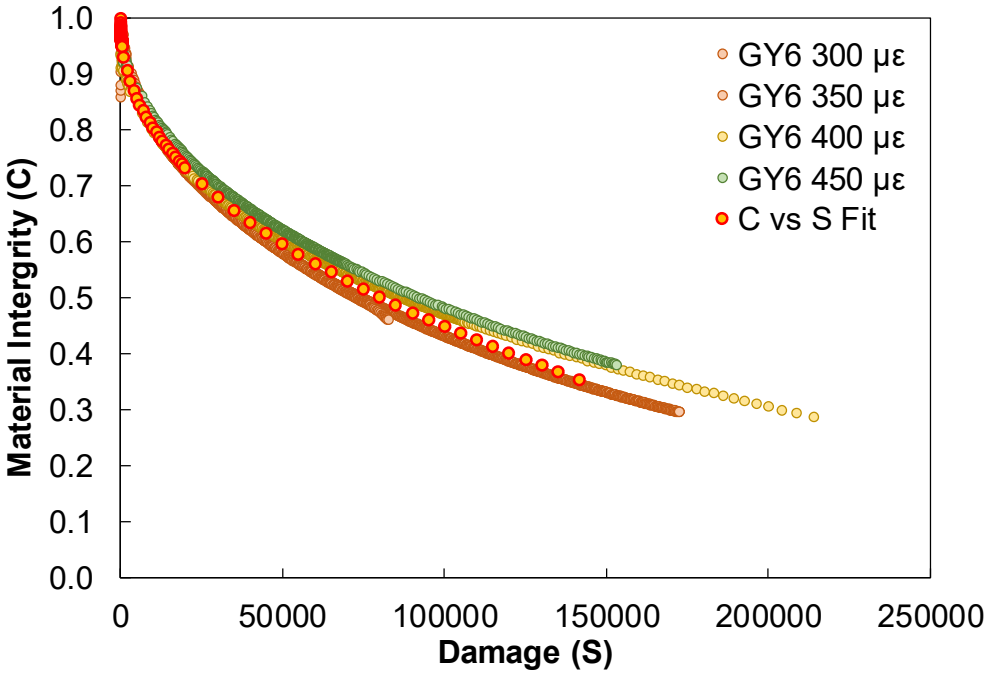

Figure C- 26 C vs S Curve for GY6 with Data at All Strain Levels.

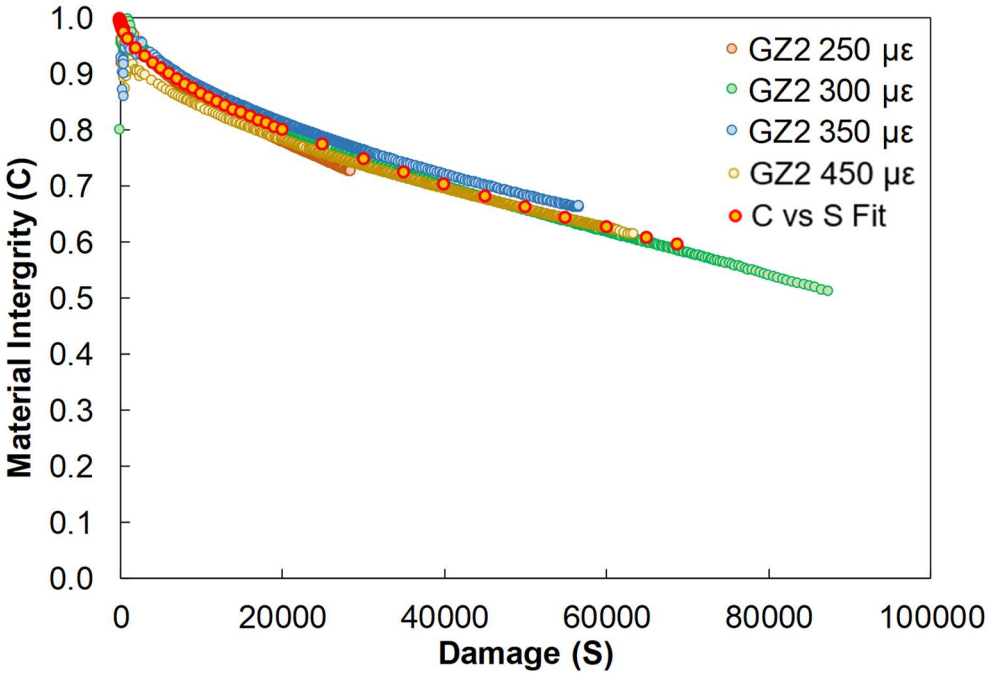

Figure C- 27. C vs S Curve for GZ2 with Data at All Strain Levels.

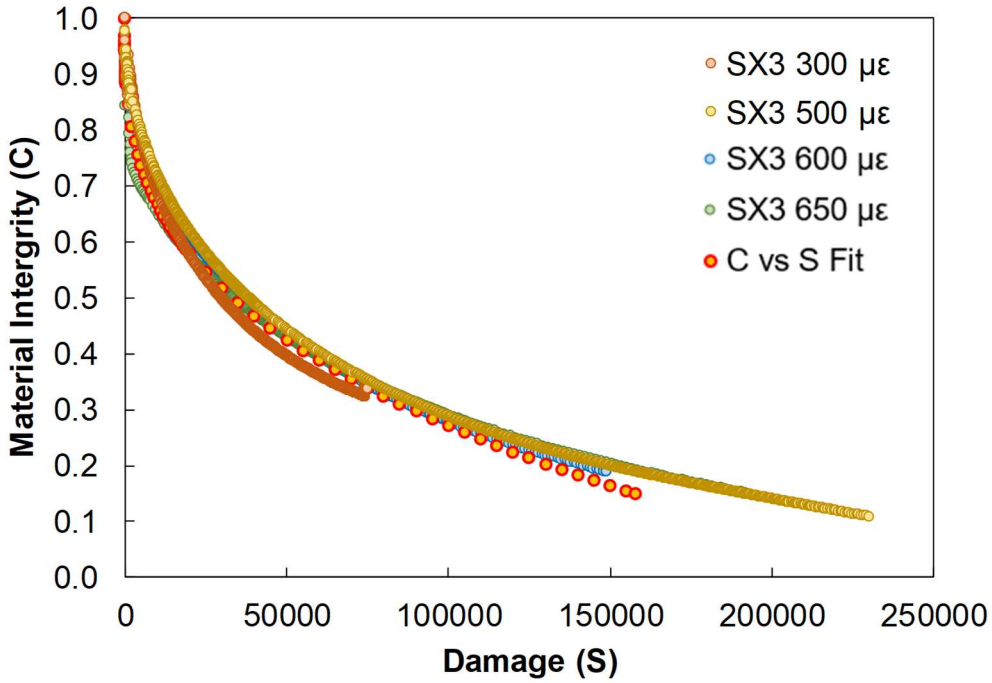

Figure C- 28. C vs S Curve for SX3 with Data at All Strain Levels.

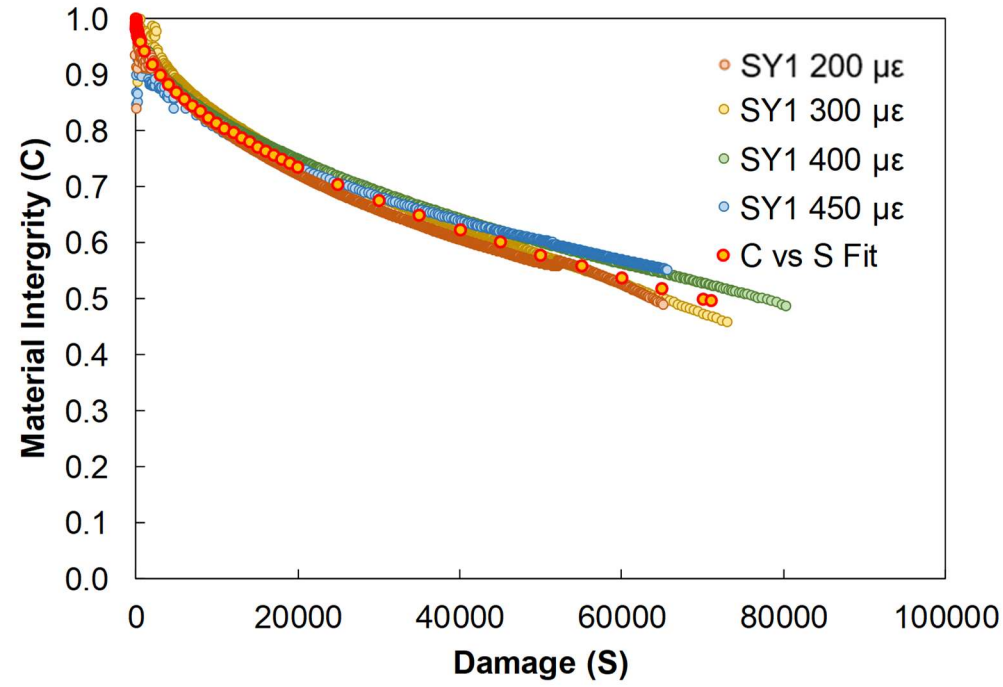

Figure C- 29. C vs S Curve for SY1 with Data at All Strain Levels.

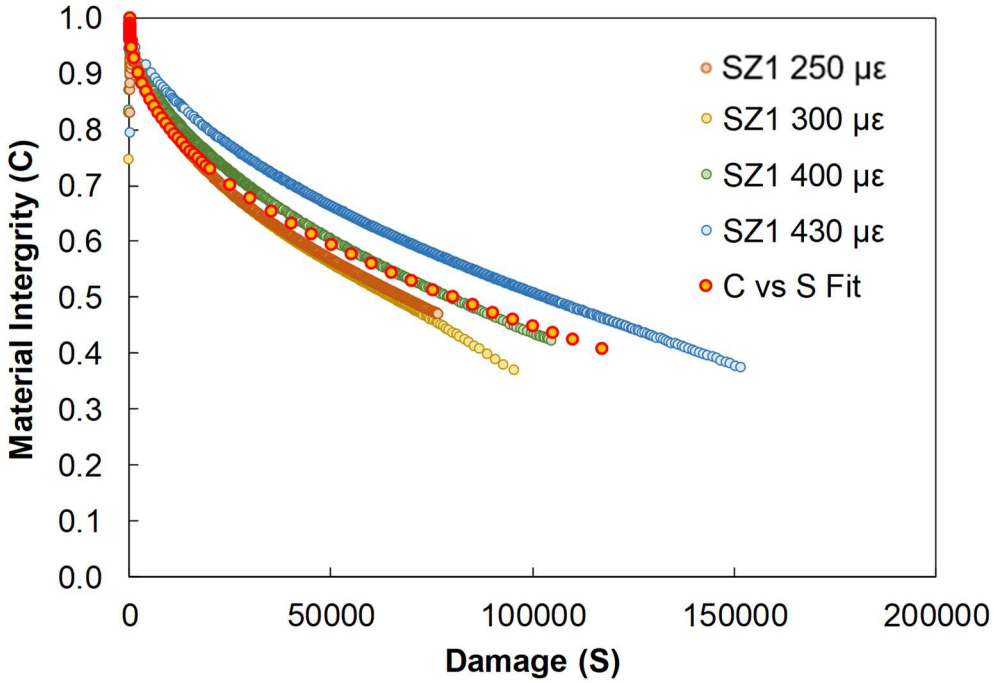

Figure C- 30. C vs S Curve for SZ1 with Data at All Strain Levels.

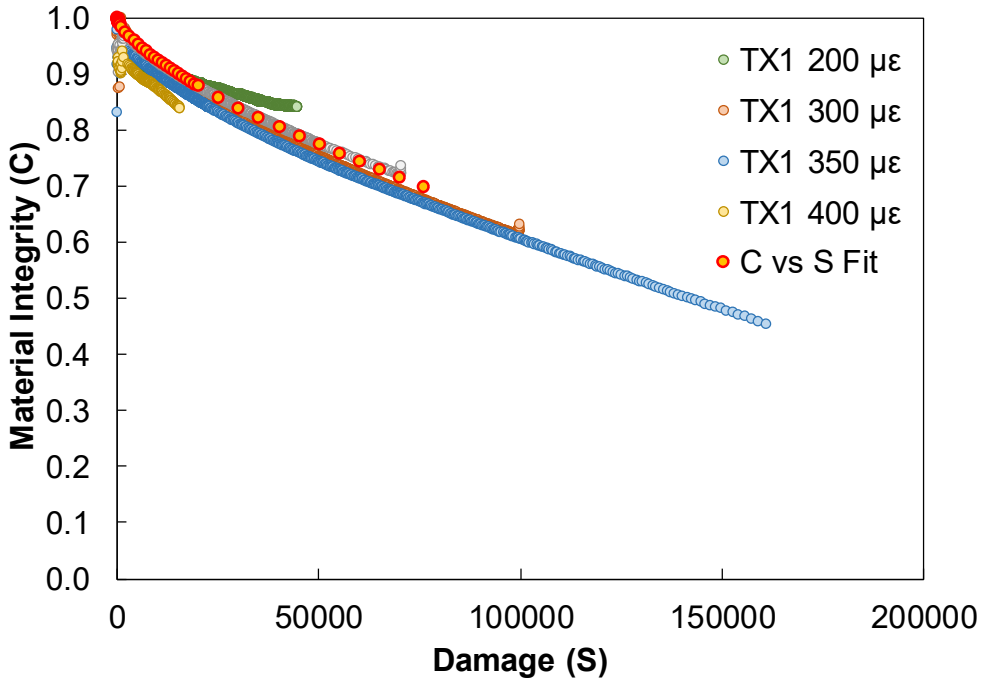

Figure C- 31. C vs S Curve for TX1 with Data at All Strain Levels.

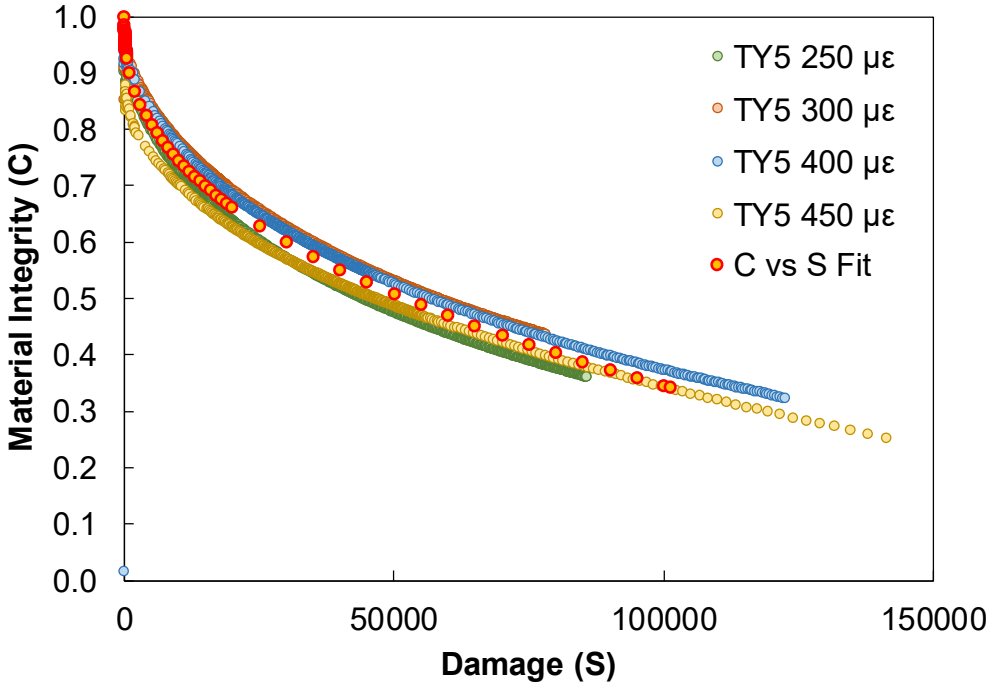

Figure C- 32. C vs S Curve for TY5 with Data at All Strain Levels.

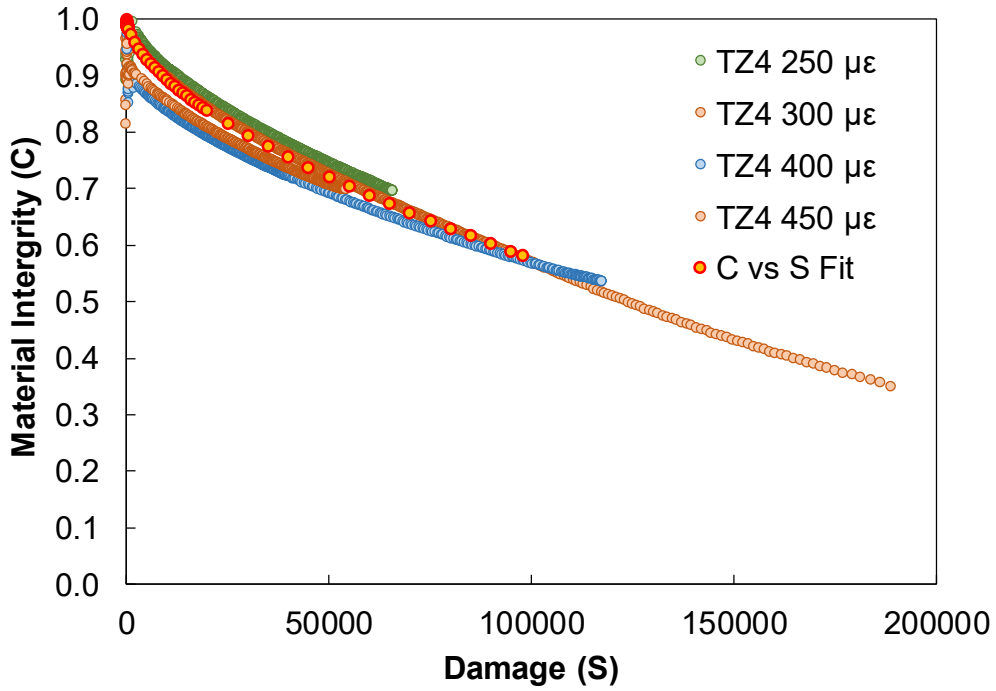

Figure C- 33. C vs S Curve for TZ4 with Data at All Strain Levels.

Axial Fatigue Test Data

As mentioned in Chapter 8, the axial fatigue test was performed at four strain levels for each mixture and the data was analyzed using the viscoelastic continuum damage theory (S-VECD) formulation as explained in Appendix A. The result of the S-VECD model is the damage characteristic curve or the *C* vs. *S* curve. In Chapter 8, only the fitted *C vs. S* curve was shown. In the figures below, the *C vs. S* data at all four strain levels along with the fit function is shown for each of the nine mixtures. Also, the regression coefficients C_1 and C_2 of C-S relationship are provided in Table C- 27.:

Table C- 26. Actual Number of Cycles to Failure and the Input Machine Strain on the Sample

Mixture	Input Machine Strain	No. of Cycles to Failure (N_f)	Actual Strain @ 80th Cycle (με)		Mixture	Input Machine Strain	No. of Cycles to Failure (N_f)	Actual Strain @ 80th Cycle (με)
TY5	250	57878	256		TX3	500	3090	422
	300	57355	243			600	2290	529
	350	18811	319		TA3_B	400	163495	259
	400	9534	364			450	78943	335
TB5	250	528634	151			500	9908	383
	300	44959	264			480	3387	432
	400	13911	278		TA4	300	68940	212
	450	9506	341			350	7330	235
TB2	300	812306	201			400	1420	330
	400	144355	281			450	1897	310
	500	33739	355		TA2_B	300	273929	224
	600	11901	454			350	92582	272
TD0.5	300	123594	202			400	19679	363
	400	41677	281			450	12919	338
	450	23705	309		TA3	300	60620	221
	500	298	381			350	52818	236
TX3	300	288673	219			400	1699	310
	400	35326	273			450	13309	305

Table C- 27. Best Fit Coefficients C_1 and C_2 of C-S relationship

Mixture	Coefficients	
	C_1	C_2
TY5	0.0058	0.4104
TB5	0.0028	0.4615
TD0.5	0.0021	0.4801
TA4	0.0012	0.5401
TA3-B	0.0064	0.3982
TB2	0.0041	0.4272
TA2-B	0.0039	0.4471
TA3	0.0014	0.5246
TX3	0.0047	0.4459

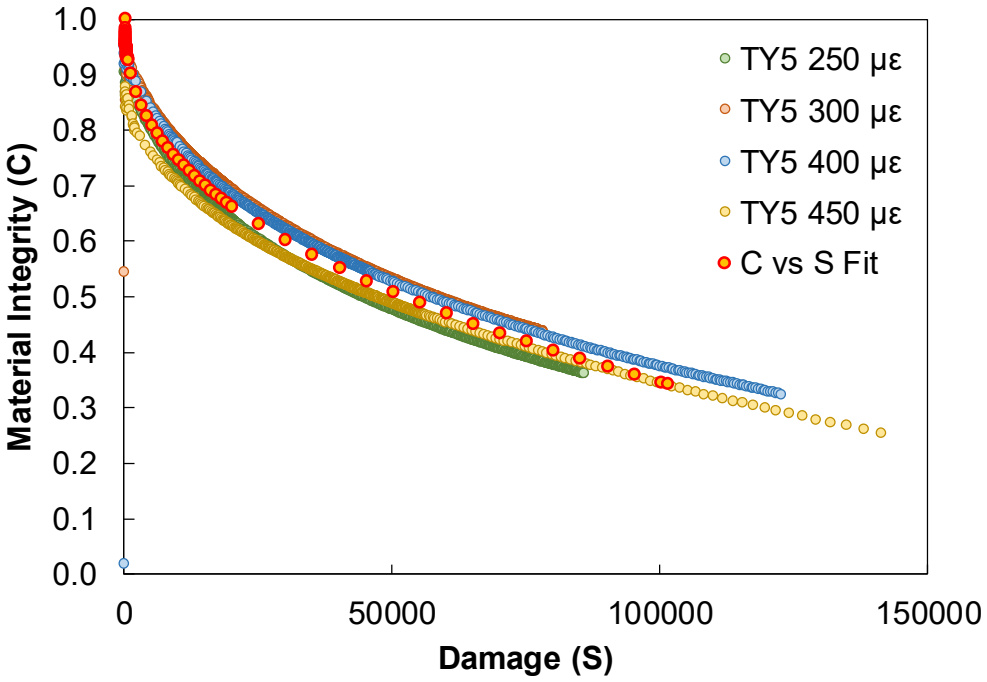

Figure C- 34. C vs S Curve for TY5 with Data at All Strain Levels.

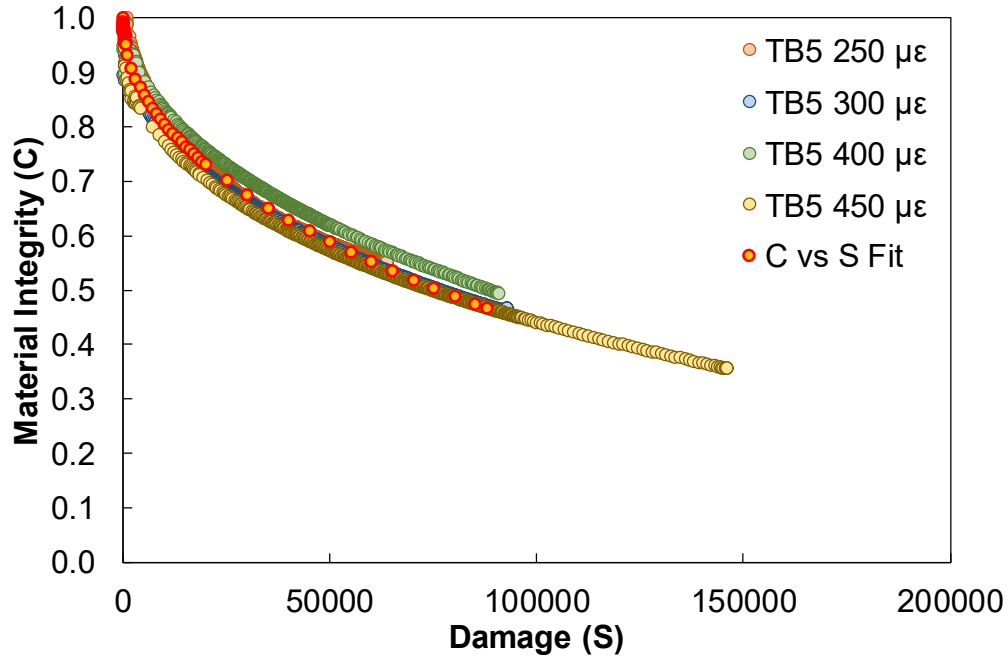

Figure C- 35. C vs S Curve for TB5 with Data at All Strain Levels.

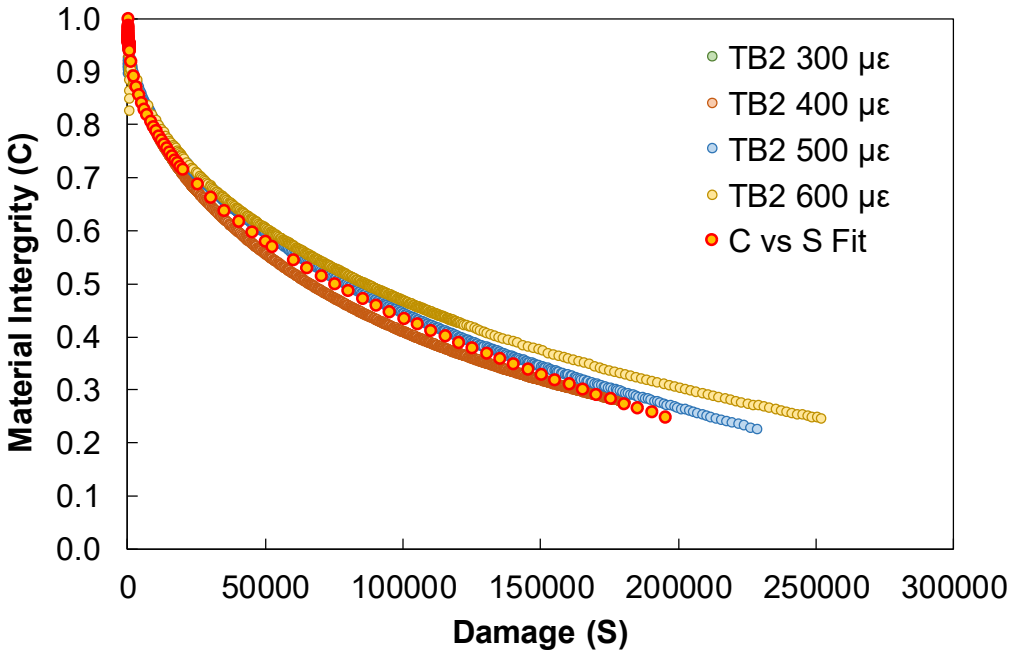

Figure C- 36. C vs S Curve for TB2 with Data at All Strain Levels.

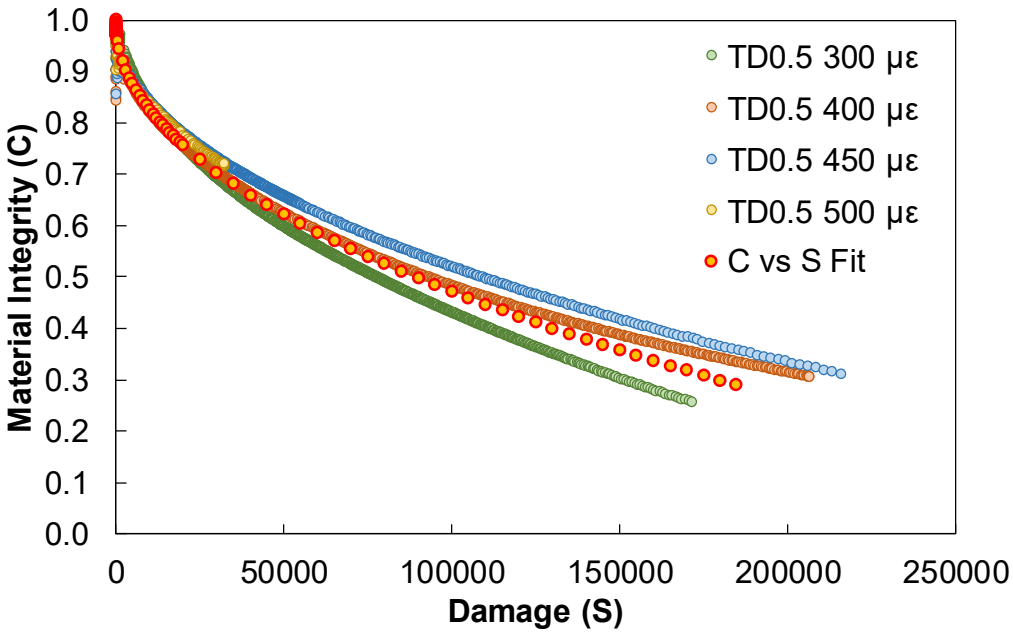

Figure C- 37. C vs S Curve for TD0.5 with Data at All Strain Levels.

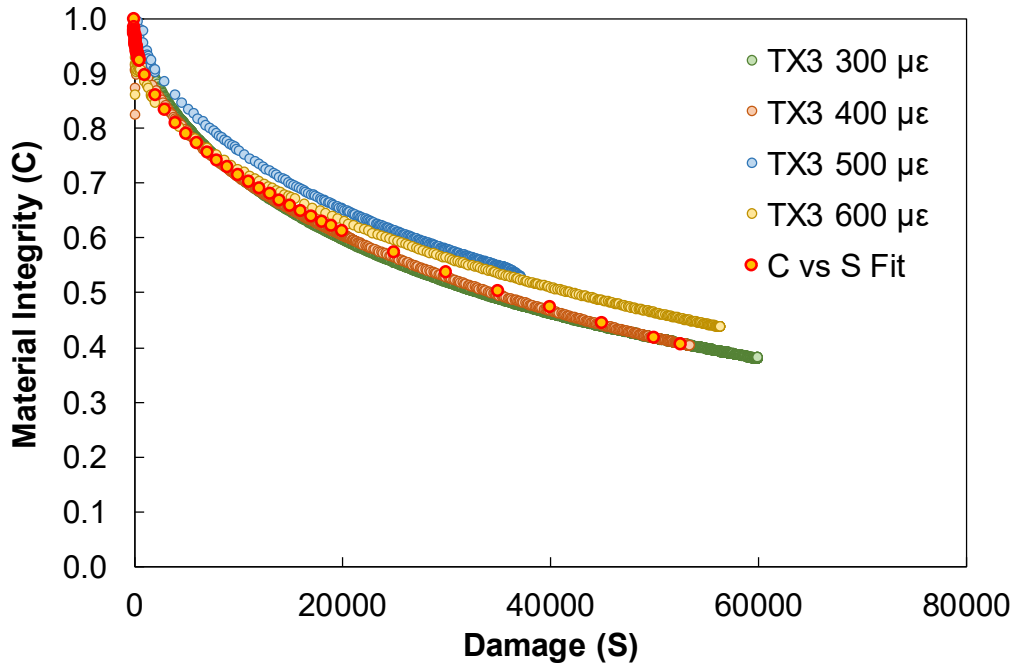

Figure C- 38. C vs S Curve for TX3 with Data at All Strain Levels.

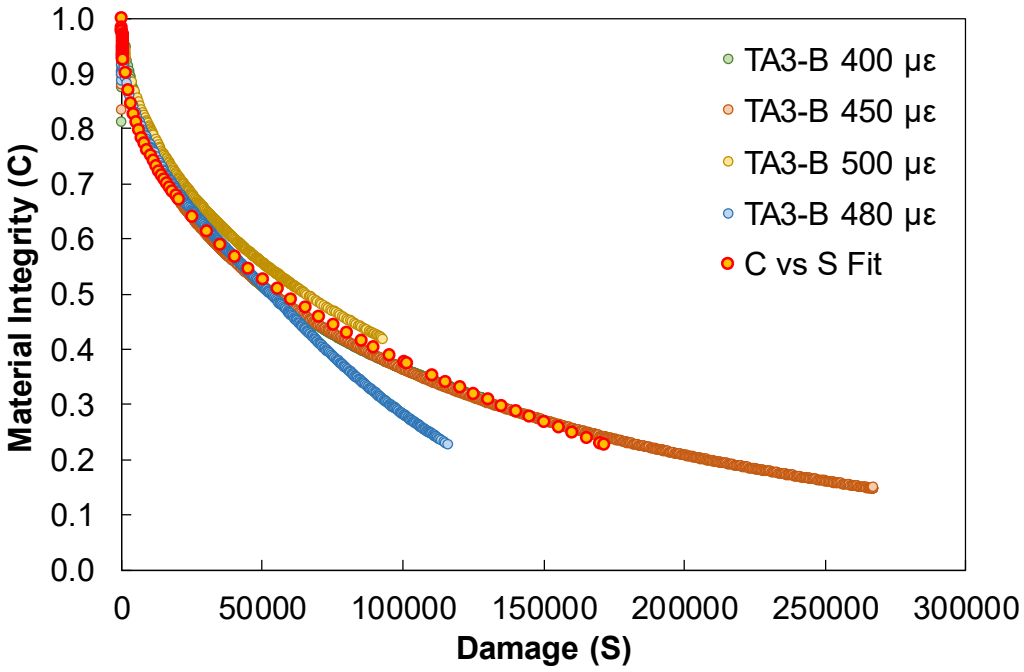

Figure C- 39. C vs S Curve for TA3-B with Data at All Strain Levels.

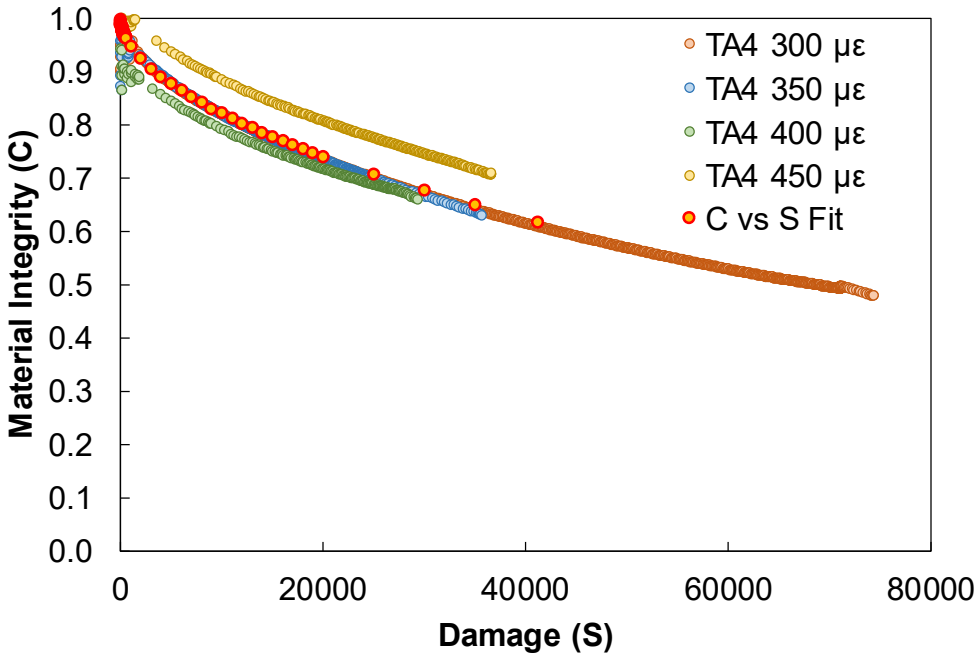

Figure C- 40. C vs S Curve for TA4 with Data at All Strain Levels.

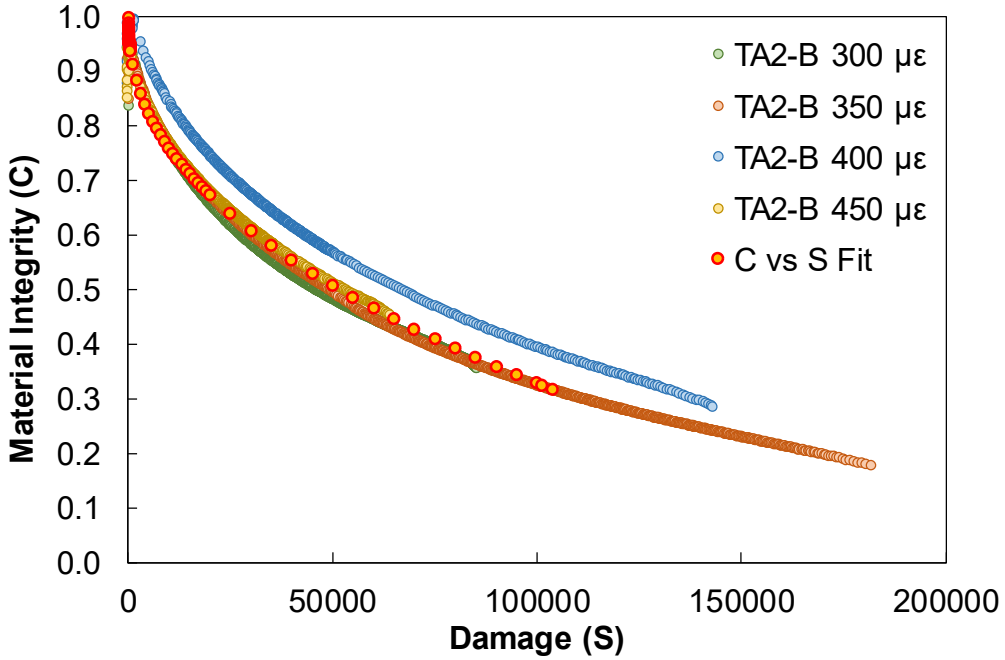

Figure C- 41. C vs S Curve for TA2-B with Data at All Strain Levels.

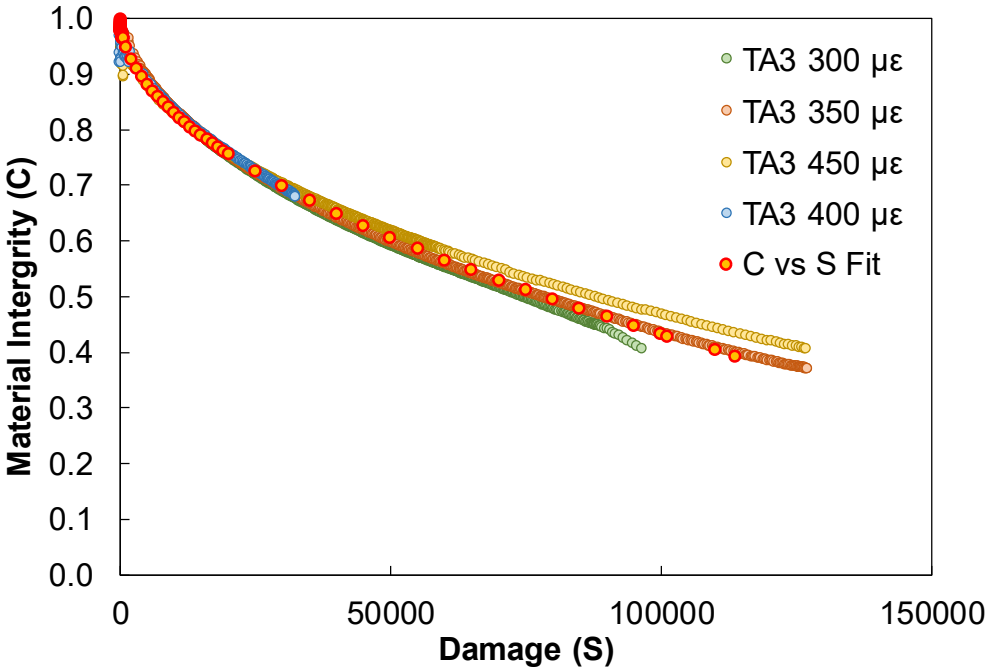

Figure C- 42. C vs S Curve for TA3 with Data at All Strain Levels.

Axial Fatigue Test Data Group 3

The axial fatigue test was performed at four strain levels for each mixture and the data was analyzed using the viscoelastic continuum damage theory (S-VECD) formulation as explained in Appendix A. The result of the S-VECD model is the damage characteristic curve or the *C* vs. *S* curve. In Chapter 7, only the fitted *C vs. S* curve was shown. In the figures below, the *C vs. S* data at all four strain levels along with the fit function is shown for each of the nine mixtures. Also, the regression coefficients C_1 and C_2 of C-S relationship are provided in Table C- 29:

Table C- 28. Actual Number of Cycles to Failure and the Input Machine Strain on the Sample

Mixture	Input Machine Strain	No. of Cycles to Failure (N_f)	Actual Strain @ 80th Cycle (με)	Mixture	Input Machine Strain	No. of Cycles to Failure (N_f)	Actual Strain @ 80th Cycle (με)
TY5	250	57878	256	TX3	500	3090	422
	300	57355	243		600	2290	529
	350	18811	319	TA3_B	400	163495	259
	400	9534	364		450	78943	335
TB5	250	528634	151		500	9908	383
	300	44959	264		480	3387	432
	400	13911	278	TA4	300	68940	212
	450	9506	341		350	7330	235
TB2	300	812306	201		400	1420	330
	400	144355	281		450	1897	310
	500	33739	355	TA2_B	300	273929	224
	600	11901	454		350	92582	272
TD0.5	300	123594	202		400	19679	363
	400	41677	281		450	12919	338
	450	23705	309	TA3	300	60620	221
	500	298	381		350	52818	236
TX3	300	288673	219		400	1699	310
	400	35326	273		450	13309	305

Table C- 29. Best Fit Coefficients C_1 and C_2 of C-S relationship

Mixture	Coefficients	
	C_1	C_2
TY5	0.0058	0.4104
TB5	0.0028	0.4615
TD0.5	0.0021	0.4801
TA4	0.0012	0.5401
TA3-B	0.0064	0.3982
TB2	0.0041	0.4272
TA2-B	0.0039	0.4471
TA3	0.0014	0.5246
TX3	0.0047	0.4459

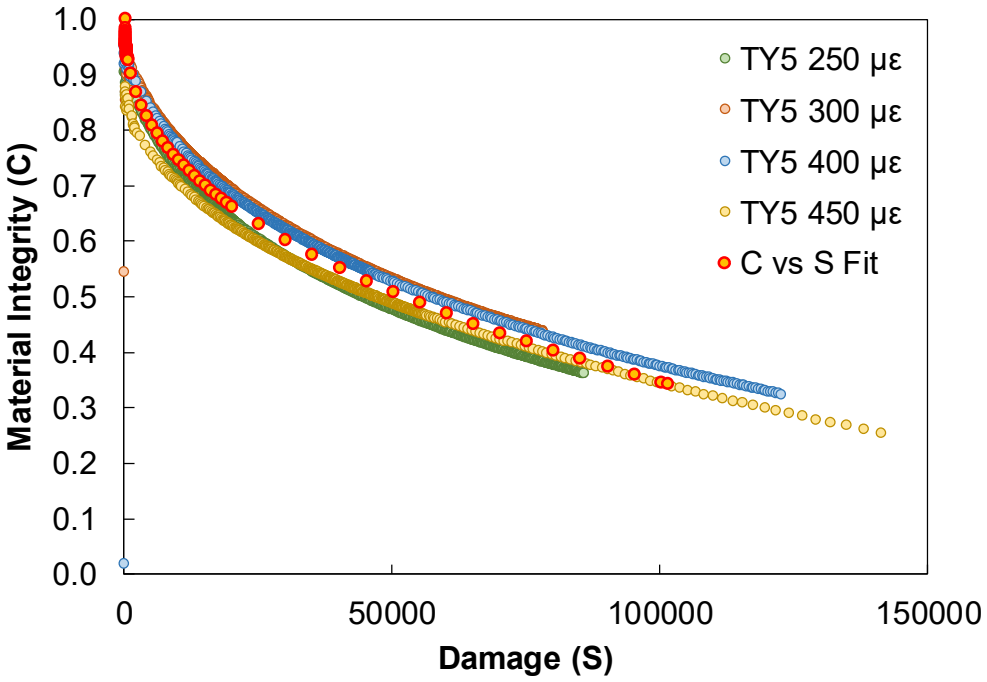

Figure C- 43. C vs S Curve for TY5 with Data at All Strain Levels.

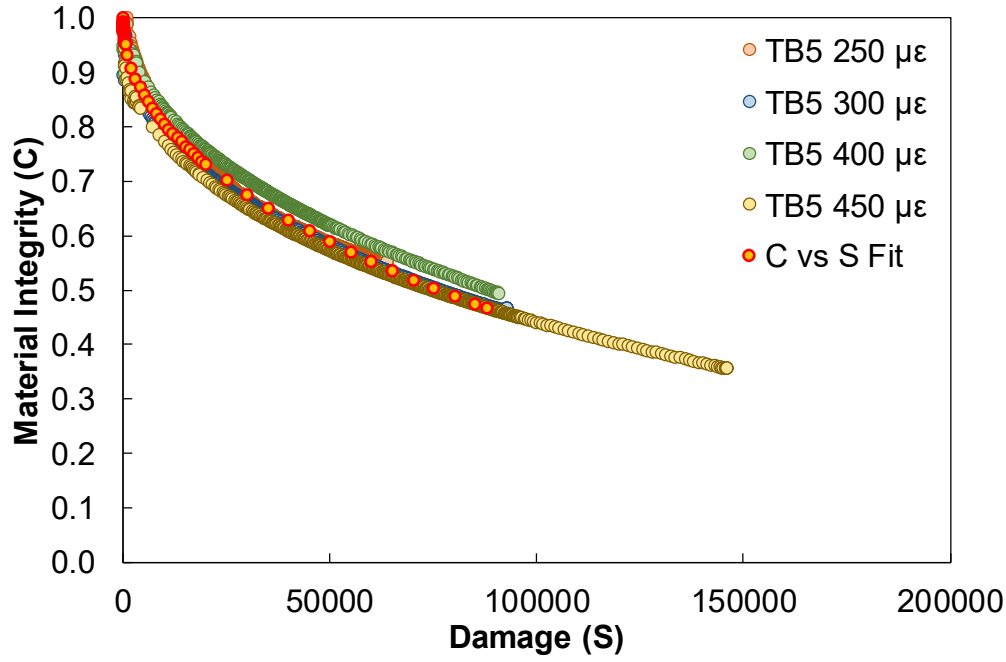

Figure C- 44. C vs S Curve for TB5 with Data at All Strain Levels.

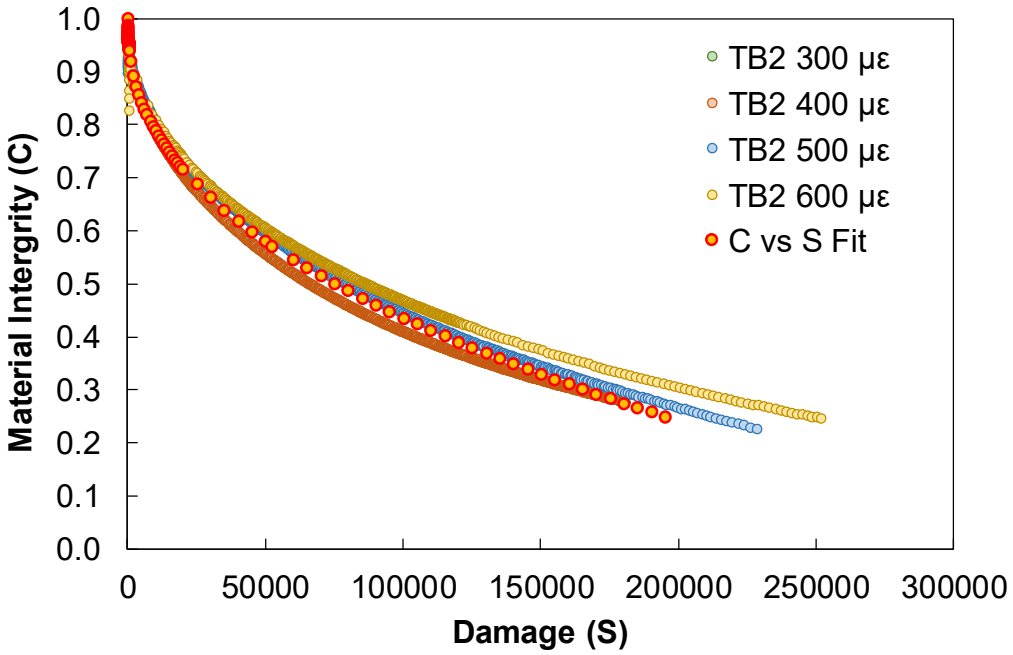

Figure C- 45. C vs S Curve for TB2 with Data at All Strain Levels.

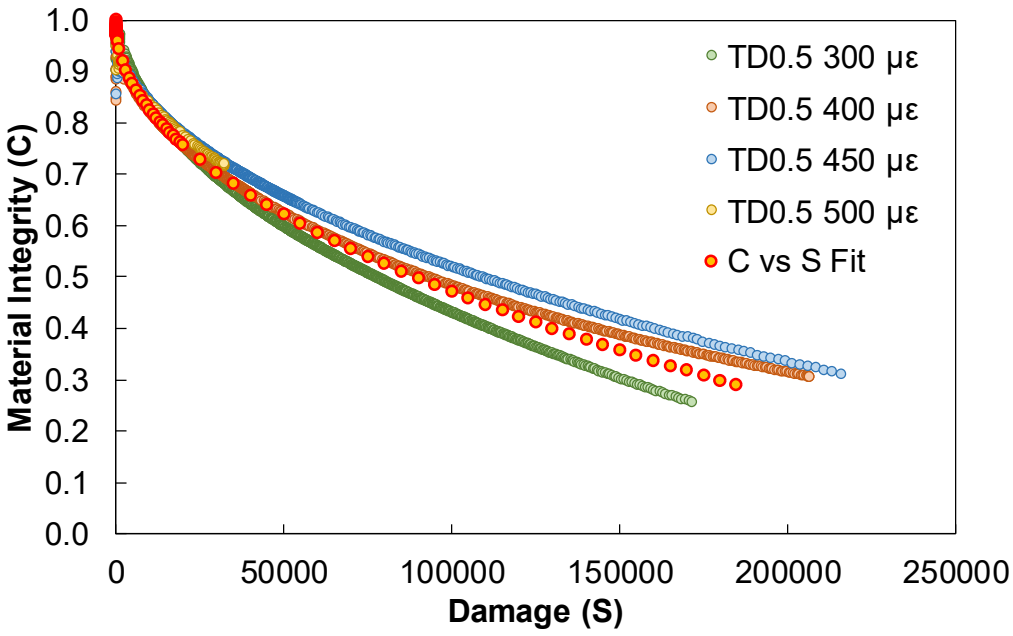

Figure C- 46. C vs S Curve for TD0.5 with Data at All Strain Levels.

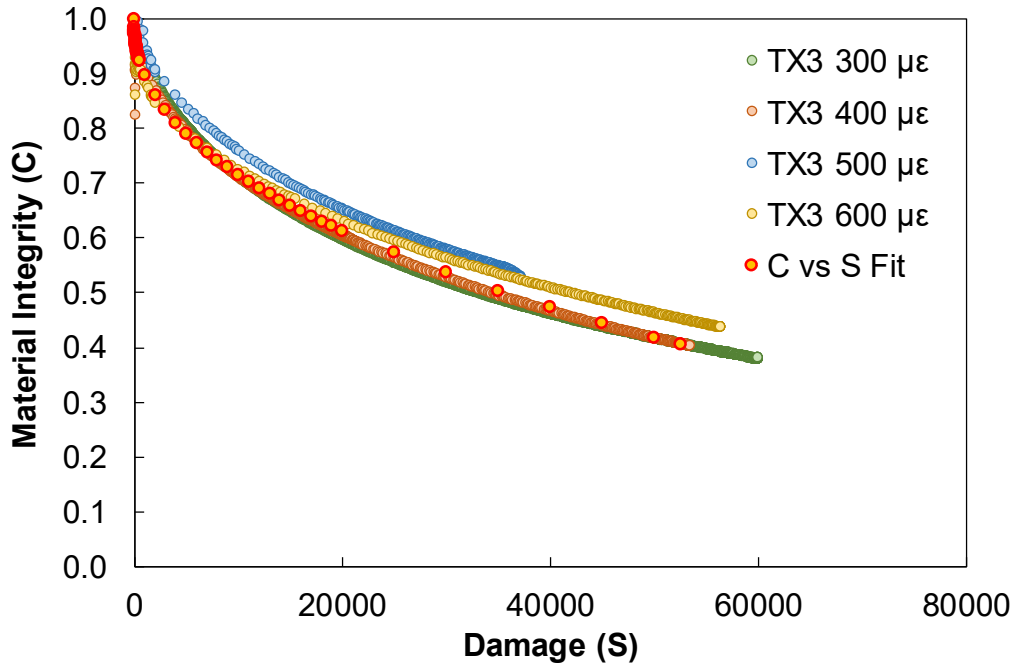

Figure C- 47. C vs S Curve for TX3 with Data at All Strain Levels.

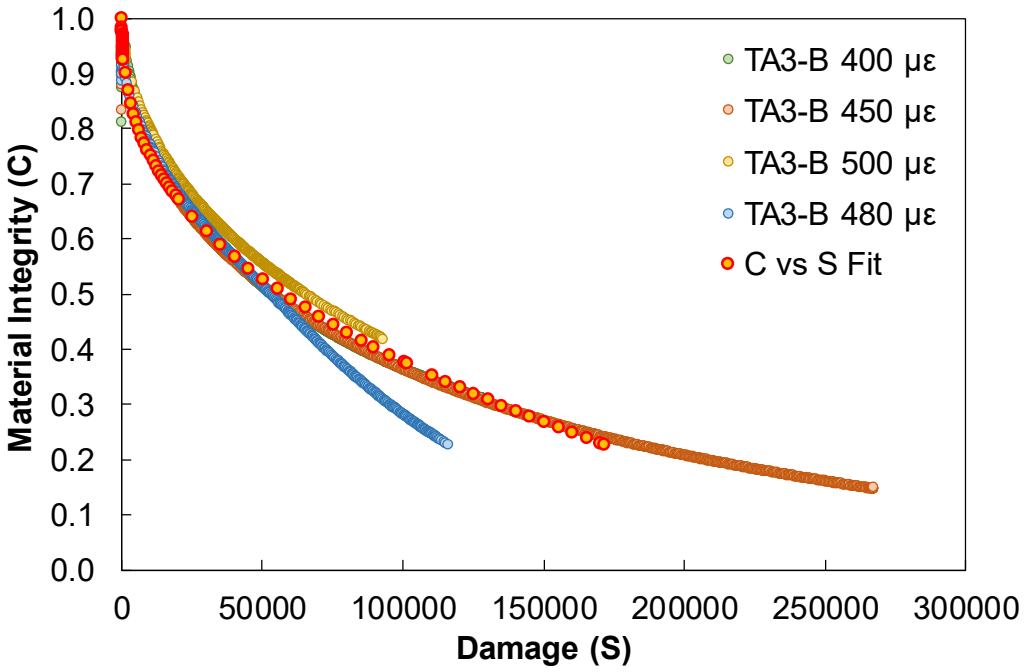

Figure C- 48. C vs S Curve for TA3-B with Data at All Strain Levels.

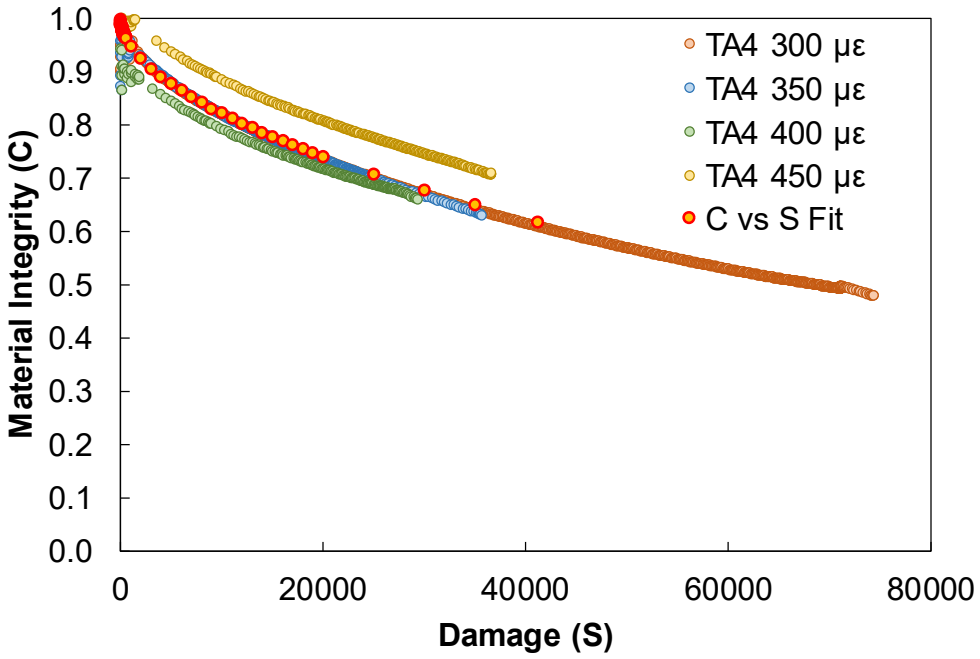

Figure C- 49. C vs S Curve for TA4 with Data at All Strain Levels.

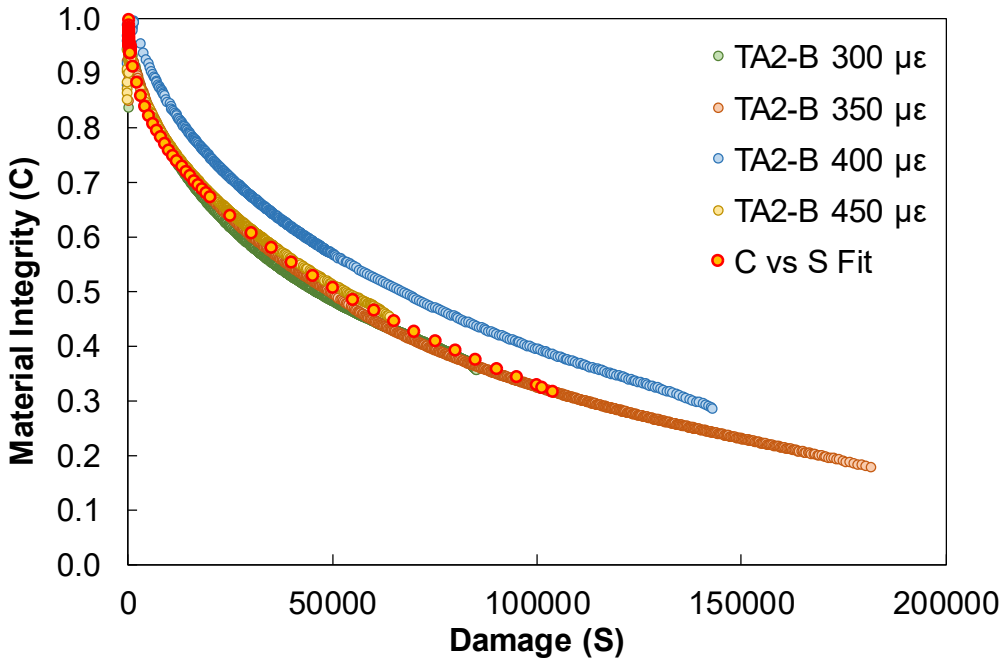

Figure C- 50. C vs S Curve for TA2-B with Data at All Strain Levels.

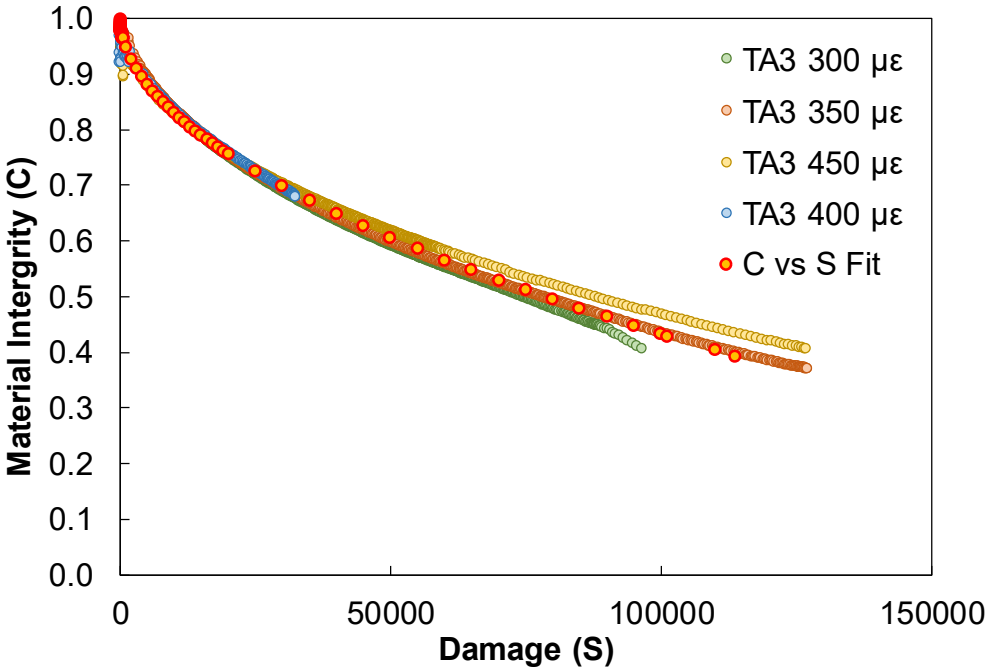

Figure C- 51. C vs S Curve for TA3 with Data at All Strain Levels.